Proceedings

Guang-Zhong Yang and Ara Darzi (Eds.)

---

# The Hamlyn Symposium on Medical Robotics

22-25 June 2013

Imperial College London, UK

Proceedings of
The Hamlyn Symposium on Medical Robotics
22-25 June 2013, Imperial College
London, UK
ISBN: 978-0-9563776-4-7

# Preface

The 6th Hamlyn Symposium on Medical Robotics was held at The Hamlyn Centre for Robotic Surgery and The Royal Academy of Engineering in London, UK on 22-25$^{th}$ June, 2013.

The theme for this year's symposium was "*co-operative control and perceptual docking*" and there was an impressive line-up of leading scientists and engineers in collaborative robotics, navigation and image guidance, in particular, as invited speakers. The speakers invited included Professor Robert Howe and Dr Reiza Rayman, who both provided insights into the cutting edge developments in this field. The keynote was delivered by Gary Guthart, who provided an overview of "*The daVinci System at 14: Clinical Overview, Economics and Opportunities*". This year's annual Karl Storz-Harold Hopkins lecture was delivered by Professor Ferdinand Köckerling on "*Robotics in Bariatric Surgery*".

A total of 102 papers were submitted from 18 countries and after systematic peer review, 62 papers were selected for presentation at the Symposium. The topics covered ranged from training and clinical outcomes, image guidance in robotic surgery, platform design, perceptual docking, intraoperative tissue tracking and characterisation, and new clinical approaches and pilot studies.

The Hamlyn Symposium grew out of the original Imperial College's Cross Faculty Workshops on Medical Robotics funded by the Hamlyn Centre for Robotic Surgery. We are delighted that it is now established as an annual international forum for clinicians, engineers and researchers to exchange ideas and explore new challenges and opportunities in healthcare technologies. We were encouraged to see that this year senior academics and young research fellows had continued to work together to organise a series of workshops on topics including Assistive Robots, Flexible Access Surgery, Regulatory Affairs and Clinical Trials and Outcomes, held before and after the Symposium. These workshops provided a forum for focused discussion about specific research and clinical topics of medical robotics, as well as an informal environment for academic networking. Many of these workshops have resulted in further on-going interactions among the participants and joint research publications.

We would like to thank both the International and Local Programme Committees, the Workshop Organising Committee and the Local Organising Committee for giving up their precious time ensuring timely review of all the papers submitted and helping to provide an excellent symposium programme. The meeting would not be possible without the commitment and hard work of a dedicated team. In particular, we are grateful to Karen Kerr, Su-Lin Lee, Hedyeh Rafii-Tari, George Mylonas, Daniel Elson, Sejal Jiwan, Ruzanna Gulakyan, and Raphaele Raupp for their tireless effort in managing all aspects of the symposium organisation. Last but not least, we are grateful to all the workshop organisers for making all the pre- and post-symposium works a huge success. A photo album is available online (http://www.hamlyn-robotics.org/), which captures the memorable experience of the entire event.

We would like to take this opportunity to give our special thanks to Lady Hamlyn. All of this would, of course, not be possible without the generous philanthropic support from both the Helen Hamlyn Trust and Lady Hamlyn herself.

It was our pleasure to welcome the Symposium attendees to London.

June 2013, London

Guang-Zhong Yang, FREng
Ara Darzi, FRS

# Organisation

## General and Programme Co-Chairs

Guang-Zhong Yang
Ara Darzi

## International Programme Committee

| | |
|---|---|
| Howie Choset | *Carnegie Mellon University, USA* |
| Kevin Cleary | *The Sheikh Zayed Institute, Washington, USA* |
| Paolo Dario | *Scuola Superiore Sant'Anna, Pisa, Italy* |
| Simon DiMaio | *Intuitive Surgical Inc, USA* |
| Pierre Dupont | *Children's Hospital Boston, USA* |
| Hubertus Feussner | *Technical University Munich, Germany* |
| Gabor Fichtinger | *Queen's University, Canada* |
| Dennis Fowler | *Columbia University, USA* |
| Blake Hannaford | *University of Washington, USA* |
| Leo Joskowicz | *The Hebrew University of Jerusalem, Israel* |
| Jacques Marescaux | *University Hospital Strasbourg, France* |
| Bradley Nelson | *ETH Zürich, Switzerland* |
| Vipul Patel | *Global Robotics Institute, USA* |
| Cameron Riviere | *Carnegie Mellon University, USA* |
| Rick Satava | *University of Washington, USA* |
| Ichiro Sakuma | *University of Tokyo, Japan* |
| Lee Swanstrom | *University of Oregon, USA* |
| Mark Talamini | *University of California, San Diego, USA* |
| Russ Taylor | *Johns Hopkins University, USA* |
| Ashutosh Tewari | *Weill Cornell Medical College, USA* |
| Chris Thompson | *Harvard Medical School* |
| Kirby Vosburgh | *Harvard University, USA* |
| Steve Wexner | *Cleveland Clinic Florida, USA* |

## Local Programme Committee

| | |
|---|---|
| Kaspar Althoefer | *King's College London, UK* |
| Thanos Athanasiou | *Imperial College London, UK* |
| Colin Bicknell | *Imperial College London, UK* |
| Nicholas Cheshire | *Imperial College London, UK* |
| Daniel Elson | *Imperial College London, UK* |
| Leonard Fass | *GE Healthcare, UK* |
| Mohamad Hamady | *Imperial College London, UK* |
| Andreas Melzer | *Dundee University, UK* |
| Azad Najmaldin | *St James University Hospital, Leeds, UK* |
| Geoff Pegman | *RU Robotics, UK* |
| Ferdinando Rodriguez y Baena | *Imperial College London, UK* |
| Julian Teare | *Imperial College London, UK* |
| Justin Vale | *Imperial College London, UK* |

## Local Organising Committee

Karen Kerr
Sejal Jiwan
Ruzanna Gulakyan
Su-Lin Lee
George Mylonas
Hedyeh Rafii-Tari
Raphaele Raupp

# Table of Contents

## Poster Presentations

# Karl Storz-Harold Hopkins Lecture

# Robotic Technologies in Bariatric Surgery

F. Köckerling, V. Lange

*Department of Surgery and Center for Minimally Invasive Surgery*
*Academic Teaching Hospital of Charité Medical School*
*Vivantes Hospital Berlin*

*Ferdinand.koeckerling@vivantes.de*

## INTRODUCTION

Robotic surgery has undergone rapid development in recent years. In 2009 around 205,000 robot-assisted procedures were performed worldwide. In the USA there are approximately 1,400 daVinci systems in use, and 400 in the remainder of the world. One major disadvantage of the daVinci procedures is the additional variable costs of 1,600 dollars per procedure, rising to 3,200 dollars per operation when the amortization costs are included.

Equally fast-paced has been the ongoing development of bariatric surgery over the past two decades.

The gold standard in bariatric surgery is the laparoscopic Roux-en-Y gastric bypass (RYGB). Based on recent reports, some 350, 000 bariatric procedures are being performed each year worldwide. Laparoscopic RYGB is arguably one of the most challenging minimally invasive procedures in general surgery, with a steep learning curve of 75 to 100 cases to achieve the highest level of proficiency. It is therefore understandable that studies are being carried out to investigate the use of robotic technologies to facilitate conduct of bariatric surgery. However, when assessing the use of robotic technologies in bariatric surgery, a distinction must be made between conduct of the laparoscopic RYGB procedure with the daVinci system and implementation of the various steps of a laparoscopic RYGB operation with robotic instruments and devices that make the operation swifter and safer.

## MATERIALS AND METHODS

To date, no randomized comparative studies or meta-analyses have been carried out to investigate differences between the robot-assisted DaVinci-RYGB and the classic laparoscopic RYGB. There are only systematic reviews with summaries of the published case series.

## RESULTS

A systematic review by Gill et al (2011) with 1,253 patients with a mean BMI of 46.6 identified an anastomotic leak rate of 2.4%, bleeding rate of 2% and stenosis in 3% of cases [1]. The mortality rate was 0%. Another systematic review by Fourman et al (2012) found similar or lower complication rates compared with traditional laparoscopy [2]. Two studies showed shorter operative times using the robot, but 4 studies showed longer operative times. The learning curve appears to be shorter. A further systematic review with 7 studies and 1,686 patients found a significantly reduced incidence of anastomotic strictures [3]. This study showed no difference in anastomotic leaks, post-operative complications, operative time or length of hospital stay. The largest published series with 1,100 patients from two high-volume centers reported a mean operation time of 155 minutes, an anastomotic leak rate of 0.09% and a zero mortality rate [4]. These impressive data clearly show that the gold standard in bariatric surgery, the minimally invasive Roux-en-Y gastric bypass, can be routinely performed with the daVinci robot with excellent results. The learning curve seems to be shorter than that for the traditional laparoscopic RYGB.

To answer the question, with a high evidence level, of whether the Rouy-en-Y gastric bypass performed with the daVinci robot is better than laparoscopic gastric bypass, larger prospective randomized trials and meta-analyses are needed. Since the differences in outcome are apparently not too great, these studies need correspondingly larger case numbers.

In addition to robotic surgery with the Vinci system, bariatric surgery robotic technologies have been introduced to simplify and optimize the individual operative steps. These include robotic trocars, optical access systems to visualize first trocar insertion, self-retaining retract robots, such as the Nathanson liver retractor, and robotic stapling systems. There are important considerations between tissue and device interaction that can affect staple line outcomes. Stapling technologies are being developed which, via a sensor, are able to determine tissue thickness and, accordingly, apply the appropriate staple height. Likewise, the temporal course of tissue dissection between the rows of clip sutures is controlled by the device so as to assure a more precise tissue incision.

## DISCUSSION

The deployment of such robotic technologies for the individual critical RYGB steps and for simplification of the classic laparoscopic procedure represents a more cost-effective alternative to the daVinci operation,

something that plays an important role in healthcare systems where payments are calculated on the basis of Diagnosis Related Groups (DRGs).

## REFERENCES

[1] Gill RS, Al-Adra DP, Birch D, Hudson M, Shi X, Sharma AM, Karmali S. Robotic-assisted bariatric surgery: a systematic review. The International Journal of Medical Robotics and Computer Assisted Surgery 2011, 7:249-255

[2] Fourman MM, Saber AA. Robotic bariatric surgery: a systematic review. Surgery for Obesity and Related Diseases 2012, 8:483-488

[3] Markar SR, Karthikesalingam AP, Venkat-Ramen V, Kinross J, Ziprin P. Robotic vs. laparoscopiec Roux-en-Y gastric bypass in morbidly obese patient: systematic review and pooled analysis. The International Journal of Medical Robotics and Computer Assisted Surgery 2011, 7:393-400

[4] Tieu K, Allison N, Snyder B, Wilson T, Toder M, Wilson E. Robotic-assisted Roux-en-Y gastric bypass: update from 2 high-volume centers. Surgery for Obesity and Related Diseases 2013, 9:284-289

---

Every year at the Hamlyn Symposium, an invitation is extended to an outstanding researcher in the field of Minimally Invasive Surgery to present the Karl Storz-Harold Hopkins Lecture. Harold Hopkins (1918-1994) was a renowned British physicist whose work on optical physics would be used in television, laser-disc and CD players, and, of course, endoscopy. At the time, existing scopes had poor image transmission and Hopkins' introduction of a glass rod lens to these rigid scopes solved many of these problems, resulting in the creation of a Hopkins rod lens scope. When Karl Storz learned about the Hopkins scope, he agreed to invest in it and added a 'cold light' fibre optic application for illumination – a design that has not changed significantly today. During his career, Harold Hopkins was presented with many awards, not least the Fellowship of the Royal Society and Honorary Fellow of the Royal College of Surgeons. Endoscopy in every field of medicine owes its present state to this very remarkable man and we are honoured to host this annual lecture, in partnership with Karl Storz Ltd.

# Design of a Bone-Attached Robot for Mastoidectomy


N.P. Dillon[1], R.J. Webster III[1,2], T.J. Withrow[1]

[1]*Department of Mechanical Engineering, Vanderbilt University*
[2]*Department of Otolaryngology, Vanderbilt University Medical Center*
*neal.p.dillon@vanderbilt.edu*


## INTRODUCTION

The mastoidectomy is a common otologic procedure performed as a component of other surgeries such as cochlear implantation and acoustic neuroma tumor removal as well as to treat infections in the mastoid. Sub-millimetric accuracy is required to avoid damage to critical anatomic structures embedded in bone such as the facial nerve, sigmoid sinus, external auditory canal, and carotid artery [1]. This accuracy requirement and the fact that many of the critical structures are hidden within the bone, makes it a strong candidate for image-guided robotic surgery.

Several research groups have investigated the feasibility of robotic mastoidectomy using a serial, industrial robot with a surgical drill attached to its end-effector (e.g. [2-3]), an approach similar to the commercial Mako RIO robot typically used for joint repair/replacement surgeries (Mako Surgical Corp., Ft. Lauderdale, FL, USA). Using this approach, patient motion must be monitored so that the drill tip remains correctly registered with the target anatomy at all times. This registration process introduces an additional uncertainty in the overall system, and requires cumbersome error checking to prevent failure of the patient motion monitoring system. To mitigate this added uncertainty and reduce error checking burden, we propose to use a bone-attached robot.

While such a system may be beneficial for registering the robot to the patient anatomy, it also presents an additional set of design challenges. The size constraint of a robot that can be attached directly to the patient restricts the power of the actuators and the stiffness of the entire robot. The workspace of the robot is also limited with the bone-attached approach. Along with the general requirements of traditional mastoidectomy, these constraints must be accounted for in the design of a bone-attached system. This paper outlines several of these design considerations and presents the first version of the robot.

## MATERIALS AND METHODS

The forces required for robotic mastoidectomy were evaluated experimentally by milling formalin-fixed temporal bone specimens using an industrial robot under various cutting conditions. A standard otologic drill and cutting burrs were used and the experiments tested different cutting burr sizes and types, drill angles, cutting depths and velocities, and different bone types (cortical/surface bone and pneumatized bone of the mastoid). The full details of this study are given in [4].

The required workspace for a mastoidectomy robot was evaluated in terms of overall size and the angular requirements of the drill shaft so that all target points are safely reached without removing any unnecessary bone or violating critical anatomy. Ten temporal bone specimens were used in this study. The specimens were formalin-fixed bones previously used by residents in the department of Otolaryngology at Vanderbilt University Medical Center for training purposes. The set of ten was selected by an experienced surgeon who verified the mastoidectomy procedures of each and that the set of bones were representative of a broad range of patient anatomy. The bones were scanned using a Xoran xCAT ENT portable CT scanner (Xoran Technologies, Inc., Ann Arbor, MI, USA). The removed volume of bone for each mastoidectomy was segmented using custom software with a semi-automated approach. The outermost surfaces of the removed volume for each specimen (i.e. the open face of the cavity) were aligned since this is the location where a bone-attached robot would attach to the patient. An overall workspace size was calculated from this aligned set of specimens.

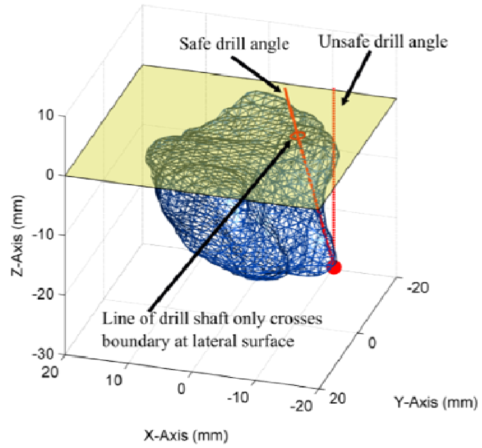



**Fig. 1** One safe and one unsafe drill orientation for a given target point. In the unsafe case, the drill shaft passes through bone outside of the target volume.

The angular workspace was calculated by examining the allowable drill angles for each specimen. The removed volume of bone was discretized into a series of target points (1 point for each voxel of the 0.4 mm x 0.4 mm x 0.4 mm scan) and each individual point was checked to determine the angles required to reach the point without the drill crossing out of the target volume at any point along its shaft (see Figure 1). Two cases were examined: 4 total degrees-of-freedom (1 angular DOF) and 5 total DOF (2 angular DOF). Figure 2 shows the orientation angles of the drill shaft relative to

the top surface of the target volume (lateral surface of skull where the robot is attached). In the 4 DOF case it was assumed that the robot could be attached to the patient at various orientations of its base (φ angle); however, this angle is fixed once the robot is attached. In the 5 DOF case, the drill was free to rotate about φ as well as θ. For each specimen, the range of angles required for the target points to be safely reached was calculated.

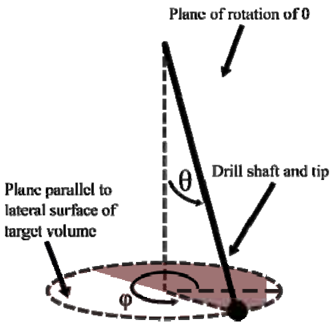



**Fig. 2** Drill orientation angles relative to the patient.

## RESULTS

The mean forces for various cutting conditions ranged from 0.4 N to 3.4 N with maximum force spikes up to 13.1 N. It was determined that larger burrs can remove a specified volume of bone in a given time with lower forces than smaller burrs and utilizing the side of the spherical burr (rather than the distal tip) by adjusting the drill angle relative to the bone surface reduced the transient force spikes. Lower forces were observed in pneumatized mastoid bone versus cortical/surface bone; however, higher variation was observed in the pneumatized bone. Finally, lower forces were observed for a given bone removal rate under cutting conditions that utilized higher cutting velocities and shallower depths rather than slower/deeper cuts.

The required workspace of the robot was calculated to be 41 mm deep with a maximum cross-sectional area at the lateral surface of the skull. The workspace at this surface can be approximated by an ellipse with major diameter of 52 mm and minor diameter of 45 mm. The cross-section decreases as the depth into the skull increases. In the angular workspace analysis, it was determined that at least 98.3% of the target points in each specimen could be reached with a 4 DOF robot (7 of 10 specimens were completely reachable). A drill tilt angle range of 45° was the maximum range required. Additionally, in our opinion, the few target points that were unreachable were not required to perform the surgical procedure. The 5 DOF case allowed for 100% of the target points to be reached for each specimen and reduced the required tilt angle to 35°.

The prototype of this robot (see Fig. 3A) utilizes four SmarAct piezoelectric linear positioners (SmarAct GmbH, Oldenburg, Germany) with a repeatability of approximately one micrometer, travel length of 46 mm, and maximum velocity of 15 mm/s. Additionally, these actuators are available in autoclavable versions, allowing for the entire robot to be sterilized without being disassembled. Three of the actuators control motion in the x-, y- and z-directions, while a fourth actuator controls the tilt in the drill (range of -40° to +40°) through a rack and pinion and worm-wheel gear set. The worm-wheel setup is necessitated by the fact that the torque about the shaft controlling the tilt imposes a higher than allowable force along the axis of that actuator due to the forces at the drill tip and makes this joint non-backdrivable. In a future version, the rack and pinion could be replaced by a rotary positioner. The base plate has three attachment points that allow it to be positioned at several different orientations relative to the patient through a positioning frame that is anchored to the patient and scanned pre-operatively (see Fig. 3B).

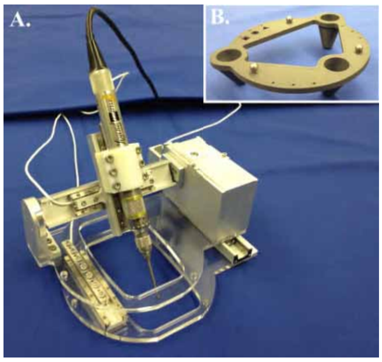



**Fig. 3** Photograph of robot prototype (A) and positioning frame (B) which attaches rigidly to the skull and connects to the robot.

## DISCUSSION

The first prototype for a bone-attached robot for mastoidectomy is discussed in this paper along with several of the design considerations. A 4 DOF robot was chosen to maximize the accuracy and stiffness of the robot while keeping the overall robot as small, light and stiff as possible. The results of the force experiments are important in both robot design and motion planning and were combined with a mastoidectomy workspace analysis to aid in the design process. Future work on this project will include verification that the accuracy of this robot meets the surgical requirements, motion planning for optimal mastoidectomy volume removal, and testing on cadaver temporal bone specimens.

## REFERENCES

[1] Labadie RF, Majdani O, Fitzpatrick JM. Image-Guided Technique in Neurotology. *Otolaryngol Clin N Am* 2007;40:611-624

[2] Danilchenko A, Balachandran, et al. Robotic Mastoidectomy. *Otol Neurotol* 2011; 32(1):11-16

[3] Federspil PA, Geisthoff UW, Henrich D, Plinkert PK. Development of the First Force-Controlled Robot for Otoneurosurgery. *Laryngoscope* 2003 March;113:465-471

[4] Dillon NP, Kratchman LB, Dietrich MS, et al. An Experimental Evaluation of the Force Requirements for Robotic Mastoidectomy. *Otol Neurotol (In Press)*

# Achieving Biocompatibility in Soft Sensors for Surgical Robots

Andrew H. Gosline[1], Veaceslav Arabagi[1], Adil Kassam, Pierre E. Dupont[1]
[1]Boston Children's Hospital, Harvard Medical School, Boston, MA, USA
andrew.gosline@childrens.harvard.edu

## INTRODUCTION

Minimally invasive surgical robotics has enabled clinicians to operate with reduced trauma due to small incisions and long, slender tools. Instrument guidance remains a limiting challenge, however, for procedures in which image quality is limited and haptic feedback is unavailable, e.g., beating-heart intracardiac procedures [1]. To address this need, our group has been investigating sensing technologies that can envelop a robot with a compliant sensing structure and provide clinicians with tissue contact and force information over its entire surface including its tip.

Soft sensors are a particularly promising candidate technology that, to date, have not been considered for medical applications. These sensors are composed of a compliant polymer structure containing channels filled with a conductive liquid. Under load, the channel cross sections deform providing pressure or strain measurements measured as changes in resistance [2].

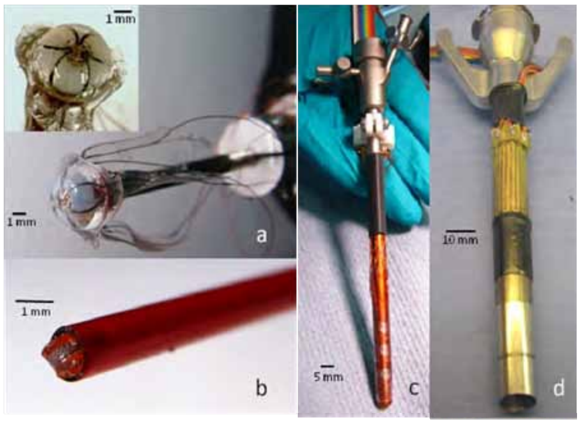



**Fig. 1** Surgical soft sensors created in our lab. (a) Robotic catheter fingertip sensor measuring contact force and contact angle [3]. (b) Tissue contact sensor with diameter of 1.5mm. (c) Neuroendoscope pressure-sensing sleeve for monitoring contact pressure with parenchymal tissue. (d) Pressure sensing laparoscopic port for the Intuitive Surgical da Vinci robot.

Manufactured using soft lithography, these sensors can have a thickness of less than 1 mm, are extremely elastic and compliant, can be manufactured with high sensor densities and can exhibit high pressure sensitivities. Our group has created and evaluated several soft sensor morphologies as shown in Fig 1. These include tip force and contact angle sensors for intracardiac surgery [3], pressure sensing to prevent cortical damage for neuroendoscopy, and pressure sensing to monitor/prevent ischemia on the laparoscopic ports of the Intuitive Surgical da Vinci system. In our work, the soft sensors were made sufficiently thin, ~400µm thick, and sensitive to loads of order 5g.

The majority of prior work in soft sensors has used the conductive liquid metal Eutectic Gallium-Indium (eGaIn). The properties of eGaIn are conducive to soft sensing. Its low channel resistance facilitates simple DC circuitry; its low viscosity enables easy injection into micro-channel geometries and its high surface tension reduces bubble formation and facilitates channel filling and sealing during manufacture. Unfortunately, eGaIn is not biocompatible and the development of alternate conductive fluids is needed for medical applications.

In recent work aimed at green chemistry, the use of ionic salt solutions was proposed. The low viscosity of aqueous salt solutions, however, confounds the production of bubble-free channels and thus, thickening agents are added to facilitate manufacture [4]. Ionic solutions also require AC excitation to prevent ion polarization at the electrodes, and a low voltage must be used to avoid electrolysis of the fluid, which can cause bubble formation and corrosion [4]. This, however, proves advantageous since transforming the signal into the digital domain increases the signal to noise ratio while requiring a relatively simple oscillator circuit to monitor channel resistance via oscillation frequency [5].

While biocompatible, however, aqueous salt solutions do not produce reliable and robust sensors because the gas permeability of the encapsulating polymer is high, which allows the water from the solution to evaporate [4]. In fact, the permeability of siloxane based polymers is so high that they can be used to manufacture permeation pumps for micro-fluidic systems [6].

The contribution of this paper is to demonstrate that NaCl saturated glycerol provides all of the necessary properties for medical soft sensors. This solution is biocompatible [7], sufficiently conductive for sensing applications, adjustably viscous for ease of manufacture and, possessing a boiling point over 300$^{o}$C, it is extremely resistant to evaporation. An initial sensor design and experimental evaluation is presented below.

## MATERIALS AND METHODS

To investigate the efficacy of NaCl saturated glycerol as a biocompatible conductive fluid, we constructed and tested several prototype sensors. NaCl saturated glycerol was made by mixing 99% pure glycerol (Sigma Aldrich G5516-500ml) with food grade NaCl until saturation. The solution was then carefully poured into a syringe through a filter to prevent any undisolved NaCl crystals from being captured. For ease of experimentation, the sensor channel geometry was manufactured using high purity silicone microtubes with

a 305µm inner diameter, and 150µm wall thickness (McMaster-Carr #51845K65). These tubes were cast into a 1.1mm thick layer of PDMS, then injected with NaCl saturated glycerol with a 30g blunt tip needle. Electrodes composed of 280µm diameter nickel-titanium wire were used for corrosion resistance and biocompatibility. These electrodes were inserted through the glycerol filled micro-tubes, then tied off with 5-0 braided silk sutures to prevent leaks. Finally, the sensor was rinsed with isopropanol, then cast in another layer of PDMS to fully seal the liquid channels to the electrode junction. Fig 2 shows a semicircular sensor design, with a radius of curvature of 1mm, for highly localized pressure sensing. The oscillation circuit as proposed by [5] was used to generate an AC square wave. The conductivity of NaCl saturated glycerol is approximately 2 orders of magnitude lower than that of saturated saline, which necessitated a rail-to-rail voltage of +/-2.5V for stable operation.

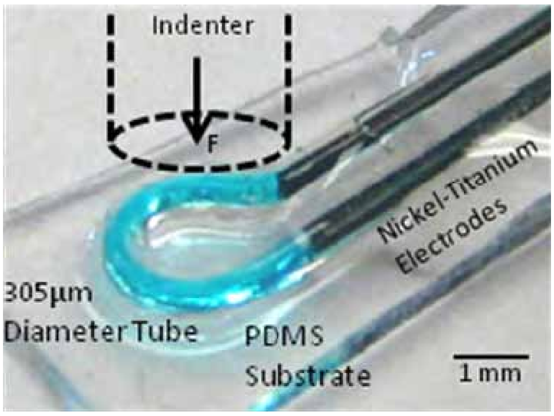



**Fig. 2** Sensor prototype. The sensor is 1.1mm thick and uses glycerol dyed with food colouring for channel visualization.

Two experiments were performed using the sensor prototype shown in Fig. 2. The first experiment measured the change in oscillator period as a function of applied force using a 2.5mm diameter PDMS indenter. The second experiment evaluated the longer-term stability of the sensor in terms of robustness to evaporation, electrolysis and electrode corrosion. For this test, the sensor was put into continuous use for 14 hours with measurements of base resistance and sensor function made approximately every hour to ensure that no adverse electrochemical effects were present.

## RESULTS

The applied force versus measured oscillator period is plotted in Fig. 3. The depicted curve is a two-term exponential function $L = 18.3\exp(0.59T) - 2785\exp(-12.4T)$, where L is the load in grams, and T is the period in milliseconds. Channel collapse was observed at ~43g load, yielding a loss of oscillator signal. Though the data was taken at increments of approximately 5g, it was possible to detect loads as low as ~2g based on the resolution of the oscilloscope's frequency analyzer.

In the second test, no bubble formation due to evaporation or change in base resistance was noted over the 14 hour test period.

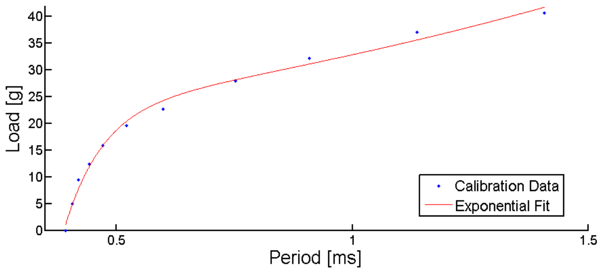



**Fig. 3** Applied Force vs. Oscillator Period

## DISCUSSION

NaCl saturated glycerol is a suitable biocompatible substitute for eGaIn in soft sensors for robotic surgical applications. The experiments discussed herein demonstrate that it is possible to fabricate a soft sensor using biocompatible materials exclusively. Future work will include: 1) sensitivity comparison between biocompatible ionic-based sensors and their eGaIn-based predecessors 2) optimization and refinement of the ionic solution to maximize conductivity and sensitivity 3) development of prototype support electronics with a focus on a low production cost, and 4) integration of the sensing system with a surgical robot platform, for bench-top and in-vivo testing.

Towards clinical adoption, we envision the use of biocompatible soft sensors with inexpensive electronics for amplification and sampling to be a disposable add-on to existing surgical robotic systems.

## REFERENCES

[1] A.H Gosline, N. Vasilyev, E. Butler, C. Folk, A. Cohen, R. Chen, N. Lang N, P. del Nido, P. Dupont. Percutaneous Intracardiac Beating-heart Surgery using Metal MEMS Tissue Approximation Tools. Int. J. Rob Res, 2012: 31(9), 1081-1093.

[2] C. Majidi, R. Kramer, and R. J. Wood, "A non-differential elastomer curvature sensor for softer-than skin electronics," Smart Mat. and Struct., 2011.20, 1–6.

[3] V. Arabagi, A.H. Gosline, R.J. Wood, P. Dupont, "Simultaneous Soft Sensing of Contact Force and Angle for Millimeter Scale Medical Robots" Proc. ICRA IEEE Int. Conf. Rob. Automat. 2013, 4381-4387.

[4] Y. Cheung, Y. Zhu, C.Cheng, C. Chao, W. Leung. " A Novel fluidic strain sensor for large strain measurement". Sensor and Actuators A: Physical, 2008: 149, 401-408.

[5] J.-B. Chossat, Y.-L. Park, R. J. Wood, and V. Duchaine, "A Soft Elastomer Strain Sensor Based on an EGaIn/Ionic Solution Hybrid Construction," Proc. Int Workshop on Smart Materials and Alt Tech for Bio-Inspired Robots and Systems at IROS, 2012.

[6] M. A. Eddings and B.K. Gale, "A PDMS-based gas permeation pump for on-chip fluid handling in microfluidic devices" J. Micromech Microeng, 2006: 16, 2396-2402.

[7] H.A.Sloviter, "Effects of the Intravenous Administration of Glycerol Solutions in Animals and Man", J. Clin Invest, 1958: 37(5), 619-626.

# 3D Ultrasound-Guided Retrieval of Foreign Bodies from a Beating Heart using a Dexterous Surgical Robot

Paul Thienphrapa[1], Aleksandra Popovic[2], Russell H. Taylor[1]

[1]ERC CISST/LCSR, Johns Hopkins University; [2]Philips Research North America

pault@cs.jhu.edu

## INTRODUCTION

Foreign bodies in the heart (e.g. thrombi, shrapnel) can cause a series of adverse symptoms, such as arrhythmia, cardiac tamponade, hemorrhage, infection, embolism, valve dysfunction, and anxiety, and have to be removed surgically[1,2]. The most frequent surgical approach for removing foreign bodies from the heart is a median sternotomy followed by an incision in the heart muscle to gain direct access to the object[3–6]. Median sternotomy is a highly invasive procedure imposing risks such as bacterial mediastinitis, inflammation, bone fracture, and vulnerability to future chest injury. Cardiopulmonary bypass (CPB), which is often used to stop the heart during surgery, is associated with risks of hemolysis, clotting, and air embolism, and can lead to extended durations of procedures as well.

To address the disadvantages of the open surgery, we propose a minimally invasive, transapical approach for retrieving foreign bodies from a beating heart. The task is carried out using a dexterous robotic capture device, with 3D transesophageal echocardiography (TEE) providing internal visualization of the otherwise occluded heart chamber, foreign body, and robot. Under intraoperative ultrasound guidance, the robot moves to secure the target; the setup is illustrated in Fig. 1. This proposed approach represents the initial steps in improving the state of care by reducing risk and mortality, improving postoperative recovery, and potentially reducing operating room times.

In our previous work, we tracked a foreign body in a beating heart phantom to study its behavior[7]. We then found that speed of the foreign body is too fast for a robot to directly pursue it[8]. To provide a relatively slow robot with the ability to retrieve an erratically moving target, we proposed the concept of guiding a robot to a selected location and ambushing the target upon its reappearance to that location. We examined alternate indirect capture strategies[7,9] that relax the level of performance required of a robot. Leading into real-time capture experiments we studied the time evolution of computed capture locations[10].

In this paper, we demonstrate the use of a high dexterity, minimally invasive surgical robot to retrieve a foreign body from a beating heart phantom. Streaming 3D TEE imaging is used to track the foreign body, compute a suitable capture location, and guide the robot to secure it. This effort differs from related works that focus on rigid tools or on manual guidance.

This work was funded in part by Philips Research North America and in part by Johns Hopkins University internal funds.

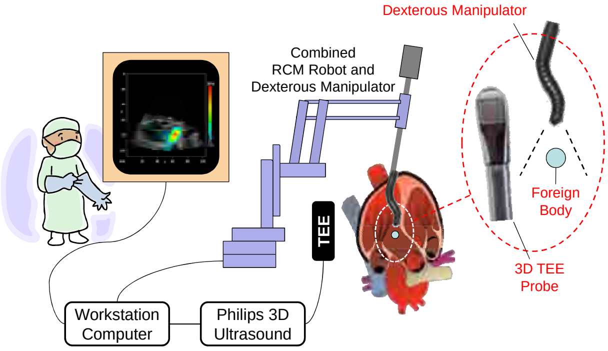



**Fig. 1** Minimally invasive robotic retrieval of foreign bodies from the heart under 3D transesophageal echocardiography (TEE) guidance.

## MATERIALS AND METHODS

The experimental setup (Fig. 2) consists of a Philips iE33 xMATRIX Echocardiography System and X7-2t 3D TEE probe, a beating heart phantom, and a high dexterity robot. The robot consists of a seven-degree of freedom (DOF) IBM/JHU Lars robot holding a JHU snake robot, a 39.5-mm long, 4.2-mm diameter dexterous end effector with four distal DOF. The robot is inserted into the left ventricle of the heart via the apex. Fig. 3 shows this arrangement in detail.

A 3.2-mm steel ball representing a foreign body such as shrapnel is placed in the phantom, and the scene is imaged using the ultrasound probe at a rate of 20 volumes per second. Tracking of the foreign body is performed using a modified normalized cross-correlation method; previous reports[7] describe this process in greater detail.

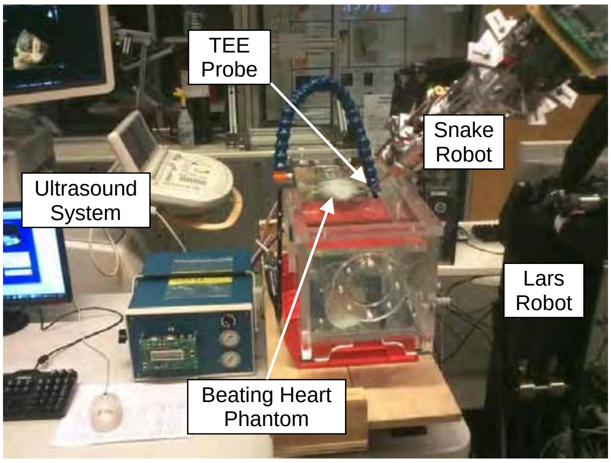



**Fig. 2** Equipment setup for real-time capture experiments.



**Fig. 3** Detailed view of the experimental setup showing the position of the TEE probe, beating heart phantom, and snake robot inserted into the heart at a point near the apex.

## EXPERIMENTS

The attractivity of a small 1.6 × 3.2 mm magnet was tested by advancing the magnet towards the foreign body and measuring the distance at which attraction occurred; this range was found to be 4.2 ± 0.8 mm over 20 repetitions. The magnet is affixed to the tip of the snake robot to represent an abstract capture device with high attractivity within the capture range and negligible effect beyond it. A one-time preoperative registration is done to relate the coordinate systems of the ultrasound volumes and the robot.

Commencing each trial, the robot is teleoperated in coarse control mode to place the tip of the snake robot at the entry point of the beating heart phantom. This establishes the virtual remote center of motion (RCM), from which point the robot operates autonomously.

Then, the foreign body is interactively selected from still images to define a template to be tracked in the live image stream. Computation of capture locations based on spatial probability is then initiated. Once a suitable capture location is found, the tracker commands the robot to said location. When the end effector reaches its destination, visual inspection is used to determine whether the foreign body has been captured. The robot is then withdrawn from the beating heart phantom, and success or failure of the attempt is recorded.

## RESULTS AND DISCUSSION

An example foreign body capture sequence is shown in Fig. 4. The foreign body was extracted successfully in 14 out of 17 attempts (82.4%). In two of the three failed attempts, the foreign body shifted to a different location after a capture location was found; this phenomenon has been noted in our prior studies. The other failed attempt can be attributed to premature withdrawal of the robot before it completed its capture trajectory.

The mean observation time before executing a capture was 29.6 ± 6.9 seconds, with extrema of 21.6 and 46.3 seconds. We reported an observation time for this method of roughly 20.0 seconds previously[10], while noting large variations between trials. Such variability can be explained by the irregular motions traced by the foreign body. In light of these considerations, the values obtained in this study appear to be within reason.

The retrieval process was completed in 97.7 ± 21.6 seconds. Though governed largely by human discretion, this figure serves as a reference in the context of cardiac procedures, which often last several hours. Potentially, the perioperative time incurred by robotic aspects would be minimal, and more sophisticated techniques can be used to improve outcomes. These results demonstrate the viability of using a slow, dexterous robot to capture an erratic cardiac target under 3D ultrasound guidance. Future work will include workflow optimization, sterility, tooling for capturing multiple types of targets, and possible integration of real-time X-ray imaging.

## REFERENCES


[1] Marshall AJ, Ring NJ, Newman PL. An unexplained foreign body in the myocardium. J. Royal Soc. Med. 2002; 95: 250–251.

[2] Symbas PN, Picone AL, Hatcher CR, Vlasis-Hale SE. Cardiac missiles. A review of the literature and personal experience. Ann. Surg. 1990; 211(5): 639–48.

[3] United States Department of Defense. Emergency War Surgery: Third US Rev, s.l., 16: Thoracic Injuries 2004.

[4] Actis Dato GM, Arslanian A, Marzio PD, Filosso PL, Ruffini E. Posttraumatic and iatrogenic foreign bodies in the heart: report of 14 cases and review of the literature. J. Thorac. Cardiovasc. Surg. 2003; 126(2): 408–414.

[5] Evans J, Gray LA, Rayner A, Fulton RL. Principles for the management of penetrating cardiac wounds. Ann. Surg. 1979; 189(6): 777–784.

[6] Nessen SC, Lounsbury DE. War Surgery in Afghanistan and Iraq: A Series of Cases, 2003-2007, s.l. Department of the Army, Office of the Surgeon General and Borden Institute, 14: Thoracic Trauma 2008.

[7] Thienphrapa P, Elhawary H, Ramachandran B, Stanton D, Popovic A. Tracking and characterization of fragments in a beating heart using 3D ultrasound for interventional guidance. MICCAI 2011; 6891: 211–218.

[8] Thienphrapa P, *et al*. A system for 3D ultrasound-guided robotic retrieval of foreign bodies from a beating heart. IEEE/EMBS BioRob 2012; 743–748.

[9] Thienphrapa P, Ramachandran B, Elhawary H, Taylor RH, Popovic A. Multiple capture locations for 3D ultrasound-guided robotic retrieval of moving bodies from a beating heart. SPIE Medical Imaging 2012; 8316.

[10] Thienphrapa P, *et al*. Intraoperative analysis of locations for 3D ultrasound-guided capture of foreign bodies from a beating heart. Hamlyn Symp. Medical Robotics 2012.

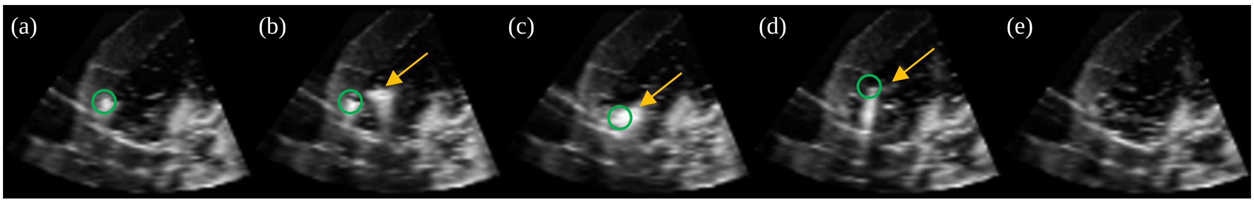




**Fig. 4** Image sequence showing different phases of foreign body capture. (a) Foreign body (circle) in the heart ventricle just before a capture location is determined. (b) Dexterous robot (arrow) approaches capture location. (c) Robot captures foreign body. (d) Robot leaving heart with foreign body attached. (e) Heart empty after foreign body is extracted.

# Virtobot - Robot System in Forensic Medicine

Wolfgang Ptacek[1], Lars Ebert[2], Martin Fürst[1], Robert Breitbeck[2], Michael Thali[2], Gernot Kronreif[1]

[1]ACMIT - Austrian Center for Medical Innovation and Technology, Integrated Microsystems Austria GmbH, 2700 Wiener Neustadt, Austria

[2]Institute of Forensic Medicine, University of Zurich, 8057 Zurich, Switzerland

wolfgang.ptacek@acmit.at

## INTRODUCTION

Virtual autopsy, or Virtopsy® [1], originated from the goal of implementing diagnostic techniques such as computed tomography (CT), magnetic resonance imaging (MRI), three-dimensional (3D) photogrammetry and surface scanning, and post mortem minimally invasive biopsy, in order to objectify medico-legal investigations [2]. The Virtopsy® concept was presented in 2000 as a systematic approach to complement or substitute standard forensic procedures [3]. For further optimization of the developed work-flow, a first prototype of a robotic system for post-mortem surface scanning and image guided biopsy has been developed and implemented at the Institute of Forensic Medicine in Bern, Switzerland, in 2008 [4]. Based on the experience from this system setup, an enhanced prototype was developed at the Institute of Forensic Medicine, University Zurich, Switzerland, and operation started in July 2012. This paper describes the Virtobot robot system in general and the new system functionality in particular. In addition, the paper reports some first performance data and experiences from routine use.

## MATERIALS AND METHODS

The Virtobot system serves as a multifunctional robotic system capable of performing major tasks of the Virtopsy® work-flow. A six axis robotic arm (Stäubli TX90L, Stäubli International AG, Pfäffikon/CH) is combined with a tailored ceiling-mounted linear guide unit (range of motion: 4 meters) which is located above the CT gantry and aligned with the CT patient couch. The base of the robotic arm is mounted onto a dedicated lifting axis to allow moving the robotic arm to a parking position above the CT-gantry in order to deal with the specific space restrictions. Different from the first prototype system in Bern, a fully automated tool changing unit now allows the robotic manipulator to use corresponding end-effectors to perform different tasks of the Virtopsy® work-flow. Figure 1 shows the three different end-effectors that are currently included and stored in a tool magazine station. In the present configuration, the following three tools are available: a precise optical 3D surface scanner (GOM ATOS Compact Scan, Gesellschaft für optische Meßtechnik GOM GmbH, Braunschweig/D), a digital SLR camera (Nikon D700, Nikon Corporation, Tokyo/JP), as well as a custom made biopsy tool (Integrated Microsystems Austria GmbH, Wiener Neustadt/A). Figure 2 shows the robotic arm equipped with the 3D-surface scanner that generates a high resolution model of the corpse in order to document patterned injuries. Scanning takes place in 5 scanning lines with 5 points each. Both lines and points can be specifically adapted via the control software. The surface data can be enhanced by adding texture data captured with the SLR camera. Aside from documentation purposes, 3D surface data can be used for virtual reconstructions of the incident [5].



**Fig. 1** Virtobot tool magazine. From left to right: 3D surface scanner, digital SLR camera, biopsy tool.

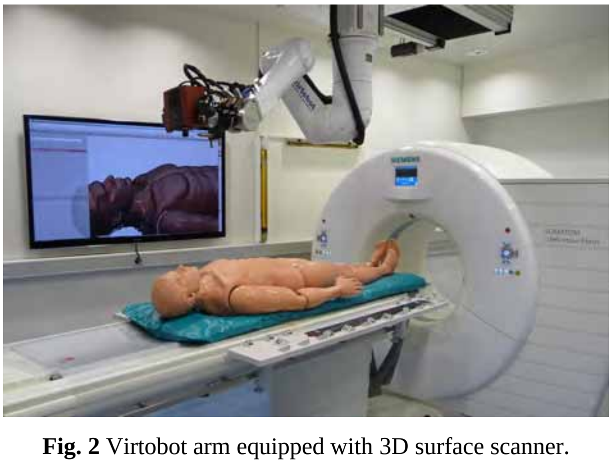


**Fig. 2** Virtobot arm equipped with 3D surface scanner.

Figure 3 shows the custom made biopsy tool that allows the automatic and precise placement of coaxial introducer needles based on CT data. The needles can be used to harvest tissue or liquid samples and place guide wires to assist pathologists in finding small foreign bodies during autopsy.

A set of software packages is integrated into the Virtobot setup for different tasks. The Virtopsy®

control center (VCC) coordinates the entire work-flow and controls the robot. During surface scanning, pre-programmed scan positions and photogrammetric photo positions can be selected in the VCC, and are processed automatically. In addition, the robotic arm can be manually controlled in joint or tool coordinates to provide additional grade of flexibility in choosing special scan/photo positions. The performed Virtopsy® work-flow is been logged and all captured data are stored. The GOM application software V7.5 SR1 operates the 3D surface scanner and the photo-grammetry camera and processes the data. It also calculates the fully textured true to scale 3D polygon model from the surface of the skin.




**Fig. 3** Biopsy tool attached to the Virtobot arm.

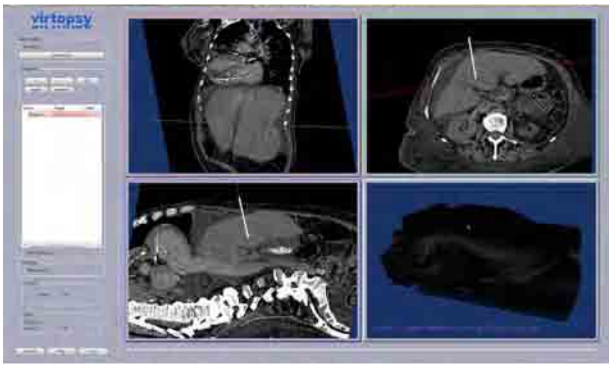



**Fig. 4** Navigation software for tissue sample path planning.

The surgical navigation software allows for biopsy trajectory planning. Passive optical markers and an infrared tracker are used to determine the position of the biopsy tool and the body in space. For registration of the CT dataset with the actual body, radiopaque tungsten balls are placed at the marker center and automatically detected by the navigation software. During trajectory planning, target and entry point, as well as the orientation of the end-effector are defined. (Figure 4)

## RESULTS

Both Virtobot systems are used in daily routine. Up to now the Bern system has been used in 52 cases; the system in Zurich has provided robotic assistance for automated surface scanning in 16 cases: six victims of traffic accidents, two cases of blunt trauma, six gunshot wounds, one knife wound, and one case of strangulation. Six of these cases are included in court forensic reports. One particular advantage of the use of the Virtobot system is the significant increase of efficiency [4]. A manual surface scan of one side of a victim using a standard tripod takes approximately 30 min. By using Virtobot, this time could be reduced to approximately 15 min.

For evaluation of the accuracy of needle placement, a preliminary accuracy study was conducted based on a biopsy phantom [4]. Calibration of the robot was performed with six pivot points and a mean RMS of 2.3 mm (±0.04 mm, $n$ = 13). The cone centre for every pivot point was determined with an accuracy of 0.5 mm (± 0.06 mm, $n$ = 78). Two phantoms were prepared and a total of 13 needles set. The mean accuracy was 3.2 mm (±1.9 mm, $n$ = 13). Up to now automatic needle placement has been performed on three real cases to obtain body liquids like urine or blood and retrieve tissue samples from organs of interest.

## DISCUSSION

The Virtobot system automates tasks that are either repetitive or require high accuracy. It allows fully automated surface documentation and post-mortem minimally invasive image guided needle biopsy. Two prototypes of the robot system have been realized so far. The demonstrated reduction of process time for the Virtopsy® work-flow by implementation of Virtobot could be further improved by updating the navigation software with an automatic registration and automation of the tool change. Within the Virtopsy® project, the Virtobot system is a valuable tool to gather objective data in a minimally invasive manner. While surface documentation of patterned injuries allows for incident reconstructions, image guided biopsy contributes to correlate radiological with histological findings, which would be impossible if tissue samples are taken during autopsy. In the future it might be possible to use the Virtopsy® findings to determine if a further autopsy is necessary to gain additional evidence in forensic cases.

## REFERENCES


[1] www.virtopsy.com.

[2] Aghayev E, Thali MJ, Sonnenschein M, Jackowski C, Dirnhofer R, Vock P. Post-mortem tissue sampling using computed tomography guidance. Forensic Sci Int 2007;166 (2–3):199–203.

[3] Thali MJ, Yen K, Schweitzer W, et al. Virtopsy, a new imaging horizon in forensic pathology: virtual autopsy by post mortem multislice computed tomography (MSCT) and magnetic resonance imaging (MRI) – a feasibility study. J Forensic Sciences 2003; 48(2): 386–403.

[4] Ebert LC, Ptacek W, Naether S, Fürst M, Ross S, Buck U, et al. Virtobot - a multi-functional robotic system for 3D surface scanning and automatic post mortem biopsy. Int J Med Robot 2010;6(1):18–27.

[5] Buck U, Naether S, Braun M, et al. Application of 3D documentation and geometric reconstruction methods in traffic accident analysis: with high resolution surface scanning, radiological MSCT/MRI scanning and real data-based animation. Forens Sci Int 2007; 170: 20–28.

# Robotic, Registered, Transrectal Ultrasound Guidance during da Vinci Radical Prostatectomy: Initial Clinical Experience

O. Mohareri[1], J. Ischia[2], C. Schneider[1], P. Black[2] and S. E. Salcudean[1]

[1]*Department of Electrical and Computer Engineering, University of British Columbia*

[2]*Department of Urologic Sciences, Faculty of Medicine, University of British Columbia*

*tims@ece.ubc.ca*

## ABSTRACT

We describe the early clinical application of a robotic transrectal ultrasound (TRUS) system for real-time monitoring of the prostate and periprostatic anatomy during robot-assisted laparoscopic radical prostatectomy (RALRP). Two patients with clinically organ-confined prostate cancer undergoing RALRP at our institution agreed to participate in this CREB-approved (clinical research ethics board) pilot study. Before docking the da Vinci robot, our robotic TRUS system [1] was attached to the foot of the operating table using the MicroTouch Brachytherapy stabilizer passive arm (CIVCO Medical Sloutions, Kalona, IA). A bi-plane TRUS transducer (Ultrasonix Medical Corporation, Richmond, BC) was placed and adjusted to provide optimal transverse and sagittal images of the prostate and its surrounding structures. The set-up of the TRUS robot and the da Vinci in the operating room is shown in Fig. 1.

The TRUS robot was used during the procedure to remotely control the rotation angle and insertion depth of the TRUS transducer to provide a full view of the prostate even when the anatomy was shifted during the procedure. Furthermore, a calibration technique [2] was performed between the TRUS transducer and the da Vinci instrument, to enable the TRUS imaging plane to automatically track the tip of the da Vinci instrument. In order to achieve automatic tool tracking, the surgeon was asked to press the tool tip of a da Vinci instrument (EndoWrist Monopolar curved Scissors) against the anterior surface of the prostate in four locations. The instrument tip, visible as a hyperechoic focal point in the B-mode images, was then located in the TRUS volume and the homogenous transformation relating the da Vinci coordinate system to that of the TRUS was obtained as previously explained in [2]. The calibration procedure was completed in less than two minutes and was valid throughout the surgery with an accuracy of within 2 mm as computed in our previous *in-vivo* animal study [3]. With such a tracking accuracy, movement of the tool tips was constantly visible in the ultrasound image, showing the location of the tools relative to the target anatomy (Fig. 2 d-f). During each procedure, real-time TRUS images were relayed to the surgeon and used to precisly identify the location of the bladder neck, the apex, and the dissection planes of the neuro-vascular bundles (NVB). Automatic tool tracking was activated during all critical stages of the surgery to faciliate real-time TRUS navigation using the same instruments being used during the procedure.

Complete robotic TRUS evaluation was successful in both patients. No major complications occurred and the transducer remained in place until the end of the procedures. We conclude that real-time robotic TRUS guidance during RALRP is feasible and safe and it can provide the console surgeon with valuable anatomic information, with the aim of maximizing oncologic and functional outcomes. The automatic tool tracking system provided an easy to use TRUS guidance system to the surgeons since the surgical tool was used to automatically control and adjust the imaging plane, making it an easy and intuitive system for surgeons to use.

## REFERENCES

[1] T. Adebar, S. Salcudean, S. Mahdavi, M. Moradi, C. Nguan and L. Goldenberg, "A robotic system for intra-operative trans-rectal ultrasound and ultrasound elastography in radical prostatectomy," in *Proc. IPCAI* 2011, LNCS 6689, pp. 79-89, 2011.

[2] T. K. Adebar, O. Mohareri and S. E. Salcudean, "Instrument-Based Calibration and Remote Control of Intraoperative Ultrasound for Robot-Assisted Surgery" *in Proc. IEEE Int. Conf. on Biomedical Robotics and Biomechatronics*, pp. 38-43, 2012.

[3] O. Mohareri, C. Schneider, T. Adebar, M. Yip, P. Black, C. Nguan, D. Bergman, J. Sorger, S. DiMaio and S. E. Salcudean, "Ultrasound-based image guidance for robot-assisted laparoscopic radical prostatectomy: initial in-vivo results," to appear in *Proc. IPCAI* 2013.

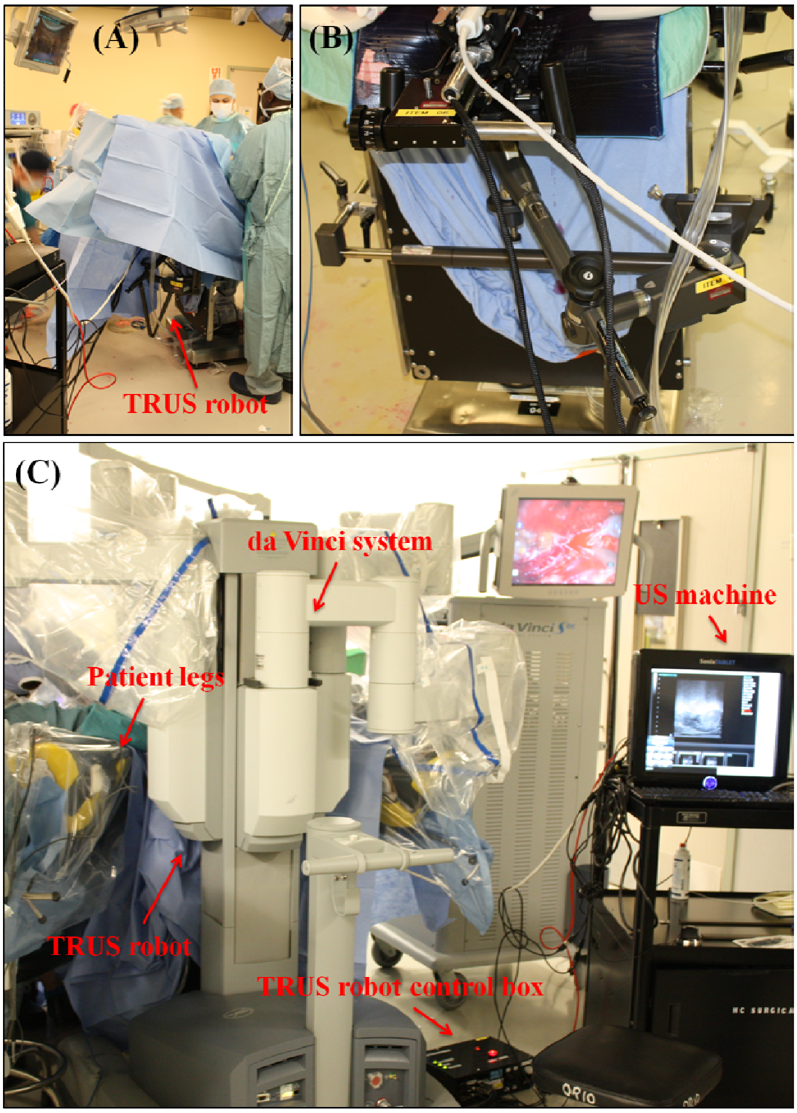



**Fig. 1** Intraoperative robotic TRUS during RALRP, (a) TRUS robot attached to the operating table in Trendelenburg position before docking the da Vinci system, (b) TRUS transducer and robot attached to the foot of the operating table using the MicroTouch Brachytherapy stabilizer passive arm, (c) operating room setup of the TRUS robot and the da Vinci system**.**

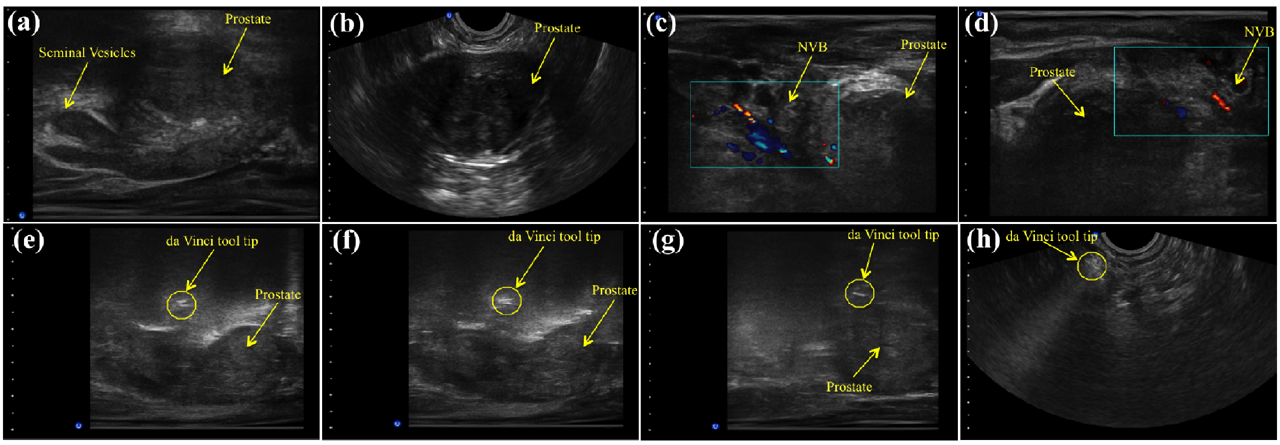



**Fig. 2** Intraoperative TRUS images of the prostate and its surrounding structures, (a) prostate and seminal vesicles in sagittal B-mode TRUS image, (b) transverse B-mode image of the prostate gland, (c, d) prostate and NVB visualization using Bmode and Doppler ultrasound, (e, f, g) da Vinci instrument tip visible in the TRUS images in different stages of the procedure while the automatic tool tracking was activated, (e) da Vinci instrument tip in transverse US image**.**

# Backlash Compensation Method for Wire Drive Forceps Mechanism under Various Loading Conditions

I. Sakuma, Y. Tsukahara, T. Ando, H.Liao, E. Kobayashi

*School of Engineering, The University of Tokyo*

*sakuma@bmpe.t.u-tokyo.ac.jp*

## INTRODUCTION

Wire drive mechanism is widely used for forceps with multi degrees of freedom. However the backlash and stick slip phenomena found in the mechanism made it difficult to control the makanism precisely. Kaneko et al proposed physical model to represent effect of friction and elongation of the wire in tendon driven mechanism with flexible sheath[1]. It was demonstrated that the amount of backlash is dependent on wire tension. The Stick-slips motion sue to static friction of the joint also affects the amount of backlash. Since Stick-slip motion is inherently unstable, it is difficult to estimate the amount of backlash under various loading conditions. In this study, we proposed a new method to compensate backlash under various loading conditions.

## MATERIALS AND METHODS

### Experimental System

To investigate changes in wire displacement and tension of the wire, the experimental system shown in Fig.1 was constructed. In the present study, pre-tension was provided by an electric motor where the generated torque by the electric motor was control to be constant by PID controller. Wire displacement was estimated by the rotation angles of the two electric motors for actuation side and pre tension generation side. The tensions of the both wires were measured by two load cells installed in both sides as shown in Figure 1. One motor was used to control the wire tension, and the other motor was used to set the rotation angle of the gear. The forceps mechanism used is shown in Figure 2. Two load cells can be used also for the estimation of applied force on two blades.

We used forceps mechanism proposed by Nishizawa et al. [2] as shown in Fig. 2. In this mechanism, the path length of the wires for the two tip blade is kept constant when the bending is generated by the mechanism. Bending of the mechanism is realized by rotating the gear 1 in Fig. 3 using two wires attached to it.

Backlash compensation

Generated torque by the electric motor was adjusted constant by a PID controller. When the direction of the gear's rotation is reversed, the motion of the gear does not follow the displacement of the wire since static friction of the joint prevents the gear from moving. The initiation of the reverse movement can be identified by monitoring the displacement of the wire of the tension control side. When the gear starts to move in reverse direction, abrupt change in wire displacement of the wire is observed in the wire tension control system. In this study, we utilized this phenomenon to detect the initiation of reverse motion. The amount of backlash due to this stick slip motion was estimated as the amount of displacement of wire of the position control side before the initiation of movement of the wire of the torque control side.

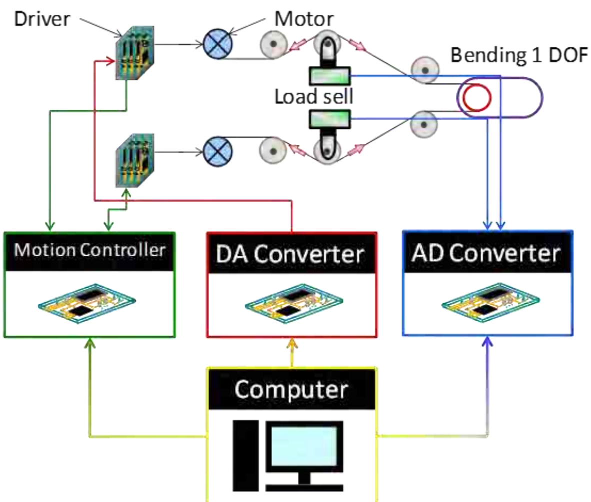



**Fig. 1** Experimental System

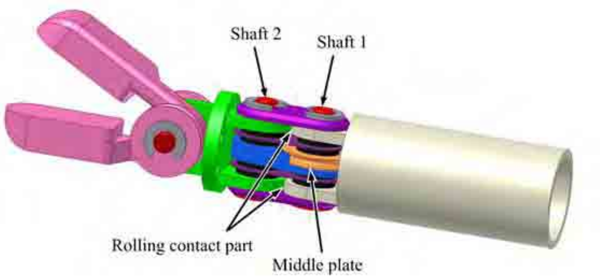



**Fig. 2** Mechanism of the 3 DOF forceps

## RESULTS

Fig.4 shows the changes in displacement of wire of the position control side expressed as "input angle", the bending angle of the forceps, and the rotation of the motor controlling the wire tension expressed as "Motor Speed". The bending angle was estimated by measuring distance between the plate attached at the tip of the forceps and laser displacement meter (LB-62 、KEYENCE Tokyo, Japan). Wire tension was controlled

as large as 10 N. The abrupt change in motor speed of the tension control motor indicates the initiation of the joint reverse motion.

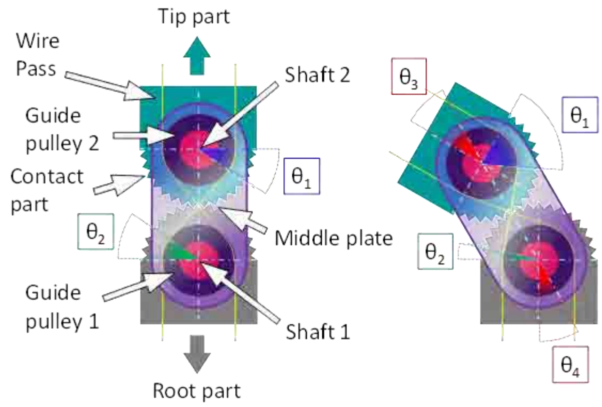



**Fig. 3** mechanism of bending joint to keep the path length of wires for the tip blade actuation [2]

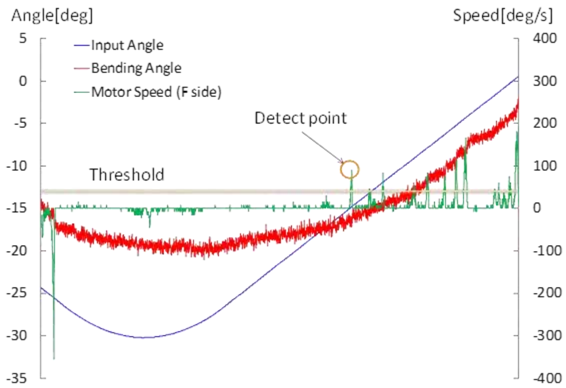



**Fig. 4** Change in displacement of wire of the position control side expressed as "input angle", the bending angle of the forceps, and the rotation of the motor that controls the wire tension expressed as "Motor Speed"

Fig. 5 shows the backlash compensation without any load at the tip of the forceps. The joint was actuated to represent triangular waveform to generate forward and backward motion. Without compensation, there was significant hysteresis between the input angle and resultant output angle.

Fig. 6 shows the backlash compensation with load as large as 50gf at the tip of the forceps. The joint was also actuated to represent triangular waveform to generate forward and backward motion.

## DISCUSSION

We proposed a method to compensate backlash based on the detection of disturbance in wire tension control system. The amount of backlash due to static friction leading to stick-slip motion was estimated as the amount of wire displacement before the initiation of motion in reverse direction. We used relatively complicated measurement system using two load cells and two motors in the present experimental system. Simpler mechanism to detect stick-slip motion should be adopted in practical design. On the other hand, reduction of stick-slip motion by adjusting the wire tension by two electric motors and estimation of external load can be implemented based on quantitative measurement of both wires' tension.

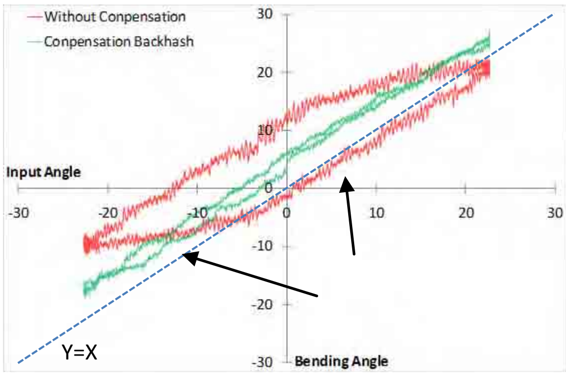



**Fig. 5** Input angles and resultant bending angles of the joint without any load at the tip of the forceps (wire tension: 10N)

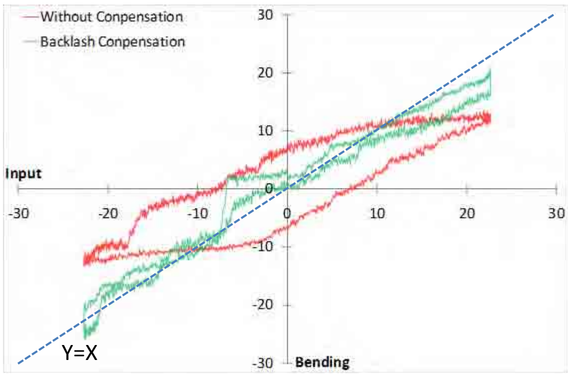



**Fig. 6** Input angles and resultant bending angles of the joint with load as large as 50 gf at the tip of the forceps (wire tension: 10N)

## REFERENCES


[1] M Kaneko, M. Wada, H. Maekawa, and K. Tanie: Considerations on Force Servo System of Tendon Drive Robotic Hands – Transmission Characteristics of Driving System and Their Influences, Journal of Robotic Society of Japan, vol.9(4) 437-444, 1991

[2] K. Nishizawa, K. Kishi, F. Tajima, K. Sudo, M. Fujie, S. Takamoto, and T.Dohi: Principles and Applications of Interference -Free Wire Driven Joint Mechanism, JSME annual meeting 2004(5), 97-98, 2004.

# A Dexterous Instrument for Minimally Invasive Neurosurgery

F. Khan, B. Carrillo, T. Looi, J. Drake

*Center for Image Guided Intervention and Therapeutic Innovation*

*The Hospital for Sick Children, Toronto, Canada*

*fouzia.khan@sickkids.ca*

**INTRODUCTION**

The state of the art instruments for minimally invasive neurosurgery, discussed in [1], only have 2 degrees of freedom (roll, and translation) which limits the dexterity and the operating workspace. This reduces the variety of procedures that can be performed in a minimally invasive manner and increases the difficulty in avoiding critical structures. Enhancing minimally invasive neurosurgery with a higher degree of freedom instrument is the motivation for developing a 4 degree of freedom robotic instrument. This paper presents the kinematics and the preliminary experimental results of that instrument.

**SYSTEM OVERVIEW**

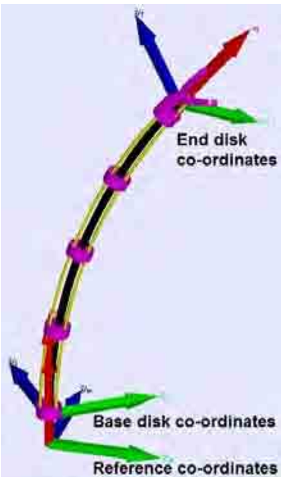



**Fig. 1** Schematic of the flexible instrument

The system consists of a master device, an actuation unit and a flexible instrument. The master device provides 3D position and 1D orientation that is the reference for the instrument's tip. The actuation unit consists of motors to drive the flexible instrument that is based on the design of the distal units presented in [2] and [3]. A schematic of the instrument is shown in Figure 1. The primary component of the instrument is the super elastic nitinol tube called the primary backbone. This backbone can be bent by applying tension on the three wires that are routed using spacer disks along the backbone. The bend is defined as the angle between the z-axis of the end disk co-ordinates and the x -axis of the base disk co-ordinates. It can be translated and rotated about the z-axis of the reference co-ordinates. A gripper with 1 degree of freedom is affixed to its end. Thus, the instrument has 4 degrees of freedom; bend, roll, translation, and a yaw that is at the gripper.

**FORWARD KINEMATICS**

The forward kinematics, the mapping from the instrument's parameters (bend, roll, translation and yaw) to cartesian co-ordinates (x, y, z, orientation), is given in equations [1] and equations [2].

$$orientation = yaw \qquad (1)$$

where, orientation is the angle between the z- axis of the end disk co-ordinates and the z-axis of the gripper co-ordinates measured about the y-axis of the end disk co-ordinates. The gripper co-ordinates are overlapping with that of the end disk co-ordinates in Figure [1].

$$\begin{bmatrix} x \\ y \\ z \end{bmatrix} = R_z(roll)p(bend) + \begin{bmatrix} 0 \\ 0 \\ t \end{bmatrix} \qquad (2)$$

where,

$$R_z(roll) = \begin{bmatrix} \cos(roll) & -\sin(roll) & 0 \\ \sin(roll) & \cos(roll) & 0 \\ 0 & 0 & 1 \end{bmatrix}$$

$$p(bend) = \frac{l}{\left|\frac{\pi}{2} - bend\right|} \begin{bmatrix} mag(bend)(1 - \sin(bend)) \\ 0 \\ mag(bend)(\cos(bend)) \end{bmatrix}$$

$$t = translation$$

$$mag(bend) = \frac{\left(\frac{\pi}{2} - bend\right)}{\left|\frac{\pi}{2} - bend\right|}$$

$$l = length\ of\ the\ instrument$$

Equations [1], and [2] have been derived under the assumption that the shape of the instrument has a constant curvature. In addition, the parameter bend is assumed to be between 0 and π.

**INVERSE KINEMATICS**

The inverse kinematics, the mapping from Cartesian co-ordinates (x, y, z, orientation) to the instrument's parameters (bend, roll, translation and yaw), is given in equations [3] – [6]

$$yaw = orientation \qquad (3)$$

$$roll = \tan^{-1}\left(\frac{y}{x}\right) \qquad (4)$$

$$bend = \min_b\left( k(b) - \sqrt{x^2 + y^2}\right) \qquad (5)$$

$$translation = z - zb \qquad (6)$$

where,

$$k(b) = \frac{l}{\left|\frac{\pi}{2} - b\right|}\left(mag(b)(1 - \sin(b))\right)$$

$$mag(b) = \frac{\left(\frac{\pi}{2} - b\right)}{\left|\frac{\pi}{2} - b\right|}$$

$$zb = \sqrt{\left(d - (x^2 + y^2)\right)}$$

$$d = 2\left(\frac{l^2}{\left|\frac{\pi}{2} - bend\right|^2}\right)(1 - \sin(bend))$$

$$l = length\ of\ the\ instrument$$

## CONTROL

A feedforward control is implemented on the prototype. Figure [2] shows a block diagram with the important functions of the control block. The inverse kinematics shown in the previous section is utilized to determine the instrument's parameters. The parameter bend needs to be adjusted as there is a discrepancy between the constant curvature assumption in the model and the curvature of the physical instrument. The adjustment function *f(bend)* is found experimentally and it is a linear function. Given the parameters, the displacement of the motors ($q_1$, $q_2$, $q_3$) that actuate the instrument can be found using equations [7] and [8]. Displacement of the other motors ($q_4$, $q_5$, $q_6$) are linear functions determined based on motor parameters.

$$q_1 = r\left(bend - \frac{\pi}{2}\right) \qquad (7)$$

$$q_2 = q_3 = -\frac{1}{2}r\left(bend - \frac{\pi}{2}\right)$$

where, $r$ is the distance from the center of the spacer disk to one of the wires.

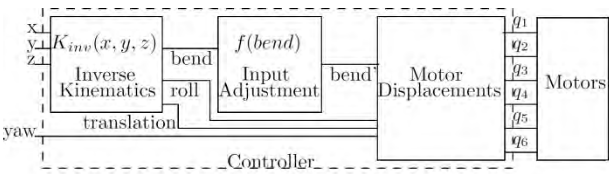



**Fig. 2** Control Block Diagram

## EXPERIMENTAL RESULTS

The prototype of the instrument, shown in Figure [3], is 2.2 mm in diameter and 28 mm in length. The master device is the Novint Falcon; the controller is implemented in MATLAB running on an Intel i7 3.4 GHz processor with a Windows 7 operating system; communication between the controller and the actuation unit is through NI-PCI6224 card. The instrument's tip tracks the position of the Falcon's handle and the orientation of the tip can be controlled using the buttons on the Falcon's handle. A demonstration of the instrument can be found at http://youtu.be/OidxryI3-Rc. The instrument can track reference signals for its bend parameter with a maximum error of a quarter degree. The bend of the instrument was measured visually using a protractor. This test was conducted 10 times for the full range that the instrument can bend. A preliminary position accuracy test was conducted that focused on position error of the instrument's tip on the x-y plane. The position error on the z axis was not tested because it is the same as the position error of the linear motor that controls the z-axis motion. The reference position ranged from 6mm to -6mm with a resolution of 1mm on both x and y axis. The instrument's tip position was measured using the NDI Aurora Electromagnetic tracker. The Euclidean norm of the vector difference between the reference and the measured position was used as the position error. The test was repeated twice and the average error was 4mm. Possible sources of position error are the discrepancies between the model and the physical instrument, or metallic interference from the actuation unit in the electromagnetic field. Feedback control would mitigate the model discrepancy issue, when the discrepancy is small. In order to resolve the metallic interference, plastic material can be used for the body of the actuation unit or a different tracking technology like infrared or charged coupled device can be utilized. Other methods to improve the accuracy will be investigated in the future.

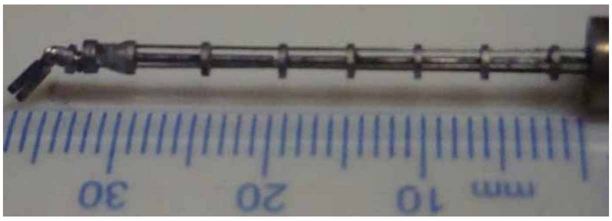


**Fig. 3** Instrument prototype

## CONCLUSION

This paper presented a four degree of freedom robotic instrument for neurosurgery. A prototype of the instrument, with dimensions suitable for pediatric neurosurgery, has been built. It can be controlled using a master device. Preliminary accuracy evaluation shows the mean error between the instrument's tip and the reference position to be 4 mm. Future works will involve improving the position accuracy, increasing the degrees of freedom and path planning for the flexible instrument.

## REFERENCES


[1] W. Ho and J. M. Drake, Minimally Invasive Pediatric Neurosurgery. Taylor & Francis Group, 2005.

[2] N. Simaan, Snake-Like Units Using Flexible Back-bones and Actuation Redundancy for Enhanced Miniaturization," IEEE International Conference on Robotics and Automation, pp. 3012{3017, 2005.

[3] K. Xu and N. Simaan, "An Investigation of the Intrinsic Force Sensing Capabilities of Continuum Robots," IEEE Transactions on Robotics, vol. 24, pp. 576-587, 2008.

# Image Guided and Robotic Assisted Minimally Invasive Cochlear Implantation

S. Weber [1], N. Gerber[1], K. A. Gavaghan[1], T. Williamson[1], W. Wimmer[1], J. Ansó[1], L. Brogna-Salas[1], D. Chen[1], C. Weisstanner[2], M. Caversaccio[3], B. Bell[1]

[1]*ARTORG Center for Biomedical Engineering Research, University of Bern,*
[2]*Institute of Diagnostic and Interventional Neuroradiology, University Hospital of Bern*
[3]*Department of ENT surgery, University Hospital of Bern*
*stefan.weber@artorg.unibe.ch*

## INTRODUCTION

Cochlear implantation, for the treatment of moderate to severe hearing loss, requires access to the inner ear for electrode insertion into the cochlea. Access is gained via a mastoidectomy in which large amounts of tissue are removed to enable visualisation and thus, preservation of close lying critical anatomy such as the facial nerve. To replace the mastoidectomy, a minimally invasive approach, in which access is alternatively gained through a tunnel approximately 20 times smaller (1.8 mm in diameter) in a procedure termed direct cochlear access (DCA) [1], has been proposed. DCA has the potential to significantly reduce invasiveness and improve surgical outcomes for hearing device implantation procedures. By replacing the surgeon's vision with a surgical plan based on preoperative 3D imaging, an image guided robotic procedure could potentially facilitate this previously unattainable minimally invasive procedure. Realisation is, however, reliant on the ability to reduce standard image guided positioning errors tenfold (less than 0.3 mm).

Whilst image guidance and surgical robots such as the DaVinci have aided in the conduction of conventional surgical techniques; improving surgeon confidence and precision for decades, to date, neither technology has been successfully applied to microsurgical applications, primarily due to an inability to obtain the required accuracy and safety levels. Additionally, alternative techniques for intraoperative risk assessment throughout the conduction of the procedure are required to cope for a loss of direct visual or video feedback. Herein, we describe the concept, design and validation of an image guided robotic system that would enable minimally invasive cochlear implantation through the facilitation of the DCA procedure.

## MATERIALS AND METHODS

An image guided robotic system dedicated to the drilling of a DCA tunnel has been developed (Fig.1). The lightweight (5.5 kg), five degrees of freedom serial robotic arm was designed to attach directly to the operating table and conducts the surgical procedure based on a preoperative plan. In order to achieve the required high positioning accuracies, techniques that enable error reduction in each of the three primary phases of the procedure (planning, registration and drilling) have been developed. Additionally, procedural safety information is calculated and fed back to the surgeon for assessment during each phase.

The robotic system is designed to drill a minimally invasive tunnel from the mastoid surface to the cochlea using the following workflow. Initially, four 3 mm surgical screws (M-5220.03, Medartis, Switzerland) are implanted in the mastoid as registration fiducials.

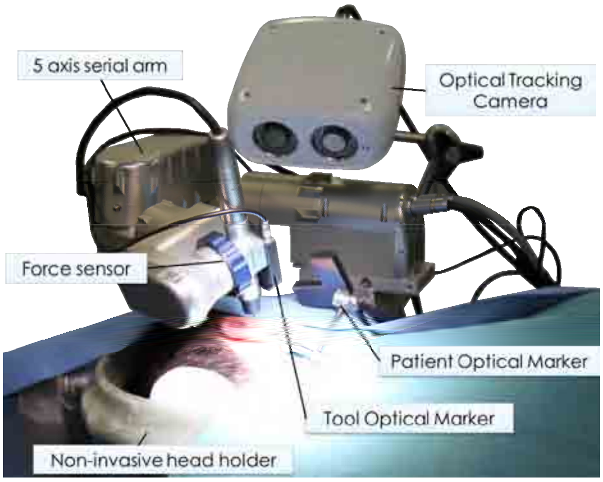



**Fig. 1** Image guided robotic system.

Secondly, a preoperative plan is produced from high resolution cone beam CT (CBCT) images with the aid of a dedicated software tool [2]. From the CBCT image dataset, critical anatomical structures to be preserved (facial nerve, chorda tympani, ossicles, ear canal wall) along with the mastoid bone are segmented. A trajectory is then defined from the mastoid surface to the cochlea, avoiding the surrounding critical anatomy (Fig. 2). Distances from the defined tunnel to segmented anatomical structures (accounting for predicted case specific registration error and average tracking error) are calculated and displayed to the user to aid in risk and patient eligibility assessment. The fiducial screws are localized within the image using a semiautomatic detection algorithm, described in [3]. The surgical plan is thereafter transferred to the robotic system.

Intraoperatively, the robot is mounted to the operating table side rail and the patient's head is immobilized. The robotic end effector is tracked relative to the patient in 3D space with a mean accuracy of 0.05 mm by a high accuracy optical tracking camera (CamBar B1, Axios, Germany) via custom made active optical markers that are attached to the tool and anchored to the mastoid.

The patient is registered to the preoperative plan via detection of the implanted fiducial screws using the robotic arm, the optical tracking system and an automatic tactile search algorithm, as per the methodology described in [3]. The registration process provides registration errors at the target of approximately 0.1 mm [3]. The preoperatively planned trajectory is thereafter drilled by the robotic system using the optical tracking camera for position control.

Throughout the drilling process the pose of the tool is verified using a force-density correlation algorithm based on real time drilling force data and image density profiles obtained from preoperative CT around the drilling site [4]. Tool position verification is displayed to the user along with the optically tracked drill position on the graphical user interface (GUI) within a virtual 3D view of the surgical scene and within a CBCT slice viewer. The GUI, which is also used for navigating the surgical workflow, is displayed on a touch screen monitor positioned beside the operating table.

A manual incision is made in the round window with a small knife, and the electrode is manually inserted through the DCA tunnel into the cochlea.

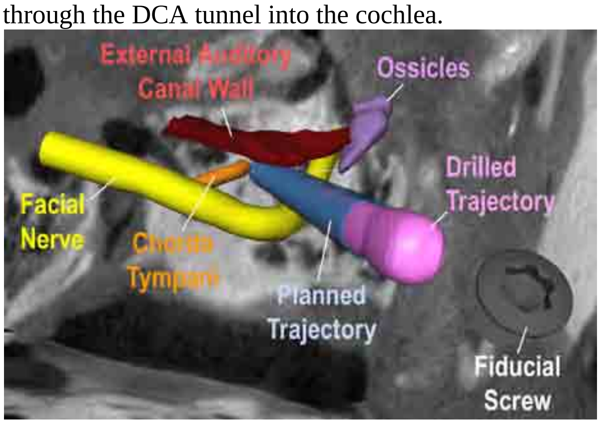



**Fig. 2** Postoperative accuracy evaluation of a robotically performed DCA on a cadaver head.

The image guided robotic system and the proposed surgical approach were evaluated in eight cases performed on four clamped (Mayfield, USA) whole cadaver heads. Two further cases were rejected during the preoperative planning phase due to an excessively narrow space between the facial nerve and the external auditory canal wall. In each case, the round window was targeted and a standard 22 contact electrode (Med-El, Austria) was manually inserted through the DCA tunnel and into the cochlea. Postoperative CBCT data was used to analyse the accuracy of the drilled tunnel and the effectiveness of the electrode insertion.

## RESULTS

DCA tunnels were drilled to the middle ear cavity with mean accuracies at the mastoid surface and target of $0.08 \pm 0.05$ mm and $0.15 \pm 0.08$ mm (N = 8) respectively.

Visual inspection of postoperative images showed that all critical structures were preserved in all cases (Fig. 2). Electrodes were inserted through the round window opening without difficulty after manually removing the bony overhang, with full insertion achieved in 7 out of 8 cases (Fig. 3). Partial insertion occurred because electrode array advancement was stopped as soon as resistance was detected.

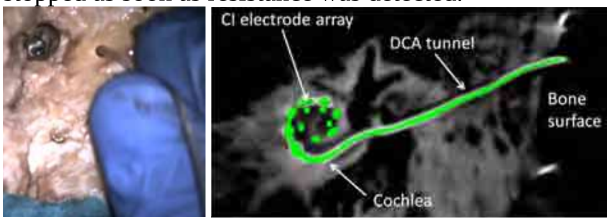



**Fig. 3** Manual electrode insertion into the DCA tunnel (Left) and post-operative CBCT image with segmented inserted electrode (Right).

## DISCUSSION

The proposed image guided robotic system has demonstrated sufficient accuracy for minimally invasive cochlear implantation. DCA procedures were performed on cadaveric specimens without damage to critical anatomical structures, and electrode insertion was performed without the need for additional insertion tools. Whilst an invasive standard neurosurgical head clamp was used in the presented study, a non-invasive head clamp that utilizes inflatable pressure pads is currently being developed (Fig. 1). Integrated preoperative and intraoperative safety and risk analysis with intuitive graphical feedback currently enable the surgeon to monitor the status of the procedure without direct visual or video feedback. Additional safety mechanisms such as the use of integrated facial nerve monitoring and intraoperative CBCT are currently being investigated and will be used to increase procedure safety and surgeon confidence in the future.

## REFERENCES

[1] Coulson CJ, Reid AP, Proops DW, Brett PN. ENT challenges at the small scale. Int J Med Robot. 2007; 3(2):91-6.

[2] Gerber N, Bell B, Kompis M, Stieger C, Caversaccio M, Weber S. A software tool for preoperative planning of implantable hearing devices. Int J Comput Assist Radiol Surg. 2012; 7(1):134-135.

[3] Gerber N, Gavaghan KA, Bell B, Williamson T, Weisstanner C, Caversaccio M, Weber S. High Accuracy Patient-to-Image Registration for the Facilitation of Image Guided Robotic Microsurgery on the Head. IEEE Trans Biomed Eng. 2013; 60(4):960-968.

[4] Williamson TM, Bell BJ, Gerber N, Salas L, Zysset P, Caversaccio M, Weber S. Estimation of tool pose based on force-density correlation during robotic drilling. IEEE Trans Biomed Eng. 2013; 60(4):969-976.

# A Filtering Approach for Surgical Registration with Unknown Stiffness

S. Tully[1], A. Bajo[2], N. Simaan[2], H. Choset[1]

[1]The Robotics Institute, Carnegie Mellon University

[2]Mechanical Engineering, Vanderbilt University

stully@ece.cmu.edu

## INTRODUCTION

Snake-like robots have the potential to reach deeper within the anatomy while reducing patient trauma. To help guide these tools, model-based image-guidance can be used to fuse live tracking data with preoperative imaging in order to visualize a robot's pose relative to the anatomy. In this paper, we introduce a new probabilistic filtering algorithm for registering live tracking data with a preoperative surface model while simultaneously estimating the surface compliance.

Registration for medical imaging is often performed using the iterative closest point method (ICP) [1] or with a number of deformable registration methods that account for organ deformation [2]. Our probabilistic approach overcomes the delay required for offline batch processing by estimating registration parameters online with an iterative extended Kalman filter (IEKF).

Existing methods for *in-vivo* registration use line-of-sight measurements (*e.g.*, 3D vision and range scanning). Our approach alternatively uses palpation to sense organ shape and compliance (*e.g*,. [3], [4]). In this paper, we extend our prior work [5] by relaxing the assumption that the organ stiffness is known. We instead simultaneously estimate organ compliance along with parameters defining the registration of the robot through the use of contact force measurements.

## MATERIALS AND METHODS

We used a ∅5mm two-segment snake robot, first presented in [7], for experimental validation, see Fig. 1. For the experiment, we performed two scans of a flexible surface (shown in Fig. 1), by palpating the surface while regulating the contact force (first at 5g, then at 25g) using intrinsic force estimation [4]. The scanned surface has two regions of different stiffness (labeled as inner and outer in Fig. 1). Our filtering method uses contact force data to infer the registration parameters that would best explain the sensor data.

**State Definition:** to register the robot to a flexible surface, we treat registration as a probabilistic filtering task in which we seek to estimate an unknown state vector $\boldsymbol{x}_k$ that defines the registration of the robot to the surface and which encodes the surface compliance,

$$\boldsymbol{x}_k = \left[\boldsymbol{x}_{k,robot}^T \quad \boldsymbol{\theta}_{k,robot}^T \quad \boldsymbol{c}_k^T \quad \boldsymbol{x}_{k,tip}^T\right],$$

where $\boldsymbol{x}_{k,robot}$ and $\boldsymbol{\theta}_{k,robot}$ represent the position and the yaw-pitch-roll Euler angles of the robot base in the coordinate frame of the surface. Vector $\boldsymbol{c}_k$ defines the

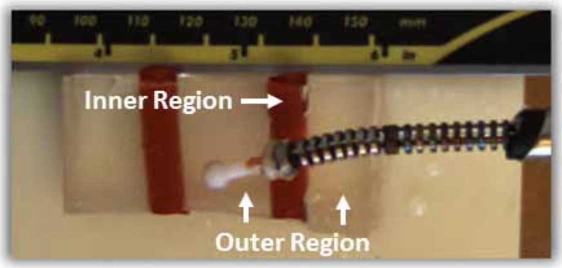



**Fig. 1** For experiments, we tested a ∅5mm continuum robot palpating a flexible surface.

**Measurements: T**he surface is assumed to be locally planar and the contact force is assumed to be normal to the surface (we lubricated the surface to ensure this assumption holds). In addition to measuring force, the robot measures its tip position relative to the base of the robot via a magnetic tracking coil (Ascension Tech., Trackstar II™) in the robot tip.

**Measurement Model:** the measurement model that can be used to correct the filter estimate upon observing sensor data (force and tip position) is as follows,

$$\boldsymbol{h}(\boldsymbol{x}_k) = \begin{bmatrix} -\boldsymbol{n}^T[\boldsymbol{s}(\boldsymbol{x}_k) - \boldsymbol{p}]/c(\boldsymbol{x}_k) \\ \boldsymbol{x}_{k,tip} \end{bmatrix},$$

where $\boldsymbol{n}$ is the surface normal, $\boldsymbol{p}$ is a point on the (relaxed) surface, and $c(\boldsymbol{x}_k)$ is a function that extracts the appropriate surface compliance given the state $\boldsymbol{x}_k$. Conceptually, this model is a spring model that equates the contact force with the surface deformation divided by the compliance. In this formulation, the function,

$$\boldsymbol{s}(\boldsymbol{x}_k) = \boldsymbol{R}(\boldsymbol{x}_k)\boldsymbol{x}_{k,tip} + \boldsymbol{t}(\boldsymbol{x}_k),$$

transforms the estimated position of the robot tip in the robot base frame to a position in the coordinate frame of the surface. $\boldsymbol{R}(\boldsymbol{x}_k)$ and $\boldsymbol{t}(\boldsymbol{x}_k)$ are the rotation matrix and translation vector, respectively, that perform this transformation based on the estimated robot base position $\boldsymbol{x}_{k,robot}$ and the robot base orientation $\boldsymbol{\theta}_{k,robot}$.

**Filter Formulation:** Our filter estimates a mean vector $\hat{\boldsymbol{x}}_{k|k}$ and covariance $\boldsymbol{P}_{k|k}$ using a static prediction step and a measurement update step that uses an IEKF update equation [6],

$$\boldsymbol{x}_{i+1} = \hat{\boldsymbol{x}}_{k|k-1} + \boldsymbol{K}[\boldsymbol{z}_k - \boldsymbol{h}(\hat{\boldsymbol{x}}_{k|k-1})] - \boldsymbol{K}\boldsymbol{H}_k[\hat{\boldsymbol{x}}_{k|k-1} - \boldsymbol{x}_i].$$

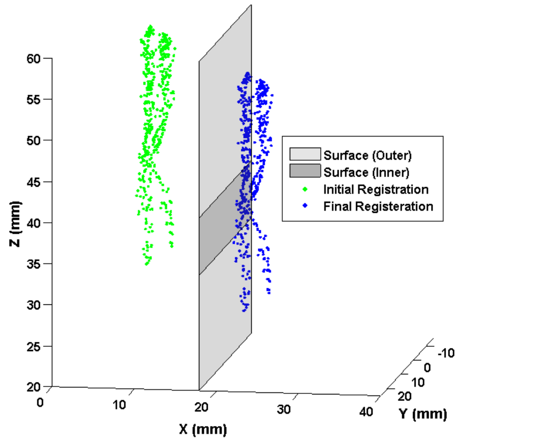



**Fig. 2** The initial (green) and final (blue) registration of contact points.

function $\boldsymbol{h}(\boldsymbol{x}_k)$ and $\boldsymbol{K}$ is the Kalman gain. Lastly, we note that we choose to instantiate a number of these filters with different initial guesses $\hat{\boldsymbol{x}}_{0|0}$. After an experiment, the highest likelihood hypothesis is reported as the registration result.

**Dataset and Experiment:** we split the palpation dataset, shown in Fig. 2, into two datasets. The first was used to infer a best approximation to the relaxed position of the surface (shown in Fig. 2 as a gray plane)[1]. This data was also used to infer the ground truth compliances (0.11 mm/g and 0.05 mm/g) for the outer and inner regions, respectively. The second dataset was used for testing our algorithm. We purposefully disturbed the test data with a translation in $x$ and $z$, resulting in a large registration error with respect to the surface (shown in Fig. 2). This was done to create a challenging registration test for our approach. Finally, we iterated through the contact points in the test dataset and applied the IEKF update equation for each point.

## RESULTS

The registration result of our probabilistic filtering method, compared to the initial registration, is shown in Fig. 2. In this figure, the initially registered contact points (in green) are poorly registered, but after the filter applies the contact force measurements, the algorithm correctly aligns the contact points to the surface such that the points are properly displaced "into" the surface due to local deformation caused by forceful palpation.

We note that, during the experiment, the estimate of the $x$ dimension of the robot becomes highly correlated with the estimate of the surface compliance. This occurs because the estimation problem is not observable until the surface is palpated at two different forces. In Fig. 3, an error plot is shown that depicts the error between the estimated compliance and the true compliance of the surface for the two (inner and outer) regions. The data illustrates the sudden drop in error when the surface is palpated at a second contact force. The final registration error in terms of aligning the robot to the *a priori* surface was **0.55mm**.

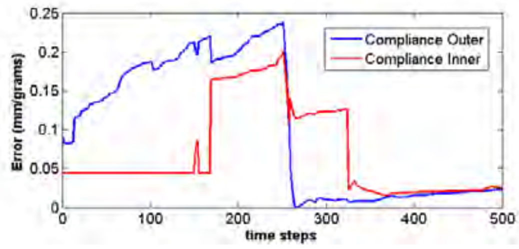



**Fig. 3** The error in the estimated compliance.

## DISCUSSION

The contribution of this work is a new method, capable of running in real-time, for registering a robot to a flexible environment. Unlike other approaches, our approach uses probabilistic filtering, which allows us to estimate the compliance/stiffness of the environment while simultaneously aligning the robot to an organ.

We note that our experiment was a proof-of-concept trial that only evaluated 2D registration (the $z$ and $x$ dimensions of the robot). For future work, we will test more complicated registration problems.

The significance of our approach is more apparent as it relates to a "chicken-and-egg problem": if the compliance of the environment is known, the expected displacement of each contact point into the surface can be determined, thus simplifying registration. Conversely, if the registration is known, the stiffness can be determined by observing the surface displacement for a given contact force. We believe that solving for both the registration and compliance requires a probabilistic approach like the one presented.

## REFERENCES

[1] P. J. Besl and N. D. McKay, "A method for registration of 3-D shapes," *IEEE Transactions on pattern analysis and machine intelligence*, vol. 14, no. 2, pp. 239–256, 1992.
[2] A. Sotiras, C. Davatazikos, and N. Paragios, *Deformable Medical Image Registration : A Survey (Research Report No 7919 Project-Team GALEN)*. INRIA, 2012, p. 65.
[3] R. E. Goldman, A. Bajo, and N. Simaan, "Algorithms for autonomous exploration and estimation in compliant environments," *Robotica*, 31 (1), pp. 71–87, Mar. 2013.
[4] K. Xu and N. Simaan, "Intrinsic Wrench Estimation and Its Performance Index for Multisegment Continuum Robots," *IEEE Transactions on Robotics*, vol. 26, no. 3, pp. 555–561, Jun. 2010.
[5] S. Tully, A. Bajo, G. Kantor, H. Choset, and N. Simaan, "Constrained filtering with contact detection data for the localization and registration of continuum robots in flexible environments," in *IEEE International Conference on Robotics and Automation*, 2012, pp. 3388–3394.
[6] B. M. Bell and F. W. Cathey, "The iterated Kalman filter update as a Gauss-Newton method," *Automatic Control, IEEE Transactions on*, vol. 38, no. 2, pp. 294–297, 1993.
[7] R. Goldman, A. Bajo, L. MacLachlan, R. Pickens, S. Herrell, and N. Simaan, "Design and Performance Evaluation of a Minimally Invasive Telerobotic Platform for Transurethral Surveillance and Intervention," *IEEE Transactions on Biomedical Engineering*, pp. 1–1, 2013.

[1] Determined by assuming the surface is planar and by performing an expensive batch estimation problem.

# Per-Oral Endoscopic Cardiomyotomy and Pyloromyotomy using a Flexible Snake Robot – Proof of Concept with a Porcine Model

T.P. Cundy, N.K. Patel, J. Shang, C.A. Seneci, C.J. Payne,
V. Vitiello, J. Clark, J.P. Teare, A.W. Darzi, G.-Z. Yang

*The Hamlyn Centre for Robotic Surgery, Institute of Global Health Innovation, Imperial College London*
*t.cundy@imperial.ac.uk*

## INTRODUCTION

Natural orifice surgery is an attractive operative approach due to reduced surgical trauma, 'scarless' cosmesis and in some cases, a more direct route to the target operative site. Ongoing concern regarding the safety of transluminal access has prompted a shift of attention towards more tangible natural orifice *endoluminal* techniques. Surgical platforms being explored are currently limited to conventional flexible endoscopes, which are known to be problematic due to a lack of adequate stability, precision and navigational control.

This purpose of this study is to explore the potential of a flexible snake robot to overcome existing technological limitations in order to make *endoluminal surgery* a more realisable paradigm. Two emerging clinical applications are targeted to demonstrate proof-of-concept; 1) per-oral endoscopic cardiomyotomy (POEM) for oesophageal achalasia or motility disorders [1,2], and 2) per-oral endoscopic pyloromyotomy (POEP) for delayed gastric emptying, gastric outlet obstruction or infantile hypertrophic pyloric stenosis (IHPS) [3].

## METHODS

A flexible snake robot, the i-Snake®, was deployed in a cadaveric porcine model setting (Figure 1). This hyper-redundant master-slave robot delivers 8 degrees of freedom (DOF) across 4 distal articulating joints and further 1 DOF via an adjustable semi-rigid neck. The four articulating joints are driven by embedded micro motors. The hybrid gear-tendon driving mechanism as described in provides a compact and stable robotic platform design [4]. External diameter of the prototype is 13mm. Two internal channels of 3.0mm and 2.4mm diameter are available for interchangeable focused energy devices and air insufflation respectively.

Five essential procedural steps for both POEM and POEP were assessed (Figure 2).

## RESULTS

Controlled and targeted actuation within the confined workspace of the foregut was attainable in this setting (Figure 1). Each procedural step was achieved for both POEM and POEP. Submucosal tunnel and myotomy lengths of 60 – 80mm were repeatedly performed. Submucosal tunnel intubation and navigation was identified as the most challenging procedural step due to limited visualization and shear forces exerted at the mucosal incision site. Mucosal or transmural perforation was not encountered. Although performed in staged intervals, estimated time for total procedural completion is 30 – 45 minutes.

## DISCUSSION

This preliminary assessment provides encouraging proof-of-concept results supporting the role of a flexible snake robot in natural orifice endoluminal surgery. Enhanced technical features and overall improved ergonomic configuration of the i-Snake® offers potentially enabling technology for *advanced therapeutic endoluminal interventions*. This requires formal quantification through ex-vivo and in-vivo feasibility testing as well as comparative assessment against existing platforms.

Optimisation of the robot for endoluminal surgery might include integration with distal caps to facilitate dissection, low friction sheath designs, alternative flexible focused energy devices and platform miniaturization for indications such as IHPS. The workspace of the foregut seems well suited to kinematic design of the i-Snake®. Additional clinical indications for benign and malignant diseases involving foregut and hindgut structures warrant consideration.

## REFERENCES

[1] Inoue H, et al. Peroral endoscopic myotomy (POEM) for esophageal achalasia. Endoscopy. 2010 Apr;42(4):265-71.

[2] Swanström LL, et al. A stepwise approach and early clinical experience in peroral endoscopic myotomy for the treatment of achalasia and esophageal motility disorders. J Am Coll Surg. 2011 Dec;213(6):751-6.

[3] Kawai M, et al. Endoscopic pyloromyotomy: a new concept of minimally invasive surgery for pyloric stenosis. Endoscopy. 2012 Feb; 44(2): 169-73.

[4] Shang J., Noonan DP., Payne C., Clark J., Sodergren M., Darzi A., Yang GZ. An Articulated Universal Joint Based Flexible Access Robot for Minimally Invasive Surgery. International Conference on Robotics and Automation, Shanghai, China. 1147-1152. IEEE (2011).



**Fig. 1** Ex-vivo porcine upper gastro-intestinal specimens with a) oesophagus detubularised and b) stomach transected in mid-coronal plane, demonstrating procedural configurations of the i-Snake® for POEM and POEP respectively. Thickness of luminal muscle layers were 3mm, 4mm and 10mm for the c) oesophagus, d) stomach and pylorus respectively.

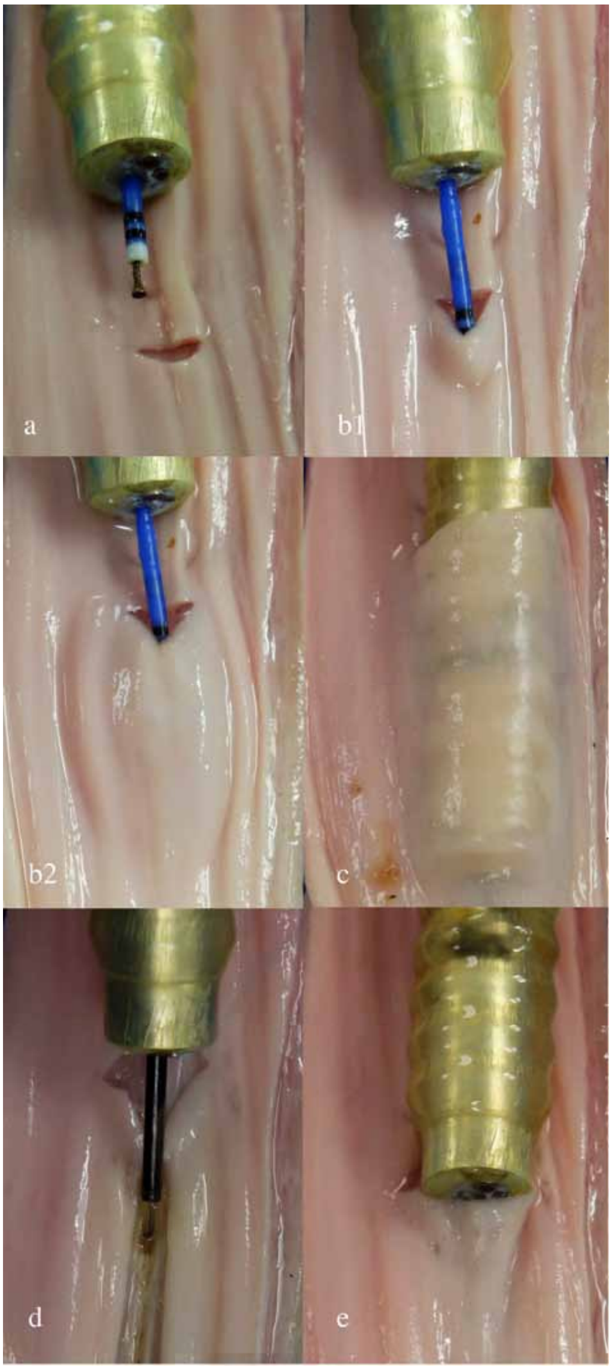


**Fig. 2** Five essential procedural steps for POEM and POEP were undertaken, defined by a) creation of a 15 – 20mm transverse mucosal incision, b1) & b2) submucosal tunneling using the HybridKnife (ERBE Elektromedizin), c) intubation of submucosal tunnel, d) myotomy using the HookKnife (Olympus) (mucosal tunnel opened for illustrative purpose only), and e) extubation of submucosal tunnel in preparation for mucosal closure (i.e. with endoclip).

# Mechanical Drive System for Enhancing Flexible Endoscopy: System Concept and Prototype Development

L. Zhang[1,2], R. Khare[1], E. Wilson[1], A. Martin[1], K. Wu[1], K. Swords[1], K. Cleary[1], C.A. Peters[1]

[1]*Sheikh Zayed Institute for Pediatric Surgical Innovation, Children's National Medical Center, Washington, DC, USA*

[2]*Tianjin University, Tianjin, China*

*kcleary@childrensnational.org*

## INTRODUCTION

Flexible endoscopy is commonly performed in many aspects of medicine, such as ureteroscopy and sinus endoscopy. Uretero-renoscopy uses flexible ureteroscopes for access and manipulation in the ureter and kidney. Uses include stone removal, diagnosis for bleeding or malignancy, as well as direct biopsy and destruction of malignant lesions. However, existing endoscope designs rely on decades-old manual controls for translation, rotation and tip flexion. Because of the complexity of movements needed for many applications, integration of a more intuitive and user-friendly control system has the potential to greatly enhance the safety, efficacy, and efficiency of these instruments.

**Related work**. To control the endoscope in flexible endoscopy, Johns Hopkins University has designed a robot for a flexible endolaryngoscope [1]. Our lab has also designed a prototype, which can be remotely controlled by a 3D mouse [2]. However, these devices are not convenient for securing and removing the endoscope and do not have a sterile interface. A steerable robot driven by two remote motors through Bowden cables is compact but its translation movement is manually controlled [3]. Based on the first generation of the prototype, our lab designed an ergonomically enhanced flexible endoscopy robotic system, including a new prototype of the robot, its control system and a system assessment software platform.

## MATERIALS AND METHODS

The second generation prototype robot has three degrees of freedom and is shown in Figure 1. A flexible ureteroscope is mounted on the robot so that each motor independently manipulates rotation, flexion and insertion (translation) of the ureteroscope, respectively. Three Maxon motors and three Maxon gear boxes (as in the first generation prototype) are used to drive three joints. To improve the usability, safety and ergonomic performance, the second version of the prototype has focused on the following points: (1) Endoscopist can efficiently secure the endoscope; (2) A sterile plastic interface between the clean ureteroscope and the robot prevents cross contamination; and (3) A rigid annular tube connected to the robot is used to support the flexible lumen of the endoscope during operation.

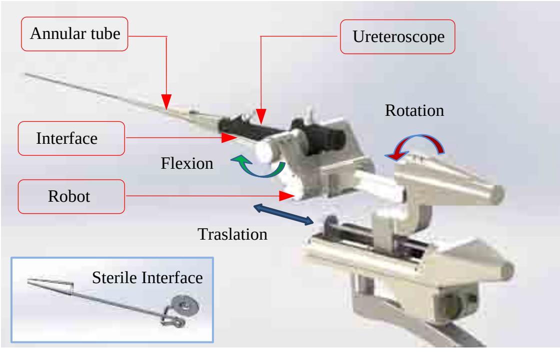



**Fig. 1** Prototype of second generation of uretoroscopic robot.

The ergonomic improvement of the securing mechanism is shown in Figure 2. A sterile interface is placed on the ureteroscope before it is mounted on the robot. One side of the sterile interface with a flat shaft is inserted into a hole in the drive shaft. The other side of the sterile interface is cone shaped and fixed in place by pushing tightly into a lock bar. Two snaps located on both sides of the lock bar secure it in position. When the snaps are pushed, a spring mechanism pulls back the lock bar, thus releasing the sterile interface. These improvements make it easy to install and uninstall the ureteroscope compare to our first prototype, which was presented at the symposium last year [2].

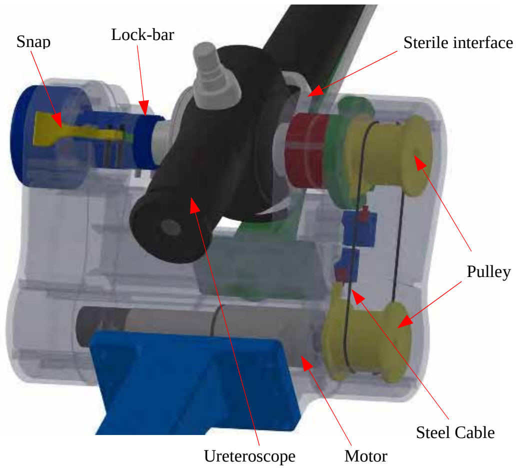



**Fig. 2** Depiction of a 3D model of fast snap-on mechanism to secure the ureteroscope and mechanism to drive tip flexion.

The architecture of the overall system is shown in Figure 3. The robotic framework is interfaced to a computer through a Galil motor controller. Interfacing software on the computer uses the Galil application programming interface to control the robotic framework. The interfacing software was implemented as a dialog-based MFC application in Visual C++ on the Windows operating system. A game controller, and foot pedals serve as the user interface devices that are also connected to the computer. The low cost and light joystick from a game controller manipulates the tip flexion/extension and the left/right rotation of the endoscope. Two foot pedals control the insertion/extraction (translation) motion of the endoscope. The input from the user interface devices is converted into control signals by the interfacing software to drive the robotic framework.

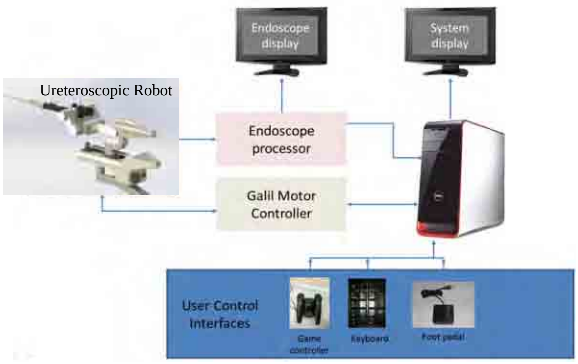



**Fig. 3** System setup for robotically assisted ureteroscopy.

## SYSTEM ASSESSMENT

An assessment software platform has been developed to evaluate operative efficiency and accuracy of the robot system. As shown in Figure 4, the ureteroscope is passed into the ureteroscopy trainer (IdealAnatomic Inc.) with colored wires inserted as task targets in the renal collecting system. Target wire is seen in inferior calyx (Figure 4b, indicated by arrow). In addition, a phantom with small colored balls fixed in a hemi-spherical space (Figure 4 (c)) has been developed to test the system's operative efficiency and accuracy to reach selected points in space. The assessment is ongoing and will be reported at the conference.

## DISCUSSION

Robotic control for a flexible ureteroscope has the potential to improve procedural efficiency and tip placement precision during procedures such as exploration of the kidney calyxes. The concept presented is also applicable to other endoscopic devices. This novel control system for flexible endoscopy offers several important advantages including wide applicability to endoscope size and type, the ability to use commercially available endoscopes without redesign, and the ergonomically advantageous user interface that can potentially enhance efficacy while reducing procedure time, tissue trauma, and instrument damage.

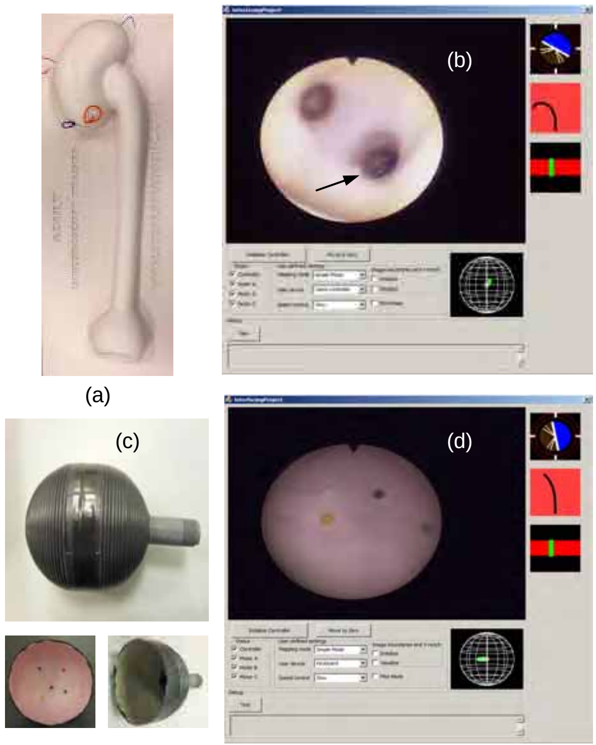



**Fig. 4** System assessment platform. (a) Ureteroscopy trainer; (b) Screen shot of interfacing software with ureteroscope in the trainer; (c) Hemi-spherical phantom; (d) Screen shot of interfacing software with ureteroscope in hemi-spherical phantom.

## ACKNOWLEDGMENTS

We would like to thank our colleagues at Vivonics (formerly Infoscitex) for their assistance with the initial concepts for this project.

## REFERENCES

[1] K. Olds, A.T. Hillel, E. Cha, M. Curry, L.M. Akst, R.H. Taylor, and J.D. Richmon, "Robotic endolaryngeal flexible (Robo-ELF) scope: a preclinical feasibility study," *Laryngoscope*, vol. 121, no. 11, pp. 2371-4, Nov. 2011.

[2] C. A. Peters, A. Burns, E. Wilson, H. Luo, K. LeRoy, J. Goldie, B. LaBrecque, K. Cleary, "Navigated Endoscopy: Prototype System for Robotically Assisted Ureteroscopy," The Hamlyn Symposium on Medical Robotics, 72-74. 2012.

[3] J. Ruiter, E. Rozeboom, M. Van Der Voort, M. Bonnema, I. Broeders, "Design and evaluation of robotic steering of a flexible endoscope," Proceedings of the IEEE RAS and EMBS International Conference on Biomedical Robotics and Biomechatronics, pp. 761-767. 2012

SINGER: a virtual SImulator for robotic NeurosurGERy


M. Niccolini[1], C. Diversi[1,2], B. Kang[1,2], V. Castelli[1,2], B. Mazzolai[1], E. Sinibaldi[1]

[1]Center for Micro-BioRobotics@SSSA, Istituto Italiano di Tecnologia,

[2]The Biorobotics Institute, Scuola Superiore S. Anna

edoardo.sinibaldi@iit.it


## INTRODUCTION

Computer/robot-assisted surgery (CAS/RAS) holds potential for therapy improvements, in terms of enhanced procedures accuracy, repeatability, safety, and reduced morbidity[1]. In particular, brain surgery still poses challenges, and a novel CAS/RAS robotic platform for neurosurgery is thus addressed, to be integrated in the operating room (OR) by enhancing human-robot interaction (Fig. 1A). In such a context, a continuous dataflow among surgeon, robotic tools and sensors is needed, and an effective human-machine interface (HMI) is fundamental to the purpose, combining surgeon decision-making with computer data processing capabilities. A graphical HMI encompassing virtual reality (VR) scenes and video streams, and allowing physical data input through a graphic user interface (UI) was therefore pursued. In particular, a virtual simulator[2] of the robotic platform was developed, serving the following purposes. Firstly, it can be preoperatively used by the surgeon in order to test procedures *in silico*, so as to gain a better comprehension of the envisioned tasks and relevant constraints. Indeed, medical images and virtual anatomical models (possibly rendering the interventional scenario from multiple viewpoints) enhance the surgeon intraoperative spatial perception. Moreover, the simulator is expected to improve surgeon practice with the robotic platform, and to boost its training by shortening the learning phase. Furthermore, once implemented in the simulator the control architecture actually used for the platform, it permits to better integrate robotic tools with sensor devices, by individually testing each component, both through a "software-in-the-loop" and a "hardware-in-the-loop" configuration. This, in turn, simplifies tuning and validation of the chosen control strategy. The developed SImulator for robotic NeurosurGERy (SINGER) is hereafter described.

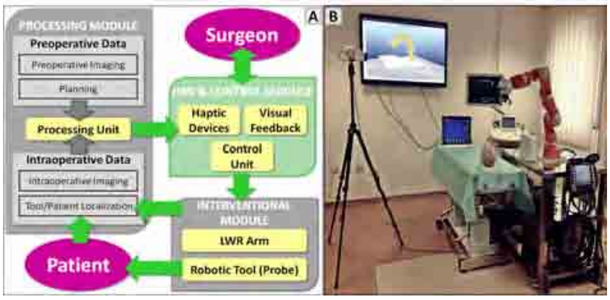



**Fig. 1** (A) CAS/RAS functional scheme. (B) Robotic platform components in the lab (HMI not shown).

## MATERIALS AND METHODS

The interventional module of the platform (Fig. 1B) consists of the LightWeight Robot IV+ (Kuka, Germany) (LWR), supporting a neuroendoscope (Karl Storz, Germany) through a purposely designed handling interface. LWR supports safe human-robot interaction and an effective integration in the OR thanks to its redundancy, high payload, reduced footprint/weight, full joints control, and inherent compliance which permits direct handling by the surgeon[3]. The HMI includes a workstation encompassing haptic devices, a manual switch for LWR safety lock, a wall display and three monitors. The wall display shows the SINGER 3D virtual scenario, while the monitors respectively show: i) preoperative images and planned tool-path (within 3D Slicer image-processing environment; www.slicer.org); ii) intraoperative images (acquired by an ultrasound system); iii) LWR status, commands and settings. Surgical tasks are preoperatively planned based on multi-modal images, and intraoperatively monitored/updated by means of the processing module, also encompassing the Hybrid Polaris Spectra (Northern Digital Inc., Canada) optical tracker (OT). SINGER was designed on a flexible software architecture, to smoothly switch between simulation and real hardware operation. Two virtual and hardware components were integrated so far, namely LWR (including the neuroendoscope with its interface) and OT. SINGER acts as a threefold agent: i) as an emulator, to provide each platform component (even a real one) with a simulated output of another component; ii) as a rendering tool, able to display data received from the real hardware; iii) as an interactive 3D UI for the real and simulated platforms. Real components communication and simulation were developed using the multi-platform block-diagram Matlab/Simulink environment. This approach permits to run the same control code in simulation, as well as in soft and in hard real-time. In particular, the simulation, which is handled by Simulink itself, neglects the issue of synchronizing simulation time with the real one. Moreover, the soft real-time modality is implemented through a customized Simulink block that slows down the simulation, based on the differential measurements of the CPU number of cycles. Finally, when stringent time synchronization with the real components is sought, the hard real-time code to be run on a Linux/RTAI machine can be directly generated by means of the Simulink Coder Toolbox. Such an approach offers the possibility to connect simulated and real components in the same Simulink

model, and to separately run each component by exchanging data through a socket connection. At a low-level, a Simulink implementation of the Reflexxes motion libraries (www.reflexxes.com) manages LWR motion generation and the smooth switching between different control functionalities. Moreover, an *ad-hoc* inverse kinematics algorithm was implemented for LWR joint-space motion control. In addition, graphic rendering of the 3D virtual scenario was developed in the V-REP environment (www.coppeliarobotics.com), which permits to control each object/model individually, and by means of different control entities (such as embedded scripts, add-ons, plugins, remote APIs, etc.). In particular, for the application at hand, components data transfer with the Simulink control module was achieved through the remote API framework. Finally, a graphical UI was developed by using the Qt framework (www.qt.digia.com); it was integrated via a socket-oriented connection with the Simulink model that handles the main control code.

As a preliminary model application for SINGER, a point-based calibration procedure[4] between LWR and OT was simulated. Such a calibration simultaneously finds two transformations matrices (by optimization), namely that one between LWR base and OT base, and that one between LWR end-effector and the tool (tracked by the OT) attached to it. To this end, seven Cartesian poses were stored in a file and subsequently commanded to the soft real-time simulated robot controller. The inverse kinematics algorithm computed the corresponding joint positions, which were sent to the V-REP robot model by means of the remote APIs. The position (in the OT frame) of the tracked tool rigidly connected to the robot end-effector was then sent back from the V-REP model to the controller. It was then stored to a Matlab file, together with the pose of the LWR end-effector, which is known in the LWR base frame. The calibration algorithm was finally run off-line, on the recorded data, and the sought transformation matrices were obtained by standard least-square minimization. Moreover, in order to simulate the white noise which generally affects real OTs, normally distributed random numbers were generated at each sample time and added to the simulated OT measurements. This way, the accuracy of the considered calibration algorithm was assessed versus noise magnitude.

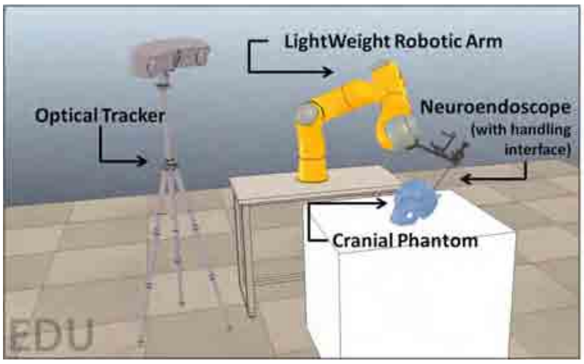



**Fig. 2** Main components of the SINGER 3D virtual scenario.

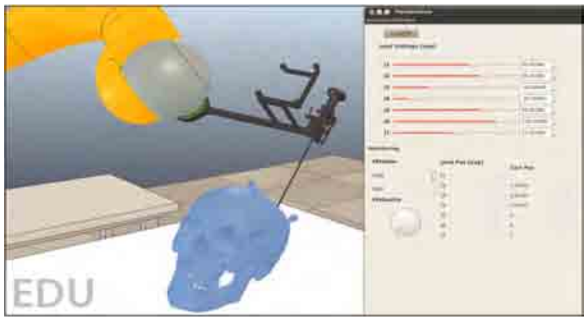



**Fig. 3** Simulated neuroendoscopic procedure, and LWR graphical UI.

## RESULTS

SINGER 3D virtual scenario is shown in Fig. 2, while Fig. 3 reports a simulated neuroendoscopic procedure, together with some details of the LWR graphical UI. Moreover, Tab. 1 shows the root-mean-square (rms) errors obtained from the simulated calibration procedure, corresponding to different magnitudes of the added noise.

**Table 1** Accuracy results of the simulated calibration procedure: rms errors on orientation and position, associated with different magnitudes of the assumed noise.

| Noise / rms Error | 0 mm | ±1 mm | ±10 mm |
|---|---|---|---|
| Orientation (deg) | $7.1 \cdot 10^{-9}$ | $8.3 \cdot 10^{-7}$ | $8.3 \cdot 10^{-2}$ |
| Position (mm) | $2.1 \cdot 10^{-4}$ | $6.0 \cdot 10^{-1}$ | 6.0 |

## DISCUSSION

A virtual simulator for robotic neurosurgery was implemented and preliminary assessed. The developed simulator can be used as an emulator, or as a rendering tool augmenting surgeon perception of the operating scenario, while also providing an interactive 3D UI for testing real and simulated platform components. The chosen architecture permits to test the control code both in “software-in-the-loop” and “hardware-in-the-loop” configurations. Furthermore, the simulator permits to use the same control code in both virtual and real scenarios. Accuracy results obtained for the considered calibration task are consistent with expectations (quantitative comparison between real and simulated calibration will be documented in a subsequent work), thus supporting the effective usability of the SINGER simulator for robotic platform development, towards more relevant neurosurgical procedures.

## REFERENCES

[1] Taylor R.H. Medical robotics in computer-integrated surgery. IEEE Trans Robot Autom. 2003;19(5):765-781.
[2] Abboudi H. et al. Current status of validation for robotic surgery simulators - a systematic review. Bju Int. 2013;111(2):194-205.
[3] Tovar-Arriaga S. et al. Development of a robotic FD-CT-guided navigation system for needle placement - preliminary accuracy tests. Int J Med Robot Comput Assist Surg. 2011;7:225-236.
[4] Strobl K.H., Hirzinger G. Optimal Hand-Eye calibration. Proc IROS. 2006;1-12:4647-4653.

# Trans-Nasal Robotic Micro-Surgery of the Throat: A Cadaveric Feasibility Study

A. Bajo[1], L.M. Dharamsi[2], J.L. Netterville[2], C.G. Garrett[2], N. Simaan[1]

[1]*Dept. of Mechanical Engineering, Vanderbilt University, Nashville TN, USA*

[2]*Dept. of Otolaryngology, Vanderbilt University Medical Center, Nashville TN, USA*

*nabil.simaan@vanderbilt.edu*

## INTRODUCTION

Trans-oral minimally invasive surgery (MIS) of the throat is usually preferred over open surgery because it preserves the integrity of the laryngeal framework, eliminates visible scars, and promotes faster recovery [1]. However, these advantages come at a price of limited access, visualization, and depth perception, lack of distal dexterity, amplified tremor, limited precision, and advanced hand-eye coordination. Hence, researchers and surgeons investigated the use of robotic assistance [2–4] for MIS of the upper airways.

All robotic MIS systems use trans-oral access into the throat. Trans-oral access requires the use of a laryngoscope, or a curved guiding channel. These devices require the mandatory use of general anesthesia. They also have been associated with several complications such as airway stenosis, coughing, gagging, laryngospasm, hypertension, and tachycardia [5]. General anesthesia entails the added costs of an operation room and it has also been associated with additional complications such as postoperative delirium, myocardial depression, and temporary renal dysfunction.

In this paper we present the approach of trans-nasal micro-surgery of the throat. This approach has the potential to reduce cost, complications, and patient discomfort by avoiding the use of the laryngoscope and general anesthesia. We believe this approach paves the way for low-cost office-based micro-surgery of the upper airways.

In [6], we presented a robotic system for trans-nasal access to the throat and evaluated it on a plastic model of the upper airways. The system and its control architecture were designed to address fundamental challenges such as safe and rapid access into the anatomy, enhanced intracorporeal dexterity, force sensing, tool delivery, and visualization.

In this paper, we present a cadaveric pilot study demonstrating the feasibility of safe trans-nasal insertion, access to the vocal folds and operating the end-effector in a realistic surgical scenario.

## MATERIALS AND METHODS

A system comprising of a ∅5mm two-segment snake robot presented in [6] and a Phantom Omni master interface has been used for these experiments. The system was mounted to the surgical bed as shown in Figure 1. Five cadavers were obtained through the Vanderbilt Anatomical Donation Program, 3 females and 2 males. After the inspection of the nasal conduit, pharynx, and larynx, only one cadaver was selected for the study. The other four were not used because the internal organs were not well preserved or the nasal conduit was obstructed.

The system can operate in both *passive* and *semi-active* modes. The passive mode is based on a standard telemanipulation architecture in which the surgeon guides the end-effector via a master manipulator while observing endoscopic images provided by a fiberscope passing through the robot's end-effector. The semi-active mode is used to reach the surgical site. During the semi-active mode the surgeon controls the insertion depth while the continuum manipulator autonomously conforms with the anatomy using compliance motion control [6].

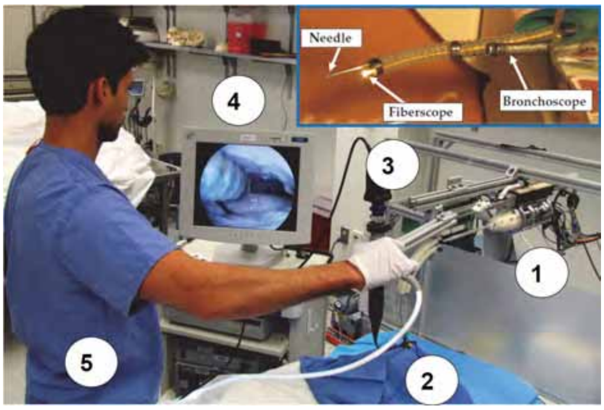



**Fig. 1** Experimental setup: (1) actuation unit, (2) magnetic tracker, (3) bronchoscope, (4) monitor, (5) surgeon.

The surgical slave is composed of a flexible passive stem and two actively bending segments. An additional DoF is provided by a linear stage, which controls the insertion of the base of continuum arm. The robotic arm has three ∅1.8 mm lumens that allow for the deployment of surgical instruments and end effectors. In order to compensate for the unknown shape of the passive segment constrained by the nasopharyngeal tube, a ∅0.9 mm electro-magnetic sensor is inserted through one of the working channels and attached to the base of the two segment continuum robot. A metal immune Ascension Tech. trakSTAR 2 flat transmitter was placed under the patient's head and it provided the position and orientation of the base of the proximal actively bending segment.

## RESULTS

A picture sequence showing the continuum robot descending into the upper airways is shown in Figure 2. Under compliant motion control, the continuum manipulator was successfully inserted through a 34Fr nasopharyngeal rubber tube. The tip of the robot exited the tube and entered the larynx right in front of the epiglottis. The controller was then switched to passive mode (telemanipulation) and the tip of the continuum manipulator was steered on the left in order to pass the epiglottis. Using visual information through the bronchoscope, the end-effector was first directed toward the endolarynx and then inserted further to reach the vocal folds. Figure 3 shows the view from the on-board fiberscope showing the tip the end-effector in the proximity of the voice box. A ∅0.66 mm needle was then deployed and the right vocal fold was punctured, simulating injection of collagen or steroids.

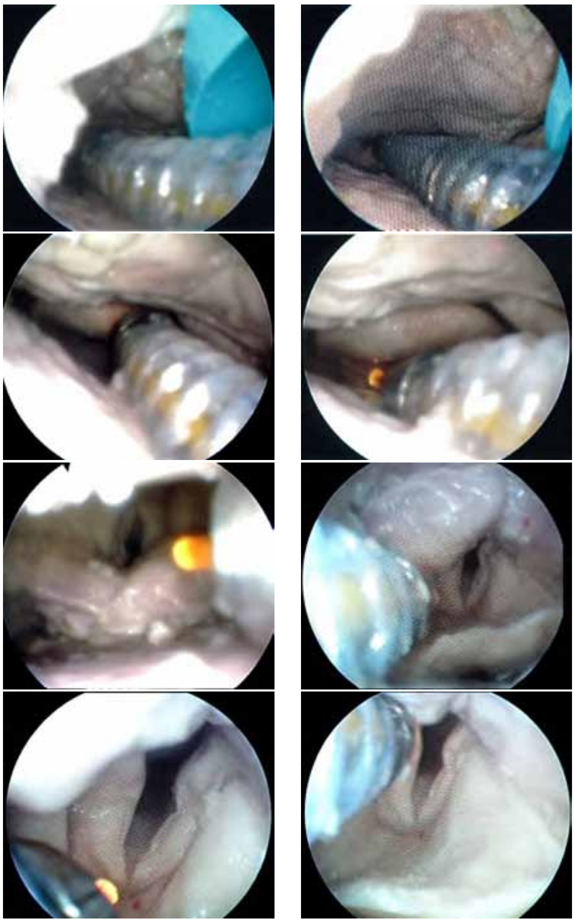


**Fig. 2** Image sequence of the insertion from the auxiliary bronchoscope inserted through the second nostril. The tip of the robot emerges from the nasopharyngeal tube, bends sidwise to avoid the epiglottis, and reaches the larynx.

## DISCUSSION

The goal of the cadaveric evaluation was to demonstrate the feasibility of trans-nasal access into the throat and the feasibility of controllable tool tip telemanipulation to target injection of vocal folds. Although some of the organs were collapsed (i.e. the epiglottis) and the surrounding tissues stiff because of the preservation process, the end-effector was able to navigate the upper airways and reach the vocal folds. Once there, instruments such as a fiberscope and a flexible needle were deployed and operated. This experiment demonstrates the efficacy of our compliant insertion algorithm in assisting the surgeon during the deployment phase and the flexibility of the control architecture in switching between semi-active and passive modes in order to navigate the upper airways.

The range of motion and speed of the end-effector remain, however, limited due to inadequate travel of the actuation pistons. The large deflection of the passive stem requires additional actuation compensation. Future research will focus on a redesign of the system in order to improve range of motion and higher end-effector speeds. Additional cadaveric experiments will be conducted in order to evaluate additional key surgical tasks such as biopsy, injection of collagen for the treatment of vocal fold paralysis, and steroid injection.



**Fig. 3** View from the on-board fiberscope showing the deployment of a needle.

## ACKNOWLEGEMENT

A. Bajo and N. Simaan were supported by NSF Career grant No. IIS-1063750.

## REFERENCES

[1] A. T. Hillel, A. Kapoor, N. Simaan, R. H. Taylor, and P. Flint, "Applications of robotics for laryngeal surgery.," Otolaryngologic clinics of North America, vol. 41, no. 4, pp. 781–91, vii, Aug. 2008.

[2] C. M. Rivera-Serrano, P. Johnson, B. Zubiate, R. Kuenzler, H. Choset, M. Zenati, S. Tully, and U. Duvvuri, "A transoral highly flexible robot: Novel technology and application.," The Laryngoscope. 2012; 122(5):1067–71

[3] N. G. Hockstein, J. P. Nolan, B. W. O'malley, and Y. J. Woo, "Robotic microlaryngeal surgery: a technical feasibility study using the daVinci surgical robot and an airway mannequin.," The Laryngoscope. 2005;115(5): 780–5.

[4] S. Wang, L. Yue, Q. Li, and J. Ding, "Conceptual design and dimensional synthesis of 'MicroHand'," Mechanism and Machine Theory. 2008 43(9):1186–1197,

[5] G. Lawson, N. Matar, M. Remacle, J. Jamart, and V. Bachy, "Transoral robotic surgery for the management of head and neck tumors: learning curve.," European archives of oto-rhino-laryngology, vol. 268, no. 12, pp. 1795–801, Dec. 2011.

[6] A. Bajo, L. M. Dharamsi, J. L. Netterville, C. G. Garrett, and N. Simaan, "Robotic-Assisted Micro-Surgery of the Throat : the Trans-Nasal Approach," IEEE ICRA pp. 232-238, 2013.

# Implanted Miniature Engineering Mechanisms in Tendon-Transfer Surgery Improve Robustness of Post-Surgery Hand Function

Ravi Balasubramanian[1], J. Montgomery[1], K.L. Mardula[1], C.H. Allen[2]

[1]Oregon State University and [2]University of Washington

ravi.balasubramanian@oregonstate.edu

## INTRODUCTION

Upper-extremity tendon transfer surgeries have been routinely performed since the 1970s for conditions such as stroke, paralysis, spinal muscle atrophy, nerve or muscle trauma, and congenital disorders. The surgery involves re-routing one or more tendons from an non-functioning muscle and directly suturing it to a functioning donor muscle in order to partially restore hand function [3, 4].

However, a fundamental aspect of tendon-transfer surgery has gone unaddressed. Oftentimes, a single donor muscle is directly sutured to multiple recipient tendons in order to actuate multiple joints. For example, take the case of tendon-transfer surgery for high median-ulnar palsy, a severe condition that disables the flexor digitorum profundus (FDP) muscle bellies and results in an inability to fully close the fingers, leading to weak grasps.

In order to restore finger flexion capability, the current surgical procedure is to directly suture the FDP tendons of all four fingers to a functioning donor muscle, such as the extensor carpi radialis longus (ECRL) (see Figs. 1a and 1b). While the direct suture is a simple method of at- tachment, it results in directly coupling the movement of the distal joints of all four fingers. As a result, the direct suture method prevents the fingers from adapting independently during physical interaction tasks such as grasping an object, fundamentally impeding post-surgery hand function. Specifically, when the hand closes in on an ob- ject during the grasping process, if one finger makes con- tact and stops, all the other fingers will stop before making contact since the motion of all the fingers is coupled (see Fig. 1b). Thus, the direct-suture attachment method re- sults in poor multi-finger power/enveloping grasping ability and may require the patient to use unnatural wrist and arm movements to complete the grasp. This is a significant issue since the ability to perform power grasps is fundamental to the activities of daily living, such as when holding objects to feed oneself [2].

In order to address this fundamental issue in tendon-transfer surgery, our group is exploring the use of im- planted passive miniature differential mechanisms [1] called "adaptive coupling mechanisms" to attach the donor mus- cle to the recipient tendons (see Figs. 1c, 1d, and 1e). In- spired by the application of these adaptive coupling mech- anisms in underactuated robotic hands [1], the key idea is that these adaptive coupling mechanisms, such as a hier- archical pulley system or seesaw mechanism, will enable each digit to continue to travel even if another digit actu- ated by the same donor muscle is stopped when it makes contact with an external object, thanks to the rotation of the pulleys or the seesaw mechanisms. Initial cadaver experiments and simulation studies we have conducted show that the implanted mechanisms enable the finger joints to adapt to the shape of the object during grasping and make complete contact [6, 7].

In this paper, we present results from a simulation study that show that the adaptive coupling mechanisms are able to accommodate for uncertainty that is typical in surgery and is typical in a grasping task. Specifically in the case of tendon transfer for high ulnar-median palsy, surgeons need to accurately choose the tendon lengths when attaching the donor muscle to the recipient tendons. If the tendon lengths are short by even 5% in the conventional procedure, some fingers would make contact pre- maturely during the grasping process, exacerbating the weak-grasp problem highlighted earlier. Also, since there is always uncertainty in each tendon's moment arm (or the mechanical advantage the tendon has over a joint) since it slides on top of the bone, any small variation in the mo- ment arm would also result in premature closing after a conventional tendon-transfer surgery. Finally, there will always be some error when placing the hand relative to the object to be grasped. Small deviations from the object center would also result in incomplete or weak grasps after the conventional tendon-transfer procedure. For each of the three cases, we present results from simulation that show that the proposed procedure using adaptive coupling mechanisms is able to accommodate such uncertainties. To our knowledge, this is the first time that the robustness of post-surgery grasping capability has been studied for tendon-transfer surgery.

## MATERIALS AND METHODS

An open-source biomechanics simulation platform OpenSim [5] was used to evaluate how the proposed modification to the high ulnar-median palsy tendon-transfer surgery improved the robustness of post-surgery hand function. The study focussed on the effect of replacing the FDP muscle with the ECRL muscle on the flexion of the metacarpophalangeal (MCP) and proximal interphalangeal (PIP) joints following the conventional and pro- posed tendon-transfer procedures.

[1] A common application of the differential mechanism is in the au- tomobile transmission, where the mechanism enables all four wheels to be driven by the same drive shaft and still allow each wheel to rotate at differing speeds when accommodating a turn.

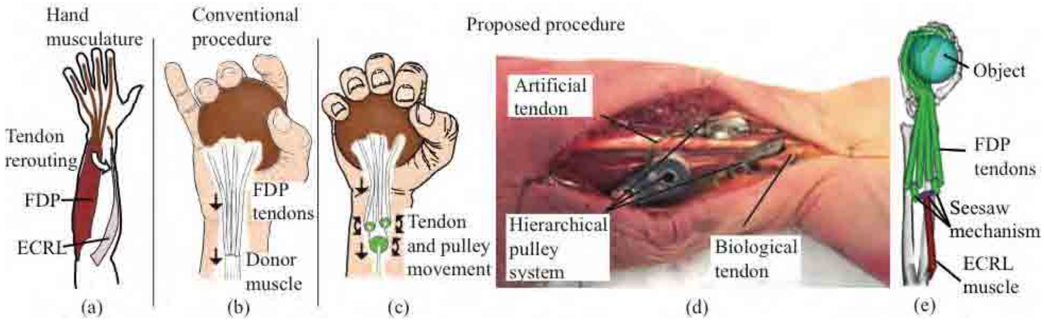



**Fig. 1** (a) Schematic representation of the hand anatomy showing the muscles and the rerouting that occurs in tendon-transfer for high ulnar-median palsy. (b) Schematic representation of the conventional procedure. The fingers do not close in completely on the object because of coupled finger movement. (c) Schematic representation of the proposed procedure with the hierarchical pulley system. The fingers close in completely around the object due to adaptive movement enabled by the pulley system (Subfigures (a), (b), and (c) are reproduced from [6]). (d) A hierarchical pulley system constructed with off-the-shelf components and implanted in a cadaver forearm. (e) An OpenSim biomechanical model of the proposed procedure using seesaw mechanisms.

The conventional four-tailed procedure was studied by adding a weightless body with full freedom of movement to the forearm to act as the interface between the ECRL muscle and the FDP tendons. The proposed procedure was studied by using a seesaw mechanism to attach the tendons to ECRL (see Fig. 1e). Three weightless bodies were added to the forearm; one was given full freedom of movement, while the others were attached to the first body and allowed free rotation about the Z axis. The ECRL was attached to the first bodys center, and the four FDP tendons were attached to the sides of the other two bodies.

A large sphere was placed near the hand center to simulate the grasping of a ball. Soft spheres were added to the fingertips to model the compliant contact between the ball and the fingertips using the Hunt-Crossley model. A forward dynamics simulation of a ball grasp was run using each model, providing a two-second linear ramp-and-hold excitation profile to the ECRL. The joint angles of each digit were measured. Three separate tests were conducted in order to measure the grasping robustness of the post- surgery hand to the uncertainty in the surgical process (in both the conventional and proposed procedure) and in the grasping task: 1) The tendons that inserted into the four fingers were shortened by 5%; 2) The moment arms of each of the tendons were varied by 5%; 3) The objects position was varied by 2 cm in three random directions. The goal was to see how these variations individually affected the total flexion of the MCP and PIP joints in a grasping task and observe if the hand was able to still make full contact with the target object.

## RESULTS

Fig. 2 shows that after the proposed procedure, the change and range of total flexion observed is small even if the tendon lengths are short or if there is moment arm variation. In contrast, the change and range of the total flexion after the conventional procedure for the same conditions is large. While not shown in Fig. 2, it was noticed that even with variation in the object's relative position with respect to the hand and variation in moment arms and the tendon lengths, the fingers made full contact with the object after the proposed procedure. In contrast, after the conventional procedure, only one finger made contact for the same conditions, resulting in incomplete grasps.

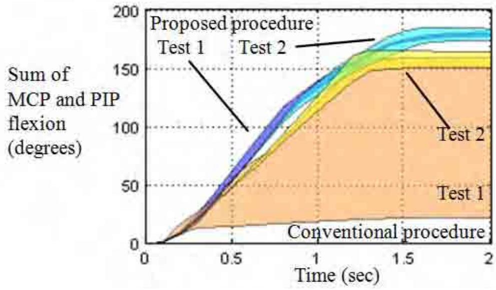



**Fig. 2** The change in and the range of total flexion at the MCP and PIP joints of all four fingers measured while grasping.

## DISCUSSION

The results indicate that the conventional procedure is highly sensitive to uncertainty in the surgical process and uncertainty in grasping tasks. In each simulation, it was noticed that a hand that underwent the conventional pro- cedure was unable to create full multifinger power grasps, an important aspect of daily living. In contrast, the pro- posed procedure enabled the fingers to accommodate the uncertainty in tendon lengths, moment arms, and object location and create secure multifinger grasps. The finger forces during the grasping process is being investigated.

## REFERENCES


[1] L. Birglen et al. Underactuated Robotic Hands. Springer, 2008.

[2] A. Bookman et al. Family Caregiver Handbook. Cambridge, MA: MIT Press, 2007.

[3] P. W. Brand and A. Hollister. Clinical Mechanics of the Hand. Mosby Year Book Incorporated, 2nd edition, 1993.

[4] W. P. Cooney et al. Opposition of the thumb: An anatomic and biomechanical study of tendon transfers. J. Hand Surg., 9A(6):777–786, 1984.

[5] S. L. Delp et al. OpenSim: Open-source software to cre- ate and analyze dynamic simulations of movement. Trans Biomed. Eng., 2007.

[6] K. L. Mardula et al. Implanted engineering mechanisms improve finger movement post tendon-transfer surgery for high median-ulnar palsy. In Internat. Conf. on Rehabilitation Robotics, 2013. (under review).

[7] J. Montgomery et al. New tendon-transfer surgery for ulnar-median nerve palsy using embedded adaptive engineering mechanisms. In Proc. Computer Methods Biomech. and Biomed. Eng., 2013.

# First Evaluations in the Control of a Novel Flexible Surgical Robot

A. De Donno, L. Zorn, P. Zanne, F. Nageotte and M. de Mathelin

*ICube, University of Strasbourg, CNRS, France.*

*adedonno@unistra.fr*

## INTRODUCTION

No-scar surgery is the last frontier in the field of minimally invasive surgery [1]. More and more surgeries are conducted with a transluminal, endoluminal or single port access, in order to reduce patient pain, bleeding and hospitalization time. Beside these advantages, no-scar surgery greatly increases difficulties for the surgeons, because the space for the instruments is small and triangulation is difficult to perform. Flexible endoscopic systems are good tools to help surgeons in performing these procedures, but normally these systems are very difficult to manipulate because of the high number of Degrees Of Freedom (DOFs). Robotics shall be a solution, assisting surgeons during operations and offering control, precision and ergonomics. In this paper we present STRAS (Single access and Transluminal Robotic Assistant for Surgeons), our new flexible teleoperated robotic system intended for endoluminal or transluminal operations.

## MATERIALS AND METHODS

STRAS is a robotized version of the Karl Storz Anubis® system. Anubis® is composed of three flexible sub-systems: a large endoscope and two insertable instruments. The endoscope consists of a flexible passive shaft (about 35 cm long) connected to an articulated distal section (about 22 cm long). This section can be deflected in two orthogonal directions (noted 2, 3, see Fig. 1) and embeds an endoscopic camera. The instruments, which have 3 independent DOFs (translation, rotation and deflection, noted 4, 5, 6, see Fig. 1), are inserted inside the main endoscope. Instruments triangulation is possible thanks to the endoscope head design. Actuated instruments, like grasper, have another additional DOF for opening / closing. Overall, the system has 10 DOFs.

The robotization process consisted in substituting all the manual motion driving with motors. For the endoscope deflections, the manual handle knobs were replaced by a set of spur and bevel gears, driven by a pair of Harmonic Drive servoactuators. The instrument actuation mechanisms are enclosed in a cylindrical hollow casing connected to the proximal end of the flexible instruments. The main endoscope is fixed on a mobile platform that allows its translation forward and backward (noted 1, see Fig. 1). The robot architecture is modular: it is possible to substitute one instrument during an operation without compromising the functioning of the whole system. Every sub-system has its own electrical case, while two Adept SMI6 controllers drive the motors controllers and manage the communication with the high level interface (a real-time Linux PC).

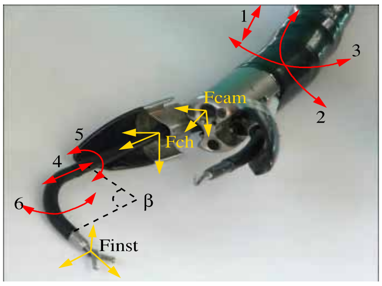



**Fig. 1** System DOFs and main kinematics frames**.**

During the normal use of the Anubis® system, two or more surgeons are requested to control each part of it. A big improvement introduced by STRAS is that a single user can teleoperate both instruments and main endoscope (the slave system) by means of two haptic interfaces (two Force Dimension omega.7, the master system). The kinematic architectures of master and slave systems are very different, so an adequate mapping between them is necessary. We are proposing four different control strategies:

- Direct axis control: each DOF on the slave system is mapped on a particular master system DOF. Several customizable mappings are possible, based on the user preferences. The default setup links left (resp. right) master interface to the left (resp. right) instrument. The endoscope control is obtained with the left interface after pressing a pedal that temporarily disconnects the left instrument.
- Speed control: the master interfaces positions, with respect to a neutral interface position, are interpreted as desired speed for the instruments. A force feedback effect on the interfaces acts as a spring, with the aim to drives the interfaces toward their neutral position when the user leaves them.
- Jacobian position control: instruments Cartesian workspaces are directly mapped onto the respective haptic interfaces workspaces; the motors velocity references are obtained by feeding the Cartesian position error to the inverse of the instrument jacobian. A force feedback effect proportional to the distance between the actual instrument and haptic Cartesian positions is applied, with the aim to keep track between the interface and the instrument movements.
- Cartesian Inverse Kinematics (IK): as in the Jacobian position control, the master interface position directly defines the instrument Cartesian position. But in this case the motors references are computed from the desired instrument tip Cartesian

position by means of an algorithm that we specifically developed to obtain a discretized IK model.

We have developed a graphical interface, which allows users to select the desired control strategy. The underlying high-level application realizes the mapping during teleoperation, filters the user input and communicates with the low-level controllers, sending the computed motors references (positions or speeds) and receiving the slave system status.

We have also developed a virtual simulator of our system, with the aim to assess the proposed control strategies in several simulated scenarios [2]. In addition to the robot kinematic model, we tried to implement inside the simulator some mechanical non-linearities effects that are currently present on the manual system, with the aim to study their effects on the system control.

## RESULTS

We have conducted several trials, involving surgeons from IRCAD and lab members, with the aim to assess the behavior of STRAS according to the chosen strategy. These trials included path following tasks in simulated environment [2] and testbed pick-and-place task in which cooperation between instruments and endoscope movements is mandatory [3].

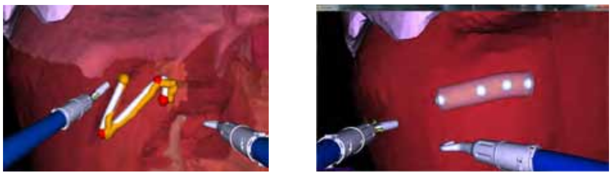


**Fig. 2** Path following tasks performed with the virtual simulator.

In the first trials, conducted with the virtual simulator (see Fig. 2), we tested the Jacobians and the Cartesian IK control strategies in two tasks that requested respectively precise instrument positioning and fast response speed. We found that, in ideal conditions, a speed control strategy permits to obtain better accuracy, because the input method allows fine variations of the actual instruments positions, with the counterpart of lower instrument reactivity. On the contrary, the direct mapping between haptic interfaces and instruments applied on position control strategies permits to obtain a faster response of the system to the detriment of accuracy. Scaling the user input could easily compensate this drawback, but in this case the user should reposition the master interfaces with a declutching system when he/she reaches the interface workspace limit. When non-linearities are added inside the simulation, a position control strategy permits to better compensate the non-linear effects. In this case, the applied force feedback effect seems to give a better control feeling and helps the system control, avoiding large user movements that cannot be followed by instruments because of non-linearities or motors limitations. This result points out the need to have correct instruments poses estimation on the real system, which could be obtained with an external sensor such as an EM tracker.

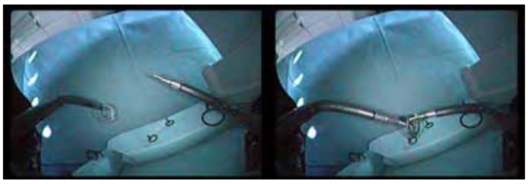


**Fig. 3** Pick-and-place task performed with the STRAS.

In the pick-and-place task (see Fig. 3) we demonstrated that a single user could perform alone a complex task that involves the whole slave system, which is impossible on the manual system. We executed a cooperation task seizing a ring on a stand with the left instrument, grasping it with the right instrument and bringing it on a nail. This task was performed in less than three minutes with a direct axis control strategy. For the moment, Jacobian strategies and Cartesian IK are not suitable for the real-time control of the robot, due to the lack of a valid measure of instruments positions. In both trials depth perception was one of the main issues.

## DISCUSSION

This paper has presented our new robotic system for endoluminal and transluminal surgery based on flexible shafts and continuum bending sections. After the initial setup, the robot can be teleoperated by a single person as demonstrated by first laboratory experiments. These trials have shown that, from a robotic point of view, the control strategy should be chosen according to the task that has to be done. From the user point of view, we have seen that individuals have very different preferences regarding master / slave mapping. Surgeons have especially appraised the fastness and the apparent fluidity of motion of the system, due to the absence of friction feeling. They have also acknowledged the ease of use and accuracy of the system.

Following these good results, authors and surgeons from IRCAD have deemed the general design of the robotic system very positive, and first trials on animal models will be carried out in the coming months. First trials also showed small architectural aspects that could be improved, but most of the remaining work lies at the control level. A dedicated master interface will also be developed for optimal control.

## REFERENCES


[1] L. L. Swanström, Y. Khajanchee and M. A. Abbas, “Natural orifice transluminal endoscopic surgery: The future of gastrointestinal surgery,” The Permanente Journal, vol. 12, no. 2, pp. 42–47, 2008.

[2] A. De Donno, F. Nageotte, P. Zanne, L. Goffin and M. de Mathelin, “A simulator for assessing control strategies for a novel flexible robot in no-scar surgery,” MICCAI 2012 Workshop on Augmented Environments for Computer-Assisted Interventions (AE-CAI)

[3] A. De Donno, L. Zorn, P. Zanne, F. Nageotte and M. de Mathelin, “Introducing STRAS: A New Flexible Robotic System for Minimally Invasive Surgery”, IEEE Int. Conference on Robotics and Automation (ICRA) 2013, Karlsruhe, May 6-10, 2013.

# Nanoparticle Ferrofluids for Tissue Manipulations in Minimal Access Surgery

Y.S. Lin, R. Roshan, P. Culmer, T. Liskiewicz, A. Neville

*Institute of Engineering Thermofluids, Surfaces and Interfaces, University of Leeds*

*mnysl@leeds.ac.uk*

## INTRODUCTION

In the last twenty years, minimal access surgery (MAS) has been widely used in abdominal surgery as it offers significant advantages, such as: smaller incision size and improved cosmesis, rapid patient recovery and reduced medical care, cost and blood loss. However, MAS is associated with a number of challenges including lack of space and limitations of conventional instruments. A significant challenge arises from the design of these instruments which have a long, thin shaft and are used through small incisions or natural body orifices.

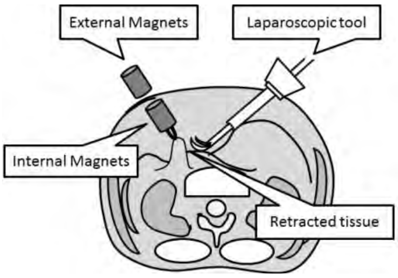



**Fig. 1** A schematic representative of cross-sectional tissue retraction using MAGS which replaces grasper and hooks tissue on to peritoneum.

In order to overcome the challenges posed by space, conventional laparoscopic tools are consistently improved to avoid any compromise for shape and working environment. A device called "Magnetic Anchoring and Guidance System" (MAGS) has been developed which effectively replaces conventional laparoscopic grasping instruments with two permanent magnets as shown in Figure 1. It applies magnets to remotely manipulate tissue from outside the abdominal wall by generating an interaction force between the two magnets [1-4]. The magnets grasp tissue and retract it to the abdominal wall. However, using several magnets in MAS is potentially troublesome for the purpose and may cause magnetic collision during surgery. There is also a chance of inadvertently tearing tissue during operation due to such strong magnetic interaction. A way to overcome these issues is to apply nano/micro scale iron colloid particles to magnetise the tissue and simultaneously manipulate them by controlling an external magnetic field [5-7]. This technique can dramatically reduce the interactions from magnets to provide an approach for tissue manipulation. Moreover, the fluidity of colloids mean that they can flow inside soft tissue to avoid tissue tearing. Consequently, the conventional grasper can be replaced and there will be more working space and clearer viewing in surgery.

Metallic particles have been used in human tissue and some clinical practice, however, the responded force associated with interaction of nanoparticles and magnetic field has not been studied well. The current research in Magnetic Resonance Imaging (MRI) has indicated that a safe range of exposure to magnetic fields ranges from 0.2 to 3 Tesla. This paper presents a study to optimise the size of particles in a carrier fluid by measuring the magnetic force of nanoscale ferrofluids (FFs).

## MATERIAL AND METHODS

FFs are widely used in mechanical and medical applications due to its unique fluidity and magnetism. FFs are composed of magnetite particles ($Fe_3O_4$) and a carrier fluid. The size of particles is usually nanoscale to ensure particles are stable in the fluid and are superparamagnetic in nature. Superparamagnetic particles magnetise in the presence of a magnetic field. The FFs used in this study are commercially available products: Liquids research Limited© and Chemicell©. The particles size is 10nm and 100nm and the quantity of FF injected in the tissue is 0.3ml.

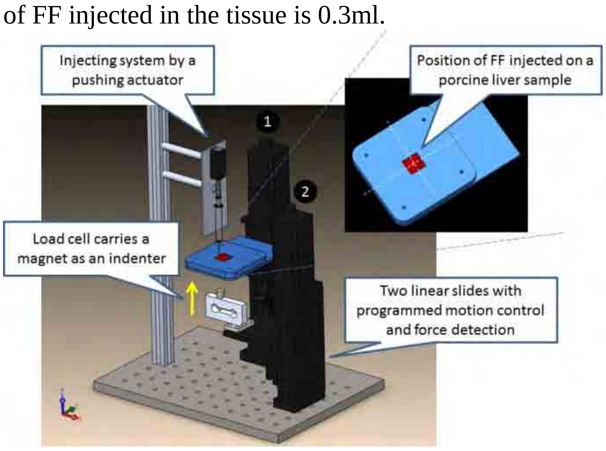



**Fig. 2** The configuration of MagRAT.

Figure 2 shows the magnetic retraction and adhesion tissue (MagRAT) tester designed to observe the effect of injection of FF in the tissue and to measure the magnetic adhesion force. The MagRAT consists of the

two linear slides (Zaber Technologies Inc.©) to control the motion of the load cell (Omega Engineering Inc.©) and the clamping plates. A permanent magnet (dia. 10 mm) is attached to the load cell to provide the force of magnetic adhesion when it is placed near the tissue containing FF, and the applied magnetic field strengthes are 0.3T, 0.5T and 0.6T. FF was injected in the tissue by an injection mechanism driven by a linear actuator (Firgelli Technologies Inc.©). The adhesion force was recorded using a LabVIEW program.

A 3cm x 3cm porcine liver tissue was placed on the clamping plates sandwiched between the top and bottom clamping plates. The clamping plates have a square hole for injecting the FF and to perform adhesion tests. The test starts with an injection of a pre-defined quantity of the FF into the tissue. A linear actuator attached to the syringe moves with a constant speed of 1mm/s to pierce the needle into the tissue. The depth of injection is controlled by advancing the linear slide in 0.5µm steps. Electrical conductivity method was applied to detect the contact of the needle to the tissue surface then starts injection process.

## RESULTS AND DISCUSSION

Figure 3 shows a typical force-time profile. This profile shows the motion of retraction in addition to the behaviour of tissue relaxation from when the probe and tissue are in contact. Here, A is the point of the injection of FF into the tissue. AB is the movement of the magnet towards the tissue. Point B is the point of maximum attraction force when the magnet is just in contact with the tissue. C is the point showing the maximum pre-load applied at the interface. The magnet is allowed to be in contact with the tissue as shown by CD. After a given time of contact, the probe retracts to measure the maximum adhesion force as point E.

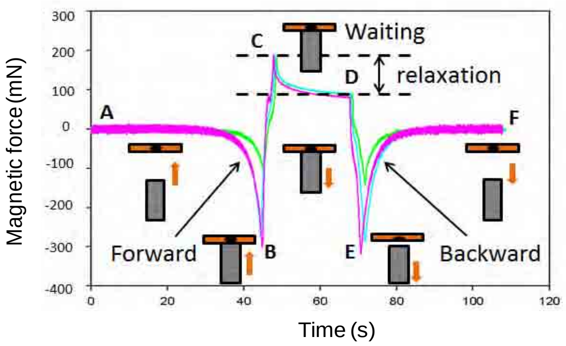



**Fig. 3** A schematic diagram of a typical force profile.

The results show that adhesion force increases with the decrease in particle size. A Micro computed-tomography (µCT 100) was used to characterise the FF particles distribution in the tissue. Samples were prepared for the micro-CT scanner and generated a series of segments. The segments showed distribution of iron particles within tissue (Figure 4(a)) at a resolution of 11.2µm. An image processing Matlab program was used to calculate the density of metallic particles in each segment, as shown in Figure 4(b). The density of particles in different segments was used as a parameter to study the effect magnetic force on the transportation of FF particles within tissue.

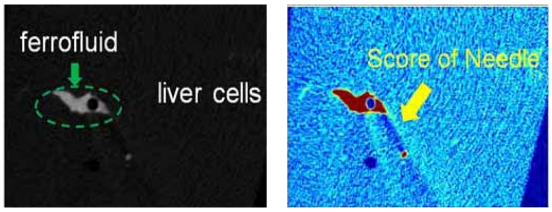



**Fig. 4** (a) The original segment of CT scan (b) after processing.

The characterisation of the particles in segments helps us to understand the effect of transportation of FF within the tissue. The magnetic field intensity and quantity of fluid injected in the tissue are directly proportional to the adhesion force. A comparison of particle size shows that the smaller the iron colloid particles, the higher the magnetic adhesion force.

This study investigates the performance of nanoscale particles and their feasibility in providing an adhesion force for tissue manipulation. This is a novel technique and our results here demonstrates that it has promise for future clinical use.

## REFERENCES

[1] M. Kume, H. Miyazawa, W. Iwasaki, F. Abe, H. Uchinami, and Y. Yamamoto, "The use of magnetic anchors in the bowel lumen for laparoscopic anterior resection of rectosigmoid colon in pigs: with video," World Journal of Surgery, vol. 32, pp. 2425-2428, 2008.

[2] G. Dominguez, I. Durand, J. D. Rosa, E. Danguise, C. Arozamena, and P. A. Ferraina, "Retraction and triangulation with neodymium magnetic forceps for single-port laparoscopic cholecystectomy," Surgical Endoscopy, vol. 23, pp. 1660-1666, 2009.

[3] J. Cadeddu, R. Fernandez, M. Desai, R. Bergs, C. Tracy, S. J. Tang, P. Rao, M. Desai, and D. Scott, "Novel magnetically guided intra-abdominal camera to facilitate laparoendoscopic single-site surgery: initial human experience," Surgical Endoscopy, vol. 23, pp. 1894-1899, 2009.

[4] S. L. Best and J. A. Cadeddu, "Use of magnetic anchoring and guidance systems to facilitate single trocar laparoscopy," Current Urology Reports, vol. 11, pp. 29-32, 2010.

[5] Z. Wang, L. Wang, B. Tang, T. Frank, S. Brown, and A. Cuschieri, "Retraction by surface ferromagnetisation of target tissues: preliminary studies on feasibility of magnetic retraction for endoscopic surgery," Surgical Endoscopy, vol. 22, pp. 1838-1844, 2008.

[6] Z. Wang, A. W. Brown, S. I. Brown, L. Wang, P. Andre, G. J. Florence, and A. Cuschieri, "Intra-luminal injection of ferro-fluid for magnetic bowel retraction in minimal access surgery," in Mechatronics and Embedded Systems and Applications (MESA), IEEE/ASME International Conference, 2010, pp. 168-173.

[7] Z. Wang, L. Wang, S. I. Brown, T. G. Frank, and A. Cuschieri, "Ferromagnetization of target tissues by interstitial injection of ferrofluid: formulation and evidence of efficacy for magnetic retraction," IEEE Transactions on Biomedical Engineering, vol. 56, pp. 2244-2252, 2009.

# Brain Surface Tissue Deformation Tracking in Craniotomies

R. Vivanti[1], O. Sadowsky[1], M. Shoham[2], L. Joskowicz[1]

[1]School of Engineering and Computer Science, The Hebrew Univ. of Jerusalem, Israel.

[2]Faculty of Mechanical Eng. Technion - Israel Institute of Technology, Haifa, Israel.

refael.vivanti@mail.huji.ac.il, josko@cs.huji.ac.il

## INTRODUCTION

Brain shift is one of the most challenging problems in image-guided craniotomy procedures [1]. In open brain surgeries, the neurosurgeon first removes a part of the patient's cranium, and then opens the dura. Due to various factors, the brain tissue deforms from its preoperatively imaged shape during the surgery. Subsequent brain deformations are caused by the loss of cerebrospinal fluid (CSF) and the reduction of intracranial pressure, as well as periodic motion due to the cardiac pulse and the respiratory cycle. The deformations on the brain surface and its interior are complex and time-dependent.

To address the challenge of compensating for brain shift during robotic and image-guided surgery, a real-time soft tissue tracking software module is necessary. This paper describes a new method for real-time quantification of brain shift during craniotomy surgery.

## MATERIALS AND METHODS

We have designed and implemented a sensor system and a processing method for soft tissue deformation tracking. Our method uses a pair of calibrated and synchronized digital cameras to capture a stereo video stream of the exposed brain surface. It estimates the deformation on the visible surface of the brain by tracking pairs of texture features on the brain surface. It removes outliers during tracking with a new paraboloid parametric model.

The proposed workflow is as follows. Prior to surgery, the stereo system is calibrated to derive the intrinsic projection parameters and the stereo relation between the cameras. The calibration parameters are computed with the open-source calibration toolkit CALTag [2] and the open computer vision library OpenCV.

At the beginning of the surgery, once the dura has been opened, we detect on the first pair of image frames a set of 2D feature points (mostly blood vessels bifurcations) on one image and match them to the other image by maximizing the Normalized Cross Correlation between the template and the search area.

Next, we perform stereo video tracking on the subsequent pairs of image frames. The matching is performed from left image to left image and from right image to right image (Fig. 1). The matching between subsequent points is also computed by maximizing the Normalized Cross correlation between the template and the search area. A prediction scheme is used to narrow the search areas and to accurately match less distinctive features. A pyramid hierarchical scheme is used for efficiency and accuracy.

For outlier detection and removal, we use a three-step outlier detection scheme: 1) Random Sample Consensus algorithm (RANSAC) with fundamental matrix; 2) RANSAC with affine transform, and, 3) a new outlier detection algorithm based on a parametric paraboloid model. The third outlier detection step consists itself of four steps: (1) computing the 3D location of each tracked point; (2) fitting a paraboloid to the 3D points using pseudo-inverse algorithm; (3) measuring the distance of each 3D point from the paraboloid, and; (4) removing the points whose distance exceeds a predefined threshold. To increase the tracking and estimation accuracy, we use sub-pixel matching in all feature-matching operations. Based on the 2D stereo tracking and the calibrated stereo relation between the cameras, we calculate the 3D location of each tracked point for each stereo frames with the non-linear triangulation algorithm in [3]. To increase the point location accuracy, we perform optical lens distortion correction in each iteration. The output is a set of 3D points and their respective trajectory in time.

## RESULTS

To evaluate the in-vitro performance of our method, we built the stereo tracking system and implemented the proposed method. It handles 12 stereo frames per sec.

We conducted an in-vitro experiment to evaluate the performance of our method. A rigid brain model was used as a phantom (Fig. 2). The model was moved in three directions along straight lines to the total distance of 10mm: Lx – along the Cartesian table *x* axis, Ly – along the *y* axes, and Lxy – along the bisector of lines Lx and Ly. Sixty different motions were measured with a Cartesian table with an accuracy of 0.001mm. Brain surface points were automatically selected and tracked, and their 3D movement was estimated. The estimated movement was then compared to the ground truth movement. This in vitro experiment showed that the overall system tracking accuracy is less than 0.5mm.

For each line trajectory, a new set of features was tracked; every feature had a 21-position path. To this 3D path, we fitted the closest line, choosing the mean as a point on the line and the direction of largest variance,

obtained from Principal Component Analysis of the points in the path, in the line direction. Table 1 shows the results of the stereo tracking positional error of the phantom surface with respect to the Cartesian displacement table measurements.

The mean Euclidean error, which is the absolute difference between the reconstructed movement and the table movement, was 0.14mm±0.48mm. The mean radial error, which is the absolute difference between the reconstructed point and the line fitted to its path, was 0.09mm±0.19mm. The mean rigidity error, which compares the reconstructed movement of one point to that of the other points, was 0.04mm±0.03mm.

While we expect the in-vivo errors to be larger, these results suggest that our method may be suitable for addressing the brain shift problem.

## DISCUSSION

We have developed a new method for near real-time quantification of brain shift during craniotomy surgery. First, feature points are detected on stereo images. Then the points are matched to the next stereo images with pyramid and prediction schemes to narrow the search areas. Three outlier detection methods are applied, including a new parametric model-based outlier detection. Finally, 3D points locations are computed and tracked while brain shift occurs. An in vitro experiment showed a mean accuracy of 0.17mm or better.

The main contributions of our work are: 1) a new texture-based tracking method that does not rely on implanted fiducials; 2) a robust tracking point selection method that allows accurate tracking; 3) a new outlier detection method based on paraboloid model fitting that does not require a preoperative image, and; 4) implementation and in-vitro validation of the method.

We are currently integrating the 3D tracking results with a biomechanical brain model, so as to propagate the brain surface deformation to its inner parts.

## REFERENCES


[1] Maurer CR et al. Investigation of intraoperative brain deformation using a 1.5-T interventional MR system: preliminary results. *IEEE Trans. Medical Imaging*, 17(5):817–825, 1998.

[2] Atcheson B et al. CALTag: High Precision Fiducial Markers for Camera Calibration, Proc. 17th Workshop Vision, Modeling, Visualization, Magdeburg, Germany, 2012.

[3] Hartley R, Zisserman A, *Multiple View Geometry in Computer Vision*, 2(2). Cambridge U. Press, 2004.



**Acknowledgment**: This research was funded by European Contract FP7-ICT-270461: ACTIVE.

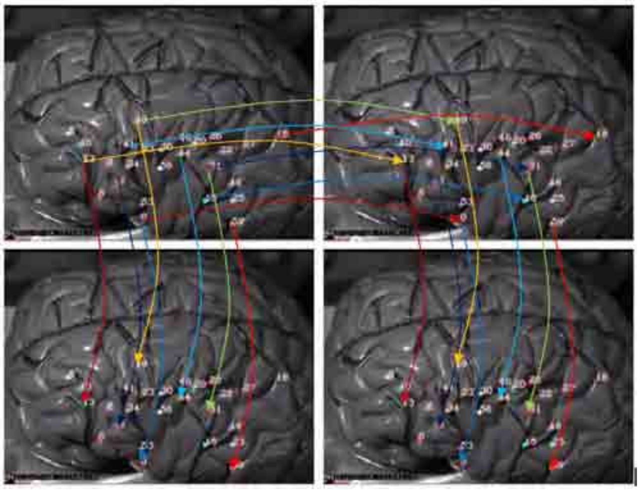



**Fig. 1** Illustration of stereo and video matching of features. The top row shows the first video frame, and the bottom the second. Stereo matching is done from left to right frame, and video tracking is done between subsequent frames from the same side.



**Fig. 2** Photograph of the experimental setup. The stereo cameras are mounted on a tripod (left) and point to the plastic brain model, mounted on a Cartesian displacement table.

**Table 1** Stereo tracking positional error of the phantom surface. The first column indicates the table line translation. The second column is the error type. The third and fourth columns are the mean and standard deviation for each case in mm.

| Path | Error type | Mean | Std |
|---|---|---|---|
| **Lx** | Euclidean error | 0.17 | 0.72 |
| | Radial error | 0.09 | 0.25 |
| | Rigidity error | 0.04 | 0.04 |
| **Ly** | Euclidean error | 0.12 | 0.22 |
| | Radial error | 0.09 | 0.17 |
| | Rigidity error | 0.04 | 0.04 |
| **Lxy** | Euclidean error | 0.12 | 0.14 |
| | Radial error | 0.07 | 0.07 |
| | Rigidity error | 0.06 | 0.02 |
| **Avg.** | Euclidean error | 0.14 | 0.48 |
| | Radial error | 0.09 | 0.19 |
| | Rigidity error | 0.04 | 0.03 |

# A Low Cost System for 3D Position and Orientation Sensing

Kilian O'Donoghue, Padraig Cantillon-Murphy

*School of Engineering, University College Cork, Ireland.*

*kilianod@rennes.ucc.ie*

## INTRODUCTION

This paper examines the development of a low cost system for determining position and orientation of a catheter in vivo. The immediate clinical application is for pulmonary localisation but the technique is relevant across clinical specialities. The system uses planar magnetic coils transmitting low frequency magnetic fields (<25kHz) and implemented on printed circuit board (PCBs), as well as a miniature pick-up coil placed at the distal end of a catheter. Low frequency magnetic fields pass though tissue with minimal distortion and attenuation, hence are well suited for use as position detection system. By measuring induced voltage in the pick-up coil caused by an array of magnetic sources at various frequencies, position and orientation can be determined by solving a non-linear system of equations.

This method of using planar coils for position detection has been demonstrated by Plotkin et al [1]. There are also a number of commercially available electromagnetic tracking systems such as Northern Digital's Aurora and Ascension's trakSTAR [2], which are used in a range of medical procedures. However these are typically prohibitively expensive and are also susceptible to magnetic interference [2]. The current work aims to develop a low-cost, high-speed, ideally open-source, alternative to current commercial systems by relying, as much as possible, on analogue signalling while maintaining low positional errors.

## MATERIALS AND METHODS

### 1. Theory of operation

The voltage induced by coil of wire in an alternating magnetic field is given by Faradays law of electromagnetic induction:

$$V = -N\frac{d\Phi}{dt} = -N\frac{d(\mathbf{B}\cdot\boldsymbol{A})}{dt} \quad (1)$$

where $N$ is the number of turns in the coil, $\boldsymbol{B}$ is the magnetic field vector in space, and $\boldsymbol{A}$ is a vector representing coil area and orientation. In Cartesian coordinates, $\boldsymbol{A}$ is given by:

$$\boldsymbol{A} = A(\sin\theta\cos\varphi\,\hat{\boldsymbol{x}} + \sin\theta\sin\varphi\,\hat{\boldsymbol{y}} + \cos\theta\,\hat{\boldsymbol{z}}) \quad (2)$$

where $A$ the cross-sectional area of the sensor coil, while $\theta$ and $\varphi$ represent the orientation in spherical coordinates. The magnetic field can be generated from a current carrying coil which results in a non-linear vector function, $\boldsymbol{B}(\boldsymbol{r})$. This vector varies spatially with the position vector $\boldsymbol{r} = \{x, y, z\}$ and decreases with distance from the coil. Considering current to vary in time as $I = I_0\sin(\omega t)$ where $\omega$ is the angular frequency of excitation, the resulting peak amplitude of measured flux at a given displacement is a non-linear function of 5 variables, $\{x, y, z, \theta, \varphi\}$, given by:

$$V = \omega NAI\left[B_x\sin\theta\cos\varphi + B_y\sin\theta\sin\varphi + B_z\cos\theta\right] \quad (3)$$

where $\{B_x,\ B_y,\ B_z\}$ are functions of $\boldsymbol{r}$ that represent the normalized magnetic field components resulting from a current of 1A flowing through the source coil.

If multiple coils at different positions are used, a system of equations can be formed which can be solved to determine position and orientation. By using different excitation frequencies for each coil, the various magnetic fields do not interfere with one another and can be regarded as independent from each other.

Plotkin et al [1] demonstrated that 8 planar coils, driven with 8 different frequencies are sufficient to accurately solve this system of equations. Our design modifies their approach by simplifying a number of elements such as the detector circuit, and improving the stability of the excitation source.

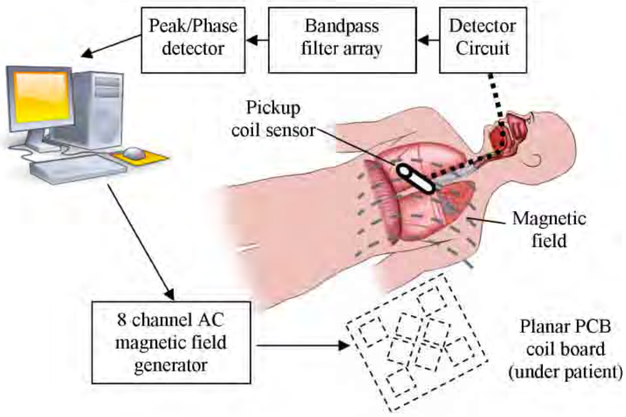



**Fig. 1** Block diagram for the entire system system. An 8 frequency coil driver circuit generates a magnetic field pattern from a planar coil array placed below the patient. The magnetic field is detected using the pickup coil sensor and the signal is then amplifed and processed. The resulting signals are sampled onto the computer where they are used to determine the position of the sensor.

### 2. AC Coil Design

The coils used for the source of the AC magnetic fields are formed as planar windings on a printed circuit board. This facilitates ease of manufacture and reproducibility, *i.e.*, each coil can be made almost identical. Square coils were chosen as they result in simpler PCB layout. In order to design and simulate the coils, the following simple expression for the magnetic field due to a current carrying filament was used [3]:

$$\boldsymbol{B}(\boldsymbol{r}) = \frac{\mu_0 I}{4\pi}\left(\frac{\boldsymbol{c}\times\boldsymbol{a}}{|\boldsymbol{c}\times\boldsymbol{a}|^2}\right)\left(\frac{\boldsymbol{a}\cdot\boldsymbol{c}}{|\boldsymbol{c}|} - \frac{\boldsymbol{a}\cdot\boldsymbol{b}}{|\boldsymbol{b}|}\right) \quad (4)$$

where $\boldsymbol{a}$ is a vector in the direction of the filament, $\boldsymbol{b}$ is a vector pointing from an observation point $\boldsymbol{P} = (x, y, z)$ to the end of the filament, and $\boldsymbol{c}$ is a vector pointing from P to the start of the current carrying

filament as seen in Figure 2. The magnetic field due to each track on the PCB was calculated using (4) and the resultant sum gives the overall magnetic field due to the coil. The required magnetic field was calculated using (1), by estimating the magnetic field necessary to induce a signal of approximately 1mV in amplitude in the pickup coil at a distance of 30cm from the source coil. This value was chosen to give a reasonable signal to noise ratio (SNR) within the field of view (FOV). The final coil design has 25 turns and a square side length of 70mm with a max current of 500mA.

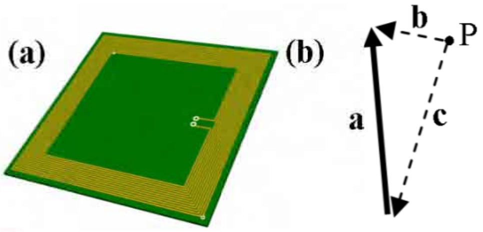



**Fig. 2 (a)** 3D representation of a single magnetic field source coil. Each coil is printed on a two layer PCB measuring 70mm × 70mm, with 25 turns in total. Each track has a width of .5mm and a thickness of 70μm. **(b)** Vectors for calculating the magnetic field due to a current carrying wire filament located at position *P* [3].

### AC field generator circuit

In order to generate the desired AC magnetic field, an analogue circuit has been designed and developed that delivers a constant AC current to the coils. By using a constant current design, variations in the coil such as resistance due to temperature rise can be neglected. The circuit is based on a typical constant current op-amp design, with an additional class B amplifier stage to boost the output power.

### 3. Pickup coil

The magnetic field sensor used is a single axis pick-up coil. Five hundred turns of 40AWG bifilar enameled copper wire (80μm diameter) form the coil which is 2mm in diameter and 8mm in length. A twisted pair cable joins the sensor to the detector circuit.

### 4. Detector circuit

In order to detect small voltages induced in the pickup coil, an off-the-shelf instrumentation amplifier, INA129 by Texas Instruments, was used to amplify the signal by a factor of 500. Once the signal has been amplified, it is then buffered into multiple parallel bandpass filters, each of which has a high Q factor (>50) and unity gain, to split up each frequency component. Following filtering, the amplitude of each voltage is recorded using a peak-detector circuit and the phase measured using a phase detector. The resulting DC voltages from both the peak detector and phase detector can then easily be measured and used to calculate the position and orientation.

### 5. Computer interface

The resulting DC voltages are sampled using a National Instruments data acquisition (DAQ) card with a MATLAB (Mathworks Corp., Natick, Massachusetts) interface. The MATLAB Optimization Toolbox is used to implement the algorithm to determine the sensor position using the measured data.

## RESULTS

The tracking algorithm, which is based on the Levenberg-Marquardt least squares method [4], was simulated using MATLAB and its performance in tracking an arbitrary trajectory was examined in the presence of random noise. The added noise is a randomly chosen value in the range -2mV to 2mV, (signal voltage typically is on the order of hundreds of mV). Figure 4 shows the trajectory and the calculated position of the sensor. The average position error is 0.47mm; each calculation took an average of 66ms on a standard laptop computer with a dual core 2.5GHz processor.

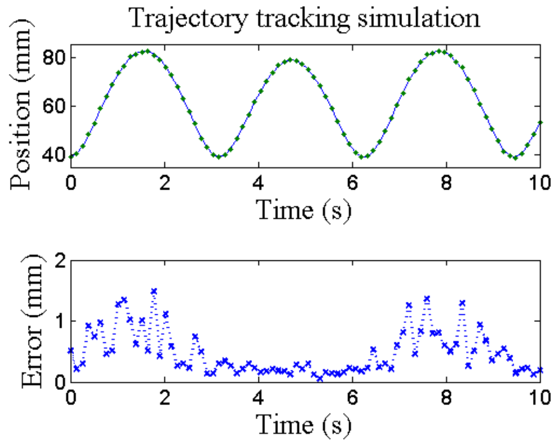



**Fig. 3** Simulation showing the performance of the detection algorithm in the presence of white noise. The magnitude of the position relative to the origin is plotted; the error is shown in the lower graph.

## DISCUSSION

The presented system represents a low cost method for catheter position determination in vivo. The drive circuit and detector utilises entirely analogue components with low position errors. PCB coil construction can facilitate very low cost. The outputs of the detector are DC voltages which can be easily measured using low cost ADCs in place of the DAQ cards used in this initial work. The overhead cost of the MATLAB algorithm could be removed by implementing the relevant solver on a more basic programming platform and this is being actively explored.

## REFERENCES


[1] A. Plotkin, O. Shafrir, E. Paperno, and D. M. Kaplan, "Magnetic eye tracking: A new approach employing a planar transmitter," *Biomedical Engineering, IEEE Transactions on*, vol. 57, pp. 1209-1215, 2010.

[2] E. Wilson, Z. Yaniv, D. Lindisch, and K. Cleary, "A buyer's guide to electromagnetic tracking systems for clinical applications," in *Proceedings of SPIE*, 2008, pp. 69182B-1.

[3] C. Sonntag, M. Sprée, E. Lomonova, J. Duarte, and A. Vandenput, "Accurate Magnetic Field Intensity Calculations for Contactless Energy Transfer Coils," in *Proceedings of the 16th International Conference on the Computation of Electromagnetic Fields*, 2007.

[4] M. A. Wolfe and M. Wolfe, Numerical methods for unconstrained optimization: an introduction: Van Nostrand Reinhold New York, 1978.

# An Ultrasound-based Methodology for Endoluminal Robot Tracking in Cardiovascular Procedures

M. Mura, G. Ciuti, P. Dario, A. Menciassi*

*The BioRobotics Institute, Scuola Superiore Sant'Anna, Pisa, Italy*

* *arianna.menciassi@sssup.it*

## INTRODUCTION

Cardiovascular diseases (CVDs) are the first cause of death globally and atherosclerotic plaque accumulating in the arteries is the leading cause of cardiac and vascular disorders. An estimated 17.3 million people died for CVDs in 2008, representing the 30% of all global deaths. Of these deaths, an estimated 7.3 million were due to coronary heart disease and 6.2 million were due to stroke [1]. Current therapies for acute CVDs aim to restore blood flow. The traditional surgical techniques for vascular problems are angioplasty and bypass grafting. Typical inconveniences of these procedures are guidance via fluoroscopy (dangerous for patients and operators) and the absence of a real removal for plaque and obstruction, which normally are by-passed or pushed against the vessel wall. In addition, although traditional diagnosis and therapy have advanced substantially, research efforts are devoted to the development of robotic-aided platforms for enhancing steerability of the interventional catheter. Recently, some remote catheter navigation systems have been introduced: they are based on steerable cable activated sheaths for catheters precise steering and coronary interventions, or on a controlled permanent magnetic field in which a magnetically equipped catheter can align and bend. All these platforms are based on catheters, they basically provide just steering and not propulsion abilities, and they cannot be adapted to wireless or softly wired endovascular devices. Moreover, another significant drawback of the mentioned platforms is related to the needs of a high radiations dose for the catheter localization for both operator and patients.

In this framework, an innovative methodology, based on a computer-aided surgery architecture and developed by the authors (MicroVAST platform – Fig. 1), combines a magnetic locomotion approach for a vascular softly tethered endoluminal robot with an ultrasound (US) transducer-based algorithm for tracking purposes [2], [3]. In this paper, the authors describe an innovative ultrasound-based methodology for endoluminal robots tracking in cardiovascular procedures. The ultrasound-based intra-operative data, together with pre-operative multimodal data (lumen centreline reconstruction for optimal path definition), would allow for the implementation of an assisted or autonomous safe propulsion of a endoluminal device in cardiovascular procedures.

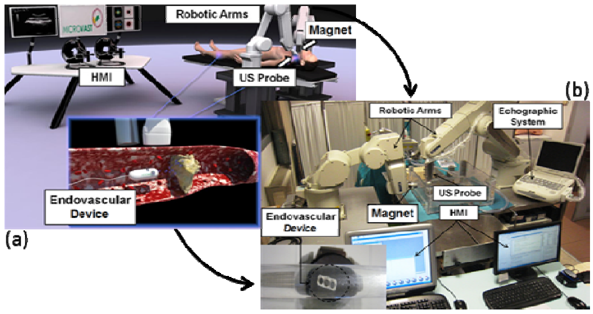



**Fig. 1** (a) Schematic representation and (b) real development of the MicroVAST platform.

## MATERIALS AND METHODS

The MicroVAST platform is composed by two teleoperated anthropomorphic 6 degrees-of-freedom robotic arms: one holding an external permanent magnet for the endovascular device navigation (*i.e.* master robot), and the other one holding the US probe for tracking (*i.e.* slave robot). The US probe (CA430E, Esaote, Italy) is a convex array transducer with a working frequency between 3.5 and 5 MHz and a radius of curvature of 40 mm. The interaction between the external magnet and the internal magnet of the endovascular device (10 mm in length, 4 mm in diameter) is used to propel the softly tethered endoluminal robot along the cardiovascular system while locomotion is supervised by the ultrasound-based methodology. In particular, the US-based control algorithm consists of the tracking of the internal device by using a combination of optical flow (OF) and segmentation techniques, with the aim to maintain a reliable and effective magnetic link along the procedure. The algorithm consists of an iterative process composed by several phases, described in Fig. 2a-f. At the beginning of the procedure, the user manually selects a region of interest (ROI) enclosing the endoluminal robot (Fig. 2b). Onto the selected ROI, specific Shi-Tomasi features of the device are extracted thus deriving the centre of mass (CoM) (Fig. 2c). A new predefined ROI is then automatically defined on the next frame based on the previous calculated CoM (Fig. 2d) and a Watershed segmentation is applied for retrieving the exact shape of the endoluminal robot (Fig. 2e). Subsequently, thanks to a pyramidal Lucas-Kanade OF algorithm, the corresponding features are found out and the new CoM of the object is calculated (as the arithmetic mean of the features positions - Fig. 2f). The described algorithm is iterated until the end of the medical procedure, and the endoluminal robot CoM and features dynamic state are

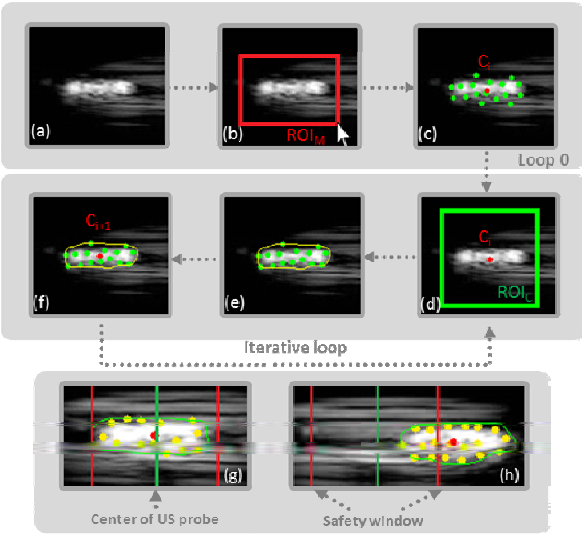



**Fig. 2** (a-f) The US-based control algorithm phases for the endoluminal robot tracking and (g-h) the high-level algorithm for the cooperative control of master and slave robot; endoluminal robot (g) inside and (h) outside a safety window.

then computed, each frame, for the cooperative control of the master and the slave robot. The master and slave manipulator are moved together and a high-level algorithm compares the position of the endoluminal robot CoM with respect to the vertical central line (green line in Fig. 2g) of the US frame; if the difference exceeds imposed safe limits (safety window, red lines in Fig. 2h - device dimension ± 20%), the master robot is retrieved in the previous safe position in order to maintain or, at least, re-establish a reliable magnetic link. In the case of a low number of features (i.e. < 4) are detected, the procedure is retrieved to a manual user control. In order to validate the US-based control algorithm performance in terms of CoM calculation accuracy, a dedicated software was implemented and an off-line video has been used for computing the difference between the derived CoM and the centre of an ellipse-shaped geometry coherently overlaid on the object frame (Fig. 3).

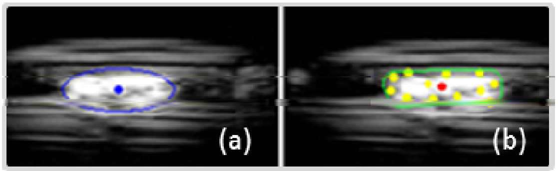



**Fig. 3** The tracking error as a difference of the (a) ellipse CoM and the (b) CoM extracted from the implemented algorithm.

Furthermore, the US-based control algorithm was qualitatively evaluated in a 3D *in-vitro* test-bench in combination with pre-operative data (fed to the robotic arm for the optimal path planning) with the aim to implement an autonomous endoluminal robot propulsion. The *in-vitro* simulator mimics the abdominal aortic bifurcation and it was developed by using a plexiglass tube (PMMA, Ø 25(e)/19(i) mm; with an acoustic impedance greater than soft tissue one) with a first straight part of 230 mm, bifurcation of 120°, length of bifurcations 120 mm and a downslope of 30°.

## RESULTS

The US-based algorithm control loop is processed with an average time of 13 ms, which is compatible with real time application, and an average number of 12 features were extracted in each frame from the segmented endoluminal robot. An average error of 0.57 mm resulted by the difference of the endoluminal robot CoM and the centre of the ellipse-shaped geometry, thus demonstrating the effectiveness and accuracy of the implemented algorithm. Furthermore, the qualitatively *in-vitro* test established the effectiveness of the implemented US-based algorithm in the endoluminal robot tracking for the accomplishment, in combination with preoperative data for path planning (*i.e.* derived lumen centreline), of a 3D autonomous safe magnetic propulsion strategy of an endoluminal robot in cardiovascular procedures (Fig. 4).

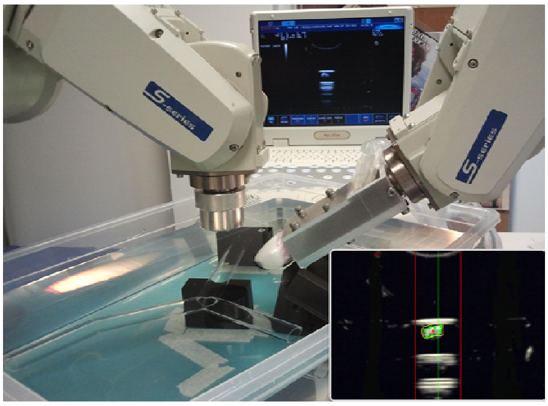



**Fig. 4** The *in-vitro* experimental test bench for evaluating the platform effectiveness; inset: screenshot of the high-level US-based control.

## DISCUSSION

The US-based intra-operative servo control demonstrated to be a feasible and accurate tracking system and, combined with pre-operative multimodal data, would allow for the implementation of an assisted or autonomous locomotion of a softly tethered endoluminal robot in cardiovascular procedures. The locomotion and tracking strategies will be applied and tested in a more realistic pathway, the EVE endovascular evaluator (Fain Biomedical, Japan) and in *ex-vivo* and *in-vivo* conditions.

## ACKNOWLEDGMENT

This work was supported by the Fondazione Cassa di Risparmio di Pisa in the framework of the MicroVAST project (http://www.microvast.it).

## REFERENCES

[1] World Health Organization: http://www.who.int/. Fact sheet N°317, updated March 2013.
[2] S. Tognarelli *et al.* Magnetic propulsion and ultrasound tracking of endovascular devices. J Robotic Surg. 2012; 6:5-12.
[3] P. Miloro *et al.* An innovative platform for treatment of vascular obstructions: system design and preliminary results. IEEE BioRob2012 conference, Rome, 2012 June 24-27; pp. 731-736.

# Salient Features of Soft Tissue Examination Velocity during Manual Palpation

J. Konstantinova[1], K. Althoefer[1], P. Dasgupta[2], T. Nanayakkara[1]

[1]Centre for Robotics Research, King's College London

[2]MRC Centre for Transplantation, DTIMB and NIHR BRC, King's College London

jelizaveta.zirjakova@kcl.ac.uk

## INTRODUCTION

The direct access to organs during Robot-assisted Minimally Invasive Surgery (RMIS) is limited and palpation is difficult to be implemented. Therefore, there is a need for the development of advanced tactile instruments to be used for intra-operative soft tissue examination and accurate localization of abnormalities, such as tumours.

Despite the availability of tactile devices for soft tissue examination [1] the influence of probing behaviour on abnormality detection has not been studied yet. Our work underlines the importance of optimally chosen speed and load during tactile examination of the simulated viscoelastic environment [2]. In this work, we study the impact of velocity during manual palpation on the detection of hard inclusions in a silicone phantom and ex-vivo porcine kidney samples. In addition, validation results based on Finite Element (FE) simulations are presented. We present the evaluation of palpation velocity and show that it is a valuable source of information for the development of probing strategies and the design of new tactile sensing devices.

## MATERIALS AND METHODS

Ten participants have been recruited to study the effects of velocity during manual palpation. All subjects had at least five years of surgical experience. Participants were asked to detect hard formations during three sets of unidirectional palpation tests using a silicone phantom and a porcine kidney sample. Three types of palpation velocities were employed during each test – slow, natural and fast. Natural velocity is defined as the palpation speed, which comes most naturally to participant.

To fabricate the soft phantom, silicone gel RTV6166 with a ratio of 4:6 and viscosity of 900 mPa·s was used. Three hard nodules, diameter of 10 mm, were embedded at different depths (3 mm, 5 mm) from the surface of the silicone material. To create the nodules, hard silicone compound RTV615 with a ratio of 10:1 and 4000 mPa·s viscosity was used.

The experimental setup, schematically shown in Fig.1, was used to measure the exerted finger pressures and palpation trajectories - the latter were used to calculate the associated palpation velocities. The applied forces were recorded with six-axis force/torque sensor MINI 40 (ATI Industrial Automation), whose normal force resolution is 0.01 N. A Microsoft Kinect sensor (640 × 480 pixel resolution and sample rate of 30 fps) was used to track the position of the hand in three dimensions with the help of the Microsoft Visual C++ OpenCV package. The position accuracy for the Kinect sensor is 1-2 mm. This value was obtained experimentally for an average palpation velocity.

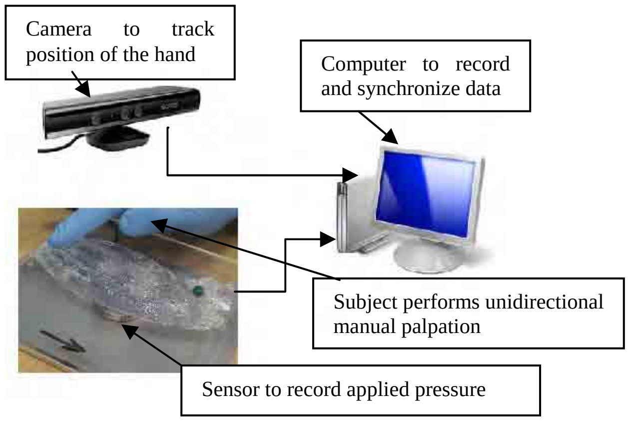



**Fig. 1** Schematic representation of the experimental setup

Data processing and statistical analysis was implemented in MATLAB 7.12.0 and R statistics i386 2.15.2 software. A three-way analysis of variance (ANOVA) was used to test the statistical significance of the palpation factors. The confidence level for null hypothesis rejection was set to 95%, for $p < 0.05$.

To understand the responses of soft tissue during various palpation conditions, FE simulations were conducted in ABAQUS 6.10.1. The silicone phantom ($50 \times 30$ $mm^2$ planar block) was modelled based on the studies shown in [3]. The size of each finite element was set to 1 $mm^2$ using a quadrilateral element type. The modelled nodule had a 10 mm diameter and was embedded at two different depths (3 mm, 5 mm) corresponding to the experimental setting. A finger during palpation was modelled as a rigid sphere with a diameter of 20 mm. The modelled soft tissue surface was assumed to be lubricated during palpation experiments; therefore, the contact between simulated tissue and indenting body was set as frictionless. The sphere was indenting the silicone phantom model by 3 mm at the initial step of the FE simulation.

## RESULTS

Firstly one needs to test the effect of various palpation factors, such as palpation material, performance of each subject, and applied force and velocity, on the detection rate of hard nodules. Among all factors, the effect of the

target material, silicone phantom or ex-vivo organ, was significantly ($F_{(4.00)} = 6.23$, $p < 0.0001$) influencing the detection rate. This result demonstrates that the palpation conditions should be chosen according to the given environment.

This implies that the impact of the traversing velocity should be studied for a given type of target material (for this case - a silicone phantom). Therefore, the ANOVA test is conducted again for the experimental data of palpation for the silicone phantom. It was detected that the used velocity ($F_{(4.24)} = 8.97$, $p < 0.00001$) and the applied force ($F_{(4.24)} = 16.67$, $p < 0.00001$) are significantly influencing the detection rate of hard formations.

The above result supports the importance of correctly chosen force and velocity for soft tissue examination. Thus, it is required to study the influence of the velocity magnitude. According to experimental conditions, the velocity magnitude was subjectively defined by each subject. To exclude individual bias, velocity data for all trials was divided into three groups using k-means clustering. Three clusters are presented in Fig. 2. An overview of detection rates and velocity magnitudes for each cluster and correlation with experimental results is provided in Table 1. According to the velocity measurements, the highest detection rate is observed for a slow palpation velocity with a magnitude, which does not exceed 125 mm/s.

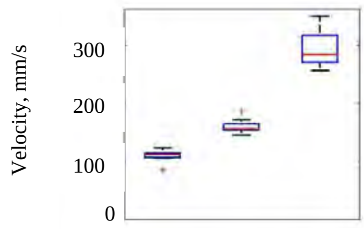



**Fig. 2** Clusters of velocity distribution for slow, natural and fast palpation velocity

**Table 1** The impact of palpation velocity

| Cluster | Detection Rate % | Velocity Magnitude, mm/s | Correlation with Experiments, % |
|---|---|---|---|
| Slow | 87 | 85 - 123 | 55 |
| Natural | 82 | 144 - 220 | 38 |
| Fast | 69 | 256 - 350 | 75 |

The experimental measurements of velocity magnitude are used in our FE simulations. Fig. 3 displays the simulated soft tissue model with the deformation above the nodule. The detection rate of a hard nodule depends on the stress magnitude in the target tissue. A subject senses the higher force for the unit area when the stress in the material is higher. Fig. 4 displays the stress magnitude for the indentation contact point for two different depths of the location of a hard nodule. As expected, a slower speed of palpation induces a higher magnitude of stress. A larger depth of the nodule leads to a smaller stress response from the area above it, especially for fast and natural velocity.

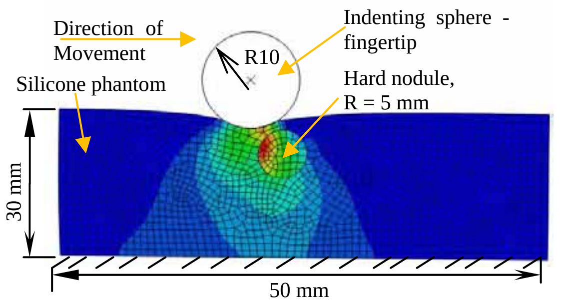



**Fig. 3** Finite element simulation of silicone phantom indented with a fingertip above the nodule location (depth 3 mm).

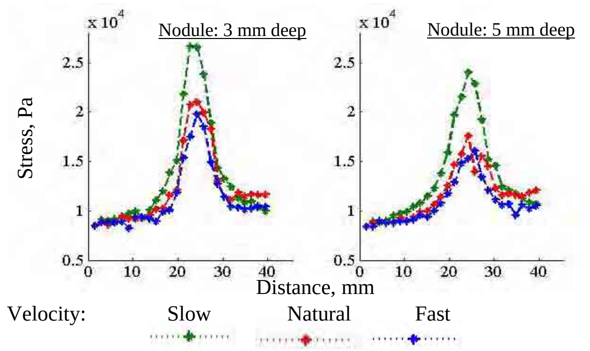



**Fig. 4** Stress distribution for different depths of nodules – 3 and 5 mm: (green – slow velocity, red – natural; blue – fast).

## CONCLUSIONS

This work underlines the importance of correctly chosen palpation behaviour for a given palpation environment. By means of experimental studies and FE simulations, we have demonstrated the impact of velocity during manual palpation. We believe that these studies will be useful for the creation of advanced probing control strategies, and development of tactile sensing methods that can be integrated with RMIS. It is planned to carry out more extensive studies with a tele-manipulation setup in the future.

## ACKNOLEDGMENT

The research is funded by the NIHR Biomedical Research Centre based at Guy's and St Thomas' NHS Foundation Trust and King's College London.

## REFERENCES

[1] H. Liu, O. Elhage, P. Dasgupta, B. Challacombe, D. Murphy, L. Seneviratne, and K. Althoefer, “A haptic probe for soft tissue abnormality identification during minimally invasive surgery,” in *Advances*, 2009, pp. 417–422.

[2] J. Zirjakova, K. Althoefer, P. Dasgupta, and T. Nanayakkara, “Probing Behaviour for Soft Tissue Stiffness Measurement,” in *World Congress of Endourology*, 2012, pp. A20–A21.

[3] K. Sangpradit, H. Liu, L. D. Seneviratne, and K. Althoefer, “Tissue Identification using Inverse Finite Element Analysis of Rolling Indentation,” in *IEEE International conference on Robotics and Automation ICRA*, 2009, pp. 1250–1255.

# Robotic Steering of Cardiac Ultrasound Imaging Catheters

L.J. Brattain[1,2], P.M. Loschak[1], C.M. Tschabrunn[3], E. Anter[3], R.D. Howe[1]

[1]*Harvard School of Engineering and Applied Sciences, Cambridge, MA, USA*
[2]*MIT Lincoln Laboratory, Lexington, MA, USA*
[3]*Harvard-Thorndike Electrophysiology Institute, Beth Israel Deaconess Medical Center, Harvard Medical School, Boston, MA, USA*
*brattain@seas.harvard.edu*

## INTRODUCTION

We have developed a system for steering cardiac imaging catheters to automatically visualize heart structures and instruments. The goal of this system is to improve the efficacy, speed, and safety of imaging during catheter-based arrhythmia treatment procedures. Many cardiac arrhythmias can be effectively treated by radiofrequency (RF) catheter ablation [1], but the primary real time imaging modality is x-ray fluoroscopy, which does not effectively distinguish soft tissues and exposes patients and clinical staff to ionizing radiation. Real time visualization of intracardiac structures is needed to further improve the efficacy of catheter ablation procedures.

Intracardiac echocardiography (ICE) catheters are routinely used during ablation procedures for their high-quality ultrasound soft tissue visualization. A major challenge during catheter ablation is the lack of acute lesion assessment, and ICE visualization of lesion growth has the potential to improve acute procedural outcomes. However, manual use of ICE requires specialized training and maintaining continued alignment of the imaging plane is a significant challenge. Existing robotic catheter systems (e.g. Hansen Medical, http://www.hansenmedical.com, Stereotaxis, http://www.stereotaxis.com, [2]) enable teleoperation of catheter controls and reduce radiation exposure, but they do not solve the problem of steering an ICE imaging plane towards a desired structure.

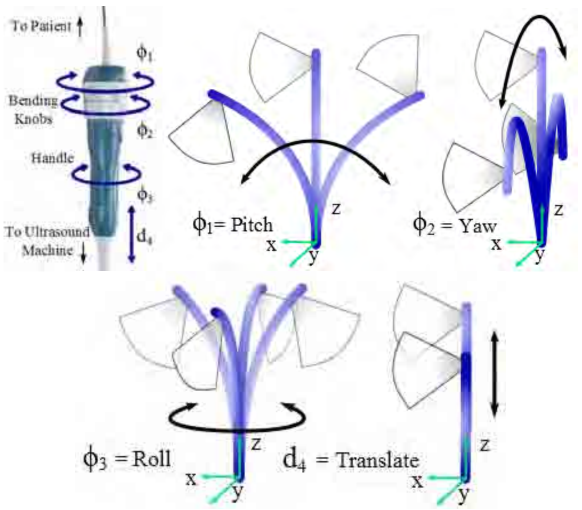



**Fig. 1** ICE catheter actuated degrees of freedom with corresponding tip and imaging plane motions

MIT Lincoln Laboratory work is sponsored by the Department of the Air Force under Air Force contract #FA8721-05-C-0002. Opinions, interpretations, conclusions and recommendations are those of the authors and are not necessarily endorsed by the United States Government. Harvard University work is supported by the US National Institutes of Health under grant NIH R01 HL073647.

In this study our system manipulates an ICE catheter in a water tank to visualize a phantom. Multiple images are stitched together to create a volume of the target structure. This enablement of real time visualization during catheter ablation has potential to facilitate improved long-term treatment of cardiac arrhythmias.

## MATERIALS AND METHODS

ICE catheters have an ultrasound array transducer in the tip of a steerable catheter which transmits images to the clinician in real time. The catheter handle has four actuated degrees of freedom (DOF) that create tip motion (Fig. 1). Two bending knobs can be individually actuated to achieve pitch (left-right knob), yaw (posterior-anterior knob), or a combination of both. The catheter handle can be rotated and translated.

The system consists of a catheter manipulator, kinematic and control algorithms, and visualization enhancement. The off-the-shelf catheter is articulated by DC motors connected to belts for rotation and a lead screw for translation. Kinematic algorithms were derived to control catheter motions which are difficult to achieve manually. Specifying a desired position for the ICE catheter tip requires 3 DOF. Since the catheter possesses 4 DOF, the extra DOF can be applied to constrained orientation control. By adjusting both knobs in conjunction with handle rotation, the imaging plane may be rotated about the catheter axis at the tip while the physical location of the catheter remains constant. Fig. 2(a) shows a simulation of a catheter with its imaging plane rotating about the catheter tip axis, where the green lines represent the same vector in each imaging plane. Fig. 2(b) shows the joint actuation required for achieving this motion. A closed form solution for inverse kinematics of the catheter tip based on orientation was used to calculate the knob adjustments [3].

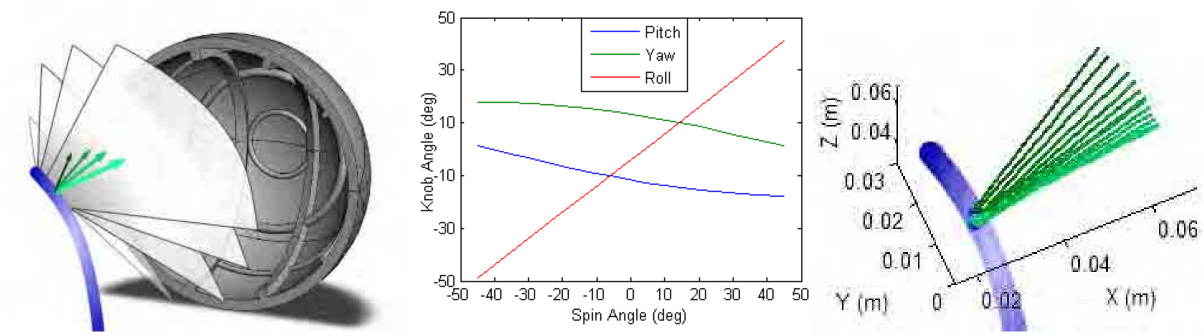



**Fig. 2** (a) Schematic of imaging plane rotation while visualizing CAD model of phantom, (b) example handle inputs for large image plane rotation, (c) data for 23° total imaging plane rotation

A series of images obtained during plane rotation across a region may be spatially registered into the Cartesian coordinate frame and interpolated into a reconstructed 3D volume model of the cardiac cycle. Electromagnetic (EM) trackers with RMS position errors on the order of 1.4 mm (trakSTAR, Ascension Technology) were mounted to the catheter tip for reconstruction. EM tracking is typically used for electroanatomic mapping in many interventional catheter labs. For testing purposes, this technique was applied to image an object of known dimensions that was fabricated on a high-resolution 3D printer. The phantom was designed with distinctive 3D features that would visualize well under ultrasound and be useful for catheter tip localization during calibration.

## RESULTS

Robotic steering data for an ICE catheter is shown in Fig. 2(c), where the green lines represent the same vector in each imaging plane and the color intensity represents the order in which rotations occurred. The imaging plane rotated in 13 steps averaging 1.8° per step for a total of 23°. During rotation the total tip motions were constrained to within ±2.0 mm in every direction, which is an acceptable error tolerance given the accuracy of the EM tracker system and sufficient for safe procedural use. Fig. 3 shows 13 image slices reconstructed to visualize a region of the phantom.

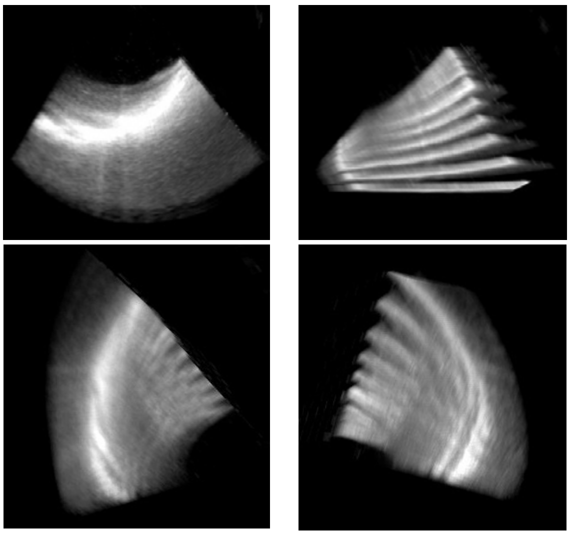


**Fig. 3** Ultrasound image slices stitched into a volume

## DISCUSSION

The tests described in this study signify the first use known to the authors of applying ICE catheter position and orientation kinematics to robotically enhance clinicians' visualization abilities. Fig. 2(c) showed that the system was able to rotate the imaging plane using the kinematic algorithms without significantly displacing the location of the catheter. This could enable clinicians to move the ICE catheter to a safe location and image structures that are difficult to focus on by manual manipulation. Reconstructed volumes can be useful in performing diagnoses or lesion assessment during ablation.

This approach can enable other visualization techniques, such as allowing a user to choose an angle from which to image a target object from a set of possible viewing angles, and then automatically steering the imaging device to the proper position and orientation for monitoring catheter-tissue interactions.

The capabilities demonstrated in this study are meant to be a proof of concept for the use of a robotic system to control ICE imaging. Future work will correct for system inaccuracies (such as friction, backlash, imperfect curvature, etc.), apply safety boundaries based on the known locations of surrounding heart structures, and use image processing to assist in navigation. Kinematic algorithms for imaging can be applied to many catheter-based procedures involving visualization of various organ systems via long, thin, flexible imaging tools. This robotic system, specifically, has the potential to greatly increase clinicians' visualization capabilities while reducing procedure times and training times related to mastering the use of ICE.

## REFERENCES

[1] Baim DS, Grossman's Cardiac Catheterization, Angiography, and Intervention, Lippincott Williams & Wilkins, 2005.

[2] Koolwal B, et. al. "A fast SLAM approach to freehand 3-D ultrasound reconstruction for catheter ablation guidance in the left atrium," Ultrasound in Medicine and Biology, Vol. 37(12), pp. 2037-2054, 2011.

[3] Loschak PM, et. al. "Automated pointing of cardiac imaging catheters," Proc. IEEE Int. Conf. Robotics and Automation (in press), 2013.

# Collaborative Robot-assisted Endovascular Catheter Navigation using Learned Models


H. Rafii-Tari, J. Liu, S.-L. Lee, G.-Z. Yang

*The Hamlyn Centre for Robotic Surgery, Imperial College London, UK*
*{h.rafii-tari11, j.liu}@imperial.ac.uk*


## INTRODUCTION

Remote-controlled catheter navigation systems have attracted a growing interest in recent years for endovascular surgery [1]. However, most systems are designed based on master-slave platforms with limited automation and collaborative control, without considering natural motion patterns and tool interactions used in bedside practice. While previous studies on catheter kinematics are geared towards endovascular skill assessment [2], it is believed that this information can be used in a learn-from-demonstration framework to automate certain parts of the surgical procedure while reducing the cognitive workload of the operator [3]. This study proposes a learning-based approach for generating optimum motion trajectories from multiple demonstrations, using a proximal catheter position sensor, and automating the catheter motion using a robotic driver within a collaborative setting through which the operator maintains control of the guidewire. Learning the underlying skill and characteristic motion patterns of endovascular navigation to enable semi-autonomous robotic catheterisation can help improve catheterisation tasks while providing more ergonomic operator-robot interactions.

## MATERIALS AND METHODS

The framework and experimental setup were first presented in [4] and are depicted in Fig. 1. The designed sensor measures the linear and rotational motion of the catheter applied by the operator at the proximal end, using two non-contact magnetic rotary encoders and a roller based mechanism. Using this information, motion models were learned from multiple demonstrations performed by expert and intermediate-level operators and different trajectories were extracted for each group.

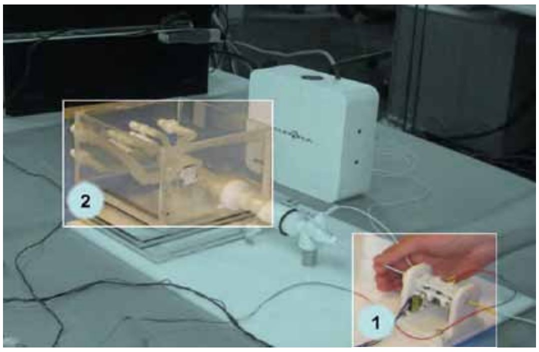



**Fig. 1** Experimental setup depicting the position measurement unit (1) and phantom of the aortic arch (2)**.**

The procedure was cannulation of the innominate artery in an anthropomorphic phantom of a type I aortic arch. Trajectories were validated using a robotic catheter driver with a similar design to the measurement unit.

This study expands and further validates the robustness of the proposed framework by learning motion models from completely inexperienced operators, and replicating the generated trajectories on the robotic driver. The models are learned from 9 demonstrations of the task by 3 inexperienced operators. To create smooth trajectories in the presence of inter- and intra-operator variability while automating the procedure in stages, the linear and radial position signals from the proximal sensor are divided into three phases based on the path: the descending aorta (phase A), the aortic arch (phase B) and cannulation of the innominate artery (phase C). The signals across each phase are synchronized using a combination of dynamic time warping and linear time normalization. Gaussian mixture models (GMM) are used to create a probabilistic representation of the phase data and smooth trajectories that capture the characteristic features of the training data are extracted from the models using Gaussian mixture regression (GMR) [5]. Trajectories are applied to the robotic driver to automate the catheter motion and the cannulation is performed 10 times across inexperienced operators. Guidewire manipulation is controlled manually by the operator, and the system awaits operator input at the end of each phase before continuing catheter advancement, to allow for collaborative control with the operator.

Catheter tip positions, measured from a 6 DoF electromagnetic position sensor attached to the tip, are obtained in the manual training phase as well as the robotic phase to validate the performance of the system. Different metrics corresponding to catheter tip velocity, acceleration, and smoothness of tip motion (the accumulative change in slope of the displacement signal) are extracted for each phase. Differences between these are assessed using nonparametric analysis (Wilcoxon rank-sum test, $P < 0.05$). Further analysis on repeatability of catheter movement is also provided.

## RESULTS

Fig. 2 shows the catheter tip displacement and paths from the robotic drive based on the learned model against examples of the respective training set, depicting much smoother and more homogeneous motion with the robot compared to the manual catheterization.

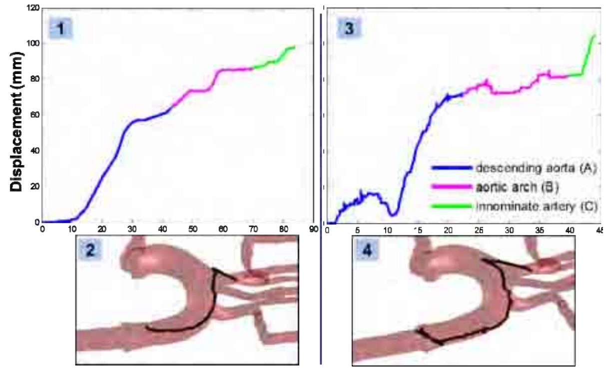



**Fig. 2** Catheter tip displacement and path for robot-assisted catheterisation (1,2) compared to manual catheterisation (3,4).

The significant differences ($P < 0.05$) between robot-assisted catheterisation and the corresponding manual training set for the median values of the metrics at each procedural phase are shown in Table 1. The results depict much smoother catheter motion with the robotic approach, as a result of steadier movement with less back/forth motion, thereby showing the ability of the robot-assisted framework to reduce possible vessel wall contact and the risk of embolization in the higher-risk areas of the procedure (phases B and C).

**Table 1** Median Values for Statistically Significant Differences between Robot-assisted Learned Procedures vs. Manual Training Data

| Section | Metric | Robotic | Manual |
|---|---|---|---|
| Descending Aorta | Mean speed (mm/s) | 3.45 | 10.44 |
| | Mean accel. (mm/s$^s$) | 67.94 | 278.49 |
| | Smoothness (mm) | 52.69 | 158.70 |
| Aortic Arch | Mean speed (mm/s) | 2.78 | 10.06 |
| | Mean accel. (mm/s$^s$) | 52.74 | 264.42 |
| | Smoothness (mm) | 28.11 | 73.04 |
| Innominate | Mean speed (mm/s) | 2.99 | 11.80 |
| | Mean accel. (mm/s$^s$) | 56.78 | 257.03 |
| | Smoothness (mm) | 18.49 | 24.71 |

Fig. 3 compares the maximum catheter tip velocities and accelerations (median values) between the robot-assisted approach and the manual training data at each phase over all procedures. The significant differences observed show that safer and more stable catheter motion at lower speeds and accelerations can be achieved by the robot, which can correspond to less sudden movements and deflections at the catheter tip and a reduced risk of damage to the arterial wall.

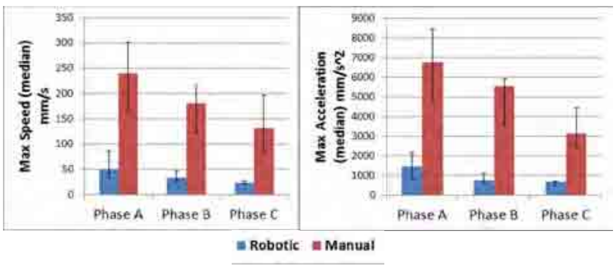



**Fig. 3** Maximum catheter tip speeds and accelerations (median values) for robotic-assisted vs. manual training data. Error bars represent the interquartile ranges.

Table 2 shows the standard deviation in catheter tip displacement for the robotic drive, as compared to the manual approach. The results show that more repeatable catheter motion can be achieved with the learned trajectories implemented on the robotic catheter driver, as opposed to manual catheterisation.

**Table 2** Standard Deviation in Mean Catheter Tip Displacement for Robot-assisted vs. Manual Catheterisation

| | Robotic STD (mm) | Manual STD (mm) |
|---|---|---|
| Descending Aorta | 4.53 | 8.96 |
| Aortic Arch | 3.47 | 4.93 |
| Innominate Artery | 2.23 | 3.13 |

## DISCUSSION

This study extends our previous study using a proximal position sensor to generate learned trajectories from multiple demonstrations of a catheterisation task, and using these towards robotic automated catheter navigation in a collaborative framework whereby the operator can maintain control of the guidewire [4]. This paper further validates the robustness of the proposed approach by learning motion models and encoding the underlying structure of movement from completely inexperienced operators, and successfully validating this through automated catheter navigation using the robotic driver. The results show significant improvements in the smoothness and stability of catheter tip motion with reduced number of movements, which could translate to reduced vessel wall contact and damage to the arterial wall. The study provides important insights into shared-control robotic navigation platforms that utilise the bedside catheterisation skills of operators. The approach can have further applications toward creating metrics for automated skill assessment, by comparing motion models obtained from inexperienced operators against learned models from experts, thereby also improving training and assessment of catheterization skills.

## REFERENCES

[1] Riga CV, Bicknell CD, Rolls A, Cheshire NJ, Hamady MS. Robot-assisted fenestrated endovascular aneurysm repair (FEVAR) using the Magellan system. J Vasc Interv Radiol. 2013; 24(2): 191-196.

[2] Thakur Y, Holdsworth DW, Drangova M. Characterization of catheter dynamics during percutaneous transluminal catheter procedures. IEEE Trans Biomed Eng. 2009; 56(8): 2140-2143.

[3] Reiley CE, Plaku E, Hager GD. Motion generation of robotic surgical tasks: Learning from expert demonstrations. IEEE EMBS. 2010; 967-970

[4] Rafii-Tari H, Liu J, Lee SL, Bicknell C, Yang GZ. Learning-based modeling of endovascular navigation for collaborative robotic catheterization. Submitted to MICCAI 2013.

[5] Calinon S, Guenter F, Billard A. On learning, representing, and generalizing a task in a humanoid robot. IEEE T Syst Man Cy B. 2007; 37(2): 286-298

# Workspace Analysis and Calibration Method for Mobile Image Overlay System used for Image-Guided Interventions

M. Anand[1], T. Ungi[1], T., A. Lasso[1], P. U-Thainual[1], J. Jayender[2], J. Fritz[3], J. A. Carrino[3], F. A. Jolesz[2], G. Fichtinger[1,3]

*[1]Laboratory for Percutaneous Surgery, Queen's University, Canada;*
*[2]Surgical Planning Laboratory, Harvard Brigham and Women's Hospital, USA;*
*[3]Department of Radiology and Radiological Science, Johns Hopkins University, USA.*
*manjunath.anand@queensu.ca*

## INTRODUCTION

Previously, a static image overlay guidance system has been proposed for aiding needle placement interventions [1,2]. In this technique, a 2D computer display image is reflected by a semi-transparent mirror, so that the virtual image appears floating inside the patient in correct 3D position. This system provides accurate transverse image guidance for musculoskeletal interventions of the shoulder, hip and spine [3,4]. The previous static mounting of the system was either fixed to the CT/MR imaging system [1] or on a floor-mounted frame over the patient table [2,3]. This mounting required careful calibration before each procedure, and was prone to misalignments due to structural deformation or unintended physical contact with the device. Furthermore, the static mount limited the access to the patient and excluded clinically relevant ranges of motions of the tool and the physician. To overcome those limitations, we propose the Mobile Image Overlay System (MIOS). The potential applications of MIOS are musculoskeletal needle injections, parathyroidectomy, percutaneous nephrolithotomy and percutaneous access to blood vessel.

## MATERIALS AND METHODS

MIOS consists of mirror-monitor configuration called as viewbox similar to [1,2] and attached to a floor mounted articulated counter-balanced system. It is equipped with optical markers on the viewbox to measure the pose of the image overlay plane during the entire procedure. An optical marker (reference marker) is attached to the patient's skin, near the location of the intervention to allow tracking of the virtual image plane pose relative to the patient. A set of CT or MR visible fiducial markers are placed on the patient before image acquisition. These fiducial markers are touched using an optically tracked stylus to register the acquired image with the reference marker's coordinate system by using landmark registration. The system can be used for exploration of the image volume by a moving image slice overlaid on the patient. The software will display the correct image in real time corresponding to the position of the image overlay plane tracked by the tracker w.r.t the patient. After locating the target point in the image overlay plane inside the patient, the system is firmly locked in this position and the needle trajectory is drawn on the image slice in the software, which gets updated in the image overlay plane for needle guidance. MIOS overcomes the practical difficulty of accurately positioning the static image overlay system [1,2] by the motion tracking of the viewbox.

**Workspace analysis**: The spine needle injection and parathyroidectomy are the two critical procedures which defines the constraints for workspace analysis. Workspace analysis defines the i.) optimum angle between mirror and monitor for maximum viewing angle up to which the complete depth of the image overlay can be seen through the mirror and orientation of viewbox w.r.t articulated arm; ii.) directions of the required motion; iii.) sufficient gap between the viewbox and patient while the system is positioned over the patient; iv.) oblique rotation of +/- $35^{o}$ of the image overlay plane; v.) sufficient vertical space for needle injection. The study was conducted using CAD software "Creo2.0". Previously proposed $60^{o}$ system (Fig. 1a) in [1,2] and newly proposed $90^{o}$ system (Fig. 1b) are considered for the study.

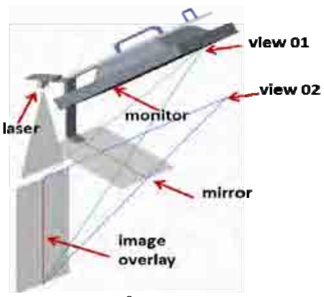



**Fig. 1a** $60^{o}$ MIOS

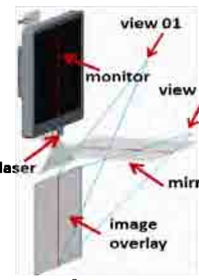



**Fig**. **1b** $90^{o}$ MIOS

**Calibration method**: The image overlay plane has to be registered to the image reslicing plane in the software and physical position of the patient. Two calibration methods were studied: i.) indirect calibration (Fig. 2) and ii.) direct calibration (Fig. 3). Indirect calibration is the conventional method and uses calibration phantom to register the image overlay plane with image reslicing plane in the software. It requires manual alignment of the viewbox until the markers in the virtual image appears in perfect alignment with the markers on the calibration phantom. The direct calibration method is a novel approach to register the image overlay plane directly to the image reslicing plane in the software, without the needs of physical calibration phantom. The tracker determines the pose of the passive markers on the viewbox and the virtual markers displayed in the image overlay plane. The transformation matrix is determined between image overlay plane and viewbox from the maker pose measured. During the procedure,

the viewbox is continously tracked by the tracker and using the computed transformation matrix, the actual position of image overlay plane relative to the patient is determined.

For oblique image display, three concepts were studied: i.) five bar link mechanism; ii.) monitor rotation only; iii.) viewbox rotation about fixed target axis (Fig. 5).

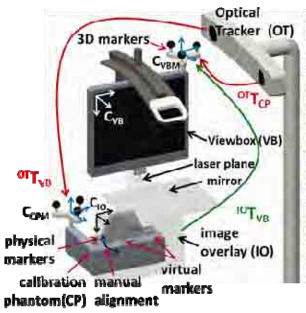



**Fig. 2** Indirect calibration

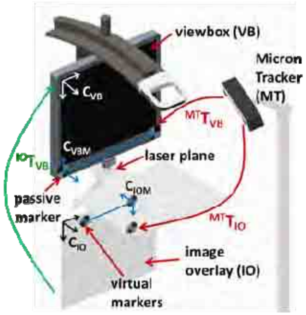



**Fig. 3** Direct calibration

## RESULTS

The workspace analysis reported the newly proposed 90° system (Fig. 1b) to be optimal with viewing angle up to 35° as compared to 15° for the previously proposed 60° system (Fig. 1a). For oblique images, the rotation of the whole viewbox (Fig.5) was practically feasible as compared to five bar link mechanism or monitor rotation concept. The requirement of +/- 35° oblique rotation was not satisfying with both concepts due to reduced user viewing angle and mirror interference with the patient. The optimal oblique rotation angle is +/- 15° and it will be considered as a limitation of the MIOS. Alternatively, the system can be rotated about 90° around the vertical axis to view the oblique details in the image overlay plane.

The conceptual view of the MIOS is shown in Fig. 4 and the first prototype developed is shown in Fig. 6. The system shall have four directions of motion as shown in Fig. 5: i.) movement of +/-5cm along longitudinal axis; ii.) rotation of +/-90 ° about vertical axis of the image plane; iii.) oblique rotation of +/-15° about the target point of needle insertion and iv.) movement of +/-10cm along vertical axis to accommodate patients of different abdominal size.

The 90° system has additional benefits compared to the 60° system: i.) increased clearance between mirror and the patient; ii.) reduced system inertia as the system is mechanically balanced about the image overlay plane and iii.) increased viewing angle which also improves the view ability for tracker.

The direct calibration method is expected to reduce the calibration time with simplified calibration steps. Direct calibration can be done away from the patient space and doesn't require initial phantom calibration step.

## DISCUSSION

Based on successful pre-clinical testing of the static image overlay system [3,4], MIOS promises to become an even more useful tool for image-guided surgical navigations. The mechanical design of the MIOS needs to be worked further for precise movement of viewbox along longitudinal and patient vertical axes, enable the viewbox rotation to view oblique images up to +/- 15°. Phantom and cadaver studies need to be performed to evaluate the accuracy of direct calibration method and to refine the clinical workflow. The initial studies shall focus on procedures with negligible effect of respiratory. However it is possible to compensate the effect of respiration as the patient-attached markers are constantly tracked by the tracker.




**Fig. 4** MIOS concept

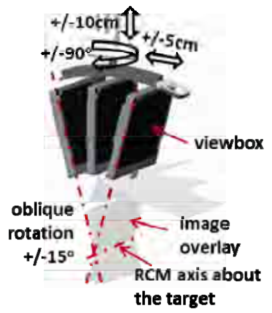



**Fig. 5** Ranges of motion

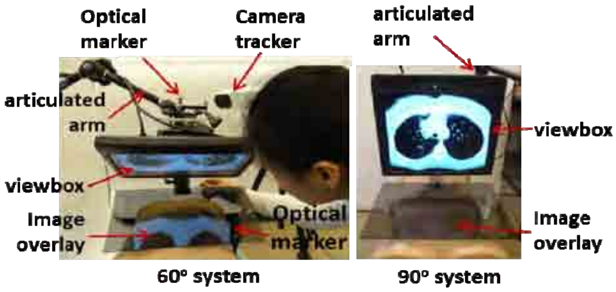



**Fig. 6** MIOS prototype

This work was funded by the NIH grant number R01 CA118371, USA. The Discovery Grant of NSERC, Canada. National Center for Research Resources and National Institute of Biomedical Imaging and Bioengineering of the NIH USA, through grant numbers P41EB015898 and P41RR019703. Gabor Fichtinger was funded as Cancer Care Ontario Research Chair.

## REFERENCES

[1] Fichtinger *et al*. "Image overlay guidance for needle insertion in CT scanner," IEEE *Transactions on Biomedical Engineering*, (52:8), 2005, pp. 1415-1424.

[2] Fischer *et al*. "MRI image overlay: Application to arthrography needle insertion," *Computer Aided Surgery* (12:1), 2007, pp. 2-14.

[3] Fritz *et al*. "Augmented Reality Visualization with Use of Image Overlay Technology for MR Imaging-guided Interventions: Assessment of Performance in Cadaveric Shoulder and hrography at 1.5 T," *Radiology* (265:1), 2012, pp. 254-259.

[4] Fritz *et al*. "Augmented reality visualization using an image overlay system for MR-guided interventions: technical performance of spine injection procedures in human cadavers at 1.5 Tesla," *European Radiology* (23), 2013, pp. 235-245.

# Smooth Active Constraints Employed for Position and Force Control in Robot Assisted Surgery

A.S. Proesch, S. Bowyer, F. Rodriguez y Baena

*Department of Mechanical Engineering, Imperial College London, UK*
*f.rodriguez@imperial.ac.uk*

## INTRODUCTION

The method of hybrid position-force control is currently used in industry to control the position of a robot tool, as well as the contact forces experienced at the tool-tip through interaction with a surface. This paper explores the use of such a hybrid control [1] strategy to enforce active constraints [2], also known as virtual fixtures [3], in both Cartesian and force space. Active constraints are a collaborative robot control strategy which can be used to guide a human operator towards a predefined target, or prevent them from entering 'unsafe regions'.

Active constraints and virtual fixtures have been widely used within the literature to limit the position of surgical tools to operate only within predefined "safe regions", in order to avoid damaging close-proximity tissue outside this region. However, it would still be possible to damage tissue within this safe region by accidentally applying excessive force at the tool-tip. A hybrid control of both position and force would thus act to prevent tissue damage both outside and inside the predefined safe region. However, a conflict between position control and force control arises at the regional constraint boundary, if the force control contains a component directly perpendicular and opposite in direction to the regional constraint boundary. This paper thus explores an extension of the hybrid force-position control concept to the field of surgical robotics, where the possible conflict at the regional constraint boundary is addressed by a scaled selection matrix.

## MATERIALS AND METHODS

Hybrid position-force control, as first developed by Craig and Raibert[1], assigns a coordinate frame to the tool tip, applying position and force control along independent, orthogonal axes. The method uses a rigid selection matrix that defines each axis either as position or force controlled. Hence, for pure force control of all axes when the user is in the "safe region", the selection matrix for position control, $S_p$, would contain only zeros, and the force control selection matrix, $S_f$, would be equal to the idenity matrix through the relationship

$$S_f = I - S_p$$

At a regional constraint boundary, i.e. when requiring pure position control along one axis, the designated local coordinate frame, *{L}*, for hybrid control is thus defined as having its z-axis normal to the closest point on the boundary, as shown in Fig. 1, leaving the two other axes force controlled.

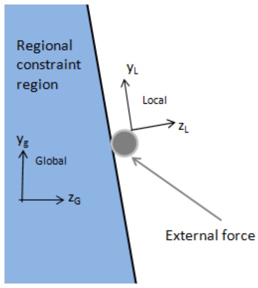



**Fig. 1** Illustration of the frame used for the definition of position and force control. The force controlled y- and x- axes are tangent to the regional constraint boundary, and the local z-axis is fully position controlled.

The orthogonal force, *F**, and position, *P**, errors are calculated by transforming the selection matrices from the local to the global frame, and multiplying them by the raw force and position errors, *F* and *P*:

$$F^* = T_{G-L}\, S_f\, T_{G-L}^{-1}\, F$$
$$P^* = T_{G-L}\, S_p T_{G-L}^{-1} P$$

where $T_{G-L}$ is the transform from the global to the local frame.

The selection matrix for position control will be different for two states of either pure force control in the "safe region" (zero position control selection matrix), or hybrid position-force control when the user penetrates the regional constraint (non-zero position selection matrix). The change from pure force control to hybrid control creates the potential for instability in the control system at the regional constraint boundary, as the position selection matrix rapidly changes form. Hence, a smooth transition region, as seen in Fig. 2, is needed between the states of force control and hybrid control as the tool-tip approaches a regional constraint, avoiding the risk of instability.

To avoid this instability, the position control selection matrix is defined by the variable $\alpha$ for position control along the local z-axis

$$S_p = \begin{bmatrix} 0 & 0 & 0 \\ 0 & 0 & 0 \\ 0 & 0 & \alpha \end{bmatrix}$$

The transition between the two states of the position control matrix is then implemented as a function of proximity, *d*, to the regional constraint, where pure force control along all axes is implemented when $d > d_{min.}$, and hybrid position-force control for $d \leq 0$.

Within the transition region, the position selection matrix varies with $\alpha$ defined as:

$$\alpha = \begin{cases} 0 & d > d_{min} \\ 1 - d/d_{min} & 0 < d \leq d_{min} \\ 1 & d \leq 0 \end{cases}$$

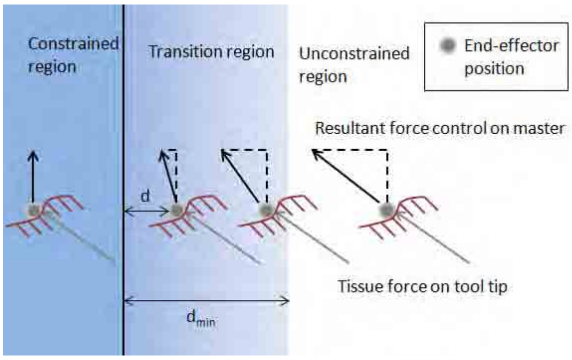



**Fig. 2** Illustration of the control transition region. To ensure orthogonaity between position and force control at the regional constraint boundary, the transition region attenuates the component of the force control normal to the regional constraint surface.

To validate the proposed active constraint control architecture, a teleoperated system was assembled with a constrained slave – a Stäubli TX90 robotic arm (Stäubli Ltd.) – and a haptic master – a Phantom Omni (Sensable Technologies, Inc.) – controlled, using the *Orocos Real-Time Toolkit* [4] and the Stäubli LLI as described in [5]. A regional constraint was projected onto a soft, flat surface which oscillated at 0.3 Hz orthogonal to the constraint boundary. The regional constraint was marked with a 10 mm thick strip along the oscillating surface, and the test subjects were asked to follow this strip along the length of the test surface. The test evaluated the accuracy of the position and contact force under the four control methods; hybrid position-force control, position control, force control, and no active constraint support (i.e. unconstrained teleoperation with no haptic feedback).



**Fig. 3** Picture of the hardware setup on the left, with the Phantom Omni master in the foreground and the Stäubli TX90 slave in the background. The picture on the right shows the setup of the oscillating surface, seen as a grey foam block on the bench under the Stäubli TX90 tool.

## RESULTS

Performance of the different control methods was evaluated based on positional root mean square (RMS) error and contact force error. The results are shown in Fig.4 and Fig.5.

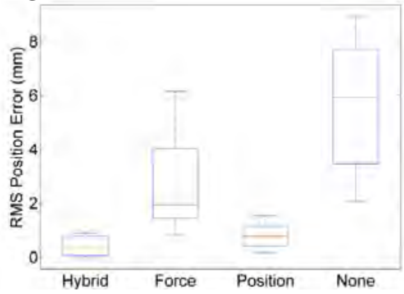



**Fig. 4** Comparison of RMS position error distribution for tests using the four active constraint control methods.

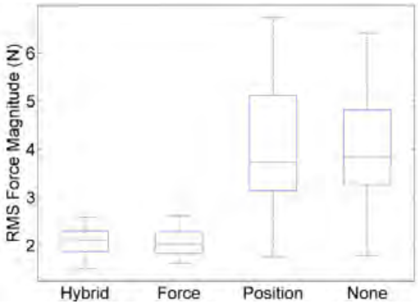



**Fig. 5** Comparison of RMS force error magnitude distribution for tests using the four active constraint control methods.

## DISCUSSION

From Fig. 4 and Fig. 5, it can be seen that there was significant improvement in RMS positional and force errors when implementing active constraints over non-constrained cases, with the hybrid controller also performing as well or better with regards to force and position constraints, when compared to their single mode control equivalents. This supports the claim that hybrid position-force control can be implemented to simultaneously reduce both the positional error and the excessive tool/tissue interaction force in robotic assisted surgery. The primary focus of future work will be testing the proposed controller when external forces and regional constraints are the product of less structured environments.

## REFERENCES

[1] J. Craig and M. H. Raibert, "A systematic method of hybrid position/force control of a manipulator," IEEE Compsac '79, Chicago, IL, Nov. 7, 1979.

[2] B. Davies, M. Jakopec, S. J. Harris, F. Rodriguez y Baena, A. Barrett, A. Evangelidis, P. Gomes, J. Henckel, and J. Cobb, "Active-constraint robotics for surgery," Proc. IEEE, vol. 94, no. 9, pp. 1696–1704, 2006.

[3] L. B. Rosenberg, "Virtual fixtures: Perceptual tools for telerobotic manipulation," in Proc. IEEE Virt. Real. Annual Int. Symp., sept. 1993, pp. 76 –82.

[4] The Orocos Project (Open Robot Control Software), http://www.orocos.org/ , 21/03/2013

[5] S. Bowyer and F. Rodriguez y Baena *A Research Platform for Active Constraints in Robotic Neurosurgery* In proceedings of the Hamlyn Symposium on Medical Robotics, p. 53-54, 2011.

# ASTRO: A Novel Robotic Tool for Laser Surgery of the Prostate

S. Russo, P. Dario, A. Menciassi

*The BioRobotics Institute, Scuola Superiore Sant'Anna*

*s.russo@sssup.it*

## INTRODUCTION

Transurethral laser surgery of the prostate for the treatment of benign prostatic hyperplasia (BPH) is traditionally performed via the resectoscope (Fig. 1), a telescopic straight instrument that allows only translation and rotation along/about its longitudinal axis, thus dramatically limiting dexterity and tactile feedback at the tip. These issues represent a limitation since, in most procedures, the laser tip must be in contact with prostatic tissue [1]. In particular, the closer the contact, the better will be the distribution of laser energy and consequently tissue ablation will be more homogeneous; homogeneous ablation avoids formation of craters that can entrap tissue fragments, debris and perfusion liquid that partially absorb and scatter the incident light thereby hindering laser effect [2]. A number of attempts to achieve force and tactile sensing in minimally invasive surgery (MIS) are reported in literature [3]-[7]. Different actuation strategies for flexible, continuum and snake-like robots for MIS can be found in [8]-[11]. In this paper, we present the design and preliminary evaluation of a novel, miniaturized, flexible robotic tool for laser assisted transurethral surgery of BPH. The aim of the system is to allow a more homogeneous tissue ablation, in order to speed up surgical procedure duration and recovery time. The design includes an optical fiber based tactile sensor system to monitor contact between prostatic tissue and laser, and a cable driven actuation mechanism to steer the tip of the laser. Preliminary study demonstrated the theoretical ability of the system to sense contact forces up to 0.4 mN and to steer the tip in 3D of about ± 10 °.

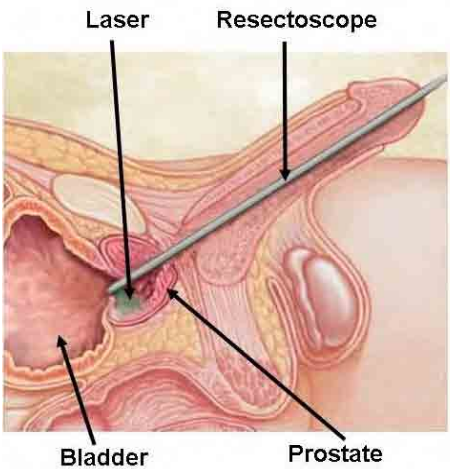



**Fig. 1** Overview of prostate laser ablation procedure. The resectoscope is inserted through the urethra to access the prostate.

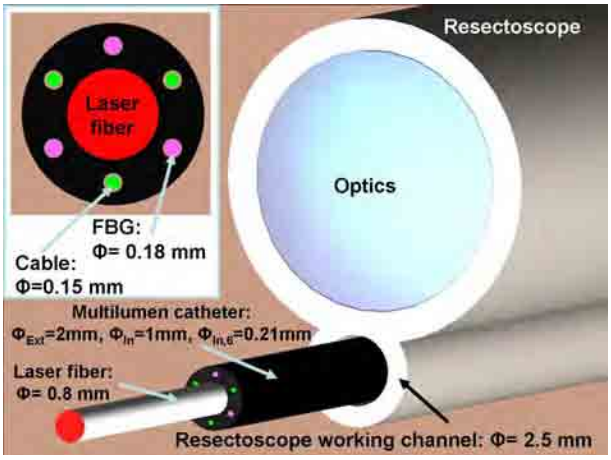



**Fig. 2** CAD model of the ASTRO system and detail of the section.

## MATERIALS AND METHODS

This paper presents the design of a novel, miniaturized, flexible robotic tool for transurethral laser surgery of BPH: ASTRO (Actuated and Sensorised Tool for laseR assisted surgery of the prOstate), shown in Fig. 2. ASTRO consists of a flexible multilumen catheter with an outer diameter of 2 mm ($\Phi_{Ext}$), in order to be inserted in the working channel of a commercial resectoscope (Karl Storz 27042LV: Φ= 2.5 mm), and a central working channel of 1 mm ($\Phi_{In}$), which will allow the insertion of a commercial laser fiber for the ablation of the prostate. Moreover, ASTRO has six small lumens ($\Phi_{In,6}$= 0.21 mm), around the periphery forming the vertices of a hexagon, to integrate sensors for contact detection between laser and prostatic tissue, and cables for actuation. Three Fiber Bragg Grating (FBG) sensors (SmartFBG, Smart Fibres) are integrated in a way to allow 3 DOF contact force sensing at the tip of the laser. The multilumen is in black opaque polyamide (PA12) in order to ensure optical isolation between the laser and the FBG sensors. Young's modulus of PA12 is 1.1 GPa, thus allowing the multilumen to serve both as a mechanical continuum for strain transmission between laser and sensors (that have a coating of polyimide with a Young's modulus of 2.5 GPa), but also to be flexible enough to be bent by cables. The melting point of PA12 (178 °C) is compatible with the application since temperature of prostatic tissue vaporization is around 100 °C. Moreover, the temperature drops dramatically as soon as we move away from the ablation site, because of saline solution's continuous flow inside the resectoscope sheath. FBG technology has been chosen because of its small dimensions (Φ= 0.18 mm), electromagnetic interference immunity, sterilizability,

and biocompatibility. These sensors are affected by cross-sensitivity of temperature and strain, the shift in Bragg wavelength Δλ being expressed as:

$$\Delta\lambda = k_{\varepsilon}\varepsilon + k_T \Delta T \qquad (1)$$

where $k_\varepsilon$ is the strain sensitivity, $\varepsilon$ is the strain, $k_T$ is the temperature sensitivity and $\Delta T$ is the variation of temperature. Redundant FBG sensors are used to compensate for errors due to temperature effects, such as in [5]. Thanks to the saline solution's continuous flow, we can assume that temperature variations will not be high at the sensor level: three FBG sensors are embedded parallel within ASTRO at 120° from one another, at 2 cm away from the tip of the laser. In this way, sensors experience the same $\Delta T$, but different strain in terms of compression and tension, and therefore the temperature compensation can be performed easily. Three nylon cables (Φ= 0.15 mm), that will be actuated by motors, are fixed at the tip of ASTRO and used for laser steering. FEA simulations were performed in order to assess the adequacy of sensor and actuation strategy choices.

## RESULTS AND DISCUSSION

The best positioning of the FBG sensors, along with the minimum detectable ASTRO contact force, were estimated with FEA. Iterations of decreasing contact force, applied at the ASTRO tip, versus computed strain measured at the FBG level were performed: the results of the simulations are reported in Fig. 3 (a). Since the FBG strain resolution is given as 0.4 με, the minimum force that can be measured, positioning the FBG sensors at 2 cm from the laser tip, resulted in 0.4 mN, as shown in Fig. 3 (b). As regards actuation, the necessary pulling force, to be applied on a cable by a motor, for steering the laser to reach a proper contact with prostatic tissue, was estimated with FEA. Since the diameter of the prostatic urethra in a healthy prostate is around 6 mm and the ASTRO tip is 2 cm length (shown respectively as $d$ and $l$ in Fig. 4 (a)), a tip bending of ± 10 ° ($\theta$) was estimated to be sufficient to have a proper contact in all cases. Thus, the required pulling force resulted in 12 N, as shown in Fig. 4 (b). Future works will be the fabrication and testing. In conclusion, the proposed system could allow a homogeneous treatment of BPH, shortening the operative and recovery time. Furthermore, it is compatible with current commercial instrumentations (resectopes and laser fibers).

## ACKNOWLEDGEMENTS

This research is supported by MILoRDS Project (Minimally Invasive Laser Robotic assisted Diagnosis and Surgery) funded by Tuscany Region, POR CReO Fesr 2007-2013.

## REFERENCES

[1] M. Issa, et al., The Evolution of Laser Therapy in the Treatment of Benign Prostatic Hyperplasia, Reviews in Urology, 7, 9, 2005.

[2] H.Kang, et al., In Vitro Investigation of Wavelength-Dependent Tissue Ablation: Laser Prostatectomy Between 532nm and 2.01 mm, Lasers in Surgery and Medicine, 42, 237–44, 2010.

[3] E. Van Der Putten, et al., Haptics in minimally invasive surgery – a review, Minimally Invasive Therapy, 17:1, 3–16, 2008.

[4] P. Puangmali, et al., State-of-the-Art in Force and Tactile Sensing for Minimally Invasive Surgery, IEEE Sensors Journal, 8, 4, 2008.

[5] I. Iordachita, et al., A sub-millimetric, 0.25 mN resolution fully integrated fiber optic force sensing tool for retinal surgery, Int. J. Comput. Assist. Radiol. Surg., 4(4), 383-90, 2009.

[6] Y. Hu, et al., Bioinspired 3-D Tactile Sensor for Minimally Invasive Surgery, Journal Of Microelectromechanical Systems, 19, 6, 2010.

[7] P. Polygerinos, et al., Measuring Tip and Side Forces of a Novel Catheter Prototype: A Feasibility Study, IEEE/RSJ International Conference on Intelligent Robots and Systems, 11-15, 2009.

[8] Y. Fu, et al., Steerable catheters in minimally invasive vascular surgery, Int J Med Robotics Comput Assist Surg, 5: 381–391, 2009.

[9] K. Harada, et al., Bending laser manilupator for intrauterine surgery, IEEE International Conference on Robotics and Automation, 611-616, 2007.

[10] H. Mingyen, et al., Towards the development of a SMA-actuated MRI-compatible tendon-driven neurosurgical robot, IEEE International Conference on Robotics and Automation, 683-688, 2012.

[11] K. Ikuta, et al., Pressure Pulse Drive: A Control Method for the Precise Bending of Hydraulic Active Catheters, IEEE Transactions on Mechantronics, 17(5), 876-883, 2012.

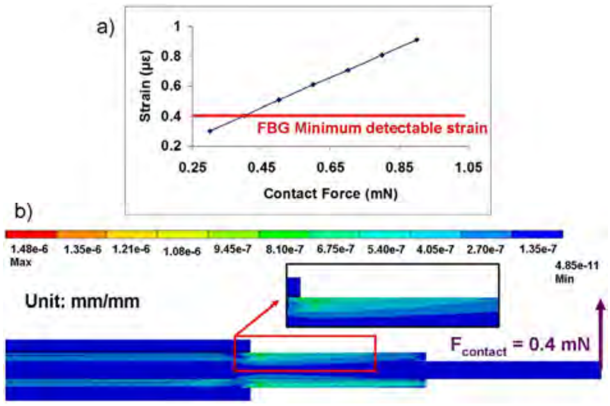



**Fig. 3** Evaluation of minimum detectable contact force of ASTRO system: a) contact force applied versus computed strain measured at the FBG level, b) FEA: Von Mises stress in the section of ASTRO system with 0.4 mN contact force applied.

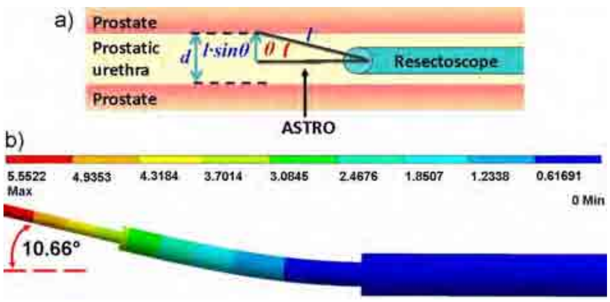



**Fig. 4** ASTRO tip steering: a) estimation of necessary tip bending, b) FEA: tip steering with 12 N cable pulling force.

# Improvement of Target Registration Accuracy with Anatomical Landmarks


Jongho Chien[1], Jaeyeong Park[2], Sangseo Jeon[1], Jaesung Hong[1]

[1]*Department of Robotics Engineering, Daegu Gyeongbuk Institute of Science and Technology, Daegu, Korea*

[2]*Kyungpook National University, Medical Device and Robot Institute of Park*
*jhong@dgist.ac.kr*


## INTRODUCTION

Point-based registration using surface fiducial markers is the most commonly used method for patient-image registration since the surface markers are not invasive and are easily identified in the patient and image [1, 2]. However, registration accuracy gradually decreases proportionally to the distance from the surface where the markers are attached [3, 4]. Since surgical targets are located within the patient body, high accuracy is required in regions relatively far from the skin. Fiducial registration error (FRE) is automatically calculated by the navigation system, but the FRE cannot guarantee the real accuracy of the target registration. To decrease target registration error (TRE) around the target rather than FRE around the skin markers, additional points should be incorporated for the registration near the target organ. In this study, we propose a method that uses an anatomical landmark around the target as an additional fiducial point for the registration to decrease TRE.

## MATERIALS AND METHODS

To take an anatomical landmark as a reference point, an ultrasound system (ACUSON X300, Siemens, Germany) was used. An optical position sensor (Polaris Vicra, NDI, Waterloo, Canada) was utilized to detect and track the surgical tool and ultrasound probe. 3D Slicer (Brigham and Women's Hospital, Boston, USA), which is free, open-source software, was used as basic platform software in this research.

Figure 1 shows the whole system configuration for patient-image registration using deep anatomical landmarks. Surface fiducial markers are markers that is attached to the patient skin and identified in the medical images for registration. Reference marker is a set of infrared reflecting markers that are attached to the patient to compensate patient movement. Anatomical landmarks could be sharp corners or edges of bone, vessel, or any specific point of organs in the body that can play a role as markers for the registration.

Figure 2 represents the suggested method to acquire an additional fiducial point using ultrasonography for patient-image registration. Optical sensors were attached to the ultrasound probe, and the optical tracking system was used to track the position of the probe. By calibration between the ultrasound image and the ultrasound probe, the position of the ultrasound image can be transformed to the position of the optical tracking system. Additional fiducial points were taken from the ultrasound images using the optical position sensor that recognizes the position of the ultrasound probe. After transformations between the anatomical landmarks and the ultrasound probe ( ${}^{R}_{U}T$ in Fig. 2), the anatomical landmarks were treated as the markers for registration, as with surface markers.

To evaluate the improvement in the accuracy of the proposed method, a phantom experiment was designed. An acrylic box filled with pure water was used with the ultrasound system. The tracking system tracked both the phantom and the ultrasound probe. The ultrasound probe detected landmarks inside the phantom. With the aforementioned transformations, which were calculated during the calibration, landmarks were used as fiducial markers for the registration. Based on the fiducial points, the paired point registration method was performed between a reconstructed image of the computed tomography (CT) volume data and the phantom.

Two experiments were performed. First, seven fiducial makers attached to the surface of the phantom were used for the registration. Second, in addition to the seven fiducial markers attached to the surface of the phantom, one deeply seated landmark was additionally used for the registration. We measured the FRE and TRE in each experiment. TREs were measured using three points of the landmarks inside the phantom except for the point that was used for the depth fiducial marker in the registration.

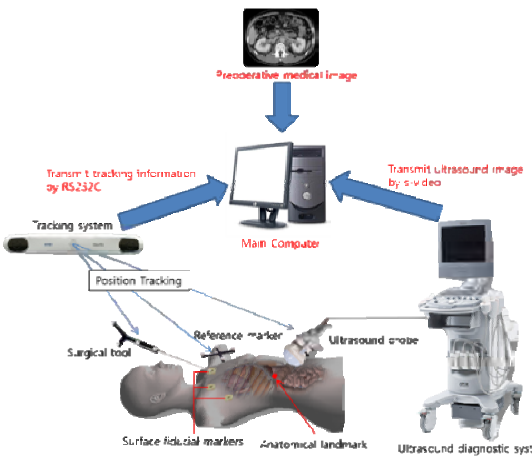



**Fig. 1** System configuration of the proposed method

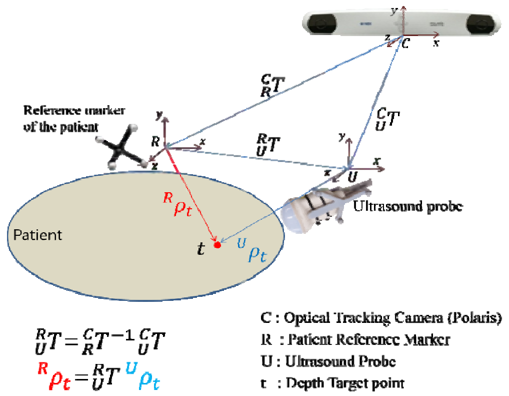



Fig. 2 The proposed method to acquire deep fiducial positions for patient to image registration

## RESULTS

The registration accuracy with and without an anatomical landmark was examined by using seven surface markers and one additional anatomical landmark. Figure 3 shows the FREs and TREs. FREs without and with an anatomical landmark were 0.76 ± 0.12 mm and 2.13 ± 0.37 mm. TREs without and with the anatomical landmark were 1.46 ± 0.31 mm and 1.27 ± 0.39 mm for TRE1, 1.69 ± 0.41 mm and 1.89 ± 0.73 mm for TRE2, 1.24 ± 0.47 mm and 0.95 ± 0.47 mm for TRE3, and finally 1.65 ± 0.74 mm and 1.04 ± 0.53 mm for TRE4. Except for TRE2, the additional use of the anatomical landmark caused an increase in FRE, but a meaningful decrease was observed in TRE.

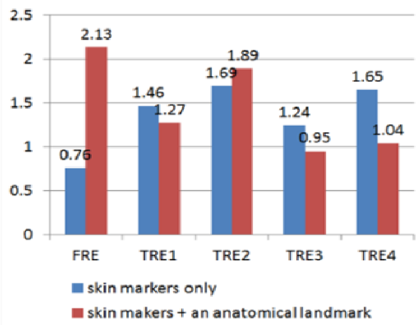



**Fig. 3** Registration error with and without an anatomical landmark

## A POSSIBLE APPLICATION

The proposed system could find its clinical application in orthopedic surgeries in terms of the depth of the surgical target, and the availability of anatomical landmarks. Specifically, the proposed system could assist surgical navigation for epiduroscopic (EDS) procedure, which is one of our ongoing research works. Our EDS navigation system tracks positions of a surgical tool (catheter) by electromagnetic tracking system (EMTS) and a patient body by optical tracking system (OTS) rather than both of them by only EMTS. The additional use of the OTS aims at utilizing relatively high tracking accuracy of the OTS in both the registration and the navigation. In the patient-image registration of our EDS navigation system, if we can include deeply seated landmarks obtained intra-operatively by the ultrasound system as well as surface markers in the fiducial point set, the registration error would be reduced, and in turn, the navigation accuracy is expected to be highly improved.

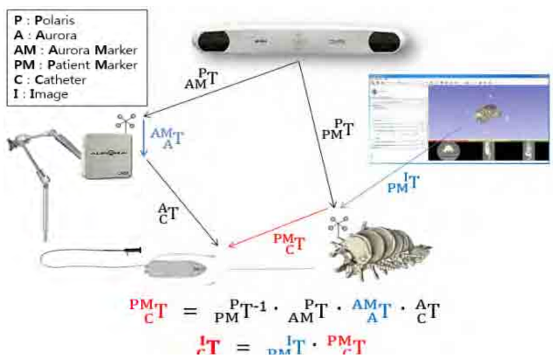



**Fig. 4** Surgical navigation system for epiduroscopic procedure

## DISCUSSION AND CONCLUSION

We found out that TRE can be reduced by simultaneously using the deeply seated anatomical landmark as well as skin-affixed markers. In the phantom experiment, we confirmed that the target registration accuracy was improved when the additional points were used. Although the anatomical landmark affects the improvement of the accuracy, we have to compromise and use the limited number of anatomical landmarks because, in general, they are very few around the target. In addition, if the error caused by the distortion of ultrasound image and insufficient accuracy of the ultrasound probe calibration is reduced, patient-image registration will be more accurate, and TRE will be more decreased in the future. Although the FRE was increased due to the distortion and insufficient calibration accuracy, the reduced TRE shows the feasibility of the method.

## ACKNOWLEDGEMENTS

This work was supported in part from MIREBrain Convergence Science Center of DGIST (12-BD-0402) and a research and development program (Medical Image-guided Otorhinolaryngology, and neurosurgical minimally invasive multi-DOF surgical robot systems) of the Ministry of Trade, Industry and Energy of Korea (10040097).

## REFERENCES

[1] J. Hong, M. Hashizume, “An effective point-based registration tool for surgical navigation”, Surg Endosc, Vol. 24, pp. 944-948, 2010.

[2] J. Hong, N. Matsumoto, R. Ouchida, S. Komune, M. Hashizume, “Medical navigation system for otologic surgery based on hybrid registration and virtual intraoperative computed tomography”, IEEE Trans Biomed Eng, Vol. 56, No. 2, pp. 426-432, 2009.

[3] J. M. Fitzpatrick, J. B. West, C. R. Maurer, “Predicting error in rigid-body point-based registration”, IEEE Trans Med Imag, Vol. 17, No. 5, pp. 694-702, 1998.

[4] W. Zhang, G. Shen, C. Wang, Y. Liu, “Effect of Fiducial Configuration on Target Registration Error in Image-Guided Surgery-A Experiment Study”, Biomed Eng Inform, Vol. 4, pp. 1477-1481, 2010.

# Towards an Endoscopic Device for Laser-Assisted Phonomicrosurgery

Dennis Kundrat, Andreas Schoob, Benjamin Munske, Tobias Ortmaier

*Institute of Mechatronic Systems, Leibniz Universität Hannover, Germany*
*dennis.kundrat@imes.uni-hannover.de*

## INTRODUCTION

The human larynx can be affected by laryngeal cancer and tumors. Particularly, malignant or benign pathologies of the vocal folds influence the patient's life significantly because swallowing, breathing, and voice production are disrupted. In case of surgical treatment, phonomicrosurgery is considered as state-of-the-art technique for preservation and improvement of functionality. Operative preparation involves laryngoscopy in anaesthized patients for direct laryngeal exposure. Intra-operatively, surgeons employ operating microscopes for transoral examination and observation of surgical procedures. Tissue manipulation on the vibratory edge of the vocal fold is performed manually with long microsurgical instruments (e. g. forceps and scissors). Less soft tissue trauma and improved cutting accuracy is expected from extending the conventional optical setup with laser sources and manually operated micromanipulators for beam deflection. This configuration enables simultaneous control and observation of the laser incision. However, the quality of surgical training and the surgeon's dexterity determine the postoperative outcome due to the non-ergonomic design of the current setup.

In order to overcome these limitations, robots have been introduced in different medical applications. With respect to laryngeal surgery, robot-assisted access has been established in transoral robotic surgery (TORS). The commercial da Vinci System (Intuitive Surgical, Inc.) has successfully been used in TORS of laryngeal lesions by utilizing microinstruments [1] and $CO_2$ laser [2]. Haifeng et al. developed a master-slave serial robot with 7 degrees of freedom (DoF) for this specific use [3]. Simaan and Rivera-Serrano et al. introduced highly articulated, snake-like robots which have been adapted from prior applications in laparoscopic and thoracic surgery [4, 5]. Furthermore, Mattos et al. proposed a teleoperated robotic system for visual planning and safe laser cutting [6]. Despite recent developments in robot-assisted laryngeal (laser) surgery, these procedures still have restrictions. For instance, serial manipulators equipped with conventional microinstruments require a direct line-of-sight to the vocal fold which cannot be guaranteed for all patients. In this context, flexible robots perform appropriately but their design prevents a high-density integration in the distal end. Besides, both kinematics require large external mechanisms. This paper reports on the first steps towards an endoscopic system for laser-assisted phonomicrosurgery. The objective of the proposed device is to overcome the aforementioned limitations by means of minimizing the working distance between laser manipulator and tissue surface from 400 mm for conventional systems to approx. 20 mm. The proposed approach decreases the distance by inserting a laser delivering endoscopic device into the patient and its subsequent feeding closed to the surgical site in the larynx. The distal integration of a beam deflecting microrobot (developed by MiNaRoB, FEMTO-ST, France) enables to ablate pre-planned laser incision paths on the tissue surface. Additional vision devices and kinematic mechanisms in the distal end extend the surgeon's view and facilitate pre-positioning with respect to the lesion. In this regard, preliminary design, actuation, and control principles are presented.

## MATERIALS AND METHODS

Initially, design constraints and specifications are determined by analyzing medical and technical aspects of laryngeal surgery. Device dimensioning is therefore influenced by the anatomic nature of the upper airway. A transoral access to the surgical site requires an insertion of the device through the mouth, subsequent feeding of the distal part through pharynx and hypopharynx to reach the vocal fold in the larynx. The involved anatomy is characterized by a long and narrow soft tissue tube with a patient-dependent cross-section of 15 - 21 mm. Thus, prospective designs of the endoscopic shaft should not exceed a maximum diameter of 20 mm to enable gentle feeding.

Further on, current surgical procedures comprise suspension retraction to elevate the epiglottis and straight laryngoscopes for vocal fold exposure. This methodology often causes pre- and postoperative complications due to overstretching of the patient's neck. The proposed concept should obviate the need for direct line-of-sight by integrating the entity of required devices for visualization and manipulation into the distal end. In order to facilitate the insertion, the shaft should be pre-curved, comparable to curved blade laryngoscopes. According to the technical specifications, the microrobot deflects the laser beam in a range of ±25° and the stereo camera setup shows a restricted field of view of approx. 65°. With regard to these limitations, additional DoF of the distal end are required for pre-positioning and visual examination of the surgical site. Within this context, a mechanical compensation of respiratory movements is not required due to a vision-based tissue tracking. Therefore, the minimum joint angle for orientation adjustment in two axes and the working distance between vocal fold and distal end are determined to ± 20° and approx. 20 mm, respectively.

This configuration should facilitate stereo vision feedback to the surgeon and three-dimensional tissue recovery for augmented reality.

**RESULTS**

The proposed distal end design (see Figure 1) is characterized by high-density integration. Current components for vision applications include a stereoscopic setup with chip-on-the-tip cameras showing a resolution of 720 x 580 pixels and a single or multiple fiber based whitelight or narrow band imaging (NBI) illumination. Moreover, image fibers are connected to proximally located high-speed cameras for vision-based control (visual servoing) of the beam deflecting microrobot in order to ensure a precise laser cutting path. Furthermore, a tool channel with a diameter of 3 - 4 mm is integrated to feed additional instruments to the surgical site. The alignment of the components is optimized regarding the central position of the microrobot and an appropriate camera view with small baseline. For protection and assembling purposes, distal parts are mounted to a custom support that can be inserted and fixed to the housing. Furthermore, the support connects the distal end to a kinematic module satisfying the aforementioned specifications.

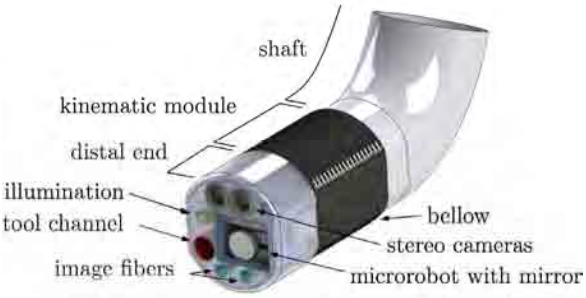



**Fig. 1** CAD model showing distal end, kinematic module protected with bellow and transition to shaft (outer diameter 20 mm)

This module enables at least two rotational and one translational DoF. Two different kinematic chains are considered appropriate (see Figure 2). On the one hand, a three-legged parallel robot (e. g. 3-PRS or 3-PSR) allows reducing the overall size but requires push/pull rods or precision engineered telescopic legs. On the other hand, a serial kinematics with three DoF comprising a universal joint with intersecting axes connected to a prismatic joint is proposed. In this case, safe joint actuation is implemented with wire-based mechanisms located outside the patient. Both joint designs are structurally optimized to achieve a maximum of inner space to incorporate further devices. For protection purposes, the module is covered with a bellow. Additionally, a stable manipulation platform is provided by employing a rigid endoscopic shaft and a connection to the patient's mouth gag. This also favors a reliable power and signal transmission.

Low-level control is implemented on a main controller which delegates position data to motor drivers. These allow overcurrent sensing and encoder analysis. High-level control is established by an ethernet connection between the embedded device and a main computer which runs a Robot Operating System environment (www.ros.org).



**Fig. 2** CAD models of kinematic module: parallel (l.) and serial (without prismatic joint) (r.) configuration

**DISCUSSION**

In this contribution, first developments of an endoscopic device for laser-assisted phonomicrosurgery are presented. Primarily, state-of-the-art systems are discussed and the new device is motivated by emphasizing clinical benefits for patient and surgeon. Despite not having finalized the mechatronic system design, a significant enhancement is expected by integrating a beam deflecting microrobot and vision devices directly into the distal end. This obviates the need for direct laryngoscopy and therefore provides a gentle intervention. Furthermore, the integration of imaging components allows surgeons to employ stereo vision, surface recovery, and tracking for safe laser guidance and visual feedback. In the next step, prototypes will be manufactured to evaluate feasibility and performance in experimental studies.

**ACKNOWLEDGEMENT**

This research has received funding from the European Union FP7/2007-2013 under grant agreement µRALP – n° 288233.

**REFERENCES**

[1] F. T. Kayhan et al. Transoral robotic cordectomy for early glottic carcinoma. *The Annals of otology, rhinology, and laryngology*, 121(8):497 – 502, 2012.

[2] R. G. F. Blanco et al. Transoral robotic surgery of the vocal cord. *Journal of laparoendoscopic & advanced surgical techniques*, 21(2):157 – 159, 2011.

[3] L. Haifeng et al. A master-slave robot system for minimally invasive laryngeal surgery. *In IEEE International Conference on Robotics and Biomimetics*, 782 – 787, 2009.

[4] N. Simaan et al. A dexterous system for laryngeal surgery. In IEEE International Conference on Robotics and Automation, volume 1, 351 – 357, 2004.

[5] C. M. Rivera-Serrano et al. A transoral highly flexible robot: Novel technology and application. The Laryngoscope, 122(5):1067 – 1071, 2012.

[6] L.S. Mattos et al. Next-generation micromanipulator for computer-assisted laser phonomicrosurgery. In IEEE Engineering in Medicine and Biology Society (EMBC), 4555 – 4559, 2011.

# Accurate Dense Feature Matching in Endoscopic Videos


Gian-Luca Mariottini, Gustavo A. Puerto-Souza

*Department of Computer Science and Engineering, University of Texas at Arlington, USA.*

*gianluca@uta.edu, gustavo.puerto@mavs.uta.edu*


## INTRODUCTION AND RELATED METHODS

Feature matching is a core component in many endoscopic-imaging applications, such as Augmented Reality (AR) [1] or soft-tissue shape recovery [2]. Differently from feature tracking [3], feature matching recovers corresponding features between two images without any assumption about the small camera motion, or about the 3-D geometry of the observed scene (e.g., known organ motion due to periodic breathing). As such, they can be used for accurately recovering tracked features lost after strong organ deformation, fast camera motion, or prolonged occlusion. Existing feature-matching algorithms are characterized by limiting assumptions, and have not yet met the necessary levels of accuracy, especially when used to recover features in distorted or poorly-textured tissue areas. Figure 1 shows an example obtained by using the Hierarchical Multi-Affine (HMA) feature-matching algorithm [4].While HMA can predict well on average the position of corresponding features in the image after the sudden camera motion, HMA exhibits large errors (green lines) when predicting the position of features on the organ's boundaries (green circles). These large errors are caused by the absence of geometric constraints (the colored polygons correspond to affine mappings) because of the paucity of supporting image features in such highly-distorted or textureless areas. In this paper, we present a novel feature-matching algorithm that accurately recovers the position of image features over the *entire* organ's surface. Our method is automatic, it does not require any explicit assumption about the organ's 3-D surface, and leverages Gaussian Process (GP) Regression [5] to incorporate noisy matches in a probabilistically sound way. We evaluated our approach over a large database of more than 100 *in vivo* endoscopic-image pairs, which showed an improved accuracy and robustness when compared to [6].

## METHODS

We refer to $(\mathbf{x}, \mathbf{y})$ as a generic pair of corresponding features extracted in the image before, $\mathcal{I}^t$, and after, $\mathcal{I}^q$, the organ motion, respectively.

The initial set of sparse matches from HM $\mathcal{M} \triangleq \{(\mathbf{x}, \mathbf{y})\}$. are used to estimate a *non-rigid and dense* function $f(\mathbf{x})$ that maps any generic image point $\mathbf{x}_* \in \mathcal{I}^t$ to its corresponding image point $\mathbf{y}_* \in \mathcal{I}^q$. $f(\mathbf{x})$ can be written as, $\mathbf{y}_* = f(\mathbf{x}_*) + \epsilon$, where $\epsilon \sim \mathcal{N}(\mathbf{0}, \sigma^2 \mathbf{I})$ is a zero mean Gaussian noise with standard deviation $\sigma$.

The sparse matches $\mathcal{M}$ are used as input to a Gaussian Process, which describes the posterior distribution of the latent function *f* as, $p(f|\mathcal{M}) \propto p(\mathcal{M}|f)p(f)$, where

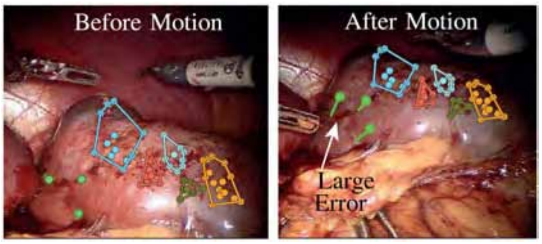



**Fig. 1** The feature matching method in [4], exhibits large pixel errors (green line) when predicting the correspondences on organ's (kidney) boundaries.

$f(\mathbf{p}) \sim \mathcal{GP}(\mu(\mathbf{p}), k(\mathbf{p}, \mathbf{q}))$, **p** and **q** being two generic vectors. Since a GP is completely determined by its mean and covariance matrix, we define $\mu(\mathbf{p}) = \mathbf{p}$, as the deterministic mean of the non-rigid function *f*. The GP covariance matrix is defined as, $k(\mathbf{p}, \mathbf{q}) = \lambda exp\left(-\frac{||\mathbf{p}-\mathbf{q}||^2}{2\rho^2}\right) + \sigma^2 \delta(||\mathbf{p}-\mathbf{q}||)$, where $\lambda$ is the amplitude of the process variance, $\rho$ is the length of the process variation, and $\delta$(y)=1 when y =1 or 0 otherwise. Note that $p(f|\mathcal{M})$ captures the interaction between the *observed* correspondences and the latent function *f*, while $p(f)$ represents the *a-priori* knowledge about the non-rigid mapping in terms of the GP mean and covariance.

We denote as **X** and **Y** the 2×n matrices containing all the *n* 2-D HMA matche $\mathcal{M}$ . Also, consider the 2 × m matr $\mathbf{X}_*$: containing the *m* features to be prec $\mathbf{Y}_*$ ed, and Y as the corresponding points, to be predicted by the GI $\mathbf{y}_{*i} = f(\mathbf{x}_{*i}) + \epsilon$. Then, the joint distribution of both the observed values, **Y**, and of the target valu $\mathbf{Y}_*$ under the prior is given by,

$$\begin{bmatrix} \mathbf{Y} \\ \mathbf{Y}_* \end{bmatrix} \propto \mathcal{N}\left( \begin{bmatrix} \mathbf{X} \\ \mathbf{X}_* \end{bmatrix}, \begin{bmatrix} \mathbf{K}(\mathbf{X}, \mathbf{X}) & \mathbf{K}(\mathbf{X}, \mathbf{X}_*) \\ \mathbf{K}(\mathbf{X}_*, \mathbf{X}) & \mathbf{K}(\mathbf{X}_*, \mathbf{X}_*) \end{bmatrix} \right)$$

Where each $(i, j)$ entry for the matrix $\mathbf{K}(\mathbf{X}, \mathbf{X}) \in \mathbb{R}^{n \times n}$, $\mathbf{K}(\mathbf{X}_*, \mathbf{X}) \in \mathbb{R}^{m \times n}$, and $\mathbf{K}(\mathbf{X}_*, \mathbf{X}_*) \in \mathbb{R}^{m \times m}$ are defined as $k(\mathbf{x}_i, \mathbf{x}_j)$ for vectors $\mathbf{x}_i$ and $\mathbf{x}_j$ belonging to $\mathbf{X}$ or $\mathbf{X}_*$, respectively. Then, the predicted values for the non-rigid function evaluated on $\mathbf{X}_*$ are given by [5],

$$\mathbf{Y}_* = \mathbf{X}_* + \mathbf{K}(\mathbf{X}_*, \mathbf{X})\mathbf{K}(\mathbf{X}, \mathbf{X})^{-1}(\mathbf{Y} - \mathbf{X}).$$

The covariance matrix $k(\cdot, \cdot)$ strongly depends on the values of the *hyper-parameters* $\lambda, \rho$ and $\sigma$. For each image pair, we estimated these parameters by first computing the marginal log-likelihood of the model with respect to sparse matches $\mathcal{M}$, as, $p(\mathbf{y}|\mathbf{x}, \sigma, \rho, \lambda) = -0.5(\mathbf{y}-\mathbf{x})^T \mathbf{K}(\mathbf{Y}, \mathbf{Y})^{-1}(\mathbf{y}-\mathbf{x}) - 0.5 \log |\mathbf{K}(\mathbf{Y}, \mathbf{Y})| - 0.5\, n \log 2\pi$. Finally, this log-likelihood is differentiated with respect to each hyper-parameter and maximized by using a conjugate-gradient optimization method. An example of these dense predicted (blue) points $\mathbf{y}_*$ is illustrated in Fig. 2(a).

## EXPERIMENTAL RESULTS AND DISCUSSION

We validated our method on a large and manually annotated *Surgical-Image* dataset with more than 100 cases extracted from more than six real partial-nephrectomy surgeries [4]. This dataset contains images with resolution 704×480 extracted before and after prolonged camera occlusions, organ deformation, camera retraction/insertion, and large illumination changes. We used our HMA Toolbox (implemented on Matlab and publicly available at [7]) to match SIFT features extracted from both images. The set of sparse correspondences $\mathcal{M}$ was selected as those SIFT matches with a reprojection error less than 15 pixels of error. We compared the accuracy of both our algorithm as well as of the HMA method, by measuring the pixel reprojection errors and the computational time on an Intel i7-2.20 GHz CPU with 8GB of RAM.

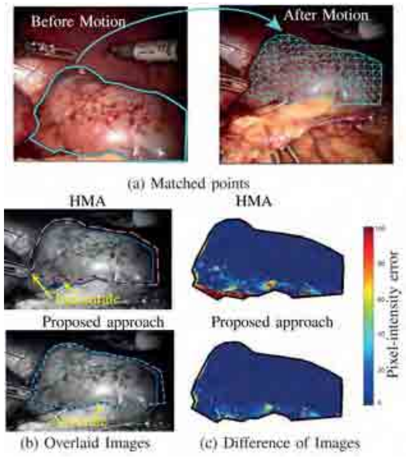



**Fig. 2** (a) Estimated matches using the proposed approach. (b) The organ's boundaries are not mapped correctly with HMA. Our approach is more accurate. (c) Absolute pixel difference between the reference organ's image and the one mapped by HMA or by our proposed method.

The results are summarized in Table I. The second column shows the average pixel-reprojection errors (in terms of mean and standard deviation) for both algorithms. The third column contains the average over the 25% largest pixel-reprojection errors which reflect the mapping accuracy of the methods over the most challenging areas such as the organ's borders or textureless regions.

**Table 1** Average errors (pixels) over the 100 image pairs

| *Alg.* | Avg.Err. [pixels] | Last Quartile Avg.Error |
|---|---|---|
| **Our method** | $\mathbf{3.13 \pm 3.09}$ | $\mathbf{6.21 \pm 3.63}$ |
| HMA | $4.1 \pm 4.09$ | $8.65 \pm 4.23$ |

The proposed approach showed a reduction of the average error of 23%, with an increased computational cost of only 16.7% (15-pixels meshgrid), or of 60% for the dense matching. The average time required for *Sparse feature-matching phase* was 0.05±0.006s, while the *GP regression phase* requires on average additional 0.011 ± 0.002s for the meshgrid, and 0.032 ± 0.002 seconds for dense matching.

The advantages of our proposed approach are evident in the qualitative example shown in Fig.2. The correspondences detected by our method between the two images are illustrated in Fig. 2(a). We only show the organ contour and the corresponding mesh to give an intuition of the mapping without cluttering the image with extra information. Fig. 2(b) shows the warped organ's boundaries from the image before to the image after the occlusion for both our approach and HMA. Here the dotted lines indicate the boundaries of the warped organ, while the solid (blue) line represents an *approximate* manually selected ground-truth used as a reference for the comparison. Observe that our method can accurately map the organ's boundaries. Finally, in Fig. 2(c) we show the absolute pixel difference between the warped patch and the image after the motion. It is evident that our method achieves reduced error (i.e., darker images).

## CONCLUSIONS

We presented a feature-matching algorithm that accurately and densely recovers the position of image features over the entire organ's surface. Our method is fully automatic, it does not require any explicit assumption about the organ's 3-D surface, and it combines the speed of sparse feature-matching with the probabilistic modeling of GP Regression. We demonstrated the effectiveness of our algorithm under a large endoscopic dataset with 100 image pairs. The evaluation was performed by measuring the reprojection errors with respect to manually annotated ground-truth. The proposed algorithm achieved high accuracy when compared to state-of-the-art method, in particular for features closer to organ's boundaries. In addition, the proposed method exhibits a comparable computational time with respect to sparse feature-matching methods.

## REFERENCES

[1] D. Cohen, E. Mayer, D. Chen, A. Anstee, J. Vale, G.Z. Yang, A. Darzi, and P. Edwards. Augmented reality image guidance in minimally invasive prostatectomy. *Prostate Cancer Imaging. Computer-Aided Diagnosis, Prognosis, and Intervention*, pages 101–110, 2010.

[2] P. Mountney, D. Stoyanov, and G.Z. Yang. Three-dimensional tissue deformation recovery and tracking. *Signal Processing Magazine, IEEE*, 27(4):14–24, 2010.

[3] D. Stoyanov, G. Mylonas, F. Deligianni, A. Darzi, and G.-Z. Yang. Soft-tissue motion tracking and structure estimation for robotic assisted MIS procedures. *Proc. of the 8th Int. Conf. on Med. Image Comp. and Comp-Ass. Int.*, pages 139–146, 2005.

[4] G Puerto-Souza and G. Mariottini. A fast and accurate feature-matching algorithm for minimally-invasive endoscopic images. *IEEE Transactions on Medical Imaging (in Press)*, 2013.

[5] C. Rasmussen and C. Williams. *Gaussian processes for machine learning,* MIT press Cambridge, MA, 2006.

[6] G.A. Puerto-Souza and G.L. Mariottini. A comparative study of correspondence-search algorithms in mis images. In *Proc. of the 15th Int. Conf. on Med. Image Comp. and Comp-Ass. Int.*, pages 625–633, 2012.

[7] HMA feature-matching toolbox. [Web:] http://ranger.uta.edu/%7egianluca/feature%5fmatching .

# Multimodal Reconstruction for Image-Guided Interventions

Philip Pratt[1], Archie Hughes-Hallett[2], Aimee Di Marco[1], Tom Cundy[1], Erik Mayer[2], Justin Vale[2], Ara Darzi[2], Guang-Zhong Yang[1]

*[1]The Hamlyn Centre for Robotic Surgery, Imperial College London*
*[2]Department of Surgery and Cancer, Imperial College London*
*p.pratt@imperial.ac.uk*

## INTRODUCTION

While the use of preoperative imaging for minimally invasive surgical guidance has been successfully translated into the operating theatre [1], many of the difficulties associated with the reduced sensory experience remain. This approach works well as a roadmap, allowing the surgeon to appreciate the macroscopic anatomy (figure 1). However, it must be combined with an intraoperative phase designed to account for structural change induced by dissection, and tissue deformation in general. Adopting robotic partial nephrectomy as the exemplar intervention, this study assesses the feasibility of a novel technique for fusing dense stereo scene reconstructions with intracorporeal freehand 3D ultrasound segmentations. In this instance, the fact that the resulting geometry can be viewed from any arbitrary position makes it a potentially invaluable aid in the pursuit of optimal nephron sparing resections.

## MATERIALS AND METHODS

Following the work of Taylor *et al*. [2], porcine kidneys were injected with an agarose-based mixture to form completely endophytic phantom lesions. In practice, human kidneys will typically be covered in a layer of perinephric fat, further occluding the target. Currently practical intraoperative ultrasound methods [3] are suitable for verifying tumour location, but are very difficult to employ as a guide during resection. This is due to the fact that visualisation of the relationship between organ and lesion is transient, and that the viewpoint is necessarily constrained.

The key observation is that it is possible to perform dense 3D scene reconstruction and freehand 3D ultrasound scanning *in the same coordinate system*. The captured data is therefore registered by construction, takes account of deformation, has permanence, and can be viewed from multiple virtual viewpoints, as required during resection. Moreover, since this can be performed quickly ‘on the fly’, it can be repeated as the dissection induces increasingly large-scale changes.

Prior to data capture, the intrinsic and extrinsic parameters of the da Vinci (Intuitive Surgical, Sunnyvale, CA, USA) stereo camera were calibrated [4,5]. Figure 1 illustrates the steps used to reconstruct surface geometry: image undistortion and rectification; generation of the disparity map using a semi-global block matching algorithm [6]; reprojection to 3D geometry and rotation back into the unrectified camera frame; construction of a pixel-dense triangular mesh; decimation through quadric metric edge collapse [7]; and mesh smoothing using a windowed *sinc(x)* function interpolation kernel [8]. The resulting vertex positions were then projected, with camera distortion, into the current frame to give corresponding texture coordinates.

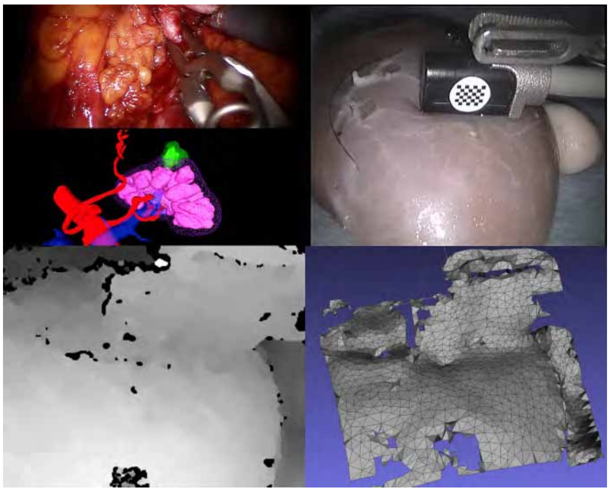


**Fig. 1** Surface reconstruction (left-to-right from top): live human intraoperative guidance; porcine kidney with lesions; disparity map; and surface geometry following decimation and smoothing**.**

Tracked in real time with the help of a robust vision-based algorithm [3], an Aloka UST-533 microsurgery probe (Hitachi Aloka Medical Ltd., Tokyo, Japan) was first calibrated using the dual pattern approach, as shown in figure 2. Ultrasound slice images and their respective transformations into the camera coordinate system were accumulated, such that a complete volume could be extruded using trilinear interpolation. The 3D geometry was then segmented [9] and realised as a mesh, or visualised directly with HDVR volumetric rendering [10].



**Fig. 2** Ultrasound image acquisition (left-to-right): probe calibration using water-filled Z-phantom and dual pattern technique; and typical ultrasound slice showing subsurface extent of phantom tumour**.**

## RESULTS

Figure 3 illustrates the resulting surface and subsurface reconstructions, viewed from different positions, together with a cross-section of the porcine kidney for reference. In addition to straightforward alpha-blending, an extension of the *inverse realism* [11] technique was used to combine the reconstructions. Rather than use a fixed window in the viewport, the new two-pass method first renders a mask, painted onto the surface mesh texture, to a temporary frame buffer. This is then combined with a rendering of the virtual organ surface, before being composited with the 3D ultrasound representation. This way, the window appears to move with the organ surface and reveals subsurface anatomy as the viewpoint is rotated and translated. In practice, one or more such views will be visualised in stereo via the console TilePro™ auxiliary video inputs.

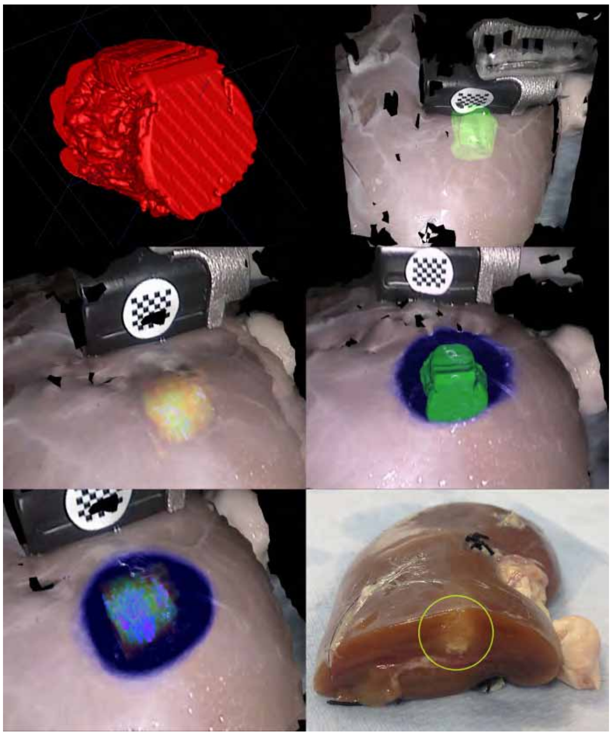


**Fig. 3** Reconstruction results (left-to-right from top): partially-truncated tumour segmentation; alpha-blended subsurface anatomy rendered both from its mesh representation and volumetrically with a false colour transfer function; alternative views showing the *inverse realism* extension window; and an actual tissue cross-section for comparison.

## DISCUSSION

The study results acquired to date strongly suggest that the proposed multimodal reconstruction method will prove to be an invaluable image guidance tool. Furthermore, since all of the physical components are ready for human use, in terms of sterilisation, for example, then once validated, the approach can immediately translate to the operating theatre.

Quantitative validation experiments are planned, in which 3D CT scans of contrast-enhanced lesions will be compared against reconstructed geometry. Although the reported accuracy [3] of the probe calibration process is high, with mean ultrasound and direct sight super-imposition error less than 0.7mm, it is necessary to prove that any deformation caused by the sweeping back and forth of the probe is not significant. Further developments to mitigate such an effect are also imminent. These include autonomous robot control of probe sweeps, based on reconstructed surface geometry, and the introduction of force sensors at the probe-manipulator coupling.

Opportunities also exist to improve freehand ultrasound slice interpolation and segmentation [12]. In addition, disparity map averaging over multiple video frames will be assessed as a means of improving the accuracy of dense surface reconstruction. Clearly, the described approach lends itself well to other surgical interventions, including non-robotic procedures, and can act as an effective canvas for the persistence and subsequent review of pathological data acquired at the cellular level, using microscopic imaging modalities.

## ACKNOWLEDGEMENTS

The High Definition Volume Rendering® SDK is used under licence from Fovia, Inc..

## REFERENCES

[1] Pratt, P., Mayer, E., Vale, J., Cohen, D., Edwards, E., Darzi, A., Yang, G.Z.: An effective visualisation and registration system for image-guided robotic partial nephrectomy. J Robotic Surgery (2012) 6:23-31
[2] Taylor, G., Johnson, D., Hogg, D., Cadeddu, J.: Development of a renal tumor mimic model for learning minimally invasive nephron sparing surgical techniques. J Urology (2004) 172:382-385
[3] Pratt, P., Di Marco, A., Payne, C., Darzi, A., Yang, G.Z.: Intraoperative ultrasound guidance for transanal endoscopic microsurgery. MICCAI Part I (2012) LNCS 7510:463-470
[4] Zhang, Z.: A flexible new technique for camera calibration. IEEE Trans Pattern Analysis & Machine Intelligence 22(11):1330-1334
[5] Bradski, A., Kaehler, A.: Learning OpenCV: computer vision with the OpenCV library. O'Reilly Media Inc., Sebastopol, CA
[6] Hirschmüller, H.: Stereo processing by semiglobal matching and mutual information. IEEE Trans Pattern Analysis and Machine Intelligence (2008) 30(2):328-341
[7] Hoppe, H.: New quadric metric for simplifying meshes with appearance attributes. Proc IEEE Vis Conf (1999)
[8] Taubin, G., Zhang, T., Golub, G.: Optimal surface smoothing as filter design. ECCV (1996) LNCS 1064:283-292
[9] Yushkevich, P., Piven, J., Cody-Hazlett, H., Gimpel-Smith, R., Ho, S., Gee, J., Gerig, G.: User-guided 3D active contour segmentation of anatomical structures. Neuroimage (2006) 31(3):1116-1128
[10] http://www.fovia.com
[11] Lerotic, M., Chung, A., Mylonas, G., Yang, G.Z.: pq-space based non-photorealistic rendering for augmented reality. MICCAI Part II (2007) LNCS 4792:102-109
[12] Gooding, M., Kennedy, S., Noble, A.: Volume segmentation and reconstruction from freehand three-dimensional ultrasound data with application to ovarian follicle measurement. Ultrasound Med Biol (2008) 34(2):183-195

# Towards an Ontology for Orthopaedic Surgery, Application to Hip Resurfacing

Paulo J.S. Gonçalves[1,2]

[1]Polytechnic Institute of Castelo Branco (IPCB), Portugal,
[2]Instituto Superior Técnico, Univ Tec de Lisboa, IDMEC, LAETA, Lisbon, Portugal
paulo.goncalves@ipcb.pt

## INTRODUCTION

One on the main benefits of introducing robots in the operative room is to increase the precision and accuracy of the surgical tasks, which follows a given clinical workflow, i.e., the knowledge from the surgeons. So, it is convenient to have proper know-ledge sharing and communication between surgeons and robots.

In this paper, ontologies are used to model the workflow/knowledge required to accomplish each surgery task in detail, allowing successful surgeries, and also to represent that knowledge in a machine-readable format. The ontological model obtained, i.e., its formal description, is of major interest to setup a surgical robot, e.g., a service robot manipulator applied in surgery, that will perform the surgery in a co-worker scenario with the surgeon, delivering the expected increase in accuracy and precision. The application presented in this work was developed under the HIPROB project http://www.echord.info/wikis/website/hiprob, and is related to Hip Resurfacing (HR) prosthesis surgery. It is an alternative to Total Hip Replacement (THR), especially for younger patients that may require hip joint revisions in the future. However, HR is more complex than THR, and requires precise and accurate following of the planned surgical workflow. To the authors' best knowledge, there is no generic framework for process modelling and formal definition that is specific to robot-assisted surgery. Moreover, in this work is included an ultrasound probe to track the bone alignment during surgery, as presented in [1].

## MATERIALS AND METHODS

While developing the orthopaedic surgery ontology, for HR, a five-step development process was adopted, called ontology development 101 [2]. Basically, this process defines the domain and scope of the ontology; reviews existing ontologies; identifies classes and properties; identifies and implements an upper ontology; and implements the ontology in a formal representation. The ontology domain and scope was defined when the author was asked to automate the HR surgery, following the contacts with surgeons in Lisbon and Castelo Branco Hospitals. A set of interviews was conducted with the surgeons to better define the domain of the approach. Existing ontologies from the medical and the robotics fields were reviewed, e.g., from the BioPortal [3], OpenCyc (http://www.cyc.com/platform/opencyc), the Surgical Ontologies for Computer Assisted Surgery [4], the Open Robots Ontology ORO [5] and KnowRob [6]. They were considered as the basic source of contents and partially covered the knowledge needed to develop the proposed ontology. The ontology was implemented using Protégé, a free and open-source platform that provides a suite of tools to create domain model and knowledge base application using ontologies. The underlying language for ontology definition used by Protégé is the Web Ontology Language, OWL.

## RESULTS

The classes and their properties were identified using the existing definitions on the base ontologies, like *BodyStructure*, *Surgeon* from the BioOntology [3] and *ImagingDevice*, *SurgicalDevice* defined in [4]. From this and the functional requirements obtained from the surgical workflow for HR surgery, new classes and properties were defined for the pre and intra operative surgery phases, e.g., *IntraOperativePhase* and *PreOperativePhase*. Also *ActuatedMechanism* was defined and its sub-classes (derived from ISO standard no.8373 and [7]). A particular property from the proposed ontology is that the ultrasound probe *US_probe* (a sub-class of *US_imaging*) *isAttachedTo* the *EndEffector* and *isUsedIn* the *IntraOperativePhase*. Computer tomography imaging *CT_imaging isUsedIn* the *PreOperativePhase*. Please refer to figure 1 to 3, where portions of the ontology are depicted.

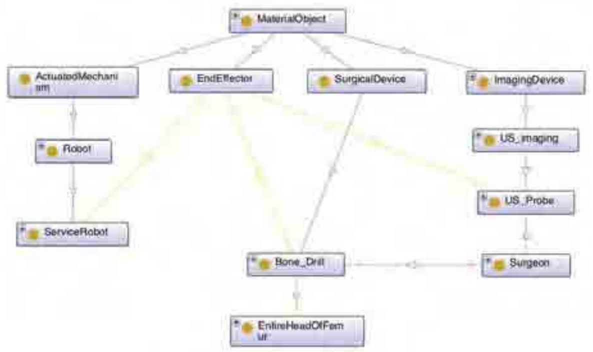



**Fig. 1** A fraction of the orthopaedic ontology, related to the robot and medical devices. Solid lines indicate class hierarchy, and dashed lines connections between classes.

The next step is to implement an upper ontology. For that the OpenCyc was used because it is interchangeable amongst other robotic and biomedical ontologies. Also provides a basic structure, generalizable to domain specific ontologies. OpenCyc is used as the main source to design the structure and also to define HR surgery ontology classes and its properties.

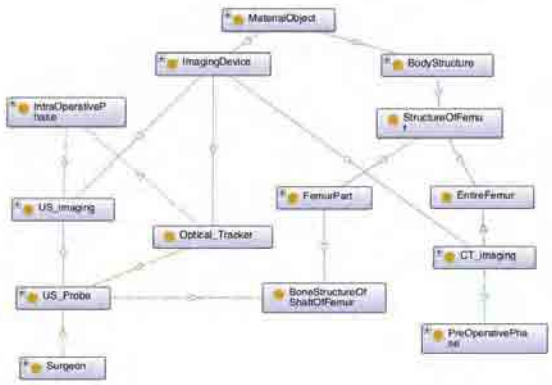



**Fig. 2** A fraction of the orthopaedic ontology, related to imaging concepts. Solid lines indicate class hierarchy, and dashed lines connections between classes.

The ontology was implemented in OWL, and a set of classes was defined specifically for the HR surgery setup, e.g., *Bone_Drill*, *US_Probe*. The knowledge management module for cognitive architectures in robotics ORO, is used to map the robot services to the orthopaedic ontology. ORO is an open-source framework that can be used within the ROS framework to control a robot. This model includes, amongst other features, the capability to knowledge classification based on SWRL rules, using Pellet, an OWL 2 Reasoner for Java http://clarkparsia.com/pellet.
The ORO server performs reasoning as the following example:

```
for tools in kb["?tool rdf:type SurgicalDevice ",
        "?tool isAt EntireHeadOfFemur"]:
 print tools.
```

this query can return the *Bone_drill* or an *Optical_Tracker*, i.e., two tools that can work in the head of the femur.

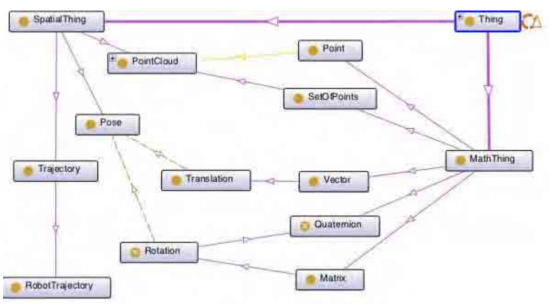



**Fig. 3** A fraction of the orthopaedic ontology, related to Spatial and Mathematical things.

## DISCUSSION

For HR surgery several medical imaging systems could be useful like magnetic resonance, computer tomography, and ultrasound. In the current application, two types are needed, ultrasound for intra-operative operation and computer tomography for the pre-operative stage. Surgical tools, some to be used by the robot, e.g., *Bone_Drill*, and other to be used by surgeons like reamers, should be defined. Knowledge from the human body must also be shared with the robot via the ontology, e.g., femoral head. HR robotic surgery specific equipment like a service robot, and the optical tracking systems, should be set in the ontology. In the following, are discussed two sub-sets of knowledge representations for the tackled surgery.

For the robotic drilling of the head of the femur, figure 1 presents the related classes. The Robot, Surgical Devices and Imaging Devices all derive from the class Material Object. It is possible to verify that the surgeon can also operate the *Bone_Drill*, e.g., in a co-worker scenario. Usually, a second surgeon operates the *US_Probe*. A second robot, depending on the chosen setup for HR Robotic Surgery, can also operate it.

Figure 2 depicts the medical imaging devices needed for HR Robotic Surgery in a minimal setup [1] i.e., *CT_imaging* (pre-operative scenario), *US_imaging* and *Optical_Tracker* (both in the intra-operative scenario). The *CT_imaging* device performs a 3DScan of the entire femur, represented as a *PointCloud*, used for intra-operative registration with the 3D data obtained from the *Polaris_Tracker* and the *US_probe*, when the latter obtains images from the shaft of femur.

By this way, in this paper, is shown that is possible to represent knowledge, using ontologies, for Surgery.

## ACKNOWLEDGEMENT

This work was partly supported by the Strategic Project, PEst-OE/EME/LA0022/2011, through FCT (under the Research Group: IDMEC/LAETA/CSI), and EU-FP7-ICT-231143 project ECHORD. To the IEEE working group: Ontologies for Robotics and Automation.

## REFERENCES

[1] Torres P., Sanches J., Martins JMM. 3D femur reconstruction using a robotized ultrasound probe. 4th IEEE RAS & EMBS Int. Conf. on Biomedical Robotics and Biomechatronics, 2012: 884-888.

[2] Noy N, McGuinness D. Ontology development 101: a guide to creating your first ontology. Stanford knowledge systems laboratory technical report KSL-01-05 and Stanford medical informatics technical report SMI-2001-0880, 2001.

[3] Noy NF, Shah NH, Whetzel PL, Dai B, Dorf M, Griffith N, et al. BioPortal: ontologies and integrated data resources at the click of a mousse, Nucleic Acids Res, 2009; 37: 170-173.

[4] Neumuth D., Loebe F., Herre H. and Neumuth T. Modeling surgical processes: A four-level translational approach. Artificial Intelligence in Medicine. 2011; 51: 783-791

[5] Lemaignan, S. and Ros R. and Mosenlechner L. and Alami R. and Beetz M., ORO, a knowledge management module for cognitive architectures in robotics. Proc. of the Int. Conf. on Intelligent Robots and Systems. 2010

[6] Tenorth M. and Beetz M. KnowRob -- Knowledge Processing for Autonomous Personal Robots. Proc. of Int. Conf. on Intelligent Robots and Systems (IROS). 2009 : 4261-4266

[7] Haidegger T., Barreto M. E., Goncalves P.J.S., Habib M., Ragavan V., Li, H., Vacarella A., Perrone R., Prestes E., Ontology Applications and Standards in Service Robotics, accepted for Robotics and Autonomous Systems, 2013.

# Ex-Vivo Robotic Trials for Thyroidectomy with Novel Retraction


A. Arora[1], N. Tolley[1], Z. Awad[1], V. Luzzato[2], M. Oldfield[2], F. Rodriguez y Baena[2]

[1]*Department of Otolaryngology, St Mary's Hospital, Imperial College Healthcare NHS Trust, London, UK*

[2]*Department of Mechanical Engineering, Imperial College London, UK*

*asitarora@doctors.org.uk*


## INTRODUCTION

Critical to robotic thyroidectomy is the deployment of a custom designed lifting device inserted through an axillary incision. Several bed-mounted retractors have been developed for clinical practice. Compared to South Korea, where over 3000 procedures have been performed, patients in the UK and US undergoing robotic thyroidectomy have significantly larger thyroid pathology. Their BMI is also significantly higher[1]. These factors necessitate a larger working space than may be afforded by the existing devices. Improving exposure of the surgical field is essential for the technique to become popularised in a Western population.

We have previously reported an alternative retractor design[2]. This is patient-mounted rather than bed-mounted to increase the working space. The initial prototype underwent load testing and two sequential design iterations following cadaver evaluation. The prototype tested here is modular, creates a 5cm vertical opening and is based on a secure interaction with the clavicle (Fig 1). It has a smaller external footprint and locking mechanism, smoothed edges and reshaped blade in comparison with the previously reported iteration[2].

The objective of this study was to compare this latest prototype (the Imperial retractor) with 2 bed-mounted devices used in clinical practice (the Chung and Modena retractors) (Fig. 2).

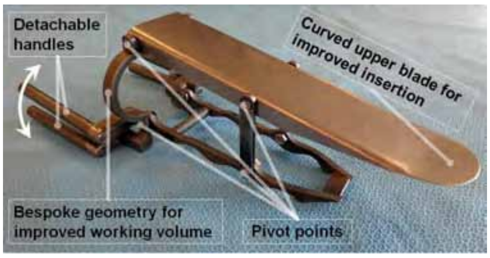



**Fig. 1**: The Imperial retractor.

## MATERIALS AND METHODS

Robotic thyroidectomy was performed using the daVinci SI robot [Intuitive Surgical] in a fresh frozen cadaver by three thyroid surgeons familiar with the robotic approach. Initial exposure was achieved through a 6cm axillary incision with the cadaver positioned in standard fashion (supine with ipsilateral arm elevation). Using a Chung retractor coupled with a spring balance, the load required to create a 5cm vertical opening was measured. The time taken to assemble, insert and secure the three retractors was recorded. The robot was then docked with four instrument arms (5mm Debakey forceps, 5mm Maryland dissector, 8mm Prograsp and 12mm dual channel endoscope) inserted through the incision.

The console surgeon performed a series of standardized tasks that reciprocated key steps in robotic thyroidectomy: i) mobilization of superior thyroid pole ii) dissection off the recurrent laryngeal nerve (RLN) iii) mobilization of the inferior pole iv) dissection of isthmus and contralateral lobe. An interactive task was also performed using a pledget exchanged between the console and bedside surgeons. Three surgeons each performed the console and bedside tasks.

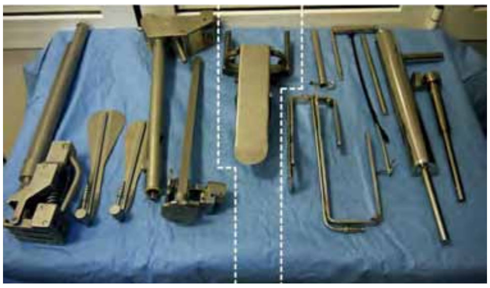


**Fig. 2** From left to right, the three retractors used in this study: Modena retractor, Imperial retractor and Chung retractor.

Evaluation of the retractors and ease performing the tasks was recorded on a 1-10 categorical Likert-type scale (LTS) with 10 being the most positive outcome. The number of instrument arm clashes and repositions that occurred while performing the tasks was recorded. Retractor stability was assessed by measurement of slippage out of the body. Finally, the ipsilateral arm was dropped to the bedside and observations of the exposure of the thyroid in this configuration were recorded.

## RESULTS

The load of 20-25N to create access was considerably lower than the previously reported 84N and is attributed to the use of a 'fresh-frozen' cadaver rather than a preserved specimen with phenol and glycerine.

Results relating to the ease with which the three retractors could be deployed are shown in Table 1. Surgeon familiarity with the bed-mounted designs and a

crude fastening device on the Imperial retractor account for the lower satisfaction rating for the ease of setup. All retractors suffered from tissue slippage, but exposure was not adversely affected with the Imperial design.

**Table 1** Deployment of the retractors. A low trauma LTS score is desirable, while a high LTS score indicates satisfaction with the ease of setup and tissue slippage.

| Task | Chung | Modena | Imperial |
|---|---|---|---|
| Setup time (s) | 113 | 208 | 60 |
| Ease of setup (LTS) | 8 | 8 | 7.7 |
| Tissue slippage (mm) | 12 | 25 | 12 |
| Tissue slippage (LTS) | 6.0 | 1.0 | 10.0 |
| Trauma (LTS) | 10.0 | 10.0 | 1.0 |

All retractors enabled the console surgeon to perform the tasks for an ipsilateral lobectomy. However, the exposure created by the Imperial retractor (Fig. 3) resulted in higher LTS feasibility scores (Table 2). The prevention of tissue encroachment enabled more flexibility in positioning the robot arms hence fewer cumulative clashes. This was particularly evident when excising the contralateral thyroid lobe.

**Table 2** Console surgeon evaluation of tasks with mean LTS score, standard deviation and (cumulative number of clashes). A high LTS score is desirable.

| Task | Chung | Modena | Imperial |
|---|---|---|---|
| Superior pole | 6.7±1.2 (6) | 8.0±1.0 (6) | 9.3±0.6 (0) |
| RLN | 7.7±0.6 (0) | 8.0±0.0 (0) | 8.7±1.2 (0) |
| Inferior pole | 6.7±0.6 (3) | 7.0±2.0 (4) | 8.3±0.6 (1) |
| **Contralateral lobe** | **1.0±1.7 (6)** | **5.7**±1.2 **(7)** | **7.7**±0.6 **(0)** |
| Pledget exchange | 7.7±1.2 (3) | 7.0±1.0 (9) | 9.3±0.6 (0) |



**Fig. 3** The exposure offered by the Imperial retractor.

A well-maintained working volume and flexibility in the docking position of the robotic arms (Fig. 4) accounted for the bedside surgeons' higher mean feasibility scores with the Imperial retractor compared to the bed-mounted alternatives (Table 3).

**Table 3** Bedside surgeon evaluation of tasks indicated by mean LTS score, standard deviation and (cumulative number of repositions). A high LTS score is desirable.

| Task | Chung | Modena | Imperial |
|---|---|---|---|
| Superior Pole | 4.0±3.0 (2) | 6.7±1.5 (5) | 9.3±1.2 (0) |
| RLN | 4.7±2.1 (0) | 6.0±1.7 (0) | 9.3±0.6 (0) |
| Inferior Pole | 3.7±2.9 (1) | 5.3±2.1 (9) | 8.7±1.5 (0) |
| Contralateral Pole | 1.0±1.0 (2) | 3.3±3.2 (6) | 7.3±1.2 (0) |
| Pledget exchange | 4.7±2.5 (0) | 6.0±1.7 (0) | 9.3±0.6 (0) |

## DISCUSSION

In stability and deployment the Imperial retractor is favorable to the existing bed-mounted designs. By preventing tissue encroachment, the Imperial device retains exposure despite tissue slippage. The Imperial retractor also remained stably fixed on the clavicle. In contrast, the Modena retractor required complete repositioning due to tissue slippage. Elimination of clashes and repositions, with the ability to perform total thyroidectomy, were the main benefits of the Imperial device. No retractor allowed sufficient exposure when the ipsilateral arm was dropped to the bedside



**Fig. 4** External view of the Imperial retractor and docked daVinci robot arms during console surgery.

A further iteration based on the outcome of the robotic trials is shown in Fig. 5. Access to the incision is opened up by creating a single central support around which all the robotic arms can easily be directed. A ratchet mechanism is employed for improved deployment and variable opening heights.

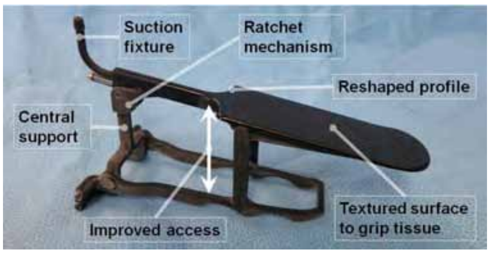



**Fig. 5** Rapid prototype of retractor with arms detached, based on outcome of the robotic trials. Revised features highlighted.

In conclusion, the Imperial retractor is a flexible and easily deployed alternative to existing retractors. Enhancements based on the robotic testing described here will lead to imminent clinical trials.

## ACKNOWLEDGEMENT

This work was made possible by funding from the Medical Engineering Research Collaboration Kick-start Scheme. Rapid prototype and contribution to its design provided by HinKell Development Ltd.

## REFERENCES

[1] Kandil EH. et al. Robotic transaxillary thyroidectomy: An examination of the first one hundred cases. J Am Coll Surg. 2012 Apr; 214(4): 558-64.

[2] Arora A. et al. Bespoke fixtures for robotic thyroidectomy. Proceedings of the Hamlyn Symposium on Medical Robotics, 2012: 65-6.

# Automated Cognitive Load Detection with Electroencephalography: Towards Brain-Computer Interfacing in Robotic Surgery

K. Shetty[1], T. Zander[2], D.R. Leff[1], R. Lorenz[2], G.-Z. Yang[1], A.W. Darzi[1]

[1]The Hamlyn Centre for Robotic Surgery, Imperial College London, U.K.

[2]Dep. of Biological Psychology and Neuroergonomics, Team PhyPA, TU Berlin, Germany

a.darzi@imperial.ac.uk

## INTRODUCTION

Minimally Invasive Surgery (MIS) driven by patient demand and benefits in outcome, imposes certain limitations on the surgeon. Sensorimotor discordances, distorts the surgeon's perception making it mentally more challenging to perform MIS than its traditional open counterpart, thereby requiring longer to attain proficiency [1]. In particular, MIS knot-tying (MISKT) is arguably the most challenging surgical manoeuvre and serves as a barometer to perform advanced MIS. Moreover, the influx of new technology that supports MIS necessitates the operators' vigilance to attend to auditory alarms that alerts the surgeon to a faulty technical device or declining status of the monitored patient. These may also be in the form of interruptions from other members of the team that require immediate decisions on patient management outside of the operating room. On average, surgeons are interrupted 13.5 times whilst operating [2]. Mental resources are finite and the impact of the secondary task (e.g. decision making) on the simultaneously performed primary task (i.e. technical) has shown that with expertise there is variable degradation of one or both task performances [3, 4, 5]. We hypothesize that with increasing task complexity (MIS versus open knot-tying) and in the presence of a secondary task (sustained auditory attention) an increase in cognitive load and performance degradation would be demonstrable. Unlike other studies that measured performance degradation and mental workload using subjective questionnaires, stress and eye-gaze patterns, we aim to use electroencephalography (EEG) to directly observe these phenomena.

## MATERIALS AND METHODS

Participants (n=9) comprised of 8 residents (PGY3-8) and 1 attendee aged 32.2 ± 3.3 years (mean ± S.D.). 15 minutes for warm-up to practice surgical manoeuvres relevant to the trial were mandatorily provided. Participants initially performed open hand knot-tying (OHKT) and MISKT (primary tasks) as illustrated in **Figure 1**, for a fixed period of 200 seconds (Application Data). Subsequently, in addition to performing OHKT/MISKT participants were required to simultaneously count the number of high-toned beeps randomly introduced amongst a series of low tone beeps (secondary task) for same time period (Calibration Data). The order of tasks was randomized to minimise learning and other temporal effects, e.g. fatigue. During control tasks participants performed the secondary task (auditory) alone. EEG was recorded from a 32 impedance-optimized electrodes (Brain Products, Gilching, Germany) transmitting signals wirelessly to a standard personal computer. A passive Brain Computer Interface (BCI) [6] was setup using the toolbox BCILAB [7] to discriminate trials from the low cognitive load condition (OHKT) to those from the high load condition (MISKT). Features were extracted from logarithmic band-poer estimates of the signal with a spatio-temporal filter derived by the spectrally weighted Common Spatial Patterns method [8]. Three filter pairs were calculated with optimized frequency weights between 7 and 23 Hz. A regularized linear discriminant analysis (LDA) was used to estimate an optimal discriminating hyper-plane in the resulting feature space. Performance estimates were calculated on the Calibration Set by a five times repeated five-fold cross validation with margins of five [7]. The resulting classification approach was then applied on consecutive epochs of one-second length from Application Set to simulate an online application. Secondary performance measures for the primary task were number of OHKTs/MISKTs performed in the time period and for the secondary task were accuracy in the number of high toned beeps counted. Subjective workload (NASA-TLX) was assessed based on task complexity [9].




**Fig. 1** Participant performing open hand knot-tying (left) and intracorporeal laparoscopic knot-tying (right) in a box trainer, whilst brain behaviour was assessed with EEG.

## RESULTS

Participants found MISKT significantly harder than OHKT (Wilcoxon signed-rank test, (p=0.012) and the secondary task alone (p=0.025) as indexed from group

averaged NASA-TLX scores displayed in **Table 1.** There was no significant difference between NASA-TLX scores for OHKT and the auditory task (p=0.55). Participants found dual tasks significantly harder than mono tasking.

**Table 1** Group averaged NASA-TLX scores for each task.

| Task | NASA-TLX score (mean ± S.E.) | *p* value |
|---|---|---|
| Mono OHKT | 16.99 ± 2.85 | Dual vs. Mono OHKT **(0.018)** |
| Mono MISKT | 48.79 ± 6.07 | Dual vs. Mono MISKT **(0.012)** |
| Auditory | 24.33 ± 6.07 | Auditory vs. Dual OHKT and MISKT **(0.017 and 0.011)** |
| Dual OHKT | 51.03 ± 7.42 | |
| Dual MISKT | 67.55 ± 6.91 | |

Although performance deterioration was observed in the secondary task with increasing primary task complexity it did not reach statistical significance. Average number of OHKTs and MISKTs performed was 117.7 and 13.1 respectively. EEG data of participant 1 and 2 were insufficient and for participant 8 was disregarded as it lacked markers for each task. An example of subjects activation and frequency weights calculated by Common Spatial Patterns (**Figure 2)** displays mental workload, bilateral motor, auditory and visual activity as processes underlying the classification.

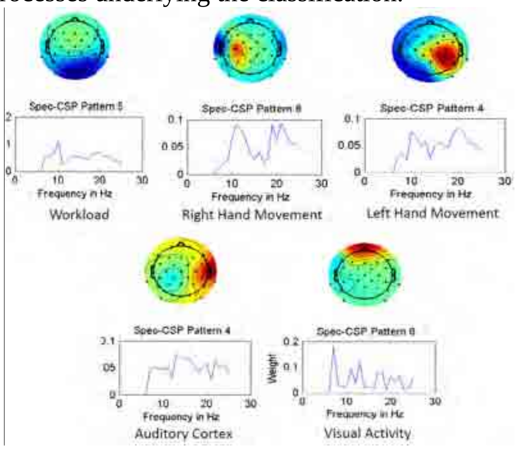



**Fig. 2** Activation patterns and frequency weights calculated by Common Spatial Patterns.

Average classification of subjects into low and high cognitive demand (OHKT *vs.* MISKT) was 89.4% on calibration and 87.8% on application. One subject (subject 5) showed comparatively poorer classification compared to rest who accurately classified up to 100% as seen in **Table 2**. On a subject level, successful classification of work into high and low cognitive demand conditions for each second of the experiment was achievable. The crossvalidation estimates are accurate, showing no significant difference ($p<0.01$) from the application performance.

## DISCUSSION

Mental workload varies depending on the operative task complexity. During high mental workload states that demand greater attentional resources they are unlikely to cope with distractions due to a lack of free cognitive resources. The results from classification of EEG data alone of 1 second length demonstrate accurate and reliable discrimination of a low-demand (OHKT) and high-demand task (MISKT). This work highlights the potential to build a platform that detects online the cognitive load status of the surgeon and visually communicates that information to the rest of the operative team by employing a passive BCI system. An example of the applicability of such a system would be to help inform other members to avoid any interruptions when the surgeon is in a high cognitive load state. Future work needs to investigate how well the current methodology translates to low and high demand conditions *in vivo*.

**Table 2** Classification accuracies for each subject from crossvalidation and application of the classifier.

| Participant ID | Calibration (%) | Application (%) |
|---|---|---|
| 1 | 87 | n/a |
| 2 | 92 | n/a |
| 3 | 84 | 89 |
| 4 | 91 | 76 |
| 5 | 67 | 70 |
| 6 | 97 | 94 |
| 7 | 98 | 100 |
| 8 | n/a | n/a |
| 9 | 99 | 98 |
| **Average** | **89.4** | **87.8** |

## REFERENCES

[1] Korndorffer JR Jr, Dunne JB, Sierra R et al. Simulator training for laparoscopic suturing using performance goals translates to the operating room. J AmColl Surg: 2005 201:23–29.

[2] Healey AN, Selvadis N, Vincent CA. Measuring intra-operative interference from distraction and interruption observed in the operating theatre. Ergonomics. 2006; 15; 49(5-6): 589-604.

[3] Hsu KE, Man FY, Gizicki RA, et al. Experienced surgeons can do more than one thing at a time. Surg Endosc. 2008; 22(1): 196-201.

[4] Zheng B, Tien G, Atkins SM et al. Surgeon's vigilance in the operating room. Am J Surg. 2011; 201(5): 673-7.

[5] Zheng B, Cassera MA, Martinec DV et al. Measuring mental workload during the performance of advanced laparoscopic tasks. Surg Endosc. 2010; 24(1): 45-50.

[6] Zander TO, Kothe C. Towards passive brain-computer interfaces: applying brain-computer interface technology to human-machine systems in general. JNE. 2011; 8: 025005.

[7] Delorme A, Mullen T, Kothe C et al. EEGLAB, SIFT, NFT, BCILAB, and ERICA: New Tools for Advanced EEG Processing, Computational Intelligence and Neuroscience, vol. 2011. 2011: 1–12.

[8] Tomioka R, Dornhege G, Aihara K, Mueller KR. An Iterative Algorithm for Spatio-Temporal Filter Optimization. 2006: Brain Computer Interface Workshop and Training Course 3rd, 22–23.

[9] Hart S, Staveland LE.Development of NASA-TLX (Task Load Index): Results of empirical and theoretical research. In Hancock PA & Meshkati N (eds.), Human Mental Workload. 1988: 139-183. Amsterdam: North-Holland.

# Vibration-Induced Frictional Reduction for Magnetically Guided Intracorporeal Devices

M. Sfakiotakis[1,2], N. Pateromichelakis[1], D.P. Tsakiris[1]

[1]Institute of Computer Science, Foundation for Research and Technology – Hellas,Greece

[2]Dept. of Electrical Engineering, Technological Educational Institute of Crete, Greece

{sfakios,nikospat,tsakiris}@ics.forth.gr

## INTRODUCTION

One of the most promising approaches to recently emerge for the active guidance of miniature intra-corporeal robots (such as capsule endoscopes, involves external magnetic fields interacting with a small permanent magnet inside the device [1, 2]. Depending on the proposed method, the applied force/torque vectors are adjusted by either controlling the current supplied to stationary electromagnetic coils, or by changing the position/orientation of one or more permanent magnets outside the patient. In this context, reducing the frictional forces encountered by the micro-robot would ensuingly lower the required strength of the external magnetic fields, yielding multiple benefits for the design and functionality of the overall system, related to cost, size, safety, and EMI considerations, while potentially also allowing for smoother and more precise steering of the device by the doctor. Although various studies have investigated the reduction in friction that occurs when vibrations are superimposed to the contact surface between metals and/or plastics [3], few have considered this concept for intracorporeal medical devices [4, 5].

## MATERIALS AND METHODS

**Computational Model:** A platform of mass $M$ moves over a substrate with normal-wise compliance, modeled as a Voigt element with damping $b$ and stiffness $k$ (Fig. 1). An eccentric mass $m$, rotating with constant velocity $\omega$ at a radius $r$ about the platform's center-of-mass $O$, generates normal and tangential harmonic excitations, respectively obtained as $C_y(t) = mr\omega^2\cos(\omega t)$ and $C_x(t) = mr\omega^2\sin(\omega t)$. The platform's equations of motion are:

$$M\ddot{y}(t) = Mg + C_y(t) - F_N(t) \quad (1)$$

$$M\ddot{x}(t) = F_{ext}(t) + C_x(t) - F_R(t)\ , \quad (2)$$

where $F_N(t) = ky(t) + b\dot{y}(t)$ is the normal contact force (applied for $y(t) \geq 0$), and $g$ is the acceleration of gravity. The horizontally-applied external force $F_{ext}$ represents the effect of the magnetic guidance system, and is here assumed to be constant (in practice it would depend on the position /orientation of the platform with respect to the external magnetic field). $F_R(t)$ denotes the platform-substrate friction force, here described by linear viscous damping combined with a modified version of the Dahl model, the hysteresis characteristic of which has been shown to be significant in the context of frictional reduction by vibrations [3]. Specifically,

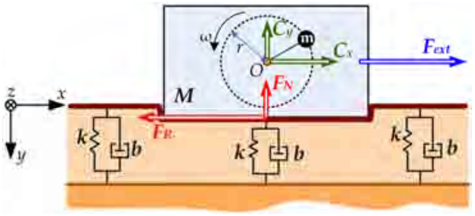



**Fig. 1** Mechanical model of the system.

$$F_R(t) = \mu(t)F_N(t) + \delta\dot{x}(t) \quad (3)$$

$$\dot{\mu}(t) = \frac{\mu_k}{x_b}\dot{x}(t)\left|1 - \frac{\mu(t)}{\mu_k}\mathrm{sgn}(\dot{x}(t))\right|\mathrm{sgn}\left(1 - \frac{\mu(t)}{\mu_k}\mathrm{sgn}(\dot{x}(t))\right),$$

where $\delta$ is the viscous coefficient, $\mu(t)$ is the time-varying Dahl friction coefficient, $\mu_k$ is the kinetic Coulomb coefficient, $x_b$ is the "breakaway" displacement, and $\alpha$ determines the stress-strain curve shape [3].

***Ex-vivo* experimental setup:** Fig. 2 depicts the setup for assessing the effect of vibrations for movement over *ex-vivo* bovine liver. The test platform, made from ABSplus, has a 39 mm x 18 mm footprint, and integrates a ∅10 mm pager motor (nominal velocity 11200 rpm @3 V) for generating the vibrations. A high-precision digital force gauge (*Alluris FMI-210A5*), mounted on a servo-controlled linear stage, measures the frictional resistance of the prototype, as it is being pulled over or through the environment of choice, at different imposed velocities. The laser interferometer (*micro-Epsilon optoNCDT1402-10*) allows measurement of the capsule's vertical displacements, resulting from the vibrations, with a 1 μm resolution. Data from the two sensors are streamed in real-time to a work-station PC, where a LabView-based user interface facilitates adjustment of the various motion control and data acquisition parameters.

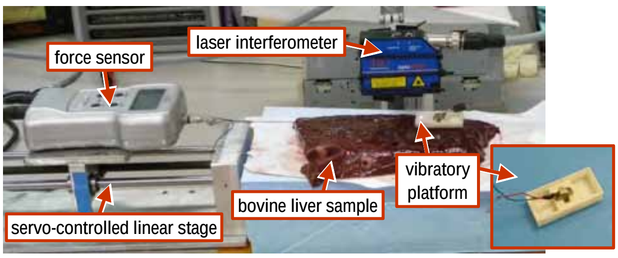



**Fig. 2** Experimental setup employed in the *ex-vivo* tests.

The system parameters, corresponding to the model (1)–(3), are shown in Table 1. The values for $k$, $b$, $\mu_k$ and $\delta$ were obtained by appropriate identification tests, while

**Table 1** Simulation parameters.

| | | |
|---|---|---|
| $M$: $9.96 \cdot 10^{-3}$ kg | $k$: 181.2 N m$^{-1}$ | $\mu_k$: 0.89 |
| $m$: $0.32 \cdot 10^{-3}$ kg | $b$: 1.29 N s m$^{-1}$ | $\alpha$: 0.5 |
| $r$: $0.86 \cdot 10^{-3}$ m | $\delta$: 3.94 N m$^{-1}$ | $x_b$: $1 \cdot 10^{-3}$ m |

those for $\alpha$ and $x_b$ were estimated on the basis of matching the simulations with the experimental data in Fig. 4.

***In-vivo* experimental setup:** A vibratory capsule prototype, powered by an on-board battery and weighing 5.8 g, was connected via surgical string to a force sensor mounted at the distal link of a robot arm (Fig. 3). Using an endoscope, the capsule was inserted in the anaesthetized swine's colon, about 350 mm from the anus. The robot arm was then commanded to move so that its distal link translated horizontally at a constant speed of 6 mm/s, with the sensor collecting data as the capsule was being pulled out of the colon. Two such runs were performed, one without vibrations and one with the vibratory motor operating at 3.7 V.

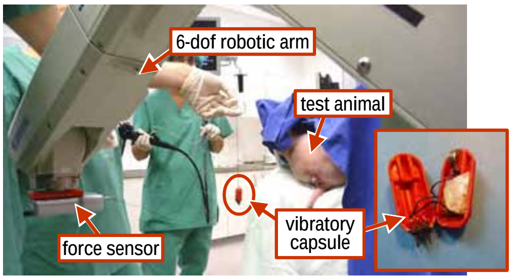



**Fig. 3** Experimental setup of the *in-vivo* tests.

## RESULTS

The *ex-vivo* test-stand was used to measure the force required for pulling the platform at a constant velocity of 6.13 mm/s over the liver sample, in the presence of vibrations, whose frequency was adjusted via the voltage applied to the pager motor. Corresponding simulations of the model (1)–(3) were performed, where, for different values of $\omega$, the magnitude of $F_{ext}$ was iteratively updated to obtain its appropriate value for the system to achieve an average steady-state velocity of 6.13 mm/s. The combined results, shown in Fig. 4, indicate that the use of vibrations yields considerable frictional reduction, which increases (up to 41%, when $\omega$ = 220 Hz) with the vibration frequency.

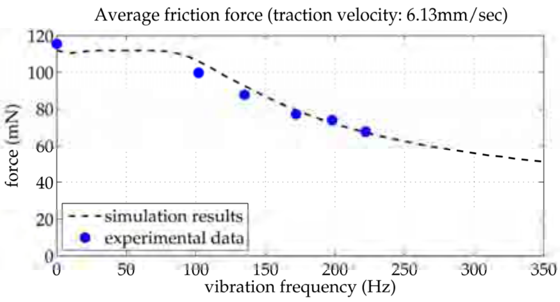



**Fig. 4** Average friction, as a function of the vibration frequency, for movement of the vibratory platform over bovine liver.

Moreover, the simulation results can be seen to closely match the experimentally obtained ones.

The *in-vivo* results, shown in Fig. 5, indicate a 39% reduction in the average force when vibrations are employed during movement through the porcine colon, noting that forces considerably higher than those for movement over liver were recorded, possibly due to the increased pressure exerted on the capsule from the walls of the colon.

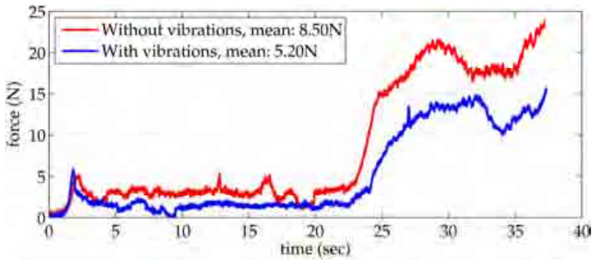



**Fig. 5** Forces recorded during the *in-vivo* tests.

## DISCUSSION

Our findings suggest that vibrations can effectively reduce the average friction forces for magnetically-guided intracorporeal devices. Concerns regarding the vibratory motor power consumption could be alleviated by its intermittent, on-demand activation, and/or by the adoption of wireless power transfer technologies [6].

This work was supported in part by the European Commission, through the R&D projects VECTOR (FP6-033970) and OCTOPUS (FP7-231608). The authors wish to thank M.O. Schurr, S. Schostek, C. Fleisch, and M. Melbert of Novineon Healthcare Technology Partners GmbH, for their assistance with the *in-vivo* tests.

## REFERENCES

[1] F. Carpi, "Magnetic capsule endoscopy: The future is around the corner," *Exp. Rev. Med. Dev.*, vol. 7, pp. 161–164, 2010.

[2] M. Gao, C. Hu, Z. Chen, H. Zhang, and S. Liu, "Design and fabrication of a magnetic propulsion system for self-propelled capsule endoscope," *IEEE Trans. Biom. Eng.*, vol. 57, no. 12, pp. 2891 –2902, 2010.

[3] C. C. Tsai and C. H. Tseng, "The effect of friction reduction in the presence of in-plane vibrations," *Arch. Appl. Mech.*, vol. 75, no. 2, pp. 164–176, 2006.

[4] T. Shin-Ei, K. Yuyama, M. Ujihira, and K. Mabuchi, "Reduction of insertion force of medical devices into biological tissues by vibration," *Jap. J. Med. Electr. Biol. Eng.*, vol. 39, no. 4, pp. 292–296, 2001.

[5] G. Ciuti, N. Pateromichelakis, M. Sfakiotakis, P. Valdastri, A. Menciassi, D. P. Tsakiris, and P. Dario, "A wireless module for vibratory motor control and inertial sensing in capsule endoscopy," *Sens. Act. A Phys.*, vol. 186, pp. 270–276, 2012.

[6] R. Carta, M. Sfakiotakis, N. Pateromichelakis, J. Thoné, D. P. Tsakiris, and R. Puers, "A multi-coil inductive powering system for an endoscopic capsule with vibratory actuation," *Sens. Act. A Phys.*, vol. 172, no. 1, pp. 253–258, 2011.

# Multispectral Imaging using a Fast Filter Wheel System during Vascular Surgery

N.T. Clancy[1,2], M. Ebner[3], J.S. Crane[2], R. Corbett[4], N. Duncan[4], C. Caro[5], D.S. Elson[1,2]

[1]The Hamlyn Centre for Robotic Surgery, Imperial College London, UK,

[2]Department of Surgery and Cancer, Imperial College London, UK,

[3]KARL STORZ GmbH & Co. KG, Tuttlingen, Germany,

[4]Department of Medicine, Imperial College London, UK,

[5]Department of Bioengineering, Imperial College London, UK.

n.clancy@imperial.ac.uk

## INTRODUCTION

Visualisation of oxygenation of the *vasa vasorum* as a means of assessing oxygen transport from the lumen to the vessel walls may be a valuable tool for the study of haemodynamics at anastomotic junctions [1]. This information could then be used for prediction of neointimal hyperplasia (NIH), a thickening of vessel walls, which itself is a cause of anastomotic failure [2]. Currently, in the case of fistula failure for example, NIH is not specifically detected in individual patients but has been identified in studies as a cause of stenosis [3]. Intraoperative measurement of vessel wall oxygenation would allow further investigation of the correlation between oxygenation and clinical outcomes.

Recent work by our group has shown the applicability of multispectral imaging in the measurement of perfusion changes intra-operatively for robotic surgery applications in the bowel [4], and for organ viability monitoring following anastomoses of transplanted organs [5]. These spectral imaging systems used liquid crystal tuneable filters (LCTFs) with convenient electronic switching capabilities to extract high spectral resolution information. However, LCTFs have transmission values of less than 50%, which must be compensated for with long integration times [4].

In this paper, a laparoscopic adaptation of a fast filter wheel multispectral imaging (MSI) system is demonstrated using the recently-developed SpectroCam platform (Ocean Optics, Inc., USA). This allows high-throughput imaging at multiple spectral bands at 30 Hz. Initial *in vivo* results obtained using the system in a porcine subject show changes in oxyhaemoglobin at the anastomosis site during arterio-venous fistula creation.

## MATERIALS AND METHODS

The laparoscopic system described in this paper is built on the SpectroCam platform (Fig. 1), which is a fast filter wheel multispectral imaging device capable of accommodating up to eight separate filters. The spectral properties of the current configuration are shown in Fig. 1 (a). Acquisition of five multispectral stacks, of eight high-resolution (1392×1040 pixels) images each, can be accomplished in 0.27 s. A 30° laparoscope (KARL STORZ GmbH & Co. KG, Germany) was attached to the system using a custom-made F-mount adapter. This also housed a 50 mm focal length imaging lens that fixed the working distance at approximately 3 cm.

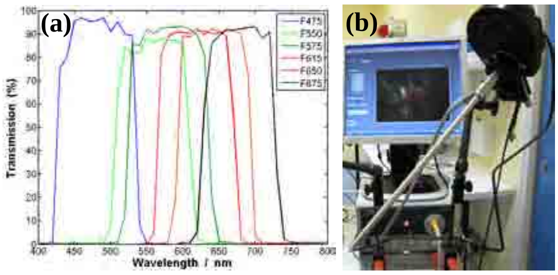



**Fig. 1** (a) Transmission characteristics of filters used, covering the visible range. (b) Photograph of MSI system with laparoscope and xenon white light source attached.

The system was used to monitor perfusion at the anastomosis site during the creation of an arterio-venous fistula in a 75 kg Yorkshire pig (conducted under a Home Office licence). The carotid artery and jugular vein were exposed through a 12 cm incision in the neck and then joined in an end-to-side anastomosis. In order to complete this, the artery was clamped upstream of the anastomosis site, flushed with saline and clamped again downstream. The jugular was clamped and divided in preparation. Static MSI images of the artery in its native state, and after clamping and flushing were acquired. A time series was then acquired as the clamps were released to monitor the perfusion change in the vein.

Perfusion and oxygenation changes were assessed by measuring the absorbance of light at each filter waveband. Reflected light was compared to the reflected light intensity from a reference standard at each waveband to calculate the experimental absorbance, $A$ (Eq. 1).

$$A = -\ln\left(I/I_R\right) \quad \textbf{(1)}$$

where $I$ is the measured intensity at a particular waveband and $I_R$ is the corresponding intensity detected from a reflectance standard. Assuming that absorption by haemoglobin is the dominant mechanism of light attenuation and that scattering losses are flat across the

wavelength range of interest then a simple model [6] can be used to predict *A*, as shown in Eq. 2.

$$A = [HbO_2]\varepsilon_{HbO_2} + [Hb]\varepsilon_{Hb} + \alpha \quad \textbf{(2)}$$

where $[HbO_2]$ and $[Hb]$ are fractional concentrations of oxy- and deoxy-haemoglobin respectively, $\varepsilon$ is the known extinction coefficient of haemoglobin (convolved with the spectrum of each filter in Fig. 1) and $\alpha$ is a constant term accounting for scattering losses. Experimentally measured absorbance spectra from each pixel location in the MSI stack were then fit by the three parameter model in Eq. 2 to calculate $[HbO_2]$ and $[Hb]$ at each point in the field-of-view.

## RESULTS

Figure 2 shows the dissected porcine aorta prior to anastomosis isolated with a sterile plastic sling. The colour image shown in Fig. 2 (a) was assembled from three of the wavebands centred on 475, 575 and 650 nm. In the oxyhaemoglobin colour map (Fig. 2 (b)), the fine network of the *vasa vasorum* is visible in the central portion of the image. Superficial droplets of blood resulting from the dissection obscure the extreme ends.

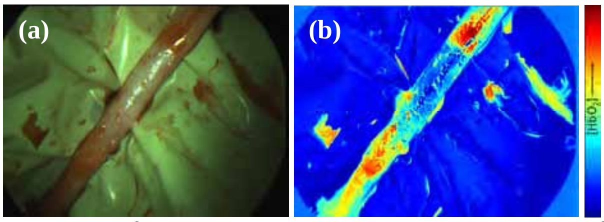



**Fig. 2** MSI of the porcine aorta. (a) Colour RGB. (b) Map of oxyhaemoglobin concentration.

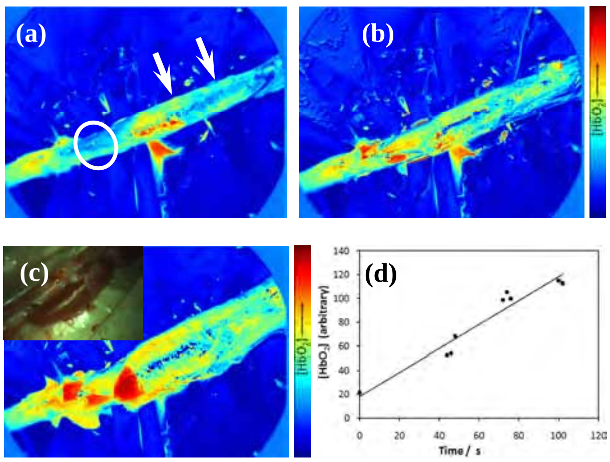



**Fig. 3** Arterio-venous anastomosis. The jugular vein is lying directly on top of the aorta (white arrows) and the location of the sutures is indicated (white circle). The change in oxyhaemoglobin concentration over time following the release of the upstream aortic clamp is shown at (a) t = 0 s (b) t = 72 s (c) t = 114 s. Inset: side view of the anastomosis. (d) $[HbO_2]$ time course for region of interest indicated in (a).

Following the clamping and flushing procedure described earlier, the jugular vein was joined to the aorta in an end-to-side anastomosis. Figure 3 (a) shows the site immediately prior to the release of the clamps with the vein lying directly on top of the artery.

The high-speed acquisition of the MIS system allows capture of the haemodynamics as highly oxygenated arterial blood begins to flow into the vein. The increase in oxyhaemoglobin is visible in Fig. 3 (d) along with the characteristic dilatation of the vein due to the increased arterial pressure.

## DISCUSSION

A new laparoscopic implementation of a multispectral imaging system has been presented. The fast filter wheel allows rapid detection of multispectral image stacks, minimising the influence of motion artefact. This was seen in the *in vivo* data in the capture of the venous dilatation. The transmission filters used have high light transmission (almost 100%), exceeding alternative systems such as LCTFs and resulting in reduced noise.

The results described here combine absorption by blood in the lumen of the vessel as well as the *vasa vasorum*. Future work will concentrate on further analysis of the origin of the absorption signal in depth and the separation of these contributors. This will allow a greater understanding of the mechanism of oxygen transport across the vessel walls. Possible applications include monitoring and predicting the success of arterio-venous fistulae and optimisation of anastomosis procedures.

## ACKNOWLEDGEMENTS

We gratefully acknowledge the assistance of Northwick Park Institute for Medical Research (NPIMR) for trial arrangements. Funding for this project was provided by ERC grant 242991 and NIHR i4i grant II3A110910038.

## REFERENCES

[1] Longest P, Kleinstreuer C. Particle-hemodynamics modeling of the distal end-to-side femoral bypass: effects of graft caliber and graft-end cut. Med Eng Phys. 2003;25:843-858

[2] Purcell C, Tennant M, McGeachie J. Neo-intimal hyperplasia in vascular grafts and its implications for autologous arterial grafting. Ann R Coll Surg Engl. 1997;79:164-168

[3] Lee T, Roy-Chaudhury P. Advances and new frontiers in the pathophysiology of venous neointimal hyperplasia and dialysis access stenosis. Adv Chronic Kidney Dis. 2009;16:329-338

[4] Clancy NT, Stoyanov D, James DRC, Di Marco A, Sauvage V, Clark J, Yang G-Z, Elson DS. Multispectral image alignment using a three channel endoscope *in vivo* during minimally invasive surgery. Biomed Opt Express. 2012;3:2567-2578

[5] Clancy NT, Sauvage V, Saso S, Stoyanov D, Corless DJ, Boyd M, Noakes DE, Yang G-Z, Ghaem-Maghami S, Smith JR, Elson DS. Registration and analysis of multispectral images acquired during uterine transplantation surgery. OSA Biomed. 2012;BSu3A.73

[6] Nighswander-Rempel SP, Shaw RA, Kupriyanov VV, Rendell J, Xiang B, Mantsch HH. Mapping tissue oxygenation in the beating heart with near-infrared spectroscopic imaging. Vib Spectrosc. 2003;32:85-94.

# Surgical Instrument Forces Exerted during Robot-Assisted Neurosurgery: A Cadaver Study

H.J. Marcus[1], K. Zareinia[2], L.S. Gan[2], F. Yang[2], S. Lama[2], G.-Z. Yang[1], G.R. Sutherland[2]

[1]*The Hamlyn Centre for Robotic Surgery, Imperial College London, UK*

[2]*Department of Clinical Neurosciences, University of Calgary, Canada*

## INTRODUCTION

The evolution of neurosurgery has been towards increasingly precise, delicate and safe surgical technique. Surgical robotics, which has the ability to eliminate tremor, reduce gain, and increase dexterity, therefore has the potential to greatly enhance surgical performance. A necessary prerequisite for the successful design and use of such robots is familiarity with the surgical instrument forces exerted by surgeons during neurosurgical procedures. The advent of surgical robotics has allowed, for the first time, the forces exerted during neurosurgical procedures to be routinely recorded [1]. The corollary is that expert performances can be analysed to determine the optimal force ranges utilised when performing robot-assisted neurosurgical procedures, allowing for the possibility of force limits to be set to improve surgical safety, and providing quantitative feedback to trainees to further their development.

The aim of the present study was to measure the surgical instrument force exerted during robot-assisted neurosurgery by performing a human cadaveric study.

## MATERIALS AND METHODS

An experimental rig was set up consisting of a platform for brain specimens, a Leica microscope (Leica Microsystems GmbH) to provide illumination and magnification, and a Quanser 6 Degrees-Of-Freedom (DOF) Telepresence System (Quanser Inc) for tissue manipulation and force measurements (See Fig 1). The robotic master-slave setup included a DENSO VP Series 6-Axis Articulated Robot and the control module (DENSO Robotics), a Gamma Multi-Axis ATI Force/Torque Sensor (ATI Industrial Automation) equipped with a 16-Bit Data Acquisition Board (National Instruments) to have accurate force measurements, and a High-Definition Haptic Device (HD2) with the capability of providing 6 DOF force/torque feedback to the operator; this configuration allowed for a continuous force feedback of up to 20.0N. The robot utilized an open-architecture interface with the QUARC 2.2 Denso Robot block-set, alongside Simulink®, Matlab® and Windows®. There were no force or position scaling involved and the ratio of force feedback from the robot sensors to the haptic controllers was set to 1:1. Calibration was independently verified using a Chatillon Digital Force Gauge with a capacity of 10N and accuracy of 0.01N.



**Fig. 1** Experimental rig consisting of a platform for brain specimens, a Leica microscope, and a Quanser 6 DOF Telepresence system

Two fresh brain specimens were utilized for the study. In each specimen, a neurosurgical trainee (HJM) was asked to coagulate the brain surface using bipolar electrocautery and then perform a sequence of simple procedures: (1) a Beaver Mini-Blade was used to incise the coagulated area, (2) the Mini-Blade was used to carry the incision to a length of approximately 30mm, and (3) a No 6 Penfield dissector was used to retract the brain approximately 5mm. These manoeuvres were carried out in the cerebrum (gyrus rectus, middle frontal gyrus, inferior temporal gyrus), cerebellum (hemispheres, vermis) and brainstem (midbrain, pons, medulla); and each was repeated twice on each side of the brain, unless it was too technically difficult to do so. In addition, the forces required to perform a corpus callosotomy and perforate the floor of the third ventricle were also measured.

The Beaver Mini-Blade and No 6 Penfield dissectors were also used to perform sharp and blunt dissection of the circle of Willis respectively. An observer carefully took note of iatrogenic injury to neurovascular structures during dissection. In cases of uncertainty, we recorded injury as having occurred.

Force vector data was generated each 0.2ms (5 KHz). A Matlab® program was developed and used to extract data each 10ms and record in an Excel spreadsheet, and

force vectors were summated. Statistical software (SPSS 20.0.0) was then used to calculate the arithmetic mean, standard deviation and maximal forces during individual procedures. The paired T-test was used to compare the surgical instrument forces exerted in each brain specimen, and on the left- and right-side of the brain. The ANOVA test was used to compare the forces exerted when performing different procedures, and between different brain regions; if significance was demonstrated post-hoc analysis was performed using the Student Newman-Keuls test. The unpaired T-test was used to compare the forces exerted when performing sharp and blunt dissection, and the manoeuvres that resulted in iatrogenic injury against those that did not. The threshold for significance was set at 5%.

## RESULTS

In all, there was no significant difference in forces exerted between the two brain specimens, and between the left- and right sides of the brains. The mean force exerted when performing stab incisions (0.01N) was significantly less than the forces required to carry the incisions (0.09N) or retract brain (0.10N). The mean force exerted when manipulating the brainstem (0.09N) was significantly greater than that required in the cerebellum (0.05N) or cerebrum (0.05N).

The mean, standard deviation, and maximal forces exerted when performing sharp and blunt arachnoid dissection around the Circle of Willis are summarized in Table 1; manoeuvres are stratified according to whether they did or didn’t result in iatrogenic injury.

**Table 1** The mean, standard deviation and maximum forces exerted when performing sharp and blunt dissection of the Circle of Willis

| | | No injury (n=34) | Injury (n=6) |
|---|---|---|---|
| Sharp Arachnoid Dissection (n=28) | Mean ± SD (N) | 0.07 ± 0.08 | 0.28 ± 0.08 |
| | Max (N) | 1.33 | 2.50 |
| Blunt Arachnoid Dissection (n=12) | Mean ± SD (N) | 0.15 ± 0.11 | 0.68 ± 0.32 |
| | Max (N) | 2.04 | 4.28 |

The mean force exerted during blunt dissection (0.33N) and sharp dissection (0.09N) was significantly different. When performing blunt dissection the mean force during manoeuvres in which iatrogenic injury occurred (0.68N) and those in which it did not (0.15N) was significantly different. When performing sharp dissection the mean force during manoeuvres in which iatrogenic injury occurred (0.28N) and those in which it did not (0.07N) was also significantly different.

## DISCUSSION

In this study we have successfully determined the surgical instrument forces exerted during a number of robot-assisted procedures on fresh cadaver brains. The measured forces varied significantly depending on the region of the brain and the manoeuvre performed. Moreover, blunt arachnoid dissection with a Penfield No 6 dissector was associated with greater force exertion, and a higher risk of iatrogenic injury, than sharp dissection with a Beaver Mini-Blade.

Existing literature on the forces exerted during neurosurgical procedures is sparse. Howard et al measured the penetration forces on 2.5mm spheres and the drag forces on a 3mm ventricular catheter advanced 20-30mm deep into the brain tissue of patients undergoing temporal lobectomy, and reported forces of 0.08N and 0.03N respectively [2]. These findings are comparable to our own, supporting the notion that the forces necessary to manipulate brain tissue are low.

Although the present study measured forces carefully using an externally calibrated system, it has several limitations. First, the cadaver brains utilised undoubtedly had different tissue properties to living brain tissue, though fresh cadaver brains were used to ameliorate this. Second, the forces exerted during the simple procedures performed may not reflect those required during the complex technical manoeuvres of actual neurosurgical operations. Third, the surgical forces exerted during microsurgery are known to be greater in novices than experts [3], and the forces applied by the neurosurgical trainee in this study are therefore almost certainly higher than if a consultant had performed it.

In future studies we plan to address the aforementioned shortcomings by analysing the data generated by the in-vivo use of neuroArm, an MRI-compatible robot incorporating haptic feedback. In contrast to the present cadaver study, such data will be obtained in real patients, undergoing complex surgery, and performed by experts.

## REFERENCES


[1] Sutherland GR, Wolfsberger S, Lama S and Zareinia K. The evolution of neuroArm. Neurosurgery. 2013; 77 Suppl 1:27-32.

[2] Howard MA, Abkes BA, Ollendieck MC, Noh MD, Ritter RC and Gillies GT. Measurement of the force required to move a neurosurgical probe through in vivo human brain tissue. IEEE Trans Biomed Eng. 1999; 46(7): 891-4.

[2] Harada K, Minakawa Y, Baek Y, Kozuka Y, Sora S, Morita A, Sugita N and Mitsuishi M. Microsurgical Skill Assessment: Toward Skill-Based Surgical Robotic Control. Conf Proc IEEE Eng Med Biol Soc. 2011; 2011: 6700-3.

# New Solution for Solid-Organ Resection Based on a Compact MIS Robot

J.M. Li[1], N.X. Zhou[2], L.A. Zhang[1], Y. Chen[1], S.X. Wang[1]

[1]*Key Lab for Mechanism Theory and Equipment Design of Ministry of Education, Tianjin University, China*

[2]*Hepatobiliary Gastroenterology Institute, PLA 2nd Artillery General Hospital, Beijing, China*

*shuxinw@tju.edu.cn*

## INTRODUCTION

Solid-Organ-Disease is one of the most common diseases in China. Due to the excessive intraoperative blood loss, solid organ surgeries are usually complicated and time consuming. To assist this kind of surgery, a compact minimally invasive surgery (MIS) robot has been developed. Several magnetic sensors, manipulated by surgeon, are used to collect the operation information, which is used to control the miniaturized slave arms. This feature makes the robot have little requirement on the operation room. To further improve the operation effectiveness, a coagulation device that can transport energy from the energy generator to the inner tissue of a solid organ through tiny incisions on patient's body wall was developed. The proposed technique was verified by an in-vitro experiment.

**Related work**. For solid organ resection, a specially designed tool, developed by AngioDynamics, has been used in open surgeries and good results are obtained [1]. With the rapid development of MIS, a laparoscopic bipolar resection device has also been developed by the company to reduce the operative trauma [2]. However, the dexterity is limited. The advanced robotic technology in MIS has already leaded a momentous change in surgery [3]. In this situation, we expected to make the solid organ surgeries easier by integrating advanced robot technology and existing technology as a whole.  And a prototype has been developed in the lab.

## MATERIALS AND METHODS

If the tissues on a solid organ are coagulated first, then little bleeding would occur when operates on the coagulated area. Energies, such as electric energy, microwave, radio frequency, and ultrasound, have been widely used in operations to coagulate tissues to reduce blood loss. This effective method is adopted to develop the robot based dexterous coagulation device.

### 1) Brief Introduction about the MIS Robot

The newly developed MIS robot system is shown in Fig. 1. The slave robot, with small size and light weight, consists of three arms, each of which can pivot around the incision set on patient's body in three directions. The collapsible structure makes the robot easy to transport. Several 3D Guidance trakSTAR sensors (Ascension Technology Corporation) embedded in different handles are used to collect the operation information of the surgeon's hands. The no-mechanical-structure design of the master system further reduces the space that occupied by the whole robot.




**Fig. 1** The newly developed MIS robot.

### 2) Instrument Design

The instrument for solid organ surgery under minimal-invasive condition is shown in Fig. 2. The diameter of the shaft is 8mm. The pretensioned steel wires are used to transmit motion/force from the driving units to the end-effector. The needle-like end-effector is designed to minimize the blood loss during the piercing process and to decrease the adherence of the solidified tissues. Four needles, two connected to positive terminal and the others connected to negative terminal of the energy generator, are used to enhance the coagulation effect.

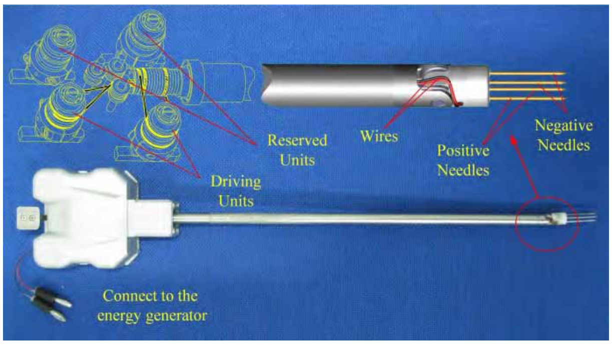



**Fig. 2** Coagulation tool for robot-assisted solid organ surgery.

The 2-DoF instrument combined with the 3-DoF slave arm can make the needles be pierced into tissues in any directions. The instruments can be quickly attached or detached from a robotic arm through the surgical

adaptor. This function is essential as the instrument has to be cleaned when too many scabs are adhesive to the needles.

**3) Operation Method**

The operation method of the proposed bloodless cut device is shown in Fig. 3. Surgeon need to distinguish the healthy tissues and the diseased ones and determine the cutting line based on diagnose results. Then the surgeon manipulates the handles to control the slave arms to position and orientate the needles. After that, the surgeon will control the needles to insert into the organ along the needles' direction carefully. When needles reach the desired depth, a signal is given to the energy generator to release energies. At the same time, needles are controlled to do automatic reciprocating motions, which can enhance the coagulation effect, as well as decrease the adherent of solidified tissues. Repeat the above process until all the tissues around the cutting line are solidified. Then, assistant can install a scalpel for the main surgeon to separate the diseased tissues from the organ. Sometimes, due to the limited length of the needles, one or more coagulation-separation processes are needed to complete the separation.

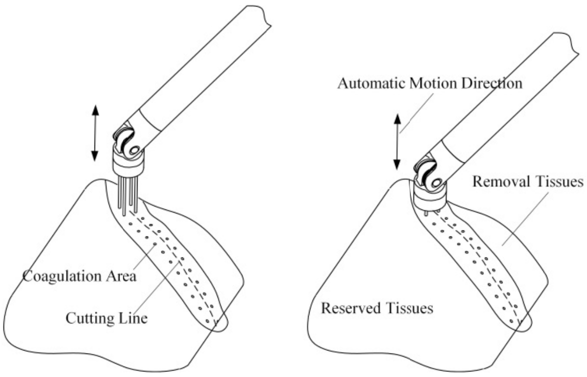



**Fig. 3** The operation method of the proposed method.

**4) Experiment**

An in-vitro experiment has been carried out. The experiment setting is shown in Fig.4. A fresh pig's liver harvested within 30 minutes was used in the experiment. Two slave robot arms, one for manipulating a forceps and the other for manipulating the coagulation device, are controlled by the operator to do 'operations' on the liver. Scene of the operation site was provided by the endoscope held by the third arm. An electrosurgical generator was applied in this experiment.

## RESULTS

It took less than 8 minutes to coagulate the tissues along the line marked on the liver. The length of the coagulation area is 13cm. Figure 5(a) shows the whole coagulation procedure. The coagulation effect was checked after dividing the liver into two parts along the cutting line, as shown in Fig. 5(b). It's clear that the section was separate into coagulated area and normal area. For the coagulated area, little bleeding may occur when doing operations in a real solid-organ surgery. For the normal area, another coagulation process is needed after the coagulated area opened.

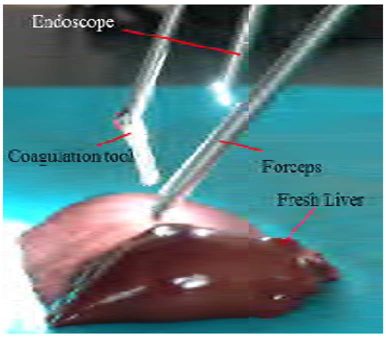



**Fig. 4** The in-vitro experiment setting.

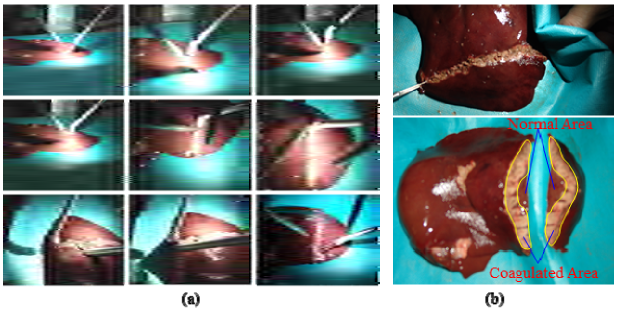



**Fig. 5** The coagulation procedure and the experiment results.

## DISCUSSION

To improve the effectiveness of the solid organ surgeries, this work transplants the routine technology in open surgery to MIS without losing the operation dexterity by means of robotic technology. A MIS robot based instrument that can transport energy to organ to coagulate tissues is proposed. The effectiveness of the proposed device was verified by an in vitro experiment. It can be concluded that the technique has great potential in clinical use. Animal experiments, however, are needed to carry out for further development.

## REFERENCES

[1] S. Andonian, A. Adebayo, Z. Okeke, B. Lee. Habib laparoscopic bipolar radiofrequency device: a novel way of creating an avascular resection margin in laparoscopic partial nephrectomy. J laparoendosc Adv Surg Tech A. 2008 Dec; 18(6): 853-856.

[2] AngioDynamics [homepage on the Internet]. Habib® 4X Laparoscopic Bipolar Resection Device [cited 2011 Oct 12]. Available from: http://www.angiodynamics.com/products/habib-4x-laparoscopic.

[3] J. Dai. Editorial: Surgical robotics and its development and progress, Special Issue on Surgical Robotics, System Development, Application Study and Performance Analysis. Robotica 2010; 28: 161.

This work is supported by the Major Program of NSFC under grant No. 51290293.

# A Fault Analysis Procedure for Surgical Robotic Systems

M. Capiluppi[2], L. Schreiter[1], P.Fiorini[2], J. Raczkowsky[1], H. Woern[1]

*[1]Karlsruhe Institute of Technology, 76131 Karlsruhe, Germany*

*{luzie.schreiter, joerg.raczkowsky, heinz.woern}@kit.edu*

*[2]Università di Verona, 37134 Verona, Italy*

*{marta.capiluppi, paolo.fiorini}@univr.it*

## INTRODUCTION

Surgical robotic systems are safety critical system, i.e. systems where errors might lead to the endangerment of human life, to substantial economic loss, or to extensive environment danger [1]. Nevertheless, currently, no safety standards for robotic surgical systems exist, but other standards for robotics are established, for instance the ISO 10218:2011 represents safety requirements for industrial robots, ISO 13485:2003 standard specifies requirements for a quality management system for medical devices and EN ISO 14971:2012 represents the application of risk management system for medical devices. Indeed, defining safety for surgical robots is not trivial, since the concept of safety in surgery is strictly operation and patient dependent [2] and involves both the aspects of safety for human-interactive robots [3] and surgical aspects [4]. Moreover, safety depends in a first instance on reliability, i.e. a system has to counteract to failures keeping its behavior inside a region of performance that guarantees the reliability of the actions performed. Failures are caused by faults, that are deviations of the system structure or parameters from the nominal situation [5], [6]. We aim at achieving a fault analysis which consists in the detection of potentially dangerous situations, potential failures and the definition of hazard risks during the whole life cycle of a surgical robotic system. This serves as a basis for fault detection and safety verification procedures.

## FAULT AND SAFETY ANALYSIS

We introduce a procedure for fault analysis in surgical robotic systems and determine some strategies for further verification of safety in such systems. When dealing with faults in a surgical context, it is necessary to distinguish between human errors [7] and technical faults. Usually human errors lead to severe damage to people and tools, with liability and legal implications. For these reasons, we are not taking them into account in a first instance and focus on the technical faults. Our objective is to obtain a system that will be able to reconfigure itself after a fault occurrence respecting some safety constraints: no risks for the human beings in the operating room (including medical staff and patient) and correct achievement of the surgical task.

To this end, we have to point out that a distinction exists between the fault analysis and the safety evaluation. Performing a fault analysis is a first step to verify if the system can be designed in a fault tolerant way, i.e. if the system will be able to achieve the desired task even if a fault occurs. Whereas the safety evaluation is aimed at avoiding that the system (whether reconfigured after a fault or not) still remains in a safe region of performances, given in the specification design phase (see [8] and references therein). Our procedure first assures fault tolerance, by analysis of the possible faults occurring in a surgical robotic system and their effects propagation. Then we will perform an evaluation of the safety requirements, through specifications obtained from the ontological description of the surgical task. The state of the art in fault analysis includes two main methods: Fault Tree Analysis (FTA) and Failure Mode and Effects Analysis (FMEA). FTA is used on the overall system to check the fault propagation in the different functionalities of the system. The fault tree represents the connections between the different failure modes, where the leaves of the tree are the faults on components. Generally, the complementary version of the fault tree is a functionality tree and each basic functionality can be associated to a component of the system [9]. FMEA is, instead, an approach that starts from the components and is not able to show the fault propagation, but it is used to assess the risk of each possible failure [10]. We will use the FTA to determine what functionalities of the overall system will be affected by component faults. This first step is needed to verify that the system is able to achieve its goal even after the occurrence of a fault. If not, then it is necessary to modify the overall system and perform a new FTA. Next step consists in assessing the safety of the surgical robotic system. To this end, safety specifications are designed, based on the ontological description of the surgical task and on technical and medical knowledge about the operation. Then a FMEA is performed, taking into account that a surgical operation can be divided into three phases: pre-operative, intra-operative, post-operative. Each phase has its own specifications in terms of safety and FMEA will be performed in each phase, with associated risks of failure. To respect safety requirements, the final step consists in making the system able to counteract to

This research has been supported by the coordination action EuroSurge (Grant no. 288233) funded by the European Commission in the 7th EC framework program.

failures and perform a formal verification of the overall system.
Here we present the first part of the procedure, associated to FTA, for a simple case study introduced in [11].

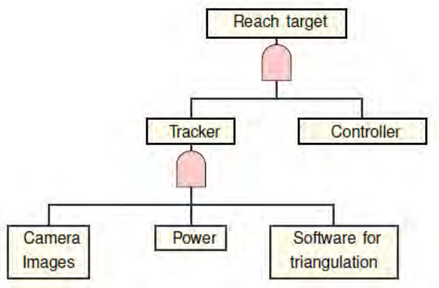



**Fig. 1** Functionality tree of the system with one tracker

Our system is composed by a manipulator with a puncturing tool moving from point A (stand-by position) to point B (located on the patient skin) and controlled in position. The end effector position is monitored by a tracker with 10 cameras that follows a marker on the end effector. The estimated position is given by triangulation and sent to the controller. The functional tree of the system is reported in Fig. 1. The target point is point B. The tracker functionality consists in having, at each sample time, an estimate of the real position of the end effector.

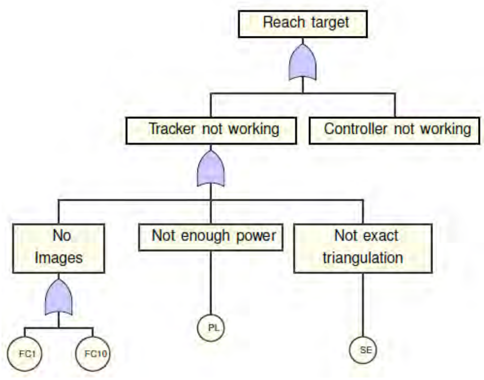



**Fig. 2** Fault tree corresponding to the functionality tree in fig. 1. (FC=Faulty Camera, PL= Power loss, SE= Software error)

The corresponding fault tree is present in Fig. 2. We focus on faults on the tracker. From the fault tree in fig. 2 it is straightforward that, if the tracker is not working (we lose the tracker functionality), the system is not able to reach the target anymore, so the system is not fault tolerant. To achieve fault tolerance it is necessary to add hardware redundancy, for example using a backup tracker, as shown by the functionality tree in Fig. 3. Since the backup tracker might have different properties from the main one, a safety specification might be that the system adapt to the backup tracker when this is activated, for example slowing down if the backup tracker has a bigger sample time, in order to reach safely the patient skin. Of course other safety specification might be verified. The safety evaluation from ontology and FMEA are work in progress.

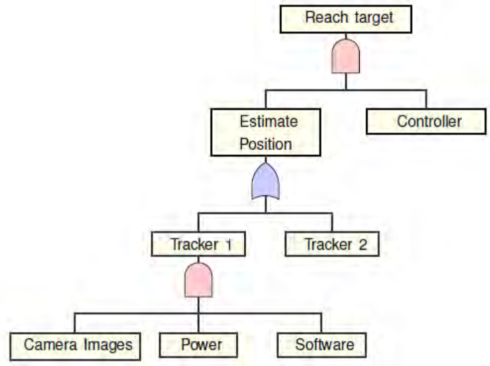



**Fig. 3** Functionality tree of the system with two trackers

## REFERENCES


[1] J. C. Knight, "Safety critical systems: challenges and directions," in Software Engineering, 2002. ICSE 2002. Proceedings of the 24rd International Conference on, 2002, pp. 547-550.

[2] P. Kazanzides, G. Fichtinger, G. D. Hager, A. M. Okamura, L. L. Whitcomb, and R. H. Taylor, "Surgical and interventional robotics-core concepts, technology, and design " Robotics & Automation Magazine, IEEE, vol. 15, pp. 122-130, 2008.

[3] Q. A. Do Hoang, J. Guiochet, D. Powell, and M. Kaaniche, "Human-robot interactions: model-based risk analysis and safety case construction," Embedded Real Time Software and Systems (ERTS), 2012.

[4] U. Rembold and C. R. Burghart, "Surgical robotics: An introduction," Journal of Intelligent & Robotic Systems, vol. 30, pp. 1-28, 2001.

[5] M. Blanke, M. Kinnaert, and M. S. a. J. Lunze., Diagnosis and fault-tolerant control. Springer-Verlag, 2003.

[6] D. P. Siewiorek and R. S. Swarz, Reliable computer systems: design and evaluation vol. 3: AK Peters Massachusetts, 1998.

[7] T. B. Sheridan and C. D. Wickens, "A model for types and levels of human interaction with automation," Systems, Man and Cybernetics, Part A: Systems and Humans, IEEE Transactions on, vol. 30, 2000.

[8] M. Capiluppi, "Fault Tolerance in Large Scale Systems: hybrid and distributed approaches," Ph. D Thesis, 2007.

[9] E. J. Henley and H. Kumamoto, Reliability engineering and risk assessment: Prentice-Hall, 1981.

[10] D. H. Stamatis, Failure Mode Effect Analysis: Fmea from Theory to Execution: Asq Press, 2003.

[11] M. Capiluppi, L. Schreiter, P. Fiorini, J. Raczkowsky, and H. Woern, "Modeling and Verification of a Robotic Surgical System using Hybrid Input/Output Automata," acctepted to European Control Conference 2013.

# Real-time Visual Stiffness Feedback for Soft Tissue Palpation in a Telemanipulation Environment

M. Li[1], J. Konstantinova[1], V. Aminzadeh[1], T. Nanayakkara[1], L. D. Seneviratne[1], P. Dasgupta[2], K. Althoefer[1]

[1]Centre for Robotics Research, King's College of London,

[2]MRC Centre for Transplantation, DTIMB and NIHR BRC, King's College London

min.m.li@kcl.ac.uk

## INTRODUCTION

Robot-assisted minimally invasive surgery (RMIS) has been widely applied in recent years [1]. It has many benefits over traditional minimally invasive surgery (MIS), such as an improvement of dexterity and enhanced 3D vision. However, the sense of touch is lost - this is considered as a significant drawback of RMIS. In order to identify the tumour location and its boundaries in cancer excision, real-time tissue probing methods using force-based sensing or tactile-based sensing have been proposed. The perception of direct force or tactile feedback (pressure information distribution) is intuitive. However, the application is limited by the relatively high cost and control complexity of tactile actuators. Alternatively, low-cost visual cues can be used to compensate for the lack of haptic sensation. Graphical overlays showing the material property distribution have been presented [2], [3]. However, the graphical overlay of real-time stiffness data on camera images may affect the clarity and quality of the original camera image. Further, it is time consuming to investigate a large tissue area using uniaxial indenting based on separate-point probing. Continuous scanning and indentation depth measurement would improve the efficiency and the rate of stiffness estimation for larger areas [4]. In this paper, we propose a visual stiffness feedback method for soft tissue palpation in RMIS, operating in real time. The novel feature of our method is a dynamically updated soft tissue stiffness map that is generated from continuous rolling indentation and is overlaid on a separate virtual soft tissue surface. We demonstrate the feasibility of the interface in a master-slave tele-operation configuration.

## MATERIALS AND METHODS

The real-time visual stiffness feedback method in a master-slave teleoperation configuration consists of the following main components: telemanipulators (a master robot and a slave robot), a vision system and a visual stiffness display. Fig. 1 shows the frame of the system design. Real-time camera images of the palpation site are provided. Sensor measurements including force and position are transmitted from the slave robot side to the master side to enable the virtual soft tissue surface reconstruction and visual stiffness feedback.

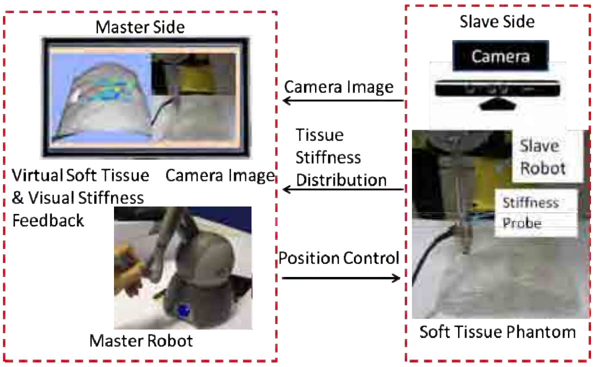



**Fig. 1** The frame diagram of real-time visual stiffness feedback for soft tissue palpation in a telemanipulation environment

The virtual soft tissue surface is displayed on a graphical interface using a mesh of triangles, whose vertex positions are acquired from a scan of the tissue contour. The indenter is moved manually across the tissue in such a way that it is just in contact with the tissue surface during the contour scan with the help of force feedback. Tissue deformation of the virtual soft tissue during palpation is shown in real time by using a geometrical deformable soft tissue model considering the influence of the indenter diameter based on predefined finite element modelling; the details of this model are presented in [5]. A real-time soft tissue stiffness estimation method is used. If a small indentation is applied and using a rigid spherical indenter, the elastic modulus of tissue can is

$$E = \frac{3f(1+\nu)}{8d_{in}\sqrt{rd_{in}}},$$

where $E$ is the elastic modulus, $f$ is the tissue reaction force normal to tissue surface, $r$ is the radius of the spherical indenter, $d_{in}$ is the indentation depth and $\nu$ is the Poisson ratio. Since we assume soft tissue incompressible, $\nu$ is set to 0.5 here. The indentation depth is calculated using the distance between the indenter position and the nearest triangle planar of the original contour. Using this indentation depth calculation method, not only the indentation depth on a planar surface can be acquired, but the indentation depth can also be calculated on uneven surfaces. In this real-time soft tissue stiffness estimation method, the acquired indentation depth and reacting force are the two inputs. The calculated elastic modulus is the output. Next, a real-time visualization of stiffness distribution is created using estimated stiffness data. The estimated elastic modulus, $E$, is stored jointly with its palpated location.

Then, this value is converted to an RGB value by interpolating between the colour representatives of current minimum and maximum stiffness values. Blue colour (R=0, G=0, B=255) represents the minimum stiffness and red colour (R=255, G=0, B=0) represents the maximum stiffness. These pairs of RGB values and palpated locations are used to update the displayed stiffness map dynamically.

To demonstrate the feasibility of the feedback method, an experiment was conducted. As shown in Fig. 2, a PHANToM Omni (SensAble Technologies Inc., MA, USA) and a FANUC robot arm (FANUC Corporation, Japan) were used as the master and slave robot, respectively. A Microsoft Kinect camera was used to obtain a live camera image. The master robot, the camera image, and the visual stiffness display were located at the user's side for remote manipulation. On the master side, an operator held the stylus of the PHANToM Omni to command the slave robot to palpate the silicone phantom organ. By looking at the live image and visual stiffness display on a soft tissue model generated from a tissue contour scan, the operator was able to acquire the stiffness distribution. The palpation trial was conducted continuously using the rolling indentation probe [4].

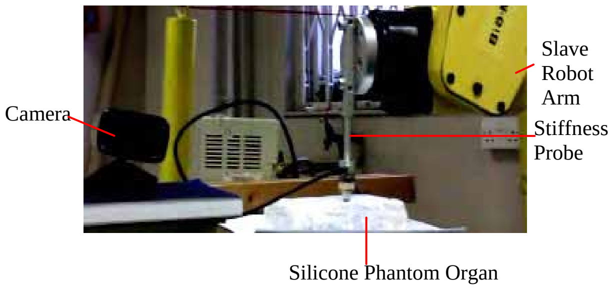



**Fig. 2** Experimental configuration of slave side hardware, including a slave robot arm, a silicone phantom organ and a camera

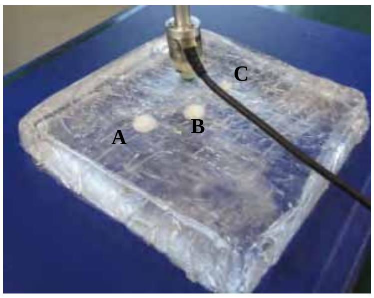



**Fig. 3** The silicone phantom organ with three embedded sphere nodules (A, B, C); the diameters of nodules are 10 mm, 8 mm, and 6 mm. the depths from sphere top to silicone surface are all 6 mm.

## RESULTS

Fig. 4 shows one picture taken during a palpation trial. A virtual soft tissue with a dynamically updated stiffness map was provided on a graphical interface at the master side. Three hard nodules were found as indicated by the coloured stiffness map, which matched the locations of the three embedded nodules in the silicone phantom. The stiffness levels of those three positions also matched the nodule sizes (A>B>C). The stiffness map helps the operator to have an informed view of the stiffness distribution.

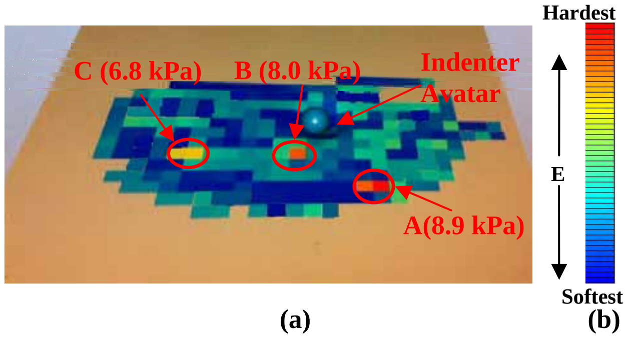



**Fig. 4** One picture (a) taken during palpation over the surface of the silicone phantom tissue. Subfigure (b) is the stiffness-colour mapping. In (a), the locations of the three embedded nodules (A, B, C) are displayed on the stiffness map.

## DISCUSSION

According to the experimental evaluation using a silicone phantom with embedded artificial tumours, the proposed real-time visual stiffness feedback method for soft tissue palpation provides a possible solution for intra-operative tumour localization in RMIS. Future work will be focussing on palpation trials on soft tissue with uneven surfaces. The Kinect camera will be used to obtain point cloud data and reconstruct the tissue surface. The method has the potential to be translated to prostatectomy, breast surgery and gynaecology to help surgeons to archive a more accurate detection of tumours.

## ACKNOLEDGMENT

The research was funded/supported by the National Institute for Health Research (NIHR) Biomedical Research Centre based at Guy's and St Thomas' NHS Foundation Trust and King's College London. The views expressed are those of the author(s) and not necessarily those of the NHS, the NIHR or the Department of Health.

## REFERENCES

[1] T. Wilson and R. Torrey, "Open versus robotic-assisted radical prostatectomy: which is better?," Current Opinion in Urology, vol. 21, no. 3, pp. 200–205, 2011.
[2] A. P. Miller, W. J. Peine, J. S. Son, and M. D. Z. T. Hammoud, "Tactile imaging system for localizing Lung nodules during video assisted thoracoscopic surgery," Proceedings 2007 IEEE International Conference on Robotics and Automation, pp. 2996–3001, Apr. 2007.
[3] T. Yamamoto, A. M. Okamura, and T. N. Judkins, "Augmented reality and haptic interfaces for robot-assisted surgery," no. November 2011, pp. 45–56, 2012.
[4] H. Liu, J. Li, X. Song, L. D. Seneviratne, and K. Althoefer, "Rolling Indentation Probe for Tissue Abnormality Identification During Minimally Invasive Surgery," IEEE Transactions on Robotics, vol. 27, no. 3, pp. 450–460, 2011.
[5] M. Li, L. D. Seneviratne, P. Dasgupta, and K. A. Althoefer, "Virtual palpation system," in International Conference on Intelligent Robots and Systems workshop "Learning and Interaction in Haptic Robots", 2012.

# Detection and Identification of Multispectral Structured Light Patterns for Minimally Invasive Surgery

J. Lin[1], N.T. Clancy[1,2], G. Boissonnat[3], D.S. Elson[1,2]

[1]The Hamlyn Centre for Robotic Surgery, Imperial College London, UK

[2]Department of Surgery and Cancer, Imperial College London, UK

[3]Department of Bioengineering, Imperial College London, UK

j.lin12@imperial.ac.uk

## INTRODUCTION

The detection of tissue surfaces during endoscopic surgery has the potential to allow patient-specific pre-operative images to be used for surgical guidance. The most commonly attempted methods include stereoscopy, SLAM, shape from shading/motion, time-of-flight, and structured lighting (SL) [1-5]. Of these, SL and time-of-flight have the advantage of not being dependent on tissue texture. Endoscopic implementations of SL are difficult due to requirements for high light levels and unambiguous feature detection, although there have been some recent reports in the literature [6-8].

In previous work, we have demonstrated an SL system that uses a supercontinuum fibre laser together with an optical fibre probe (diameter 1.9 mm) to create an array of spots that are each at a unique wavelength (~5 nm bandwidth) [6]. This approach has many advantages, including the high brightness of the pattern, detection by a standard endoscope camera, low sensitivity to tissue pigmentation, small diameter and flexibility. A beam chopper switches rapidly between SL and white light modes, providing video rate display for the surgeons [7]. A central part of the process to reconstruct the tissue surface using this system is the identification of the coloured spots. Previously an RGB-to-wavelength conversion was used to estimate the spot centres and identify them. In this paper we present a faster, more accurate and robust method to detect centroids as well as boundaries of different projected multispectral laser spots and to achieve the unique identification of each. The other stages in the imaging procedure (calibration, triangulation and reconstruction) as well as a description of the hardware used are described in previous publications [6, 7].

## MATERIALS AND METHODS

A schematic of the algorithm is displayed in Fig. 1. The RGB images collected by the camera are firstly converted into images in HSV space to separate intensity and hue information for the following steps. Thresholding is used to suppress background noise and generate a convex hull that encloses the spot pattern, and then a binary image created by a lower threshold is combined with the convex hull, generating a mask representing the region of interest (ROI). The intensity and hue maps are filtered by Wiener and Gaussian filters, to suppress noise and enhance the intensity peaks of the spot centres respectively, followed by histogram equalization. Regional maxima of the intensity map are then calculated, using the extended H-maxima transform, which correspond to the bright central areas of each spot. These are treated as initial seeds for the region growing procedure. The criteria for this are established using ranges defined by the mean and variance of all pixel intensity and hue values in each seed. The grown result is evaluated by average spot size and similarity of hue value in order to merge small spots that are in contact. Spots identified as too small or large are improved by further region growing using ‘tighter’ or ‘looser’ growth criteria. Finally, morphological transforms such as image opening and closing are used to refine the shapes and boundaries of grown spots.

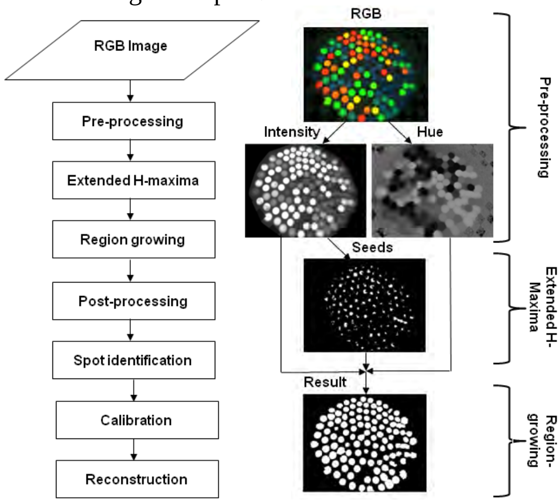



**Fig. 1** (a) General 3D reconstruction procedure. (b) Example of spot detection using region growing.

After detection each spot is identified using an algorithm that incorporates both colour and spatial information in the pattern. A Delaunay triangulation is performed on a reference image where all spots have been detected. The normalised RGB values of the vertices of each triangle are then recorded. For a particular test image a spot of interest will be a node for several surrounding triangles. To identify each spot in other images the spot with the highest number of matching neighbours is chosen. This procedure is done by matching triangles based on the similarity of their interior angles (within a defined threshold) and the Euclidian distance between their nodes’ RGB values.

## RESULTS

Seven SL images from a calibration object and *ex vivo* porcine tissue (three from a white plane, two from liver, one from kidney and one from heart) were tested using the spot detection method. The result is compared with manually-identified spots, evaluated by visual inspection and quantified in terms of sensitivity and precision. The results are shown in Fig. 2 and Table 1.

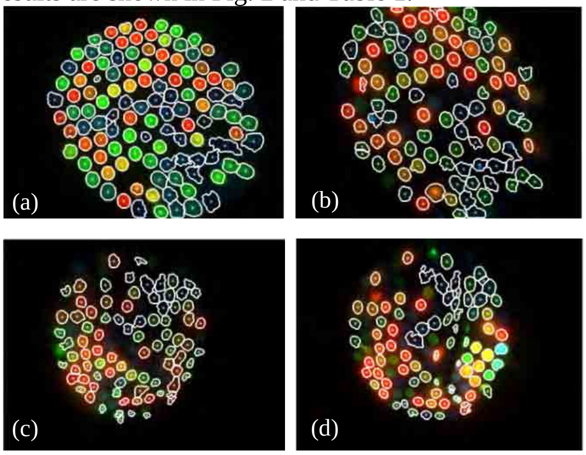



**Fig. 2** Images of detected centroids and spot boundaries overlaid on RGB images of calibration and porcine tissue surfaces. (a) White plane. (b) Liver. (c) Heart. (d) Kidney.

**Table 1** Spot detection results for seven images. Sensitivity indicates the fraction of spots correctly detected; Precision is the fraction of correct detections in all detected spots.

| Sensitivity | Precision | Surface |
|---|---|---|
| 0.9417 | 0.9912 | White Plane image 1 |
| 0.9667 | 1.0000 | White Plane image 2 |
| 0.9508 | 0.9831 | White Plane image 3 |
| 0.7672 | 0.9674 | Liver image 1 |
| 0.7500 | 0.9355 | Liver image 2 |
| 0.7297 | 0.9529 | Heart |
| 0.6102 | 0.8675 | Kidney |

The results shown in the above table indicate high sensitivity and precision for images of the white plane. However, sensitivity is lower for soft tissue. This is mainly caused by strong absorption at the blue end of the spectrum due to haemoglobin. Given that global parameters are adopted in the local maxima searching procedure, some blue spots are missing. For darker spots whose intensities are similar to those of the background, boundaries detected by region growing are also inaccurate. Furthermore, large distortions on some parts of tissue surface also result in severe spot shape deformation, introducing more detection error.

Figure 3 shows the results of the spot identification algorithm between test and reference images in a calibration dataset. The performance was evaluated by analysing the number of correctly identified spots (true positives, TP) and incorrectly detected spots (false positives, FP). The probability that a spot was labelled was calculated using $P_L=[TP+FP]/TP$ along with the probability that each labelled spot was labelled correctly ($P_{C/L}=TP/[TP+FP]$). High $P_L$ (89.8%) and $P_{C/L}$ (98.6%) values were obtained. Robustness was tested by removing spots at random and repeating the matching. As spots are removed $P_L$ decreases but $P_{C/L}$ remains stable close to 100%.

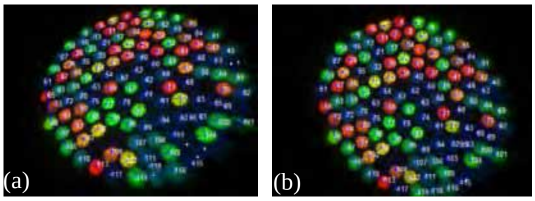



**Fig. 3** Spot identification. (a) Reference showing numbered spots and triangulation. (b) Test image with matched triangles.

## DISCUSSION

Initial results from a multispectral spot detection algorithm have been presented, indicating ability to detect spot boundaries on tissue. Identification using colour and spatial information has been demonstrated that is robust to occlusions and low brightness. The results show that the system could potentially be used in lesion detection and to aid rigid and flexible endoscopy if adapted to ‘front-viewing’ systems.

Future work will involve evaluation of the robustness of these algorithms in the presence of varying tissue type and morphology. Besides, this boundary detection method introduces a possibility for denser 3D reconstruction and adaption with near infrared cameras. Hardware modifications are also planned to alter the distribution of wavelengths of the spots and record high dynamic range images using different camera exposure times. Real-time computation would also allow a rapid reconstruction of the surface.

## ACKNOWLEDGEMENTS

Funding for this research is provided by ERC grant 242991. We gratefully acknowledge the help of Dr Lena Maier-Hein and the German Cancer Research Centre (DKFZ) in the acquisition of these images.

## REFERENCES

[1] Stoyanov D, Visentini-Scarzanella M, Pratt P, Yang GZ. Real-time stereo reconstruction in robotically assisted minimally invasive surgery. Med Image Comput Comput Assist Interv. 2010;13(Pt. 1):275-282.

[2] Mountney P, Yang GZ. Motion compensated SLAM for image guided surgery. Med Image Comput Comput Assist Interv. 2010;13(Pt. 2):496-504.

[3] Malti A, Bartoli A, Collins T. Template-based conformal shape-from-motion-and-shading for laparoscopy. IPCAI. 2012;7330:1-10.

[4] Penne J, Holler K, Sturmer M, Schrauder T, Schneider A, Engelbrecht R, Feussner H, Schmauss B, Hornegger J. Time-of-flight 3-d endoscopy. Med Image Comput Comput Assist Interv. 2009;12(Pt. 1):467-474.

[5] Wu TT, Qu JY. Optical imaging for medical diagnosis based on active stereo vision and motion tracking. Opt Express. 2007;15(16):10421-10426.

[6] Clancy NT, Stoyanov D, Maier-Hein L, Groch A, Yang GZ, Elson DS. Spectrally encoded fibre-based structured lighting probe for intraoperative 3D imaging. Biomed Opt Express. 2011;2(11):3119-3128.

[7] Clancy NT, Stoyanov D, Yang GZ, Elson DS. Stroboscopic illumination scheme for seamless 3D endoscopy. Proc SPIE. 2012;8214:82140M.

[8] Schmalz C, Forster F, Schick A, Angelopoulou E. An endoscopic 3D scanner based on structured light. Med Image Anal. 2012;16(5):1063-1072.

# Hand Exoskeleton for Remote Control of Minimally Invasive Surgical Anthropomorphic Instrumentation

A. Tzemanaki[1,2], X. Gao[2], A. Pipe[1,2], C. Melhuish[1], S. Dogramadzi[1,2]

[1]*Bristol Robotics Laboratory*, [2]*University of the West of England, Bristol, UK*

*Antonia.Tzemanaki@brl.ac.uk*

## INTRODUCTION

Minimally invasive surgery (MIS) has evolved from traditional laparoscopy, which involves the surgeon using hand held tools through small incisions on the patient's body, to robotically assisted (R-A) surgery, during which the surgeon remotely operates articulated instruments attached to the end of robotic arms. Advances in the design, articulation and flexibility of the instruments have added to the popularity of R-A MIS [1]. Nevertheless, the way that the instruments are controlled affects not only their efficacy, but also the ergonomics and the learning process for the surgeon.

In [2], we have presented a concept for hand-like instruments, each carrying an articulated 3-finger system which imitates the surgeon's fingers' exact movements. The anthropomorphic system design aims to reduce the 'cognitive gap' between the way that instruments are manipulated and the surgeon's natural hand movements. The master controls of the Da Vinci Surgical System [3] manipulate a simplified gripper attached to a 3-DOF wrist. In a very similar way, the Phantom Omni haptic device is used to control surgical instruments in various other designs of MIS instruments [4]. If the instruments to be controlled are more complex, more complex master devices are required.

Systems for motion capturing of hands span from on-the-hand hardware with finger position capturing, such as data gloves and exoskeletons, to external imaging systems based on intensive image processing and often covering a limited field of view. Data gloves, used for similar tasks, are expensive and generally lack durability [5]. Besides being non-adjustable and requiring calibration for each user, data gloves do not offer detailed joint tracking. In [6], a wrist-worn real time hand tracker is proposed, which avoids burdening of the hand with extra load. Limitations include occlusions resulting from overlapping fingers. Besides finger tracking, wrist rotation and bend tracking is very important especially during surgical tasks. However, these cannot be modelled using a wrist-worn tracker or a data glove.

Consequently, we report here on the development of a lightweight and adjustable hand exoskeleton that can sense movements of the surgeon's finger's joints and translate it to movements in the joints of the instrument, such as the one we presented in [2]. Most exoskeletons in the literature are aimed at actuation of hands or arms [7], often ending up being bulky and heavy. By removing all the motors and encoders, the design can be simplified. The following sections present the design of an initial prototype of a hand exoskeleton for control of the MIS instrumentation in the MIS concept described in [2].

## MATERIALS AND METHODS

The proximal interphalangeal (PIP) and distal interphalangeal (DIP) joints of the fingers are hinge joints capable of only flexion and extension (1 DOF each). The metacarpophalangeal (MCP) joints at the base of the index and middle finger, however, are saddle joints, and hence capable of abduction and adduction (2 DOF). The thumb can also be modelled by having two 1-DOF (interphalangeal-IP and metacarpo-phalangeal-MP) and one 2-DOF (Carpometacarpal-CMC) joints. The exoskeleton was designed according to this layout, so that it can follow the fingers' natural motion.

The angle of each joint is measured using two types of hall-effect sensors (MLX90316 and MLX90333, Melexis, Belgium) measuring 1 DOF and 3 DOF. The 1-DOF sensor can give absolute angular position of a small magnet located parallel to the sensor in a rotary type joint. The 3-DOF sensor senses the magnet position anywhere in its surroundings, being suitable for a ball type joint. In order to simplify the exoskeleton design, the PIP and DIP of the index and middle fingers were considered coupled (as they are in the human hand). Therefore, instead of having different sensors for each joint, the exoskeleton carries only one sensor for the PIP joint, while the position of the DIP is calculated by the relationship between the PIP and the DIP given in [8]. The whole structure comprises seven sensors in total: three 2-DOF (MCPs and CPC) and four 1-DOF (PIPs, IP and MP).

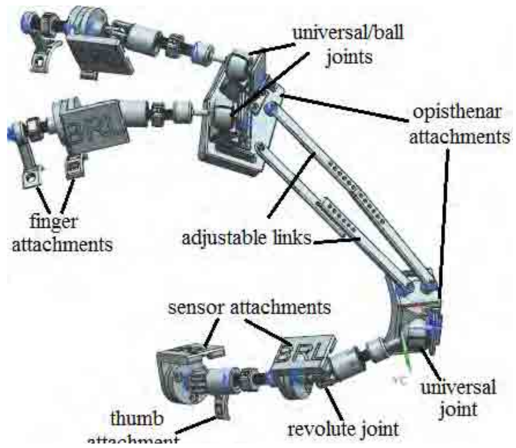



**Fig. 1** CAD drawing of the exoskeleton assembly

## RESULTS

The computer-aided drawing with the main exoskeleton components is shown in Figure 1. Each exoskeleton joint is fastened to the hand with a flexible attachment. The joints are connected to each other via adjustable links. The MCP and CPC joints were designed as ball joints in order to reduce the bulkiness and the complexity of the component. The sensors are attached at the side of each joint on the non-contacting parts, as shown in Figures 2 and 3.

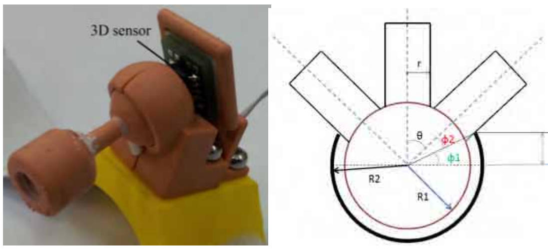



**Fig. 2** Ball joint prototype and range of motion calculation

The typical ranges of motion of each joint in degrees are: 0-90º for the MCP, 0-110º for the PIP and 0-70º for the DIP. To ensure unrestricted motion, the range of the ball joint was set to be at least 90º. From the parameters in Figure 2, the range of the ball joint can be calculated as:

$$2\theta = 2\left(90 - \phi_1 - \phi_2\right) = 2\left(90 - sin^{-1}\frac{d}{R_2} - sin^{-1}\frac{r}{R_2}\right)$$

where $R_2 = 6\ mm$, $d = 3\ mm$ and $r = 1.5\ mm$.

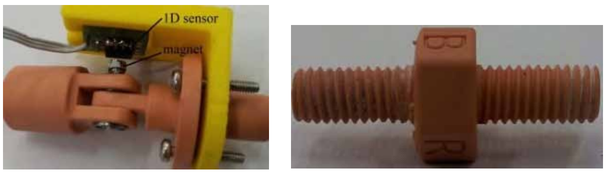



**Fig. 3** Revolute joint and double threaded adjustable link

The joints are connected to each other via double threaded links (Figure 3). One side has a left-hand thread, while the other has a right-hand thread so that, by turning the link, it can be extended (clockwise) or shortened (anti-clockwise).

## DISCUSSION

The design for a sensory hand exoskeleton presented in the previous section meets the design requirements. The double thread links not only make the mechanism adjustable to a variety of hand sizes, but also allow the exoskeleton to be lightweight (approx. 130 gr), without added material for modifications as in [7]. Furthermore, each of its joints covers a range of motion similar to, or greater than, that of a human hand, which ensures natural unrestricted hand motion and comfort. The whole structure is as compact as possible and it has twelve DOF, ten of which are actively sensed while the other two can be calculated from the neighbouring joints. The next version of the exoskeleton will include sensors for wrist motion tracking, in contrast to the methods used in [5-6], where this would not be possible.

The exoskeleton was fabricated using 3D printing (NanoCure, Envisiontec, Germany). Figure 4 shows part of the exoskeleton fitted on the side of the index finger and the electronics attached to the wrist. Sensor processing electronics will be placed in a compact box, the size of a hand watch.

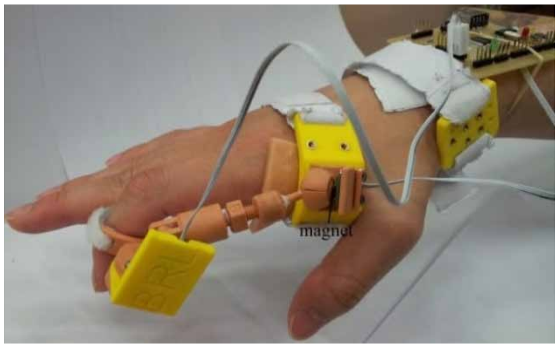



**Fig. 4** Testing the exoskeleton on one finger

In the first phase of our investigation, the surgeon will explore use of the exoskeleton to manipulate virtual objects. The sensory electronics will be connected to a PC via USB and the output of the sensors fed into a 12-DOF hand kinematic model. The user will wear the exoskeleton and the movements of his/her fingers will be simulated in real-time. This will form the basis of a surgical simulation environment, where the surgeon will be able to test the concept of controlling hand-like instruments as described in [2]. The accuracy of the structure needs to be tested and the teleoperation suitability will be evaluated in our future work. At that stage, the exoskeleton will be connected directly to two corresponding surgical hands.

## REFERENCES

[1] Freschi C, Ferrari V, Melfi F, Ferrari M, Mosca F, and Cuschieri A. Technical review of the da Vinci surgical telemanipulator. The International Journal of Medical Robotics and Computer Assisted Surgery. 2012.

[2] Tzemanaki A, Dogramadzi S, Pipe T, and Melhuish C. Towards an Anthropomorphic Design of Minimally Invasive Instrumentation for Soft Tissue Robotic Surgery. Advances in Autonomous Robotics, Springer. 2012, pp. 455–456.

[3] Da Vinci Surgery - Minimally Invasive Robotic Surgery with the da Vinci Surgical System. [Online]. Available: http://www.davincisurgery.com/davinci-surgery.

[4] Lum MJH, Friedman DCW, Sankaranarayanan G, King H, Fodero K, Leuschke R, Hannaford B, Rosen J, and Sinanan MN. The RAVEN: Design and Validation of a Telesurgery System. The International Journal of Robotics Research. 2009 vol. 28, no. 9, pp. 1183–1197.

[5] Dipietro L, Sabatini AM, and Dario P. A Survey of Glove-Based Systems and Their Applications. 2008, vol. 38, no. 4. IEEE, pp. 461–482.

[6] Kim D, Hilliges O, Izadi S, Butler AD, Chen J, Oikonomidis I, and Olivier P. Digits: freehand 3D interactions anywhere using a wrist-worn gloveless sensor. 25th annual ACM symposium on User interface software and technology. 2012, pp. 167–176.

[7] Wege A and Hommel G. Development and control of a hand exoskeleton for rehabilitation of hand injuries. 2005 vol. 24, no. 1. IEEE, pp. 3046–3051.

[8] Kamper DG, Cruz EG, and Siegel MP. Stereotypical fingertip trajectories during grasp. Journal of Neurophysiology. 2003, vol. 90, pp. 3702–3710.

# Embedded Middleware and Hard Real-time based Architecture for Robot Assisted Ophthalmic Surgery

S. Nair[1], M. Ali Nasseri[1], M. Eder[1], C.P. Lohmann[2], A. Knoll[1]

[1]*Robotics and Embedded Systems, Technische Universitaet Muenchen, Germany*

[2]*Klinikum Rechts der Isar, Technische Universitaet Muenchen, Germany*

*{nair,nasseri,eder,knoll}@in.tum.de Chris.Lohmann@mri.tum.de*

## INTRODUCTION

This paper introduces the software architecture of our robotic device for performing ophthalmic surgeries with reduced tremors and increased precision. This robot not only improves current clinical procedures but also opens new avenues for treating ophthalmic ailments. For example, Retinal Vein Occlusion currently has no generally approved surgical treatment.

The robot has been designed to be as small as an average human hand and it weighs 315 grams, which can easily be mounted on the patient's head. It comprises five piezo drives with 0.5µm precision encoders. These drives are arranged in a hybrid parallel-serial configuration. Customized power electronic controllers facilitate low level control of the drives through saw tooth type signals. The surgeon closes the loop through a visual feedback from an ophthalmic microscope. He or she controls the velocity of the tool-tip attached to the robot in Cartesian space by using a six degree of freedom (DOF) space mouse [4] (see Fig.1). It is worth mentioning that the tooltip velocities in Cartesian space are mapped to joint space velocities (considering the robot's Jacobian matrix). The velocity of each piezo drive is controlled by changing the frequency of the saw-tooth signal. The challenge is to keep the time delay between the motion of the surgeon and the motion of the robot as small as possible. Additionally, for seamless integration into ORs, the setup must be compact.

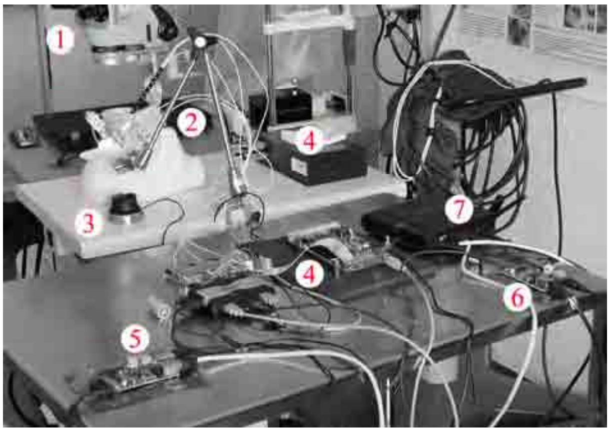



**Fig. 1** Ex-vivo experiment on a pig's eye. The current 5DOF robot is controlled using a space mouse. (1. Microscope, 2. Robot, 3. Space Mouse, 4. Power Electronic boards, 5. Robot Controller (Embedded), 6. Input Device Controller (Embedded), 7. Ethernet Switch)

In this paper we propose a middleware driven architecture using an embedded platform. The architecture supports hard real-time operation along with plug-and-play operation through low level device drivers. [4] and [5] present robotic systems for steady and micro manipulation. [8] present a component driven architecture for integration of robotics integration. In this paper we mainly focus on middleware architecture for embedded systems.

## SYSTEM ARCHITECTURE

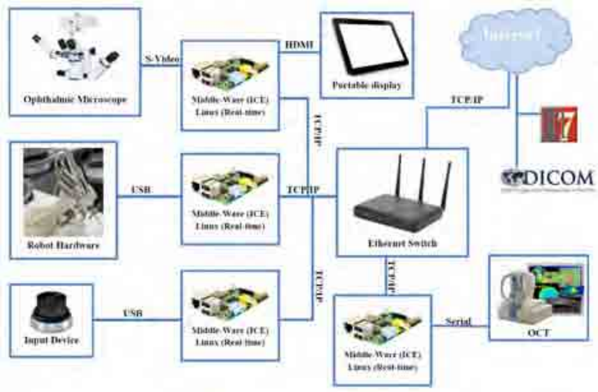



**Fig. 2** System Architecture

We have employed embedded middleware based architecture to facilitate a distributed operation and easy integration. It allows the representation of process data at a higher level of abstraction and thereby facilitating easy integration and seamless data sharing within a unified ecosystem. It also provides an API for user space application development.

The main distributed components (see Fig. 2) are the input device controller and the high level robot controller. Each component is hosted on an independent Raspberry pi board [3]. The board consists of an ARM 700 MHz processor running a Debian Linux Kernel patched for hard real-time performance. The Xenomai [1] real-time patch is used which allows the development of hard real-time applications from user space. It supports USB for I/O and Ethernet for networking purposes.

The middleware in use is the embedded extension of Internet Communication Engine (ICE) [2] and is called IceE. It uses TCP/IP as the communication medium and is platform and programming language independent. IceE allows the user with a message scripting language called Slice [2], through which the user can represent the data in the form of message objects and define interfaces for transporting these messages. Thereafter,

the slice tools automatically generate source code for the message interfaces in languages such as C++, Java, C#, Obj C, Python, Ruby and PHP. We employ the C++ development framework. In our architecture, a message interface is written for the data acquired from the space mouse by the input device controller. It consists of the translation and rotation data specified in a structure along with the interface function for transporting them over the network. Fig. 3 illustrates the message object and interface. A publish/subscribe mechanism is used wherein the input device controller hosts an Ice-Publisher. The high level robot controller implements an Ice-Subscriber to read the published message containing the data from the space mouse. This data is further processed and mapped to the robot joints through the robot inverse kinematics.

```
#ifndef INPUT_ICE
#define INPUT_ICE

module input
{
  struct InputDevice
  {
            double translation_x;
            double translation_y;
            double translation_z;
            double rotation_x;
            double rotation_y;
            double rotation_z;
  };

  interface InputInterface
  {
            void sendInputData(InputDevice input_data);
  };
};
#endif
```

**Fig. 3** Ice Message Object and Interface

Both the input device and the robot controller components contain a hard real-time process using the Xenomai Library and the real-time patched Linux Kernel. In the input device application the data from the space mouse is acquired using the spacenav library [4]. This data is then packaged in the form of the ICE message object and published using the message interface. The high level robot controller component reads this data using the subscriber and processes it for tremor reduction and motion scaling. Thereafter, the data is mapped to the robot joints through inverse kinematics. The robot itself is controlled in the velocity mode. A low-level device driver has been developed in order to control the individual piezo drives of the robot. The driver sends ASCII based motion and feedback commands to the drives through a Serial over USB protocol. This data is received by the firmware hosted on the low-level-robot control board which implements the power electronics. The complete control loop runs in a hard real-time process hosted by the high-level robot controller. Fig. 4 illustrates the robot controller consisting of the high level and low level components.

## RESULTS

The first ex-vivo clinical experiments using the setup, which is seen in Fig. 2, were performed successfully utilizing the embedded real-time architecture. The input device motions were mapped to the slave robot through velocity based control for intuitive operation. Due to the compact size and simplicity of the hardware, integration

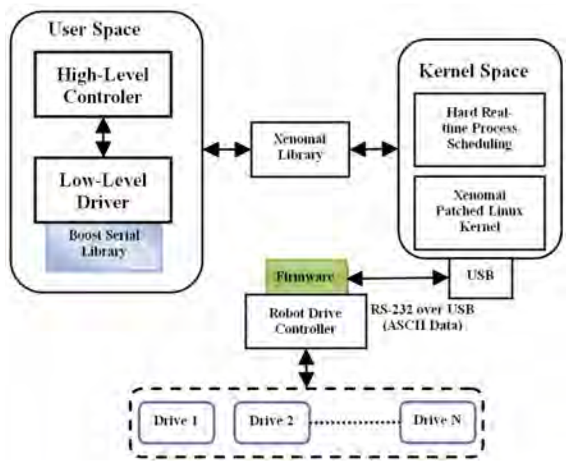



**Fig. 4** Robot Controller

of the setup in the operation room was trivial. The device was operated by ophthalmic surgeons. The real-time capabilities of the computing environment ensured a consistent cycle time of 1 msec in the input controller and the high level robot controller threads. Furthermore, the real-time mapping of the surgeon’s motion to robot motion provided intuitive operation at the scale of microns. It also significantly increases the robotic operation safety while the reaction of the robot to human commands is fast. In the next step a 3D OCT (optical coherence tomography) device is going to be integrated to the setup based on the same architecture. OCT information will be then used as additional intraocular feedbacks for the surgeons.

This works is supported by the Bundesministerium für Bildung und Forschung (BMBF; 16KT1223).

## REFERENCES

[1] P. Gerum, “Xenomai-implementing a rtos emulation framework on gnu/linux,” GNU Free Documentation License (2004).
[2] M. Henning and M. Spruiell, “Distributed programming with ice”, ZeroC Inc. Revision 3 (2003).
[3] Raspberry pi http://www.raspberrypi.org/
[4] A free, compatible alternative for 3Dconnexion's 3D input device drivers and SDK. http://spacenav.sourceforge.net (May 2013)
[5] B. Mitchell, J. Koo, M. Iordachita, P. Kazanzides, A. Kapoor, J.Handa, G.Hager, and R.Taylor, “Development and application of a new steady-hand manipulator for retinal surgery,” in IEEE ICRA, Apr 2007, pp. 623–629.
[6] J. C. Tabares, R. MacLachlan, C. A. Ettensohn, and C. Riviere, "Cell micromanipulation with an active handheld micromanipulator," Proc. 32nd Annual International Conference of the IEEE Engineering in Medicine and Biology Society, September, 2010, pp. 4363-4366.
[7] Liu, M. Balicki, R. H. Taylor, and J. U. Kang,"Automatic online spectral calibration of Fourier-domain OCT for robot-assisted vitreoretinal surgery", in SPIE Advanced Biomedical and Clinical Diagnostic Systems IX,25 January 2011.
[8] M. Y. Jung, A. Deguet, and P. Kazanzides, “A component-based architecture for flexible integration of robotic systems,” in IEEE/RSJ International Conference on Intelligent Robots and Systems, October 2010

# Application of Robot-Assisted Laparoscopic Surgery in Paediatric Urology – A Seven-Year Single Surgeon Experience

T.P. Cundy[1], N.E. Gattas[2], S.M. Whiteley[2], A. Springer[2], A.S. Najmaldin[2]

[1]*The Hamlyn Centre, Institute of Global Health Innovation, Imperial College London*
[2]*Department of Paediatric Surgery, Leeds General Infirmary, Leeds*
*azad.najmaldin@leedsth.nhs.uk*

## INTRODUCTION

The clinical uptake of robot-assisted laparoscopic surgery has predominantly been for urological indications in adult patients, with several of these procedures becoming established as standard of care. In paediatric surgical specialties, adoption of this surgical technology was initially slow and cautious but recently has seen growing enthusiasm. Adult and paediatric urological practice unavoidably share much similarity due to common anatomic regions of focus, however there are also many unique differences. For example, the proportion of congenital and acquired pathology encountered by a paediatric urologist is heavily skewed towards the former, and vice-versa for an adult urologist. The role of robot-assisted surgery for urological indications in children remains unclear. This paper examines the seven-year experience of a single surgeon following establishment of a robotic surgical service for paediatric urology.

## METHODS

All children undergoing robot-assisted urological surgery between March 2006 and March 2013 were included. One surgeon (A.S.N) performed all cases in a single institution, using the da Vinci® Surgical System (Figures 1b, 1c). All clinical data was prospectively recorded in an electronic database.

## RESULTS

There were 175 patients involving 185 procedures. The range of procedures performed included pyeloplasty (88), nephrectomy (27), heminephrectomy (21), nephroureterectomy (20), ureteral reimplantation (15), and other (14) (Figure 1a). The surgical approach was transperitoneal in all cases, with 7 cases also involving transvesical access for cross-trigonal Cohen technique ureteral reimplantation. The average patient age was 7.3 years (range 1.2 months – 19.1 years). The smallest patient in the series weighed 4.1 kilograms. Overall conversion rate was 5.7% (10/175), with the procedure being successfully completed laparoscopically in two of these circumstances. Reasons for conversion were due to unexpected issues arising with equipment or theatre staff (5/10), inadequate visualisation (3/10), lack of operative domain (1) and technical difficulty (1).

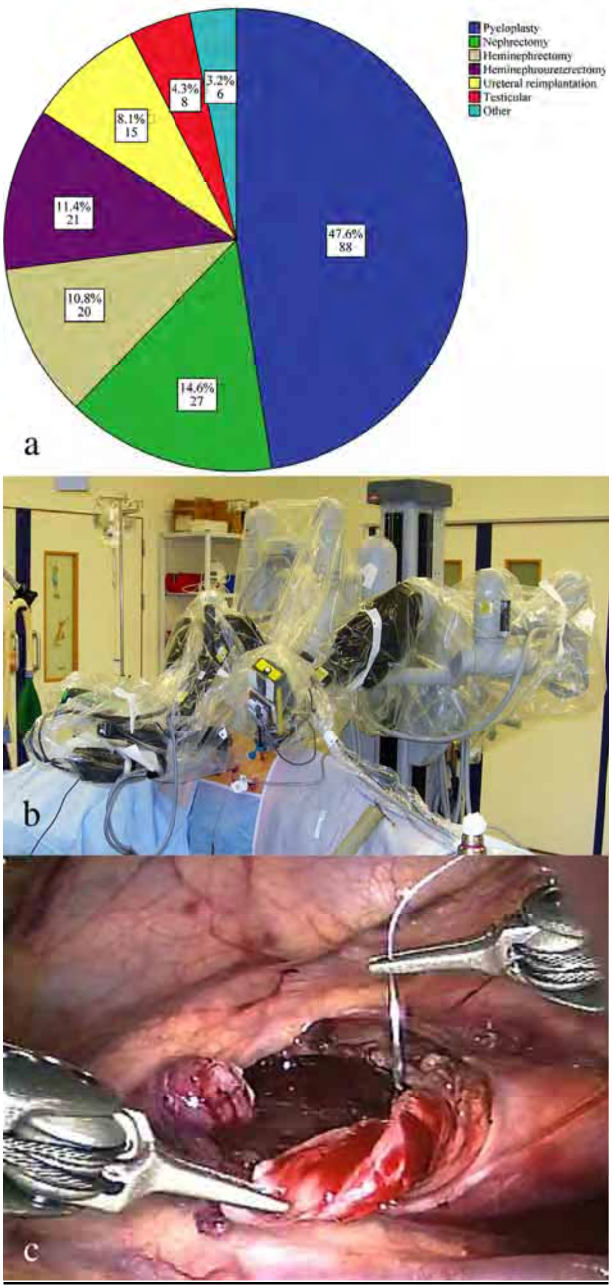



**Fig. 1 a)** Distribution of caseload by procedure, **b)** typical modified flank patient positioning and port configuration for robot-assisted pyeloplasty and **c)** left-sided transperitoneal view of a dismembered pelviureteric junction at commencement of ureteral anastomosis

One intra-operative complication occurred, involving estimated blood loss (EBL) of 200mL during heminephroureterectomy in a 12-year-old child for a non-functioning and refluxing left lower moiety. This event related to parenchymal surface bleeding and did not impact intra-operative or post-operative care (1.1 g/dL drop in post-operative haemoglobin concentration therefore EBL suspected to have been over-estimated). Overall 30-day post-operative complication rate was 5.9% (Table 1). Operating times were variable depending on the relevant procedure, ranging from 47 – 367 minutes for total operating time, and 6 – 280 minutes for console time. Median total and console operating times for pyeloplasty were 226 minutes (range 153 – 340) and 167 minutes (range 70 – 280) respectively. Median length of post-operative hospital stay was 24 hours (range 3 – 144 hours). Two patients (2.3%) required re-do robot-assisted pyeloplasty.

## DISCUSSION

The application of robot-assisted surgery in paediatric urology is diverse, reflective of the wide range of pathology and patient size encountered in this specialty. There is a dominance of reconstructive procedures. The most eligible application seems to be pyeloplasty. Smaller instruments more appropriate for paediatric patients are required, which would likely facilitate use of current robotic systems in younger patients, and be better suited for procedures in particularly confined anatomical locations such as intra-vesical ureteral reimplantation and retroperitoneal pyeloplasty. Currently available 5mm instruments are less versatile compared to 8mm instruments due to limited catalogue range and longer distal articulation length compared to the compact 8mm Endo-Wrist® design instruments. Conversion and complications rates in this series seem low and favourable in the context of conventional laparoscopy and open technique surgery. Technical advantages of robot-assistance, such as enhanced dexterity, precision, visualisation and ergonomics, might enable minimally invasive approaches to complex reconstructive urological surgery in children that otherwise would be beyond the remit of conventional laparoscopy.

**Table 1** Post-operative complications occurring in the study cohort (n = 175) graded according to the Clavien-Dindo classification [1].

| Clavien Grade | n | Description |
|---|---|---|
| I | 3 | Post-operative ileus (1), surgical emphysema (1), hypertrophic umbilicus scar formation (1). |
| II | 2 | Post-operative nausea and vomiting (1), urinary sepsis (1). |
| IIIa | 2 | Urinary retention requiring urethral catheterisation (1), stent blockage requiring saline flush (1). |
| IIIb | 4 | Stent displacement requiring replacement (1), recurrent PUJO presenting as acute hydronephrosis requiring urinary diversion and later re-do pyeloplasty (2), acute hydronephrosis due to clot obstruction prompting return to operative management (laparoscopy) (1). |
| IVa | 0 | - |
| IVb | 0 | - |
| V | 0 | - |

## REFERENCES

[1] Dindo D, et al. Classification of surgical complications: a new proposal with evaluation in a cohort of 6336 patients and results of a survey. Ann Surg 2004;240:205-13.

# Case-specific Rehearsal using a Temporal Bone Simulator: Is it Feasible and Clinically Applicable?

A. Arora[1], C. Swords[1], S. Khemani[2], Z. Awad[1], A. Darzi [3], A. Singh[4]
N. Tolley[1]

[1]Dept. of Otolaryngology, St. Mary's Hospital, Imperial College NHS Trust, London UK

[2]Dept. of Otolaryngology, Surrey and Sussex NHS Trust, UK

[3]Dept. of Biosurgery and Surgical Technology, Imperial College London, UK

[4]Dept. of Otolaryngology, Northwick Park NHS Trust, London, UK

asitarora@doctors.org.uk

## INTRODUCTION

Virtual reality (VR) temporal bone simulation provides an interactive three-dimensional recreation of the surgical environment. The intended surgical procedure may first be performed in a virtual environment using case-specific CT data uploaded onto the simulator.

The role of VR-simulated case-specific rehearsal in carotid endovascular surgery has been reported[1]. Results suggest that it facilitates case selection and improves surgical performance.

The Voxelman Temposurg has been validated for postgraduate training at Imperial College London[2]. The process of uploading data onto a temporal bone simulator for case rehearsal has not been reported. The objectives of this study were to determine the feasibility of performing case rehearsal and to identify potential clinical applications in temporal bone surgery.

## MATERIALS AND METHODS

The Voxelman TempoSurg was used. Sixteen participants were recruited comprising of 8 experienced Otologists (minimum of 400 mastoid operations as primary surgeon) and 8 Otolaryngology trainees (mean experience of 19 months)**.** All trainees had prior experience in temporal bone drilling.

Sixteen formalin-fixed cadaver temporal bones were scanned using Philips iCT 256 CT-scanner. Data was saved to a CD-ROM for upload using the data import module. Data transfer and retrieval were evaluated for slice spacing and thickness, field of view and intensity range. The time for each temporal bone upload was recorded.

Participants were assigned a cadaver temporal bone and its corresponding upload. All subjects undertook a 90-minute temporal bone dissection on the simulator before performing 3 dissection tasks on the case upload and cadaver temporal bones: extended cortical mastoidectomy, posterior tympanotomy and cochleostomy. Standardised written instructions for each task were provided. Successful task completion was judged by 2 co-authors using a task-based checklist.

The role of case rehearsal was evaluated across 4 domains and the accuracy of anatomical representation for 6 temporal bone structures recorded. Questions were rated on a 5-point Likert scale, in which 1 represented *strongly disagree* and 5 as *strongly agree*. A score of 4 was the minimum threshold for acceptability. Differences between the experienced and trainee group were analyzed with the independent t-test. A p value of $<0.05$ was considered significant.

Qualitative data was collected using videos of 90-minute focus group sessions where both groups were asked open-ended questions. The videos were saved as digital files, manually transcribed and underwent thematic analysis

## RESULTS

Each data set was approximately 156 slices, 0.33mm×0.33mm pixel size and 1mm slice spacing. All temporal bones were devoid of pathology. The entire mastoid process was inadvertently not captured in 2 temporal bone scans. There was artefact in 3 temporal bone uploads. This was due to image interference from the attached cadaver identity tags.

Optimal 3D reconstructions were created using a segmentation threshold value of 450 Hounsfied units to define the ossicular chain.

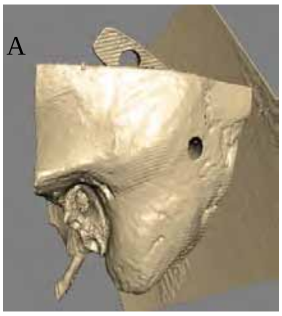



**Fig. 1** Suboptimal temporal bone VR upload due to artefact (**A**)

User activity associated with the segmentation process accounted for the majority of the upload time. The time for each upload decreased with experience (mean time: 20.7 minutes, range 10-40 minutes, $R^2$=0.9, p=0.0001).

**Table 1** Role of case rehearsal in temporal bone surgery

| Role of case rehearsal | Total Cohort (n=16) % rated Likert >4 | Total Cohort (n=16) Mean | Trainer (n=8) Mean | Trainees (n=8) Mean | p |
|---|---|---|---|---|---|
| Confidence | 75 | 4.1 | 3.6 | 4.5 | 0.06 |
| Pre-op planning | 75 | 4.1 | 3.6 | 4.5 | 0.1 |
| **Training** | 94 | 4.3 | 3.9 | 4.6 | **0.04** |
| Overall role | 81 | 3.8 | 3.6 | 4 | 0.4 |

The role of rehearsal across 4 domains is shown in Table 1. Its role for training scored highly (94%). There was a significant difference in the mean score between the trainer and trainees for this domain only (p=0.04). Thematic analysis demonstrated perceived advantages and limitations. The ossicular chain was the only anatomical structure positively rated by the experts. Dura was rated suboptimal; the most frequently reported limitation being a lack of auditory cues whilst drilling over the tegmen. Participants reported that areas of anatomical variation conveyed to the user in the virtual setting influenced subsequent task performance on the cadaver model, including degree of pneumatisation, low dura and high sigmoid sinus (n=4).

The following procedures were identified as potential applications: ossicular chain surgery, paediatric cochlear implantation and congenital bony anomalies. Rehearsal of procedures involving the facial nerve and removal of cholesteatoma were not feasible on the existing platform due to *"lack of depth perception during deeper temporal bone dissection"*.

## DISCUSSION

The study demonstrates a streamlined process to enable this application to become a useful tool for the practising otologist. The results support case rehearsal for confidence, planning and training. It allows the intended procedure to be rehearsed; improving technical skills and case familiarisation were rated highly by the trainees. Both groups strongly attributed a role to improve the understanding of anatomy and facilitating surgical planning. Qualitative data suggests that successful completion of a task in the virtual setting was able to predict success of the same task in the cadaver.

Representation of the ossicular chain was positively rated. Correspondingly, procedures involving the latter represented a potential application. There was consensus regarding lack of a role for rehearsal in facial nerve decompression due to suboptimal soft tissue reconstruction and poor depth perception when drilling deeper structures. These findings suggest that high levels of realism are necessary to enable clinical application and that a low level of realism is predictive of lack of clinical application. In this evaluation pixel size was 0.33mmx0.33mm with 1mm slice spacing. Non-isotropic image data could potentially alter accuracy.

Although experienced surgeons are not necessarily experts in surgical education, their opinion may provide a more meaningful barometer of the efficacy of simulation for case rehearsal. In this regard it was suboptimal. It is not surprising that the trainee group rated the system highly for technical improvement. Their demographics demonstrate reasonable experience which provides a basis for comparison with other methods for training. This group may find simulated rehearsal more useful than experts due to greater familiarity with computer based technology and a better appreciation of their own learning needs.

Case rehearsal should be viewed as a potentially useful adjunct to the existing methods of pre-operative patient evaluation. Further clinical study is necessary to evaluate whether simulation can improve the surgeon's perceived and actual performance and, ultimately, patient safety.

## REFERENCES

[1] Willaert WI, Aggarwal R, Nestel DF, et al. Patient-specific simulation for endovascular procedures: qualitative evaluation of the development process. Int J Med Robot 2010 Jun;6(2):202-10

[2] Arora A, Khemani S, Tolley N, Singh A, Budge J, Varela DA, Francis HW, Darzi A, Bhatti NI. Face and content validation of a virtual reality temporal bone simulator. Otolaryngol Head Neck Surg 2012 Mar;146(3):497-503

# Development of Robot-Assisted Surgery in Qatar

Osama Al-Alao[1], Jean-Marc Peyrat[2], Julien Abi-Nahed[2], Abdulla Al-Ansari[1,2]

[1]*Hamad Medical Corporation, Doha, Qatar*
*oalalao@hmc.org.qa - aalansari1@hmc.org.qa*

[2]*Qatar Robotic Surgery Centre, Qatar Science & Technology Park, Doha, Qatar*
*jmpeyrat@qstp.org.qa - jabinahed@qstp.org.qa*

## INTRODUCTION

During the last decade, there has been a significant investment in acquiring robot-assisted surgical systems in the Gulf Cooperation Council [1,2]. Nevertheless, the robot-assisted surgery (RAS) did not show a high-level of activity as explained by several key region-specific factors [2]. Qatar has witnessed a steady increase of RAS activity over the past five years. In this paper, we report details about RAS performed in Qatar and provide some insights on the obstacles hindering growth and factors that will help to overcome them.

## ROBOT-ASSISTED SURGERY IN QATAR

Since the first acquisition of daVinci® robots in 2008, 183 cases of RAS have been documented in Qatar. Urology represents most of these cases (69%) and is followed by cardiology (22%) as shown in Fig. 1. The importance of urology in RAS is the result of a constant and substantial growth with a yearly increase of cases ranging from +30% to +100%.

This increasing number of cases provided more experience to surgeons, increased their efficiency, and reduced the time spent in the operating room. Fig. 2 illustrates the latter outcome for the three most common types of urological RAS: pyeloplasty, prostatectomy, and partial nephrectomy.

In terms of patient outcome, their corresponding post-operative stay at the hospital has been shortened in average by 22% with RAS (most significant reduction for pyeloplasty with 55% reduction, as shown in Fig. 3). And complications with more than two weeks post-operative stay have the same proportion in RAS than in open surgeries (respectively 5.6% and 6.8%).

## GROWTH OBSTACLES

Even though RAS has witnessed substantial growth since 2008, it has been limited by several factors:

- An open surgery team was established side-by-side with the RAS initiative. The number of cases was split between the teams in favor of open surgery as RAS was limited by availability of mentors.

- The Hamad Medical Corporation (HMC), which is the only RAS provider in Qatar, often experience over-demand for beds and operating rooms.

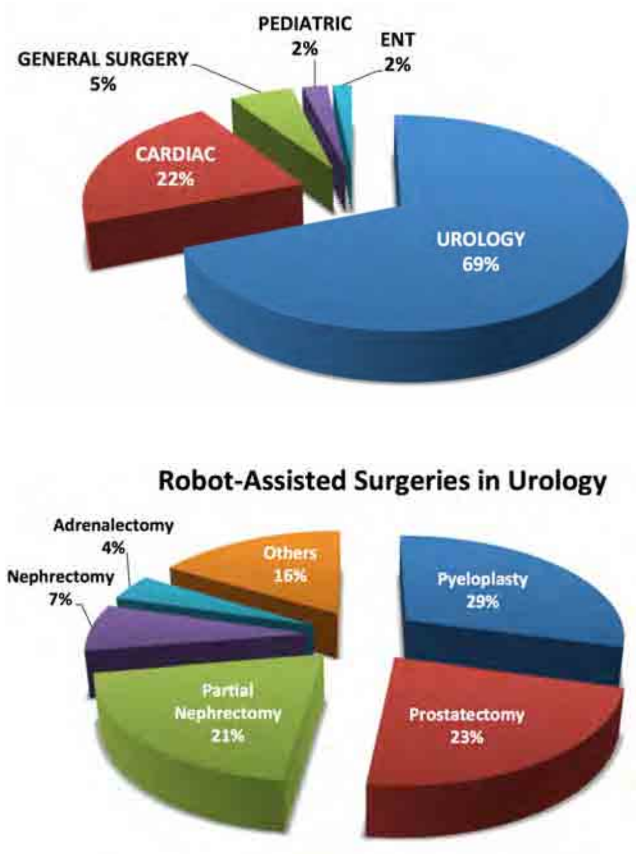



**Fig. 1** [Up] Repartition of robot-assisted surgeries (RAS) in Qatar over the 183 performed since 2008. [Bottom] Repartition of robot-assisted surgeries (RAS) in urology.

- It takes time for patients, surgeons, and anesthetists to understand, accept, and finally trust RAS as an alternative treatment replacing number of traditional interventions.

- RAS was only devoted to selected cases in urology for which patient's benefits were clearly identified (mostly in case of cancer and reconstructive cases).

- Population in Qatar is relatively young (median age of 29.9 years in 2011) due to a significant expat labor force [3]. The number of RAS candidates is thus limited.

## FUTURE GROWTH FACTORS

By understanding these limitations, we believe that the following factors will accelerate RAS growth in the next coming years:

+ RAS will expand to include more specialties (*e.g.* gynecology and bariatric).

+ HMC will increase the capacity of its hospitals.

+ RAS is gaining wider acceptance partly due to the establishment of the Qatar Robotic Surgery Centre (QRSC), a local training and research center in surgical technologies that further promotes RAS in Qatar.

+ HMC is taking the initiative to attract more international clinical experts and mentors by participating and organizing RAS-related clinical conferences and through international collaborations on research projects via QRSC.

## CONCLUSION

We have listed many factors that can accelerate the growth of RAS in Qatar. Nevertheless, we did not mention an important growth factor not only applicable to Qatar but also worldwide: the development of novel surgical robot technologies that can have a substantial impact by improving benefits of RAS over more traditional surgeries and/or expanding the application of RAS to other surgeries.

Whether through the clinical RAS programs at HMC or the research and training projects at QRSC, Qatar has grown its expertise and is preparing the ground to be the regional hub for clinical and technological innovation in surgery and related fields. Indeed, recent national strategies formulated for health [4] and research [5] confirm the national will to achieve this ambitious goal.

## ACKNOWLEDGEMENTS

We would like to thank Alborz Amir-Khalili for his help in clarifying the manuscript.

## REFERENCES

[1] Khairy GA, et al. A new era in laparoscopic surgery. Saudi Medical Journal, 2005; (26): 777-780.
[2] Abi-Nahed J, Nuyens J, and Abulaban B. Robotic-assisted surgery in the Gulf Cooperation Council. The Hamlyn Symposium on Medical Robotics, 2010; p.31-32.
[3] Qatar Population Status 2012, General Secretariat for Development. http://www.gsdp.gov.qa
[4] National Health Strategy 2011-2016. http://www.nhsq.info
[5] F. Alsuwiaidi. Speech on Qatar National Research Strategy 2012 in QNRF 4th Annual Forum. http://www.qnrf.org

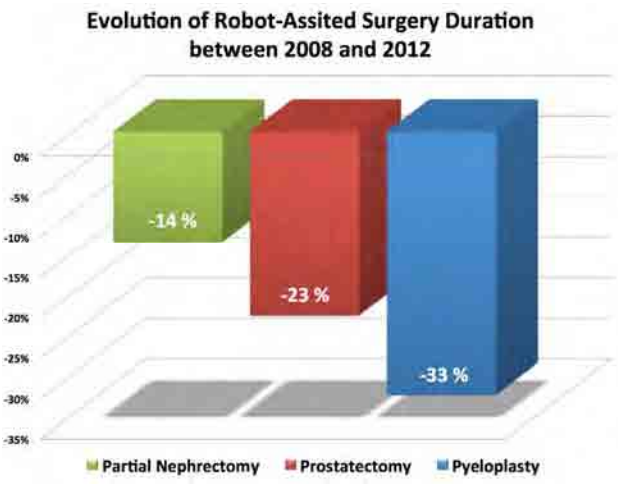



**Fig. 2** Evolution of surgery duration between 2008 and 2012 for most common urological interventions: partial nephrectomy, prostatectomy and pyeloplasty (resp. 21%, 24%, and 30% of urology cases).

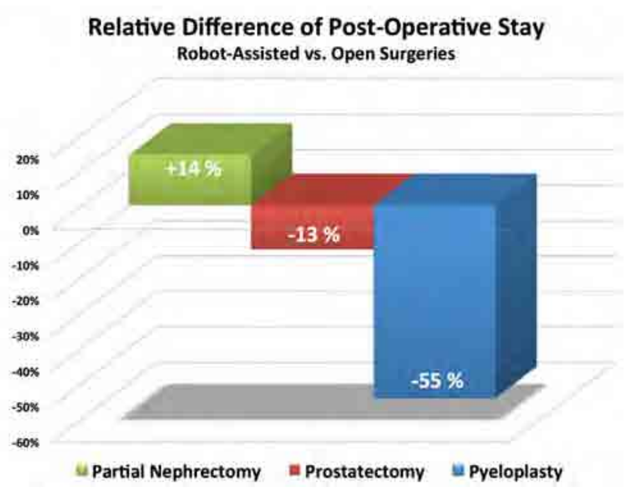



**Fig. 3** Relative difference of post-operative stay between RAS and open surgery for most common urological interventions from 2008 to 2012: partial nephrectomy, prostatectomy and pyeloplasty (resp. 21%, 24%, and 30% of urology cases).

# Operative Working Spaces in Keyhole Neurosurgery: An MRI Study

H.J. Marcus[1], A. Hughes-Hallett[1], P. Pratt[1], J. Clark[1], D. Nandi[2], A. Darzi[1], G.-Z. Yang[1]

[1]*The Hamlyn Centre for Robotic Surgery, Imperial College London, UK*

[2]*Department of Neurosurgery, Imperial College Healthcare NHS Trust, UK*

## INTRODUCTION

The central dogma of keyhole neurosurgery is the minimisation of intraparenchymal dissection and reduction of exposure and retraction of unaffected brain tissue in order to reduce approach related morbidity. The next generation of progress in this field would seek to further exploit the natural anatomical corridors and cerebrospinal fluid (CSF) pathways within the brain. The latter have already been extensively used for conventional microneurosurgery. The challenge lies in the difficulty of triangulating rigid tube-shaft instruments and performing fine dissection of delicate neurovascular structures through a narrow working channel. The construction of robotic platforms with articulated instruments may allow improved manipulation through keyhole approaches. A necessary prerequisite for these platforms is knowledge of the microsurgical anatomy of these working spaces.

The aim of the present study was to anatomically define and measure the intracranial cisterns utilised during keyhole neurosurgical approaches in a high-resolution Magnetic Resonance Imaging (MRI) brain atlas.

## MATERIALS AND METHODS

A literature search was performed to define the working spaces of the suprasellar, quadrigeminal and cerebellopontine cisterns [1]. The SRI24 multichannel atlas of normal human brain structure was used as a reference system [2]. The SRI24 atlas was recently developed using template-free registration of 3T MRI images of 24 normal control volunteers (12 male and 12 female; 12 young and 12 elderly), and is unique in being well suited to both spatial normalization and label propagation (atlas-based segmentation).

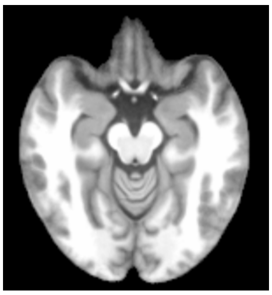


**Fig. 1** SRI24 Axial T1-weighted MRI illustrating the suprasellar cistern bordered by gyrus rectus of the frontal lobes anteriorly, uncus of the temproal lobes laterally, cerebral peduncles posterolaterally, and the interpeduncular cistern posteriorly.

Atlas files were converted to DICOM using MedCon v0.12.0. Two independent observers (HJM and AHH) measured distances on T1-weighted MRI using the OsiriX Imaging Software v5.6 (see Fig. 1), and segmented and measured volumes using itk-SNAP v2.4.0 [3]. Mean values for distances and volumes were calculated, and the concordance correlation coefficient between the two observers determined.

## RESULTS

The SRI24 atlas was crisp enough for region definition, allowing precise atlas-based segmentation. Distances and volumes are summarised in Table 1.

**Table. 1** Dimensions of the suprasellar, quadrigeminal and cerebellopontine cisterns. A-P = Anterior-Posterior; S-I = Superior-Inferior; Lat = Lateral; Vol = Volume.

| Cistern | A-P | S-I | Lat | Vol |
|---|---|---|---|---|
| Suprasellar | 25mm | 18mm | 20mm | 6525mm$^3$ |
| Quadrigeminal | 17mm | 16mm | 20mm | 2953mm$^3$ |
| Cerebellopontine | 20mm | 19mm | 15mm | 3428mm$^3$ |

The concordance correlation coefficient was: $\rho$ (precision) = 0.97, $C_b$ (accuracy) = 0.99, and $\rho_c = 0.96$.

## DISCUSSION

In this study we have successfully extracted information on the deep cisterns that are utilised in keyhole neurosurgical approaches using a novel MRI atlas that incorporates data from multiple volunteers while maintaining salient anatomical features. The suprasellar cistern was the largest of those assessed; suggesting that the keyhole supraorbital subfrontal approach may be most suitable as an index procedure for putative robotic platforms. It is likely that during actual operations the working spaces encountered will be greater as CSF is drained and instruments dynamically retract tissue.

## REFERENCES

[1] Baka JJ, and Spickler EM. Normal imaging anatomy of the suprasellar cistern and floor of the third ventricle. Semin Ultrasound CT MR. 1993; 14(3): 195-205.

[2] Rohlfing T, Zahr NM, Sullivan EV and Pfefferbaum A. The SRI24 multichannel atlas of normal adult human brain structure. Hum Brain Map. 2010; 31(5): 789-819.

[3] Yushkevich PA, Piven J, Hazlett HC, Smith RG, Ho S, Gee JC, and Gerig G. User-guided 3D active contour segmentation of anatomical structures: Significantly improved efficiency and reliability. Neuroimage 2006; 31(3): 1116-28.

# Developing a Training Tool for Intraoperative Mitral Valve Analysis

Neil A. Tenenholtz, Robert D. Howe

*School of Engineering and Applied Sciences, Harvard University*

*ntenenh@seas.harvard.edu*

## INTRODUCTION

The mitral valve is one of the four valves of the human heart. Serving as a passive check valve, a healthy mitral valve permits the flow of oxygenated blood from the left atrium to the left ventricle while preventing backflow. This is accomplished via the mutual collision of the leaflets and the tethering forces of the chordae tendineae (Figure 1). When backflow occurs, the preferred method of treatment is mitral valve repair.

Mitral valve repair is a technically challenging procedure in which the surgeon modifies the native valve tissue through a series of tissue resections and suturing. While the goal is to restore valve function, i.e., ensure proper valve closure under systolic load, doing so is difficult as the heart is arrested during the operation. As a result, rather than being directly observed, closed valve shape must be predicted through analysis of the flaccid valve and the surgeon's past experience.

In analyzing the valve, the goal is to identify regions of abnormal leaflet mobility. This is achieved by pulling the chordal insertions upward using a nerve hook. Regions of excessive or restricted leaflet motion are recorded [1]. With this information, the surgeon can then visualize and predict the shape of the loaded valve. In a pathological valve, the prediction is used to develop a repair plan to restore valve function. Therefore, not only must a surgeon be capable of implementing a desired set of valve modifications, he or she must also be able to analyze a valve intraoperatively to predict closed valve shape.

This work presents the first steps towards the development of a computer-based training platform for mitral valve repair. In it, we demonstrate it is feasible to construct a platform for assessing a user's ability to predict the closed valve shape of a flaccid valve.

## MATERIALS AND METHODS

*Simulation:* In prior work, we have developed and validated an interactive computer-based surgical simulator for valve repair [2]. The system accepts a subject-specific valve image as input and permits user interaction using a haptic input device (PHANTOM Omni). This allows for the valve to be rendered both visually and haptically. However, the use of a haptic device necessitates a 1 kHz update rate to ensure stability and haptic transparency. To produce such a fast simulation, a mass-spring approximation of a finite element model is implemented as mass-spring models are more computationally efficient than their finite element counterparts with a minimal change in accuracy [3]. Model parameters such as leaflet stiffness are taken from the results of ex-vivo mechanical testing found in literature.

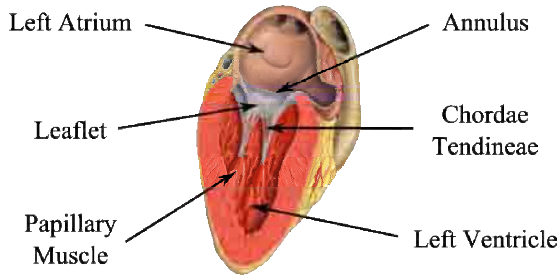



**Fig. 1** The mitral valve is a key cardiac structure that regulates the flow of oxygenated blood. (Image source: Patrick J. Lynch, medical illustrator, C. Carl Jaffe, MD, cardiologist).

Using the haptic stylus, not only can the user feel the leaflet tissue, but can also pull on a desired chordal-leaflet insertion point. To do so, a stiff spring-damper is engaged between the cursor and insertion point allowing for the stable bilateral application of forces to the user and the mesh (Figure 2) [4]. Prior to being rendered to the user, forces are scaled and transformed to align with the user's viewpoint.

*Evaluation:* This platform was used to assess the ability of subjects, namely 3rd year medical students and cardiac surgeons, to predict closed valve shape from an unpressurized valve. Subjects were first presented with visual-only renderings of four closed valves (Figure 3) with valve closure induced using the simulation platform prior to being presented to the user. Variations in closed valve shape resulted from differences in chord lengths and papillary locations (also generated with the

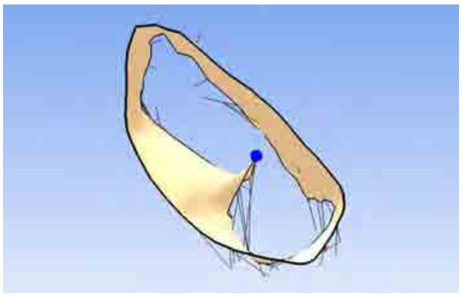


**Fig. 2** Subjects use the surgical simulator to analyze the mobility of leaflet segments. The blue sphere serves as the subjects' cursor.

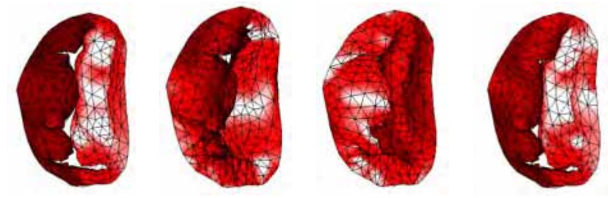


**Fig. 3** For each trial, subjects were presented with four choices of closed valve geometry and asked to select which one corresponded to the open valve presented. Note the differing locations of regurgitant orifces and/or prolapsing segments.

simulator). In an attempt to isolate the subjects' ability to predict closed valve shape, accompanying lesions typically associated with these conditions, such as changes in leaflet and annular geometry, were intentionally excluded. This was done to prevent the surgeons from integrating advanced pathology-specific knowledge that medical students might not possess.

After examining the four choices from all angles, the subjects were presented with an atrial view, that which is seen intraoperatively, of a single open, unpressurized valve on the simulation platform. They were allotted a maximum of 3 minutes to pull on various chordal insertion points using the haptic device with the goal of identifying regions of restricted and excessive leaflet motion. Upon completion of valve analysis, the subjects were again presented with the four closed valve choices and asked to select the one that he or she believed corresponded to the open valve presented. Answers and time elapsed during valve analysis were recorded. This process was repeated for a total of 10 trials per subject.

## RESULTS

Nine subjects were tested: 6 medical students and 3 cardiac surgeons. The average number of correct responses among the medical students and surgeons was 2.5 and 6.3 respectively (Figure 4). Surgeons performed better at a statistically significant level ($p=0.012$).

Time to perform valve analysis also varied between surgeons and medical students. While surgeons always used the full allotment of time (180s), medical students finished in less time ($p<0.001$), averaging only 90s per trial. This increase in speed was trial-dependent with later trials requiring less time to complete.

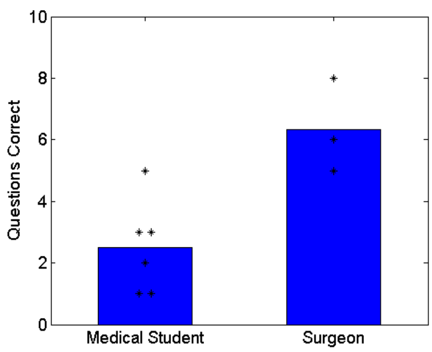



**Fig. 4** Mean performance of the subject populations is shown via the bar graph with individual subjects' scores overlayed.

## DISCUSSION

Despite a small sample size, the difference in accuracy between the two populations was statistically significant. This demonstrates not only the difficulty of the task, but also the importance of training. Even after three years of study, including coursework on cardiac pathophysiology, the medical students' responses were equivalent to random guessing. While this can be partially attributed to a less thorough understanding of mitral valve physiology, the different manner in which the two groups analyzed the valve was notable.

The cardiac surgeons were significantly more systematic in their analysis. The process was highly repeatable and consistent, always starting in the same region of the valve and progressing identically with variations occurring only after the entire valve was inspected. While this provided a consistent baseline for comparison, it also was more time-consuming explaining the significant difference in elapsed time. Conversely, the medical students used a more ad-hoc approach, pulling on all regions of the valve but in inconsistent orders and directions. Therefore, it was not surprising to see the best scores achieved by the cardiac surgeons with the top score achieved by the most experienced surgeon. All of this occurred despite the absence of traditional accompanying lesions and a preoperative diagnosis that cardiac surgeons typically receive.

In this work, we have demonstrated that our simulation platform is capable of assessing a subject's ability to analyze a mitral valve and predict closed valve shape. Given the demonstrated value of formalized training in valve analysis, we aim to couple this assessment technology with automated, personalized instruction to improve and accelerate the education of future cardiac surgeons.

## ACKNOWLEDGEMENTS

This work was supported by NIH grant R01 HL073647 and the Link Foundation Fellowship for Advanced Simulation and Training.

## REFERENCES


[1] Carpentier A, Adams DH, and Filsoufi F. Carpentier's Reconstructive Valve Surgery. Maryland Heights: Saunders Elsevier, 2010. Print.

[2] Tenenholtz NA, Hammer PE, Schneider RJ, Vasilyev NV, and Howe RD. On the Design of an Interactive, Patient-Specific Surgical Simulator for Mitral Valve Repair. IEEE/RSJ Intl. Conference on Intelligent Robots and Systems. 2011 Sept;1327-32.

[3] Hammer PE, Sacks MS, Del Nido PJ, and Howe RD. Mass-Spring Model for Simulation of Heart Valve Tissue Mechanical Behavior. Annals of Biomedical Engineering. 2011 June;39(6):1668-1679.

[4] Colgate JE, Stanley MC, and Brown JM. Issues in the Haptic Display of Tool Use. IEEE/RSJ Intl. Conference on Intelligent Robots and Systems. 1995 Aug:140-145.

# Anatomical Neck Dissection for Real Time Intraoperative *In Vivo In Situ* Soft Tissue Morphology Characterization Using Confocal Endomicroscopy

T.P. Chang, K. Sriskandarajah, T.P. Cundy, D.R. Leff, R.C. Newton, H.J. Marcus, A. Darzi, G.-Z. Yang

*The Hamlyn Centre for Robotic Surgery, Imperial College London, U.K.*
*t.chang@imperial.ac.uk*

## INTRODUCTION

Confocal endomicroscopy is a novel imaging tool that allows real-time morphological imaging at cellular and subcellular resolution. Over the last few years, its ability to differentiate characteristic morphological features of neoplastic and non-neoplastic changes of the gastrointestinal tract [1], biliary tree [1] and lung [2] has been increasingly recognised. However, its role outwith the endoluminal environment for surgical applications has been comparatively sparsely investigated. In particular, there is little reported on its ability to characterise morphological features beyond mucosal or luminal epithelial architecture. The aim of this feasibility study is to test the hypothesis that confocal endomicroscopy could be used to visualise soft tissue morphology in an intraoperative field.

## MATERIALS AND METHODS

Under the study protocol approved by the Home Office (No. 80/2297), a neck dissection was performed on an anaesthetised six-month-old white Landrace crossbreed female pig (70kg). A vertical midline incision was performed and the strap muscles, thymus, thyroid, carotid artery, internal jugular vein, trachea and esophagus carefully dissected (Figure 1) and the respective vascular pedicle / vasculature of thyroid and thymus preserved. Five mls of intravenous sodium fluorescein 10% *(Martindale's, UK)* was administered as tissue contrast and the confocal endomicroscopy miniprobe (2.6-mm diameter Ultra-Mini-O $^{TM}$) *(Mauna Kea Technologies, France)* was deployed in-situ. The miniprobe delivers a 488-nm-wavelength excitation laser light perpendicular to the surface of tissue at a confocal depth plane of 60-µm from the surface with an optical sectioning of 10-µm. The resulting emissions between 500- and 650-nm from fluorescing tissues were collected at 12 frames per second. Still confocal images were obtained with a field of view of 240-µm and lateral resolution of 1.4-µm. Real-time image mosaics (stitching of adjacent images next to each other) were created using Cellvizio, an image processing software.

## RESULTS

Within several minutes of intravenous administration of sodium fluorescein, the cellular boundaries of fat cells were easily identifiable as polygonal-shaped dark-coloured structures with thin hyperfluorescent borders. The longitudinal muscle fibers of both skeletal (strap muscles of the neck) and longitudinal muscles of the esophagus were visualised as long cylindrical structures separated by hyperfluorescent connective tissue with numerous cross-striations visible on skeletal muscles. The thyroid gland parenchyma had a distinctive appearance, with round- or ovoid-shaped follicular cells and a thin layer of hyperfluorescent secretory epithelium lining a central lumen filled with colloid. Within the cortex of the thymus gland, there were numerous vascular fibrous septae in between thymic lobules (Figure 2a-g). We were unable to visualise individual lymphocytes within the cortex of the thymus gland. There was no distinctive morphological architecture visualised on the tunica adventitia of major vessels of the neck.

## DISCUSSION AND CONCLUSION

It is evident that morphological architecture of most soft tissues within the intraoperative field of the neck could be visualised in real time using confocal endomicroscopy, hence suggesting that image acquisition of tissue morphology is not just limited to mucosal or epithelial linings of the gastrointestinal tract or lung, respectively. The clinical value of confocal endomicroscopy in neck dissection is likely to lie in its ability to identify parathyroid tissues during parathyroidectomy, and to differentiate malignant from unaffected lymph nodes. To this end, further work is planned to ascertain the morphological features of lymph nodes and parathyroid tissues. Whilst the flexibility of the miniaturised confocal miniprobe could be an advantage for deployment during minimal access neck surgery, one of its key ergonomic challenges of a hand-held probe is the surgeons' ability to consistently obtain high quality images in the presence of tissue deformation and hand tremor. This might warrant the use of a mechatronically enhanced or robotic assisted delivery platform to achieve slow and controlled actuated movements with precision.

## REFERENCES

[1] Wallace M, et al. Miami classification for probe-based confocal laser endomicroscopy. Endoscopy. 2011;43(10):882-91.

[2] Fuchs FS, et al. Confocal laser endomicroscopy for diagnosing lung cancer in vivo. Eur Respir J. 2012;[Epub ahead of print].

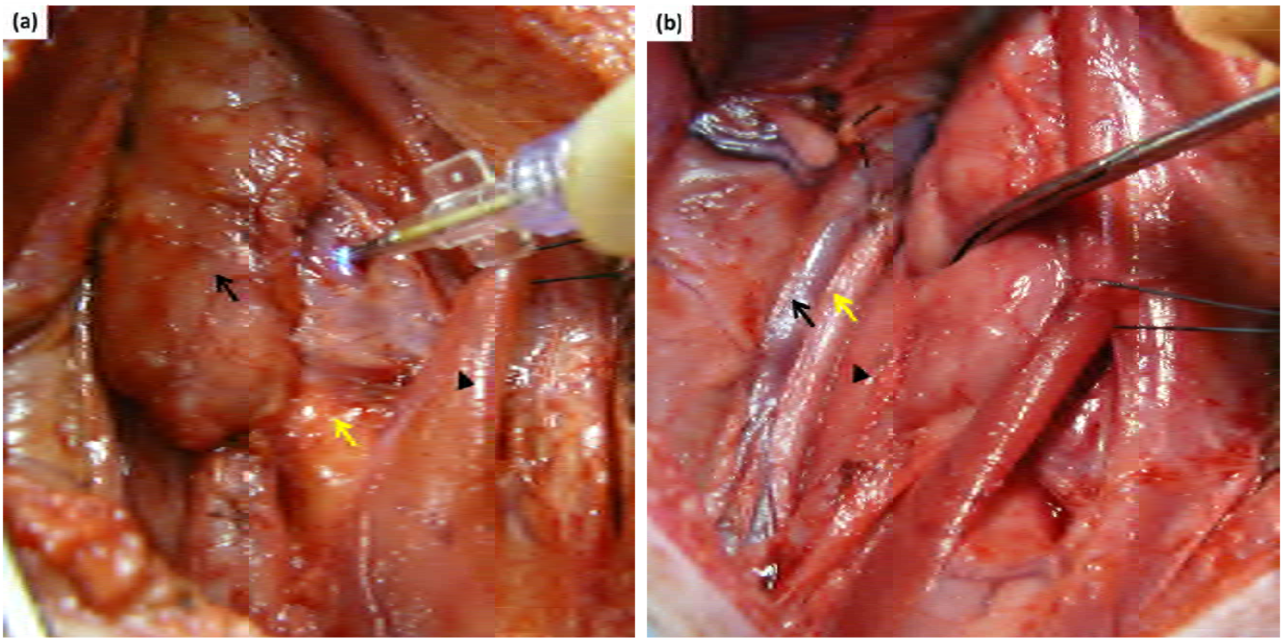



**Fig. 1** Intraoperative images of anatomical neck dissection in a porcine model. (a) Thyroid gland with a confocal endomicroscopy miniprobe deployed perpendicular to its surface, thymus (black arrow), trachea (yellow arrow) and strap muscles (arrowhead); (b) With the thymus retracted, the internal jugular vein (black arrow), carotid artery (yellow arrow) and esophagus (arrowhead) was easily visualised.

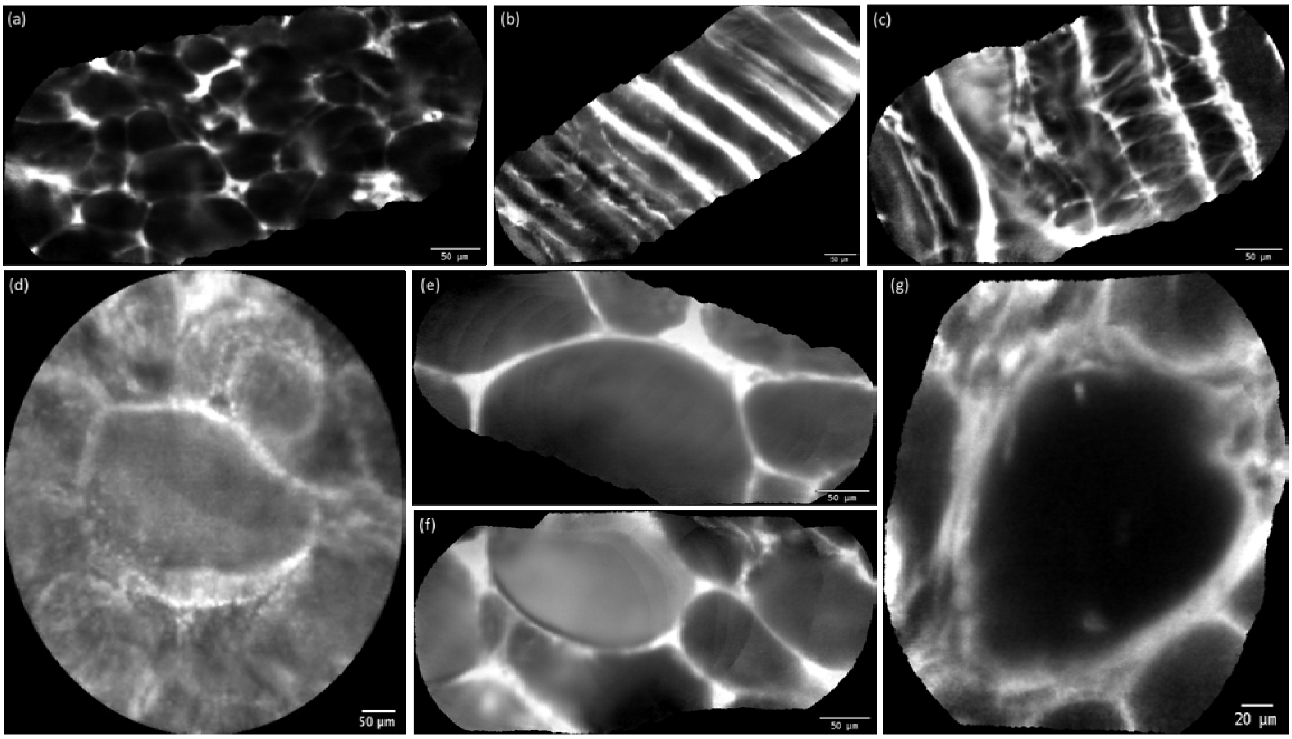



**Fig. 2** Real-time confocal endomicroscopy mosaics of soft tissues (a) Polygonal shaped fat cells; (b) cylindrical shaped longitudinal muscle cells of the esophagus; (c) striated cells of strap muscles; (d) Follicular cells of the thyroid gland using topical application of 0.05% acriflavine hydrochloride as contrast agent on cadaveric porcine models; (e) In vivo thyroid follicular cells; (f) Opaque appearance of colloid in the central lumen of thyroid follicular cells; (g) Thymus lobule with a surrounding vascular septa.

# Pre-clinical Validation and Assessment of an Innovative Bi-manual Surgical Robot for Single-Port Laparoscopy

G. Petroni, M. Niccolini, S. Tognarelli, C. Quaglia, S. Caccavaro, A. Menciassi, P. Dario

*The BioRobotics Institute, Scuola Superiore Sant'Anna, Pisa, Italy*
*g.petroni@sssup.it*

## INTRODUCTION

Single-port laparoscopy (SPL) is currently recognized as a revolutionary surgical technique that exploits a single incision (most commonly at the umbilicus level) for inserting multiple surgical instruments into the abdominal cavity, thus guaranteeing a scarless surgical intervention [1]. Despite the improved cosmesis, SPL introduces several technical restrictions for the surgeon, e.g. limited internal workspace, difficulty of triangulation and fatigue [2]. In order to overcome these drawbacks, novel instruments and innovative technical solutions are mandatory. However, robotic systems specifically designed for SPL are limited to research prototypes. The common thread of such systems is to bring an increased number of Degrees of Freedoms (DoFs) intracorporeally, thereby augmenting the available workspace and the easy of surgical manipulation [3, 4].

In this framework, a novel teleoperated robotic system for SPL has been developed by the authors group. SPRINT (Single-Port lapaRoscopy bImaNual roboT) robot is a master–slave teleoperated robotic platform for bimanual single-access surgical interventions [5]. It consists of a bimanual slave manipulator, a stereoscopic camera (Karl Storz, Tuttlingen, Germany) and a dedicated master console, through which the hand movements of the surgeon are translated and replicated by the robotic arms.



**Fig. 1 The upgraded version of the SPRINT system**: (Left) robotic platform and (Right) the console (developed at the Hamlyn Centre for Robotic Surgery by Prof. Guang-Zhong Yang).

Each robotic arm has six active DoFs plus the gripper, and by virtue of its mechanical design it achieves the workspace necessary for performing complex surgical interventions [5]. The joints sequence in each arm is a Roll-Pitch-Pitch serial chain (proximal joints), followed by a Roll-Pitch-Roll combination (distal joints). The proximal joints comprise the shoulder and the elbow mechanisms, which are actuated by external and on-board motors respectively. As for the elbow, the actuation of the distal joints (forearm, wrist, and tool rotation) is operated by on-board motors, whereas the actuation of the gripper is performed by another external motor through a sheath-cable mechanism.

As reported in [6], the dexterity of the robotic arms in a master–slave teleoperated configuration has been already verified. However, a new session test has been carried on for validating and assessing an upgraded version of the aforementioned robotic system.

From the slave side, the main advancement regarded the introduction of a new actuation mechanism of the shoulders that allows for the insertion of both the arms through an introducer of 34 mm in diameter (Fig. 1 Left). From the master side, the new master console consists of three screens (Fig.1 Right): the middle one is a 3D full-HD passive monitor that displays the images coming from the stereoscopic camera, the other two provide the surgeon with additional data and settings.

Two Phantom Omni haptic devices (Sensable Technologies Inc., Woburn, MA) and a foot pedal complete the console and allow for controlling the robot as described in [7].

As anticipated, this paper illustrates the validation of a new robotic system as an upgrade of the SPRINT robot reported in [5]. To this purpose, 3 surgeons who have never been involved in robotic assistive laparoscopy or SPL (herein referred as not experienced surgeons), and 16 student surgeons have been included in the study. Besides, the results of this study have been compared with the ones obtained in [6] with experienced surgeons in robotic surgery.

## MATERIALS AND METHODS

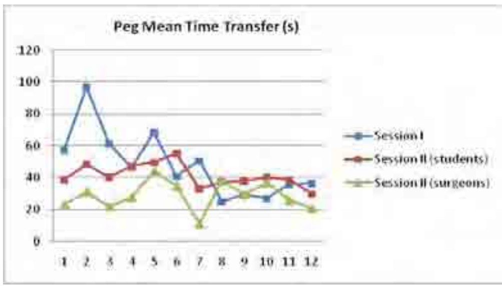
Keeping in mind that surgery can be summarized in three very basic tasks, which are exposure (grasping and lifting) dissection and tissue approximation (suturing), pick and place exercises and intracorporeal suturing tasks in a trainer box assembly were designed for a reliable pre-clinical system validation and assessment.

The first exercise consisted in a peg-transfer setup that reproduces the first task of the SAGES Fundamentals of Laparoscopy manual skills (FLS) tests [8]. The task requires the operator to pick up a peg with one robotic

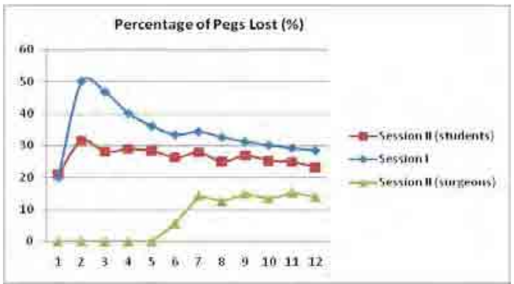
arm, transfer it to the other arm, and then place it to the other side of the pegboard respecting the numbers on the peg holder (Fig. 1 Left). The exercise was considered full-finished once all pegs were transferred, successfully or not, from right to left and vice versa. Therefore, the time spent for each peg transfer was recorded. The second test required the surgeon to perform suturing with intracorporeal knots. In this case, the time needed to tie one knot has been recorded for comparison purposes. Finally, each subject was asked to fill in a questionnaire for the qualitative evaluation of the different components/characteristics of the whole platform.

## RESULTS

The mean time taken for each peg transfer is showed in Fig. 2a. The trend of the curves indicates that the overall system allows for the completion of the tests without relevant issues (1 out of 3 peg lost after the fourth peg transfer, Fig. 2b).




(a)




(b)

**Fig. 2** (a) Peg mean transfer time, (b) percentage of pegs lost. Session I relates to the experiments performed in [6].

On the other hand, besides the fact that all the users have completed the suturing task, a large difference between experienced and not experienced surgeons emerged. The mean time to perform a surgical knot by an experienced surgeon was about 331 s, while a not experienced surgeon took about 660 s. This may suggest that while a lack of experience with robotic assistive laparoscopy can be an advantage for performing simple tasks as pick and place (Fig. 2), it becomes a drawback in case of challenging tasks such as suturing. In fact, during pick and place, experienced surgeons can be unconscionably brought to reproduce the same movements they are used to, thus resulting in a slightly deficient performance compared to not experienced surgeons. On the other hand a more complex task such as suturing re-establishes the performance hierarchies. Besides the session tests described above, one of the experienced surgeons that participated in the first test session [6] has been asked to perform the test with the upgraded version of the SPRINT platform. The measured performance, reported in Table 1, partially confirms that large timings obtained for the suturing task have to be addressed to the lack of training in robotic surgery of not experienced surgeons.

**Table 1** Experienced Surgeon: comparison between test session 1 and 2, by using the original SPRINT robot [5] and the upgraded version.

| | **SPRINT** | **SPRINT UP** |
|---|---|---|
| Peg Mean Time Transfer (s) | 24.80 | 27.18 |
| Percentage of Lost Pegs (%) | 12.5 | 8.3 |
| Suturing Time (s) | 197 | 158 |

As regards the qualitative evaluation of the system performance, we observed that each subject has a very personal judgment of the platform, especially for what concern the quality of the 3D viewing. On the other hand the majority of the subjects agree in the judgment of intuitiveness, actuation by foot, available workspace and ergonomics of the console. More precisely the overall system has been judged to be comfortable, intuitive and with a large enough workspace. Contrary, the needle driving grasping force was judged not fully satisfactory for an effective suturing task.

## DISCUSSION

Pre-clinical validation of a new robotic platform for SPL has been completed with quite satisfactory results. A protocol inspired by FLS tests has been followed: pick and place and suturing tests have been completed by all the surgeons, thus demonstrating the feasibility of the design and the overall usability of the system.

Experimental in vivo testing on large animals (pigs) is planned in future works.

## REFERENCES


[1] Romanelli J, et al. Single-port laparoscopic surgery: an overview. Surg Endosc 2009; 23:1419–1427.

[2] Galvao Neto M, et al. Single port laparoscopic access surgery. Tech Gastrointest Endosc 2009; 11:84–93.

[3] Lehman AC, et al. Dexterous miniature robot for advanced minimally invasive surgery. Surg Endosc 2011; 25:119–23.

[4] Phee S, et al. Natural orifice transgastric endoscopic wedge hepatic resection in an experimental model using an intuitively controlled master and slave transluminal endoscopic robot (MASTER). Surg Endosc. 2010; 24:2293–98.

[5] Piccigallo M, et al. Design of a novel bimanual robotic system for single port laparoscopy. IEEE/ASME Trans Mechatronics 2010 Dec; 15(6): 871-78.

[6] Petroni G., et al. A novel intracorporeal assembling robotic system for single-port laparoscopic surgery. Surg Endosc. 2013 Feb; 27(2):665-70.

[7] Niccolini et al, Real-Time Control Architecture of a Novel Single-Port lapaRoscopy bimaNual roboT (SPRINT), Robotics and Automation (ICRA), 2012.

[8] Derossis AM, et al. Development of a model for training and evaluation of laparoscopic skills. Am J Surg 1998; 175: 482–87.

# Image Guidance Framework with Endoscopic Video for Automated Robotic Anastomosis in a Paediatric Setting

Thomas Looi[1], Benny Yeung[2], Manickam Umasuthan,[2] James M. Drake[1]

[1]Hospital for Sick Children, Toronto, Ontario, Canada

[2]MDA Corporation, Brampton, Ontario, Canada
thomas.looi@sickkids.ca

## INTRODUCTION

Minimally invasive surgery (MIS) and laparoscopic tools have revolutionized surgical intervention by allowing surgeons to operate via 5-10mm tools inserted in to 3-4 trocars on the body [1]. The impact has shortened patient recovery time but it has increased the operation time due to the lack of dexterity of laparoscopic tools. A dexterous robotic tool would help overcome these constraints. In addition, advances in medical imaging such as high definition endoscopes and interventional MR imaging present an opportunity to integrate the various imaging modalities with a robotic tool [2]. Anastomosis has been selected as a surgical task because it is a challenging yet basic task to perform laparoscopically and also present in all specialities. For this project, we present early experiences in using an endoscope-based image guidance framework to automate anastomosis. In particular, the image guidance framework is designed for paediatric patients where the volume and size constraints are more pronounced.

## MATERIALS AND METHODS

A robotic system, KidArm, was developed to use image guidance as a method to automate laparoscopic anastomosis in paediatric patients. KidsArm consists of user interface, image processing unit (IPU), robotic arm and anastomosis tool. (Fig. 1)

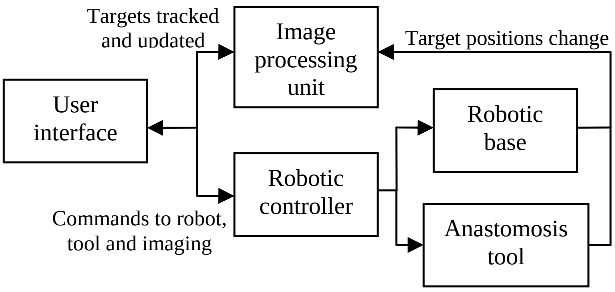



**Fig. 1** KidsArm System Design

The user interface is a dual screen workstation with the top screen capable of showing a 3D depth map and stereoscopic 3D images while the bottom is a touch screen interface for the surgeon to select suture points. The image processing unit is a pair of Basler cameras placed side by side (~3cm separation) that simulate the endoscope view and provide input in to image processing libraries. The robotic arm is a 6 degree of freedom (DOF) Denso VP6 robot. The anastomosis tool is a modified Covidien SilS Stitch™ [3] which has 2 additional joints, roll and pitch, to provide more dexterity with an ATI Mini40 6 DOF force-torque sensor mounted at the interface between the anastomosis tool and Denso VP6. An additional flexible biopsy tool has been provided for future work on automated knot management. The total DOF in the system is 8. For control and integration, robot kinematics and controllers have been designed in Simulink and implemented via Quanser QuARC interface.



**Fig. 2** Left: Robotic arm, Right: Anastomosis tool

The general testing procedure involved the following: the surgeon draws the area of interest on the touch screen interface, the IPU generates a 3D point cloud of the target area, the surgeon selects 3-5 suture points on the vessel opening (area to be sutured) and initiates the procedure on the first point, the IPU performs dynamic tracking and provides trajectory information to the robotic tip.

More precisely, the IPU provides image guidance to the robot and tool by using stereo cameras and lighting to create the 3D point cloud and track the lumen. For the image processing, OpenCV and PCL libraries were used for 3D reconstruction, rectification and camera calibration. Image feature extraction, tool target tracking and deformable lumen tracking algorithms were implemented as part of this project. The data flow diagram of the IPU are shown in Fig. 3.

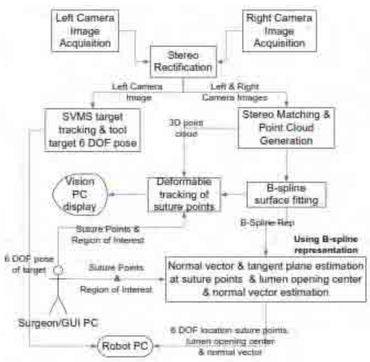



**Fig. 3** Image Processing Unit Data Flow

The 3D point cloud is generated with the semi-global block matching function from the OpenCV libraries where the IPU generates a depth map based on surface features [4]. For testing, a projector applied a set of features on to silicone lumen to make them representative of tissue.

A variety of descriptors have been previously studied for MIS reconstruction and tracking [5]. A 3D based approach was used for deformable vessel tracking. The 2D image features are matched between the left and right images to compute their 3D location. The matched 2D features was filtered by the epipolar constraint and only the 2D features whose disparity values were within the predefined range will pass to the next step. The rigid transformation is solved by 1) matching the 2D features (SIFT) between the previous and current images to establish the correspondences between the 2D-3D features; 2) Using Random Sample Consensus(RANSAC) to solve the 6DOFs rigid transformation by using the 3D locations of the 2D features computed in the previous step. The 3D point cloud obtained at each frame was first fused with the left camera image features and then fitted with a B-Spline surface. From this representation, a coordinate frame is computed at each suture point.

When the user selects a suture point from the User Interface, the IPU converts that into a 3D point along the surface of the B-spline model. Using multiple user-selected suture points, the center of the vessel opening is calculated based on the instantaneous surface normal from the B-spline model. Both the suture point and the location of the vessel opening are sent over to the Robot PC, such that the Robotic Controller can insert the suture needle into the vessel opening center.

When the target vessel is deformed, the B-spline model accommodates. Using the established geometric relationship of each suture point with respect to the structure of the vessel, the suture point and vessel openings are updated such that the system can react to the change in position or form of the target and adjust the motion as required.

The IPU also detects the unique 3D features on the Tool target that consists of a square patch of black and white features. The target mounting near the tip of the Anastomosis Tool gives the true position feedback of the Point-of-Resolution (POR) to the Robotic Controller, which is tracked by the IPU via the left camera image.

Together with the position of the suture point(s) and the Tool POR position, the IPU provides input to the control system for generating the motion command required to bring the tip of the Anastomosis Tool to the suture point via the vessel opening calculated. Registration of the Tool tip and the suture point positions onto the camera frame is done automatically.

## RESULTS

For testing, the image guidance framework was tested under 2 scenarios: a ridge-based silicone test pad with a 4cm long x 2mm gap (side-to-side anastomosis) and a pair of silicone tubes (~1cm diameter and ~4cm long) simulating human lumen (end-to-end anastomosis). With the IPU algorithm, the system successfully generated 3D point clouds for two scenarios. Fig. 4 is a 3D point cloud of simulated human lumen.

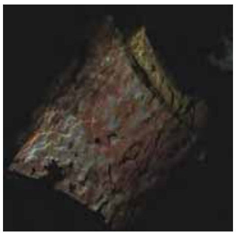


**Fig. 4** 3D Point Cloud of Silicone Lumen

Using the IPU as part of the KidsArm system, the framework was used to select target points and automatically suture the 3-5 points on each test scenario. With the first scenario, the IPU enabled KidsArm to successfully perform 3 automatic sutures (see Fig. 5) to within approximate 2 mm of the target points. The second scenario was more challenging as the physical joint limits and tool size prevented KidsArm from suturing both lumen. More work is required to miniaturize the tool to avoid the joint limits. However, for a single lumen, a total of 3 sutures were completed with similar accuracy.

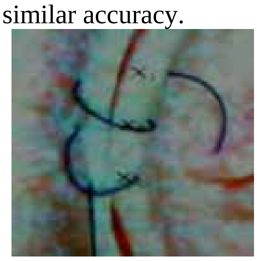


**Fig. 5** Automated side-to-side suturing

## DISCUSSION

Based on the results, it is possible to use a pair of cameras to simulate stereo endoscopic video as a means to provide image guidance for automated robotic anastomosis. The availability of natural features and deformable tracking remains a challenge. For the silicone samples, this was overcome using artificially created features of the vessels. However, this may prove to be impractical for in-vivo testing. In terms of deformable tracking, the side-to-side suturing scenario showed that our proposed IPU can perform in this constraint. In the end-to-end suturing, the deformations are greater and the vessel placement presents a challenge with respect to the robot and tool workspace. For future work, we believe that an enlarged workspace and field of view will enable image-guided anastomosis of tubular vessels.

## REFERENCES


[1] http://en.wikipedia.org/wiki/Laparoscopic_surgery

[2] TM Peters. "Image-guidance for surgical procedures". Physics in Medicine and Biology. 2006. 51:505-540.

[3] SILStitch: http://www.covidien.com/silsstitch/pages.aspx

[4] G Bradski and A Kaehler. Learning OpenCV. O'Reilly 2008.

[5] P Mountney et al. "A Probabilistic Framework for Tracking Deformable Soft Tissue in Minimally Invasive Surgery". Lecture Notes in Computer Science, 2005, Vol 3750:139-146.

# Robotic Thyroidectomy: A Prospective Case Control Study

A. Arora[1], S. Sharma[1], K. Muthuswamy[1], Z. Awad[1], J. Budge[1], A.Darzi[2], F. Palazzo[1], N.Tolley[1]

[1]*Dept. of Endocrine and Thyroid Surgery, Imperial College Healthcare NHS Trust*

[2]*Dept. of Biosurgery and Surgical Technology, Imperial College London*

*asitarora@doctors.org.uk*

## INTRODUCTION

Robotic thyroidectomy (RT) is a novel surgical technique which uses the daVinci robot through an axillary incision. It was pioneered in South Korea where small thyroid nodules (<1cm) account for the vast majority of cases due to a routine population screening programme. The technique has not been evaluated in a UK population. The objective was to compare RT with conventional surgery for performing hemithyroidectomy.

## METHOD

An ethically approved prospective case control study was conducted (Jan 2010-12). Fifteen patients underwent RT and another fifteen had conventional surgery. Patients with nodules >7cm, thyroiditis or cytology suggesting malignancy were excluded. Operative outcome measures included procedure time, blood loss and complications. Patient reported outcome measures included pain, scar cosmesis, voice handicap, swallow dysfunction and quality of life (QoL) using validated tools. Mean follow-up was 10 months (range: 3-12 months).

## RESULTS

There was no difference between the 2 groups in terms of mean BMI, age, scar length or follow up timeframe. The thyroid nodule was completely excised in all patients with no conversions in the RT group. The mean size of the lobe excised was significantly larger in the conventional group (6.1cm control v 5cm RT p=0.01). Laryngoscopy confirmed normal post-operative vocal cord function in 29/30 cases. In the RT cohort there was 1 unilateral recurrent laryngeal nerve paresis and 1 episode of shoulder dysfunction both resolving by 4 weeks. One further patient developed a seroma which required aspiration. Mean blood loss was comparable (40ml RT vs 30ml control). Mean operative time was significantly higher in RT (228min vs 85min p=0.01). Scar cosmesis was superior in RT from 2 weeks to 12 months post-op (79% vs 62% p=0.05 and 99% vs 90% p=0.02 respectively). There was no difference between the groups regarding pain, voice handicap, swallow or QoL following surgery.

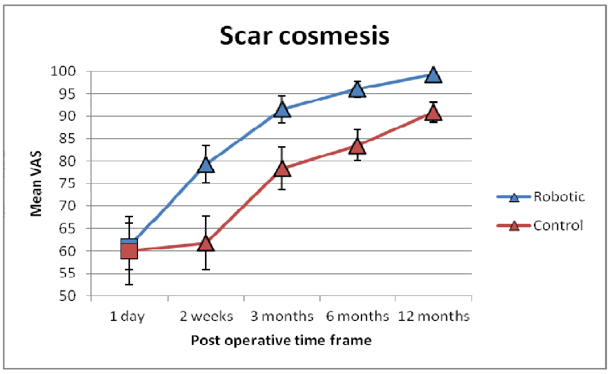



**Fig. 1** Scar Cosmesis: 100-0 VAS where 100 represents the best outcome score. The RT cohort had statistically significantly higher mean scores (represented by triangles) from 2 weeks to 1 year (p=0.05, 0.03, 0.01, 0.02).

## DISCUSSION

Far from being minimally invasive, RT involves additional dissection and risk to neurovascular structures not typically associated with thyroid surgery. The primary advantage is the avoidance of a neck scar. This is desirable in selected patients with a tendency for hypertrophic scarring. RT is safe, feasible and achieved superior cosmesis at the expense of time and cost. One patient with pre-existing osteoarthritis of the shoulder joint had dysfunction. Nerve conduction studies excluded brachial plexus neuropraxia. Subsequent arm position was modified from that popularised by Chung [1]. Improvement in trans-axillary exposure is warranted; the treatment rationale in the UK and US differs with significantly larger thyroid nodules undergoing surgery in a patient population which has a significantly larger BMI [2]. Validated training methods are essential for safe adoption. A randomised clinical study is needed to establish the clinical efficacy compared with conventional surgery.

## REFERENCES

[1] Kang SW et al. Initial experience with robot-assisted modified radical neck dissection for the management of thyroid carcinoma with lateral neck node metastasis. *Surgery.* 148:1214-1221, 2010

[2] Kandil et al. Robotic transaxillary thyroidectomy: an examination of the first 100 cases Am Coll Surg. 2012 Apr; 214(4): 558-64.

# Design and FEM Simulation of a Miniaturized Wristed Surgical Grasper

C.A. Seneci, J. Shang, G.-Z. Yang

*The Hamlyn Centre for Robotic Surgery, Imperial College London*
*c.seneci@imperial.ac.uk*

## INTRODUCTION

The development of minimally invasive and flexible access surgery gives rise to the need of surgical tools that can enhance surgeons' dexterity for manipulating tissues in narrow spaces [1]. The design also has to meet stringent safety requirements. Consequently, the robustness of the surgical tools needs to be optimized, taking into account the operating scenario. This work focuses on the design of a miniaturized wristed surgical grasper, with high robustness and dexterity.

## DESIGN

This work aims to develop a high-dexterity wristed instrument with compact sizes that can be passed through the instrument channels of the device described in [2]. Another important constraint considered, was the use of two hinge-joints design, in order to obtain sharp bending (Fig 1) of the tool, which are not often guaranteed by the use of other flexible technologies [2]. Thus, this wristed surgical tool incorporates 3 Degrees-of-Freedom (DoFs) with two pin-joints pivots laying on perpendicular planes, and the actuation of the jaws. In order to control the tool, 5 tendons are needed, each bending is driven by an antagonistic pair of tendons and the last tendon is used to close the jaws. A torsional spring is used to open the jaws when the tendon is released. The wristed grasper developed results to have very compact sizes, with a maximum diameter of 4.8mm and a length of 15mm, considering the distance between the first bending axis and the tip of the jaws.

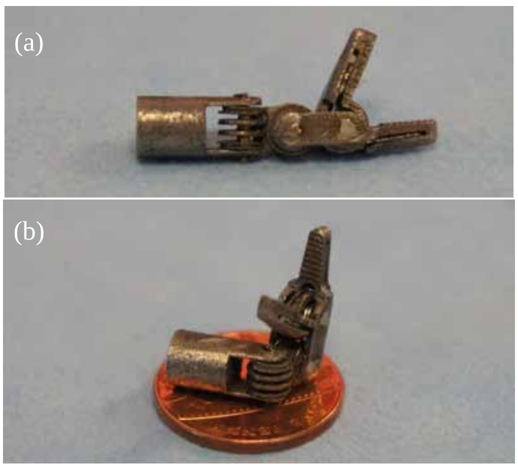



**Fig. 1** Scaled-up (20% bigger) sintered prototype. Straight (a) and Bent (b) configuration.

Starting from the proximal extremity of the tool (Fig. 2), a base allocates the holes through which two pins allow the core joint to rotate around the vertical axis. The core of the instrument is composed of a series of disks, together with six rolls, to keep the tendons in the centre of rotation, minimizing the coupling effect of the serial-tendon architecture. Two pulleys are used to control the bending in the horizontal plane of the core element. The same idea of small pins and pulleys is used to connect the core element with the first jaw. The rotation axis of the first jaw is horizontal; therefore the jaw inclination in the vertical plane can be controlled through the tendons attached to the lateral pulleys. Finally, the second jaw is connected to the first one thanks to a pulley and a pin. In the jaws two groves are realized to allocate the torsional spring for the opening function. Each pin joint can rotate in the range ±90°, thus the maximum workspace of the grasper looks like half a three-dimensional ellipsoid, with 15mm height and 11.3mm base-radius.

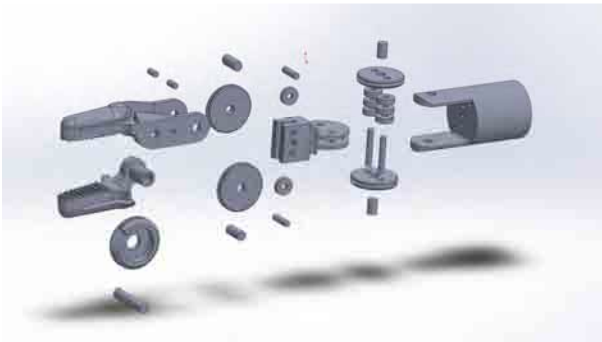


**Fig. 2** Exploded view of the CAD model.

## FEM SIMULATIONS

Simulation of four usage scenarios where the grasper interacts with tissue is conducted. The material of base, core element, pulleys and jaw is stainless martensitic steel, with aging treatment and ultimate tensile strength of 2000 MPa. The material to model the pins is spring steel ASTM A228 with ultimate tensile strength of 2300 MPa and finally the rolls have been chosen to be in titanium alloy (Ti-6Al-7Nb) with an ultimate tensile strength of 1000 MPa. In spite of the biocompatibility of the materials, the prototype (Fig. 1) has been manufactured with brass rolls for its malleability. Other assumptions that have been taken into account are related to the interaction of the tool with the tissues. In [4], it is shown that surgeons can apply maximum 10N on the tissue using laparoscopic tools. While with more focus on different types of tissue it is possible to estimate the contact interaction force of the grasper according to the softness of the tissue. In example as shown in [5], the pressure that the grasper applies on the

tissue varies from 10kPa (Colon) to 60 kPa (Liver). Consequently, considering the worst-case scenario with 60kPa, the jaws geometry presented in the paper produces a 4.8N force. Consequently, a 10N load is representative of an intense grasping action; therefore it has been uniformly applied to the 6x2mm jaws in the simulations. Considering the pulley radius of 2.14mm, the tendon needs to be tensioned about 15N. The presence of the tendons has been modelled through pressure distribution on the elements composing the tool, avoiding creating a 3D model. To find the equilibrium between forces and reactions, the FEM problem has been considered to be stationary, so a linear direct solver has been implemented. Tetrahedral elements have been used to mesh the model, considering contact interactions between the different parts. The minimum mesh element size has chosen to be 0.2mm, with a growing rate of 1.2 between neighbouring elements.

## RESULTS

The simulation results show that the compact design of the instrument is suitable for surgical applications. It can be seen from the simulation results that the places where the Von Mises stress is higher are in correspondence of the connection between the tendons and the pulleys, and of the contact component-pins. Also, it is evident that the concentration of stress at the base of the joint is due to the absence of larger fillets. The grasper has been found to be strong enough to lift a load of 500g. A potential limitation could be found in the tendons or in the arm onto which the wristed tool is mounted. These could result to be less strong than the surgical tool limiting the applicable force. Between the different scenarios, the last one resulted to be the most critical, with a high concentration of stress in the core element. This is because the middle part presents a grove to allow the passage of the tendon for closing function. Since the induced stress has a limited impact compared to the materials resistance, the design is safe for general surgical use.

## CONCLUSION

In this paper, a miniaturized wristed surgical tool is proposed, which is shown to be compact and dexterous. The FEM simulations show that the design is robust to be used for minimally invasive surgery.

## REFERENCES


[1] H. Yamashita, K. Matsumiya, K. Masamune, H. Liao, T. Chiba, T. Dohi: Miniature Bending Manipulator for Fetoscopic Intrauterine Laser Therapy to Treat Twin-to-Twin Transfusion Syndrome. Surgical Endoscopy 22, 430–435 2008.

[2] Jianzhong Shang, Christopher J. Payne, James Clark, David P. Noonan, Ka-Wai Kwok, Ara Darzi and Guang-Zhong Yang, Design of a Multitasking Robotic Platform with Flexible Arms and Articulated Head for Minimally Invasive Surgery, International Conference on Intelligent Robots and Systems IEEE/RSJ(2012) .

[3] G. T. Sung[a], I. S. Gill; Robotic laparoscopic surgery: a comparison of the da Vinci and Zeus systems; Elsevier; Urology; Volume 58, Issue 6, December 2001, Pages 893–898.

[4] J. D. Brown; J. Rosen; L. Chang M.D; M. N. Sinanan M.D.; B. Hannaford; Quantifying Surgeon Grasping Mechanics in Laparoscopy Using the Blue DRAGON System; Studies in Health Technology and Informatics - Medicine Meets Virtual Reality, Newport Beach, CA, January 2004.

[5] J. Rosen, B. Hannaford, M. MacFarlane , M. Sinanan; Force Controlled and Teleoperated Endoscopic Grasper for Minimally Invasive Surgery - Experimental Performance Evaluation; IEEE Transactions on Biomedical Engineering, 1999.

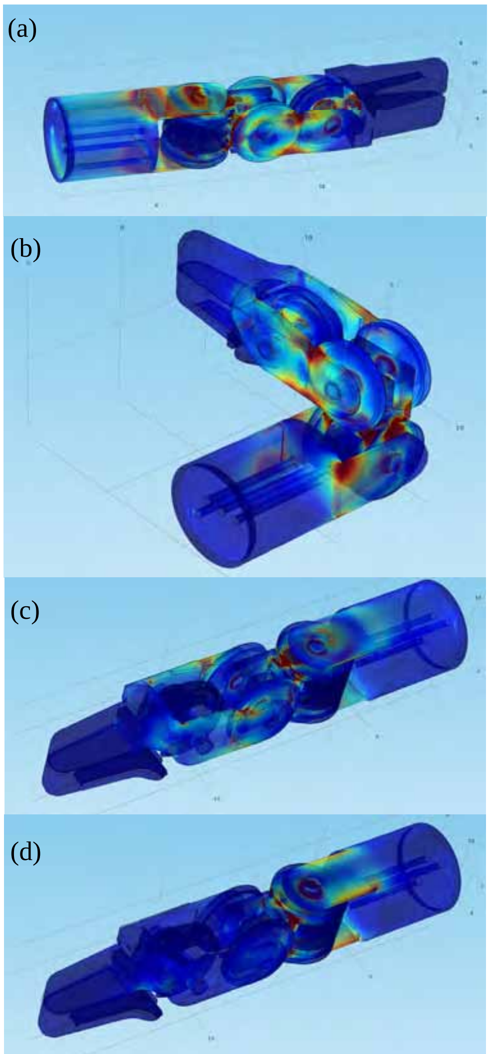




**Fig. 3** Scenario 1: grasping with straight joint. A grasping force (15N) has been applied to the superior jaw. The maximum stress has been calculated to be about 1MPa (a). Scenario 2: grasping with bent joint. A grasping force (15N) has been applied. Both the joints have been bent (90°). The maximum stress resulted about 3Mpa (b). Scenario 3: Lifting of 500g load. A load (5N) has been applied to the tip of the jaws and this generated a maximum stress of 720Mpa (c). Scenario 4: 5N later force. A lateral force (5N) has been applied to the jaws. This generated the higher stress with a maximum peak of 1300MPa (d).

# A Bio-galvanic Approach to Tissue Characterisation: Technological Considerations

J.H. Chandler[1], A. Hood[1], P.R. Culmer[1], D. Jayne[2], A. Neville[1]

[1]School of Mechanical Engineering, University of Leeds
[2]Leeds Academic Surgical Unit, St. James's University Hospital, Leeds
mn07jhc@leeds.ac.uk

## INTRODUCTION

Minimally invasive surgery is increasingly common in the treatment of cancer and has facilitated a move toward personalised surgery. This has driven clinical demand for new instrumentation that provides surgeons with improved intra-operative information, particularly to assess and differentiate between types of tissues. Current options are scarce and prognosis is typically made post operatively. The flow characteristics of bio-galvanic current have been proposed as a means to distinguish tissue type and health [1, 2]. In this scenario tissue acts as a salt bridge between two dissimilar metal interfaces. The specific electrode/electrolyte reactions determine the potential difference across the cell. Characterisation of the salt bridge resistance is possible through measurement of the combined system when current levels are modulated using external resistors. The apparent simplicity, relative to active frequency based techniques such as bioimpedance spectroscopy [3, 4], makes bio-galvanic characterisation a promising technique for intra-operative tissue characterisation. However the validity of assumptions made regarding the electrode/tissue interface reactions and mechanical contact conditions require further assessment prior to its application in clinical tissue characterisation.

## MATERIALS AND METHODS

**Bio-Galvanic Approach**: A number of processes are undertaken when determining the internal resistance of a salt bridge (e.g. biological tissue): (1) establishing the interface potentials through wet electrode/tissue contact, (2) forming a cell using an external resistance, (3) varying the level of external resistance on the cell and measuring the current response, and (4) analysing the measured data using a suitable model to determine the internal resistance. One additional step that can be taken is normalisation to the cell geometry to account for the electrode contact area and separation; results presented here are not subjected to this process in order to focus on fundamental bio-galvanic characteristics.

**Measurement Studies**: Measurements were conducted on electronic circuit models, salt solutions and on fresh *ex-vivo* porcine tissues. Animals used were bred and sacrificed in accordance with Home Office regulations (Animals [Scientific Procedures] Act 1986). Electrode materials used were zinc and copper in all cases with the half cell reactions and electrode potentials (vs. a standard hydrogen electrode) proposed by Golberg et al. [1] of:

$$Zn(s) \rightarrow Zn^{2+}(aq) + 2e^- \qquad E^0 = 0.76V \text{ (SHE)}$$

$$2H^+(aq) + 2e^- \rightarrow H_2(g) \qquad E^0 = 0.00V \text{ (SHE)}$$

Giving the full cell reaction and galvanic potential of:

$$Zn(s) + 2H^+(aq) \rightarrow Zn^{2+}(aq) + H_2(g) \qquad \Delta E^0 = 0.76V$$

**Characterisation Method:** The polished electrode surfaces were contacted with wet tissue and subsequently connected in series with an external resistance. Custom electronics and control software (LabVIEW, National Instruments) switched the external resistance between discrete values, thereby altering the current flow through the cell. Figure 1 schematically illustrates the implemented system, where the current is determined by the voltage drop, $V_2$ across the external resistance, $R_{EXT}$. The bio-galvanic cell is modelled as an ideal power source, producing a voltage equal to the open circuit galvanic potential $(OCP)$,in series with a fixed internal resistance, $R_{INT}$. Using Ohm's law the measured voltage $V_2$ can be related to the internal resistance as shown in equation 1.

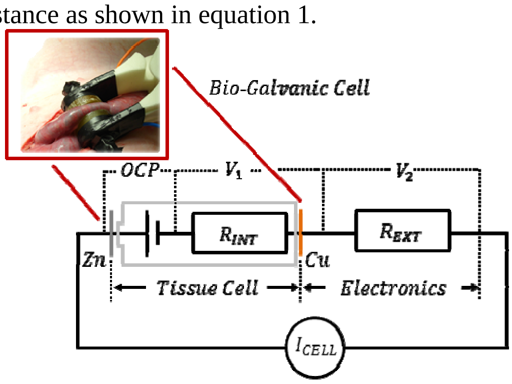



**Fig. 1** Proposed equivalent electrical model of the bio-galvanic cell under characterisation.

$$\boldsymbol{V_2} = \frac{OCP}{(\boldsymbol{R_{EXT}} + R_{INT})}\boldsymbol{R_{EXT}} \qquad (1)$$

Where $\boldsymbol{V_2}$ and $\boldsymbol{R_{EXT}}$ represent the vectors of measured voltages and corresponding external resistance values respectively. Equation 1 can be solved for $OCP$ and $R_{INT}$ using the least squares Levenburg-Marquardt algorithm [5] and re-presented as a continuous function as shown in Figure 2.

## RESULTS

Tests were conducted to demonstrate the efficacy of the electronic control and measurement system when combined with the proposed characterisation method. Figure 2 shows the raw measurement results and model fits from a physical electronic analogue, comprising of a power supply and a fixed resistor, representing $OCP$ and $R_{INT}$ respectively.

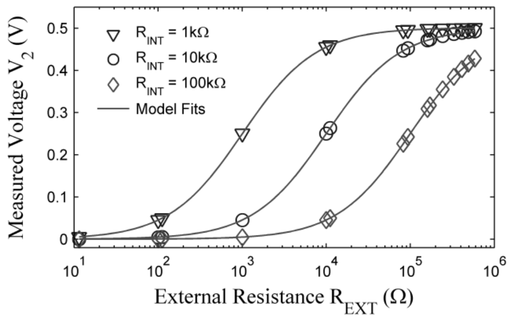



**Fig. 2** Characterisation of electronic circuit models simulating varied internal resistances with $OCP$ =0.5 V. Determined fit parameters for 1,10&100 kΩ models were 1009±0.29 Ω, 10.04±0.00 kΩ and 100.2±0.64 kΩ respectively (n=10). $OCP$ values of 0.501V were determined in all cases.

Characterisation of *ex vivo* porcine liver tissue was conducted using the same external resistor set. Figure 3 shows the results obtained for repeat measurements of liver tissue in unstrained and strained cases. Applying a significant level of strain (~50%) to the tissue results in a shift of the model fit curve, representing a reduction in tissue internal resistance.

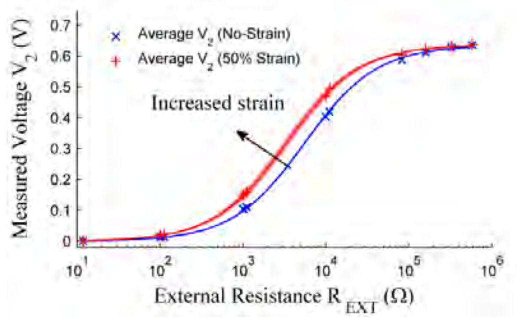



**Fig. 3** Porcine liver tissue under no-strain (blue) and 50 % strain (red). Solid lines indicate mean model fits with standard deviation presented as the shaded region (n=5).

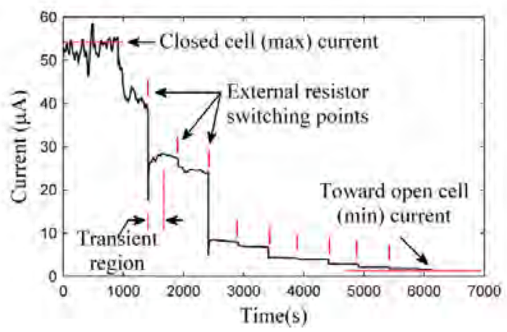



**Fig. 4** A typical current profile during a single characterisation of 0.1% NaCl(aq) at 25°C.

In order to understand how the current varies with time during characterisation, measurements were taken using a precision potentiostat (Ivium Technologies). This was conducted in a model system of 0.1% NaCl solution (equivalent in conductivity to liver tissue [6]). Typical features of the current profile are illustrated in Figure 4.

## DISCUSSION

When characterising tissues in the proposed manner, a number of significant assumptions are made: (1) the established electrode potentials are stable and due only to proposed half-cell reactions. (2) Tissue acts as an ideal salt bridge with a fixed value of resistance across a range of currents. (3) The electrode-tissue interface does not influence the measured internal resistance. (4) Internal resistance is specific to tissue type and health.

In the case of (1), variability in the order of +/- 100 mV is seen between electrochemical cells resulting from non-standard conditions. With sufficient data, non-standard potentials can be predicted using the Nernst equation [7]. The model of equation 1 can account for inter-test $OCP$ variations thus mitigating the issue while providing an additional discrimination parameter.

Measurements taken using electrical analogues (Figure 2) show the efficacy of the test system and model. Highly accurate and repeatable predictions of the fixed resistance values are shown. When extended to tissue tests (Figure 3), strong agreement is again seen over a wide current range indicating that assumption (2) appears valid. However, adjusting cell conditions e.g. applying mechanical strain shows significant influence on the determined internal resistance. Figure 4 shows that there are time-dependent properties inherent in the system. These become prominent shortly after external resistance switching signifying apparent interface phenomena; charge/discharge of the electric double layer and diffusion of ions to/from the metal surface [7]. This indicates that assumption (3) is not valid under the cell arrangement tested. Thus the determined $R_{INT}$ values may include resistance from the interfaces.

True assessment of the bio-galvanic technique is not possible without further understanding and control of the influencing parameters discussed. Variations of the electrochemical system, the mechanical conditions and the chosen electrical model must be considered. By addressing these factors, bio-galvanic measurements may show potential for intraoperative tissue assessment.

## REFERENCES


[1] A. Golberg, H.D. Rabinowitch, B. Rubinsky, Galvanic apparent internal impedance: An intrinsic tissue property, Biochemical and Biophysical Research Communications, 389 (2009) 168-171.

[2] A. Golberg, S. Laufer, H.D. Rabinowitch, B. Rubinsky, In vivo non-thermal irreversible electroporation impact on rat liver galvanic apparent internal resistance, Physics in Medicine and Biology, 56 (2011) 951.

[3] O.G. Martinsen, S. Grimnes, Bioimpedance and Bioelectricity Basics, Elsevier Science, 2011.

[4] R. Bayford, A. Tizzard, Bioimpedance imaging: an overview of potential clinical applications, Analyst, 137 (2012) 4635-4643.

[5] J. Moré, The Levenberg-Marquardt algorithm: Implementation and theory, in: G.A. Watson (Ed.) Numerical Analysis, Springer Berlin Heidelberg, 1978, pp. 105-116.

[6] T.J.C. Faes, H.A.v.d. Meij, J.C.d. Munck, R.M. Heethaar, The electric resistivity of human tissues (100 Hz-10 MHz): a meta-analysis of review studies, Physiological Measurement, 20 (1999) R1.

[7] A.J. Bard, L.R. Faulkner, Electrochemical Methods: Fundamentals and Applications, Wiley, 2001.

# Gesture Based Gaze Contingent Control of a Robotic Arm for Laparoscopic Applications

Kenko Fujii, Antonino Salerno, Kumuthan Sriskandarajah, Ka-Wai Kwok, Guang-Zhong Yang

*Hamlyn Centre for Robotic Surgery, Imperial College London*
*k.fujii09@imperial.ac.uk*

## INTRODUCTION

Recently, laparoscopic surgery has become the gold standard for treating a wide variety of pathologies. However the narrow field-of-view (FOV) when compared to open surgery necessitates a camera assistant to orientate and navigate the laparoscope. The importance of good camera handling and navigation is being recognized and is now included in the training curricula for surgical residents [1]. Despite this, assistant fatigue, hand tremor and the close proximity to the surgeon cannot be overcome from training.

To overcome these issues, robotic assisted camera control systems have been commercially proposed such as the voice activated Automatic Endoscope Optimal Position (AESOP) system from Computer Motion Inc.[2], the head-motion controlled EndoAssist [3], and the finger joystick controlled SoloAssist [4]. However these systems change the dynamics of the operation.

The purpose of this paper is to introduce a gaze contingent robotic camera control system based on real-time gaze gestures. The human visual system is used as an information gathering function rather than as a control input. It can therefore be difficult to distinguish solely from their Point-of-Regard (PoR) whether they want to move the camera or scan around the scene. Potential solutions to overcome this are using external input sources such as buttons or foot-pedals [5] and dwell-time on fixed regions of the screen [6] to convey panning. Unfortunately, these methods introduce their own limitations such as input control clutter and or the lack of zoom functionality.

One area that has not been explored in surgical camera control is the use of gaze gestures. Gaze gestures use predefined eye movements to prompt multiple camera control modes, e.g. panning and zooming. This is the first time gaze gesture recognition has been used to control a robotic arm for minimally invasive surgery. Gaze gestures have been previously used for Human Computer Interaction [7]. In this paper, Hidden Markov Models (HMMs) have been used for gaze gesture recognition to enable the surgeon to experience a hands-free control of the camera system. In the proposed system, the important role of the surgeon's eyes is restored back into the control loop of the camera.

## MATERIALS AND METHODS

In order to recognise the gaze gestures, HMMs were used. HMMs represent stochastic sequences where the states rather than being directly observed are associated with a probability [8]. In our system, a single HMM represents one gaze gesture. Two gaze gestures were used for the "pan" and "zoom" control of the camera. Both gaze gestures are 3-stroke eye movements. The "zoom" gaze gesture is defined by gazing from the center of the screen, then to the bottom left corner, back to the center, and finally back to the bottom left corner. The "pan" gaze gesture is a similar sequence but is performed by looking at the bottom right corner instead.

A total of 300 intentional gaze gestures were used to train two HMMs. From a 10-fold cross validation on various state parameters it was decided that 6 states was a good trade-off between recognition accuracy and model complexity. The gaze gesture recognition and robot control algorithm is shown in Fig. 1.

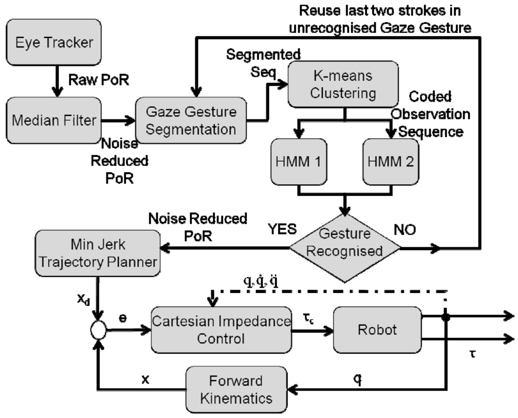



**Fig. 1** Gaze gesture recognition and robotic control algorithm.

The PoR data is median filtered, and then segmented using a velocity threshold saccade detection algorithm. The algorithm sequentially extracts 3 saccades and encodes it using k-means clustering. The encoded sequence is then tested against the respective HMMs, for "zoom" and "pan" gaze gestures. The recognized gesture is the one with the maximum inference value from HMM1 and HMM2, given that it is above the inference value threshold of 0.65 and 0.7 respectively. Once a gaze gestures is recognized, the PoR is sent to the robotic arm to control it, otherwise no input is sent to the robot. During "pan" mode, the camera will follow the user's PoR. During "zoom" mode the camera will zoom in if the PoR is above the screen horizon, while it will zoom out if the PoR is below the screen horizon. The camera is stopped by observing a stop region in the center of the screen for 500ms.

The general control scheme of the robotic camera manipulator has been based on a Cartesian impedance controller [9] that computes the command torque $\tau_c$ for

each joint according to the position error $e$ in Cartesian space and the compensation of the whole robot dynamics. The aforementioned error is estimated as the difference between a reference pose $x_d$ provided by a minimum jerk trajectory planner and actual pose $x$ retrieved from the robot's forward kinematics. The trajectory planner is updated on-line in compliance with the gaze co-ordinates $PoR = [x_{eye} \quad y_{eye}]^T$ moving the camera where the end user is looking.

## RESULTS

The experimental platform in Fig. 2 includes a Tobii 1750 eye tracker, a 10mm zero degree Stortz laparoscope, a Storz Tele Pack light box, a Kuka Light Weight Robot (LWR) [9] and an upper gastrointestinal phantom with simulated lesions inside a box trainer. Eleven surgeons participated in the clinical experiment using the system during three control modes. 1) Gaze gesture control; 2) Pedal activated control, where the user activates the camera control with a foot pedal but directs the camera with their PoR; 3) Camera assistant mode, where a novice assistant controls the camera for the subject. The same assistant took part in all trials.

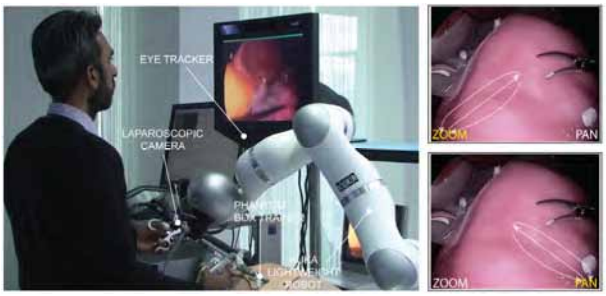



**Fig. 2** The gaze contingent camera control system (left), the "zoom" (upper right) and "pan" (lower right) gaze gestures.

To assess the new gaze contingent camera control system, the following quantitative performance measures were used; i) Recognition accuracy of the HMM gaze gestures; ii) Camera path length, for ability and efficiency; iii) Task completion time, to assess usability. Results are represented as medians with interquartile ranges in parentheses. Occurrence of false positive (i.e. when the user does not perform a gaze gesture, but the algorithm triggers a gaze gesture) and false negative (i.e. when the user performs a gaze gesture, but it is not recognized by the algorithm) gaze gestures during the experiment were counted via post-hoc observation of the recorded camera-view videos. The HMM recognition accuracy was on average 97.0% whilst the average false positive rate was 1.4% under a statistical cohort of more than 200 gestures.

Task completion time observed across all three modalities showed no significant difference (p=0.690), see Fig. 3(a). This indicates that our gaze contingent system is as competent as the established use of a camera assistant. In contrast, a significantly shorter camera path length was observed for the gaze gesture modality compared to the assistant (0.896m [0.867] vs. 1.71m [1.26]); p=0.037) as shown in Fig. 3(b).

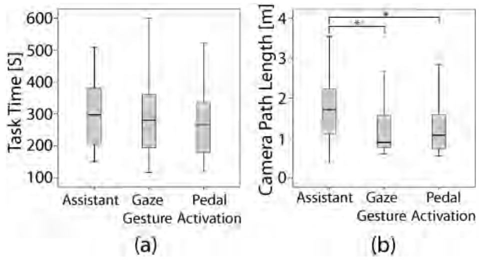



**Fig. 3** (a) Task completion time, and (b) Camera path length (m) for all control modes. *Significant p values.

## DISCUSSION

In this paper, we provided a novel approach to control a 6 DoF camera through the surgeons' PoR (i.e. 2 DoF) via the use of real-time HMM gaze gestures to pan and zoom in the Cartesian space. The ability to consistently complete a surgical navigation task has been demonstrated with the gaze gesture control scheme. The efficiency of the system is shown by the significantly shorter camera path length compared to the current standard. Validation of the HMMs showed that HMMs are effective in recognizing gaze gestures with mean experimental recognition accuracy and false positive rate of 97.0% and 1.4% respectively.

## REFERENCE

[1] S. Shetty, *et al.*, "Construct and face validity of a virtual reality–based camera navigation curriculum," *Journal of Surgical Research,* vol. 177, pp. 191-195, 2012.

[2] B. M. Kraft, *et al.*, "The AESOP robot system in laparoscopic surgery: Increased risk or advantage for surgeon and patient?," *Surgical Endoscopy And Other Interventional Techniques,* vol. 18, pp. 1216-1223, 2004/08/01 2004.

[3] S. Kommu, *et al.*, "Initial experience with the EndoAssist camera-holding robot in laparoscopic urological surgery," *Journal of Robotic Surgery,* vol. 1, pp. 133-137, 2007/07/01 2007.

[4] K. Sriskandarajah, *et al.*, "Robotic Tele-Manipulating Devices for Laparoscopy Improve Surgical Performance in Simulated Porcine Laparoscopic Cholecystectomies on the ELITE Simulator," *Proceedings of the 2012 Hamlyn Symposium on Medical Robotics,* pp. 36-37, 2012.

[5] C. Staub, *et al.*, "Human-computer interfaces for interaction with surgical tools in robotic surgery," in *Biomedical Robotics and Biomechatronics (BioRob), 2012 4th IEEE RAS & EMBS International Conference on*, 2012, pp. 81-86.

[6] D. P. Noonan, *et al.*, "Gaze Contingent Control for an Articulated Mechatronic Laparoscope," in *IEEE International Conference on Biomedical Robotics and Biomechatronics*, 2010.

[7] D. Rozado, *et al.*, "Low cost remote gaze gesture recognition in real time," *Applied Soft Computing,* vol. 12, pp. 2072-2084, 2012.

[8] L. Rabiner, "A tutorial on hidden Markov models and selected applications in speech recognition," *Proceedings of the Ieee,* vol. 77, pp. 257-286, 1989.

[9] A. Albu-Schäffer, *et al.*, "The DLR lightweight robot: design and control concepts for robots in human environments," *Industrial robot,* vol. 34, p. 376, 2007.

# Video-based Framework for Safer and Smarter Computer Aided Surgery

Suren Kumar[1], Madusudanan Sathia Narayanan[1], Sukumar Misra[2], Sudha Garimella[2], Pankaj Singhal[2], Jason J Corso[1] and Venkat Krovi[1,2]

[1]School of Engg. & Applied Sciences [2]School of Medicine and Biomedical Science
University at Buffalo (SUNY), Buffalo NY 14260 USA
ms329@buffalo.edu

## INTRODUCTION

The paramount emphasis on safety in surgical robotics has driven its incorporation at multiple levels within all stages of their development, testing, validation and deployment [1]. Nonetheless, such systems finally have come back full-circle to fundamentally rely solely on the surgeon-in-the-loop to ensure safe operation amidst a host of real-world uncertainties and complexities. For example, the finite life and slack in the cables of the passive-robotic surgical instruments lead to tool-positioning inaccuracies, requiring surgeons to compensate for this error. We would like to make a case for taking advantage of the rich information content to create automated-assists that can help make robotic surgeries smarter and safer. Specifically, in this paper we seek to develop and implement real-time video-based understanding for improved situational awareness and context-based decision support in robotic surgeries.

Current approaches for surgical safety, guidance and training are based on tool motion detection using either sensing or image-analysis methods. The former methods are either marker-based (limited by bio-compatibility, additional instrumentation and occlusions) [2] or joint sensing (using encoders or sensors and suffer uncertainties from flexible joints). While, the image-analysis methods assume clear conditions and require additional information such as accurate tool geometry and/or joint sensing [3]. Moreover, surgical tool detection and tracking, as it has been considered so far, can provide only low level feedback tasks [4] and are unsuitable to obtain holistic surgical video understanding (relationships between tools and its environment). In this work we seek to realize this objective by virtue of: (i) automated tracking of multiple objects (tools); and (ii) building semantic labels/attributes on top of our detection module to robustly learn safety critical scenarios and idealistic tool motions from the videos. Although there has been limited work on attribute labeling directly from video, we believe this will be a critical enabler in robotic surgeries towards increasing the level-of-autonomy.

## EXPERIMENTAL SETUP

Real hysterectomy procedures performed using the da Vinci Surgical System-Si (dVSS-Si) by an experienced surgeon were recorded. Such uncalibrated monocular videos (totally 16 sequences) were sliced into segments (150-300 frames per slice) for manual annotation of two different tools (clamping and cutting tool) and two attributes (blood stained and tool open or closed conditions). The annotated frames (ground truth) were ensured to cover variations including tool configurations and types, occlusion (by tissues, blood stained and other tools), specularities (light intensity, smoke) etc to enable robust classifiers. Our combined framework for tool detection, tracking and attribute labeling is presented in Fig.1. Though this preliminary study is restrictive (considers only two tools and two attributes), it can be easily extended to multiple tools and attributes.

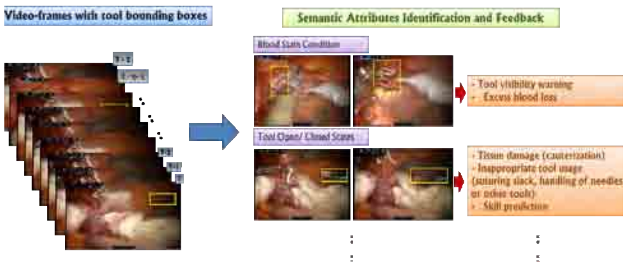



**Fig. 1** Video-based Understanding Workflow

## METHODS

**Tool Tracking:** The detectors for each tool types were learnt using state-of-the-art algorithms [5] that aided in capturing the object shape using Deformable Part Models (DPM) (consisting of star-structured pictorial structure model). DPM links root of an object to its parts using deformable springs and proved to be a suitable method for articulated surgical tools. A Latent Support Vector Machine (LSVM) classifier is then learnt to identify multiple tools by extracting Histogram of Oriented Gradients (HOG) from annotated bounding boxes as in Fig. 2. The location of the bounding box in next frame is approximated by mean flow of all pixels using a simple tracker based on dense optical flow. The resulting pixel velocities and mean velocity of the bounding box can then be used to detect scenarios like tool leaving field of view, inappropriate motions etc.

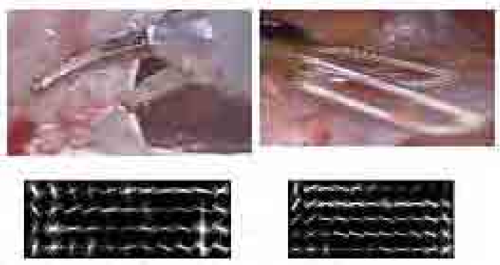


**Fig. 2** Learned HOG Templates for Different Tools

**Attribute Labeling**: The accuracy of attribute labeling is tested using manually labeled bounding box data to

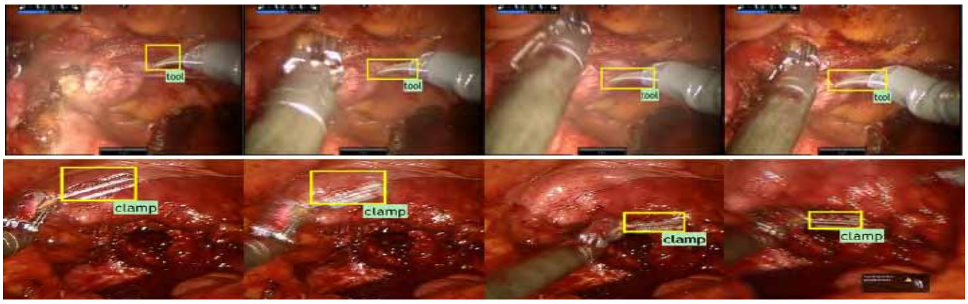



**Fig. 3** Tool Detection and Tracking Results in Real Surgical Videos [Please view in color]

obtain Pyramid Histogram of Oriented Gradients (PHOG) [6] (captures object shape at various scales). A Probabilistic Support Vector Machine (PSVM) classifier [7] is learned to estimate the probability of an attribute in each state, for e.g., probability of tool open or closed states for each frame. By further applying Bayesian inference, transition in semantic attributes is filtered to improve the accuracy using the output from a specified number of past frames [8] and assuming mutual independence [9]. Our framework is also real-time capable as it is implemented in a causal manner (current value depends on only previous frames).

## RESULTS

The combined tool detection (based on HOG) and tracking framework (using the optical flow) performed reasonably well (> 70% accuracy based on Pascal measure for a total of 4657 manual tool annotations on 2400 frames) without any restrictive assumptions on type, shape, color, view direction etc. Although the detector gives true positives and false positives, the tracker is initialized only with those detections that have high confidence score. Figure 3 shows successful tracking of a single tool with appearance changes and multiple surgical tools using only monocular videos. For the semantic labeling, same labeled datasets were compared with the classifier results (baseline SVM, SVM with filtering and the method from [10]) to evaluate their accuracy using 10-fold cross validation. The attributes labeling were also compared using RGB Histograms (capture color variations of the tool), PHOG and both of these together as inputs to our classifiers. The results are summarized in Table 1 which indicates our method with filtering performed better than the current literature [10] .

**Table 1.** Accuracy Scores for Different Features using Baseline SVM, SVM with Filtering and Method from [10] for Attributes: Blood Stained (left) and Tool Open/Closed (right).

| | Blood Stained Attribute | | | Tool Open/ Closed State | | |
|---|---|---|---|---|---|---|
| **Feature** | *Baseline* | *Ours* | *[10]* | *Baseline* | *Ours* | *[10]* |
| **RGB** | 86.41% | 88.38% | 86.73% | 82.05% | 83.17% | 82.91% |
| **PHOG** | 82.56% | 89.31% | 83.34% | 77.50% | 82.28% | 78.20% |
| **Both** | 88.32% | 92.70% | 88.68% | 85.45% | 87.09% | 84.84% |

## DISCUSSION

This work summarizes our current progress in video-understanding of real surgeries for enhanced safety and decision support systems. The multi-tool detection and attribute labeling algorithms were implemented and validated using our existing infrastructure and found to be robust to a host of scenarios and there is scope for further improvement. Future work to use multiple trackers and probabilistically merge the individual detection outputs to improve overall accuracy is currently underway. Our semantic labeling algorithm performed better than the one in current literature and showed promise for further refinement with extensive benchmark data and cross-validation comprising of more varying scenarios and appearance changes. Such a cascaded framework will prove to be useful from diverse perspectives – surgical guidance, safety, tracking and also skill assessment. We plan to combine this automated framework with our earlier work on surgical skill assessment [11] in near future to implement a tightly integrated and automated robotic-surgical training workflow.

**Acknowledgement:** We would like to acknowledge the support of NSF Award (CNS 1314484).

## REFERENCES

[1] R. Taylor, “Computer-Integrated Surgical Systems and Technology Engineering Research Center,” 1997.

[2] M. Groeger, et al., “Motion Tracking for Minimally Invasive Robotic Surgery,” *Medical Robotics*, 2008.

[3] A. Reiter, et al., “Feature Classification for Tracking Articulated Surgical Tools,” *Proc. MICCAI*, 2012.

[4] A. Krupa, et al., “Autonomous 3-D Positioning of Surgical Instruments in Robotized Laparoscopic Surgery using Visual Servoing,” *IEEE Trans. Rob. & Auto.*, 2003.

[5] P.F. Felzenszwalb, et al., “Object Detection with Discriminatively Trained Part Based Models,” IEEE PAMI, 2010.

[6] A. Bosch and A. Zisserman., “Pyramid Histogram of Oriented Gradients (PHOG),” University of Oxford Visual Geometry Group.

[7] J. Platt, “Probabilistic Outputs for Support Vector Machines and Comparison to Regularized Likelihood Methods,” *Adv. in Large Margin Classifiers*, 2000.

[8] S. Kumar, et al., “Vision-based Decision-Support and Safety Systems for Robotic Surgery,” *Proc. MedCPS*, 2013.

[9] K. Sentz and S. Ferson, “Combination of Evidence in Dempster-Shafer Theory,” 2002.

[10] S. Voros and G.D. Hager, “Towards Real-time Tool-tissue Interaction Detection in Robotically Assisted Laparoscopy,” *Proc. 2nd IEEE & RAS BIOROB*, 2008.

[11] S.-K. Jun, et al., “Minimally Invasive Surgical Skill Assessment by Video-Motion Analysis,” *Proc. 5th Hamlyn Symposium on Medical Robotics*, 2012.

# Performance and Eye Behaviour Changes Associated with Visuomotor Rotation – Relevance for Design of Robotic Telemanipulators

K. Sriskandarajah, K. Shetty, M. Sodergren, G.-Z. Yang, A. Darzi

*The Hamlyn Centre for Robotic Surgery, Imperial College, London*

*k.sriskandarajah@imperial.ac.uk*

## INTRODUCTION

Surgeons experience sensorimotor distortion whilst performing Minimally Invasive Surgery (MIS). Loss of depth perception, visuomotor misalignment and the effects of visuomotor rotation (VMR) contribute to sub-optimal visualisation of the operative field of view (FOV). During MIS, VMR occurs when the laparoscope is unintentionally rotated about its long axis, resulting in a mis-match of the percieved and actual FOV. Disorienting spatial transformations result in rotational misalignment between visual perception and motor control [1], degrading performance [1, 2] and theoretically increasing cognitive load. Robotic telemanipulators, currently in commercial use, stabilise the horizon, but are unable to correct rotation when it occurs (e.g. Aktormed SoloAssist). The impact of VMR on performance and eye behaviour was evaluated in this study. Given the predicted change in task difficulty, it was hypothesised that VMR would evoke greater change in pupil diameter, with greater observed average dwell times.

## METHODS

Eight right-handed laparoscopically naive medical students (mean age ± SD = 20.4 ±1.6 years) were recruited to perform the fundamentals of laparoscopic surgery (FLS) peg transfer task. This task requires manipulation of triangular pegs between laparoscopic instruments of either hand and placement onto a pin board. The task was performed under normal view and with the view rotated by 90° (order randomised).

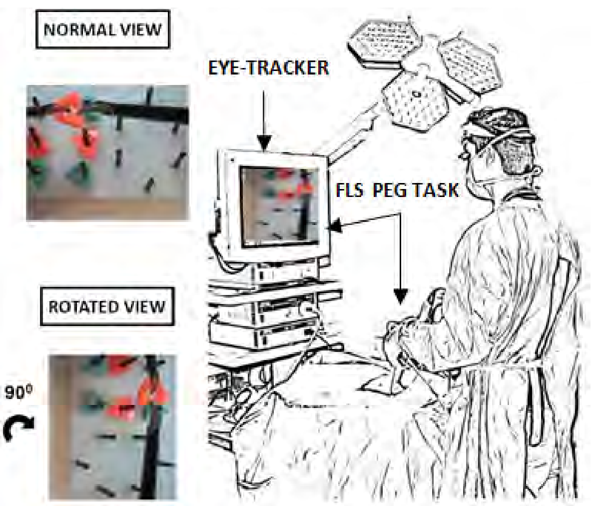



**Fig. 1** Tobii 2150C is positioned in place of a standard laparoscopic screen to allow eye-tracking whilst the peg transfer task is performed in the normal and rotated views.

During the task, the subjects were eye-tracked with a Tobii 2150C remote eye-tracker [Fig.1]. Following each task National Aeronautical Space Agency Task Load Index (NASA-TLX) questionnaires were completed. Primary outcome measures were pupil and gaze metrics (pupil diameter and dwell time), and task performance measures (time and validated objective score) [3]. The secondary outcome measure was the subjective workload (NASA-TLX) score. Statistical analysis was performed using IBM SPSS v19.

## RESULTS

Group average performance was better under the normal view versus the rotated view for task time (mean 138s vs. 296s, $p<0.001$) and objective score (mean 162 vs. -16.3, $p<0.001$). Subjective NASA-TLX scores were significantly lower in the normal versus rotated view (median 50.7 [11.7] vs. 80.7 [21.8], p=0.012), indicating higher workload when rotated. Average dwell times were significantly shorter for the normal versus rotated view task (190ms [90.0] vs. 300ms [22.0], p=0.047). Whilst, average combined pupil diameter was significantly larger in the normal vs rotated view task (6.50 [1.40] vs 5.59 [0.93], p= 0.02).

## CONCLUSIONS

VMR results in an evidently poorer technical performance compared to normal view laparoscopy in task naïve subjects. This is associated with a predicted subjective increase in workload and dwell time. However, the pupil diameter change seen was contrary to the hypothesis. It is conceivable that VMR is so challenging, that subjects are unable to engage an appropriate cognitive strategy, whilst attempting the task. Further longitudinal studies are required to evaluate the effects of repeated practice under VMR on the eye behaviour. VMR has a demonstrable effect on performance and eye behaviour, and should be actively minimised in any future design of robotic tele-manipulators.

## REFERENCES

[1] Zhang L, Cao CG. Effect of automatic image realignment on visuomotor coordination in simulated laparoscopic surgery. Appl Ergon. 2012; 43(6):993-1001.

[2] Cresswell AB et al. Methods for improving performance under reverse alignment conditions during endoscopic surgery. Surg Endosc. 1999; 13(6):591-4.

[3] Peters JH, Fried GM, Swanstrom LL, Soper NJ, Sillin LF, Schirmer B, Hoffman K; SAGES FLS Committee. Surgery. 2004; 135(1):21-7.

# Compact Modular System for Teleoperated Laparoendoscopic Single Site Surgery

O.J. Isaac-Lowry, S. Okamoto, P. Berkelman

*Dept. of Mechanical Engineering, University of Hawaii-Manoa*

*ojil@hawaii.edu*

## INTRODUCTION

Single-port access (SPA) surgery [1] aims to reduce the invasiveness and amount of visible scarring from traditional laparoscopic surgery. This alternative technique passes multiple instruments through a single incision. The navel is the dominant single site as it leaves no visible scar. Lack of triangulation resulting from a common entry point can be resolved with angled or articulated instruments. These instruments are developed to provide functionality similar to standard laparoscopic instruments.

Single-port surgery is a strong candidate for teleoperated automation. The improved dexterity, accuracy, and positional control effectively address the manual difficulties associated with re-triangulated instruments and reduced ranges of motion. A number of single-site robotic systems have been developed to meet this need. However, there are functional challenges associated with each of the design approaches. Larger systems such as the Intuitive Surgical da Vinci system [2] equipped with a single port adapter are bulky and afford limited angular motion. Smaller designs such as the miniature system from Wortman et al [3], the Aaraknes system [4], and the internal manipulator system of Won-Ho et al [5] suffer from limited translation, speed, and force complications. By addressing these functional deficiencies, our simple, compact, modular teleoperated surgical system provides advantages in portability, cost, and ease of use compared to existing systems. Our preliminary design as described by Berkelman and Okamoto [6] modifies a ViKY XL endoscope manipulator base from EndoControl SA and incorporates a set of articulated instruments actuated through two independent manipulators. The instruments are modular and rapidly interchangeable to minimize the need for additional incisions. End effector motions are coupled to non-zoom endoscope positioning motions for ease of use and with instruments removed the assembled robot can be autoclaved for simple setup and tear-down. Full description of overall system size, ranges of motion, and force generation are described in [6].

## MATERIALS AND METHODS

An annotated CAD model of system prototype is shown in Fig. 1. Key system elements are listed in [6]. Control is achieved with the teleoperation masters, motor controllers, and revised software from the previous, modular University of Hawaii surgical robot system [7]. The design of manipulator linkages does create individual end effector void geometry as the assembly inclination is swept from near horizontal to near vertical. However the additional DOF derived from assembly base rotation allows positional coverage of encountered trajectory voids with minor repositioning.

This work has been supported by a grant from Intuitive Surgical, NIH grant #5R21EB006073, and the University of Hawaii-Manoa Engineering.

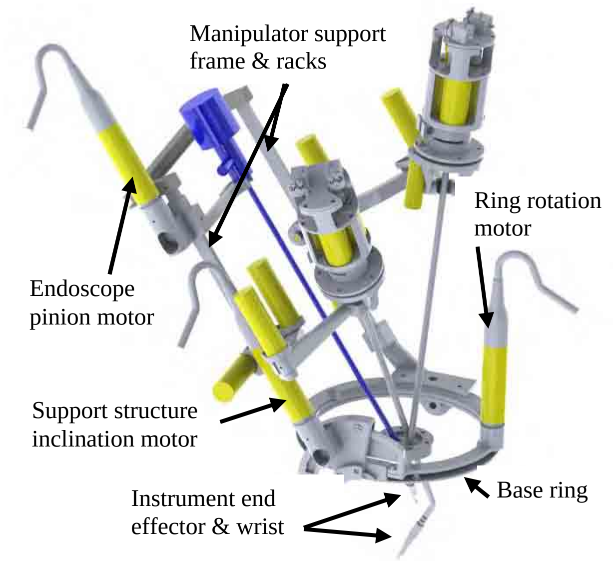



**Fig. 1** Annoted model of single-site robotic surgery system

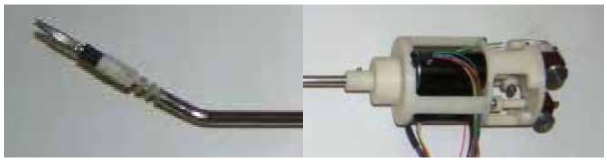


**Fig. 2** Interchangable tool tip and articulated wrist shown left. Motorized actuation assembly shown right.

To account for single trocar geometry, new modular instruments, shown in Fig. 2., were designed to properly re-triangulate end effectors in the visible endoscope field. This is accomplished using an instrument shaft with a fixed 45 degree bend and three-dimensional, fully-articulated end effector wrists. Wrist structures were redesigned to utilize interchangeable tool tips in order to improve system flexibility. Instruments have a compact actuator motor footprint to balance weight distributions and maximize manipulator range of motion. Actuator transmission systems have been redesigned to improve serviceability. The number of fasteners, components, and joints has been reduced through integration of flexible polymer features. Design for manufacture (DFM) and assembly (DFA) methods were employed to reduce instrument reproduction costs.

System prototype and instrument components were produced by 3D printing reducing overall development lead time. Additionally, total prototype design and robustness is enhanced from incorporation of accurate, fine-scale custom components.

## RESULTS

Initial prototype validation has been conducted using a single instrument setup controlled with inverse kinematics and velocity joint commands as in Fig. 3. Simple surgical dexterity tests were performed to evaluate ranges of functional motion, presence and shape of unreachable volumes, and limitations due to manipulator collisions. The author has been able to perform standard peg transfer motions at rate of up to six per minute and verified a minimal rate of single manipulator-instrument-support structure collisions. Accuracy and repeatability of end effector trajectories has been successfully evaluated via optical motion tracking using a Northern Digital Polaris Vicra. Tracking targets are installed on top of instruments as shown in Fig. 3 and measured from a stationary base frame to capture all effects from control error and manipulator, frame, and mounting hysteresis and vibrations. Fig. 4 shows real base frame end-effector motion during three consecutive traces of a 30mm square using a hand operated Geomagic/Sensable Phantom Omni teleoperation master.

The use of 3D printed manipulator and power transmission components has been demonstrated to introduce additional friction and hysteresis into system motions when compared to machined metal. However, these factors have been mitigated through component design and post –printing finishing processes.

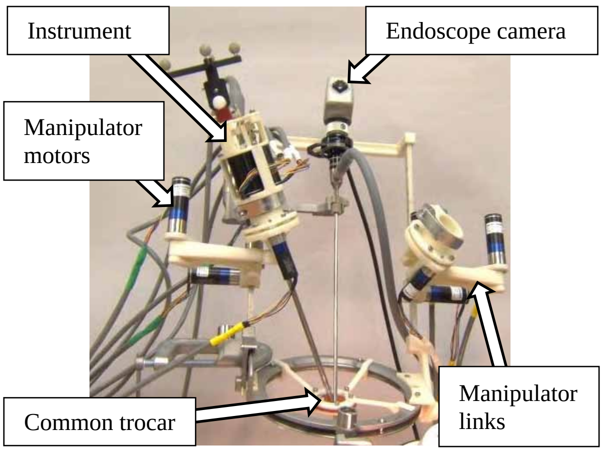



**Fig. 3 U**H Compact Laparoscopic Surgical Robot shown with one modular instrument and motion tracker installed

## DISCUSSION

Based upon preliminary results, we plan to proceed with preclinical trials to evalute two criteria: methods to improve control intuition shown by first time operators relative to trained medical students and surgeons and the total effectiveness of the system when performing established surgical tasks. Evaluated tasks are selected from the Society of American Gastrointestinal and Endoscopic Surgeons Fundamentals of Laparoscopic Surgery (SAGES FLS).

We also aim to capitalize on the rapid interchangeability of instruments afforded by a modular overall system design. Instrument manipulators will be generalized in order to accomodate other, prevalent commercial robotic articulated instruments without negatively impacting performance. Additionally, we intend to continue to explore 3D printing as a potentially viable production medium.

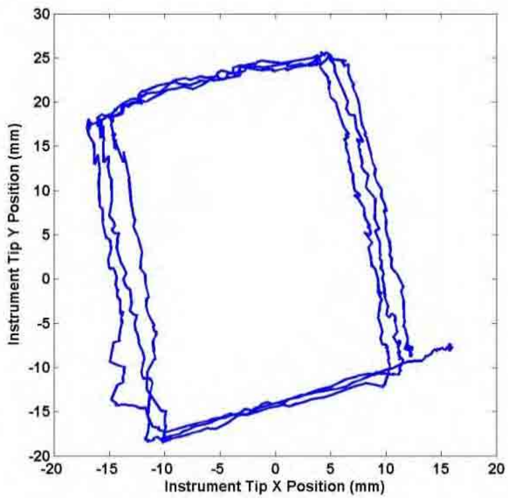



**Fig. 4** End effector motion captured with optical tracking during basic robotic dexterity exercise

## REFERENCES

[1] K. Ahmed, T. T. Wang, V. M. Patel, K. Nagpal, J. Clark, M. Ali, S. Deeba, H. Ashrafian, A. Darzi, and T. Athanasiou, "The role of single-incision laparoscopic surgery in abdominal and pelvic surgery: a systematic review," Surgical Endoscopy, pp. 1-19, July 2010.

[2] G.P. Haber, M. White, R. Autorino, P. Escobar, M. Kroh, S. Chalikonda, R.Khanna, S. Forest, B. Yang, F. Altunrende, R. Stein, and J. Kaouk, "Novel Robotic da Vinci Instruments for Laparoendoscopic Single-Site Surgery," Urology, vol. 76, no. 6, pp. 1279-1282, 2010.

[3] T. Wortman, K. Strabala, A. Lehman, S. Farritor, and D. Oleynikov, "Laparoendoscopic single-site surgery using a multi-functional miniature in vivo robot," The International Journal of Medical Robotics and Computer Assisted Surgery, vol. 7, no. 1, pp. 17-21, 2011.

[4] M. Piccigallo, U. Scarfogliero, C. Quaglia, G. Petroni, P. Valdastri, A. Menciassi, and P. Dario, "Design of a Novel Bimanual Robotic System for Single-Port," IEEE/ASME Transactions on Mechnatronics, vol. 15, no. 6, pp. 871-878, 2010.

[5] W.-H. Shin, "Surgical robot system for single-port surgery with novel joint mechanism," IEEE Transactions on Biomedical Engineering, vol. 60, no. 4, pp. 937-944, 2013.

[6] P. Berkelman and S. Okamoto, "Compact Modular System Design for Teleoperated Laparoendoscopic Single Site Surgery," IEEE/EMBS International Conference on Biomedical Robotics and Biomechatronics, pp. 905-906, Rome, 2012.

[7] P. Berkelman and J. Ma, "A compact modular teleoperated robotic system for laparoscopic surgery," International Journal of Robotics Research, vol. 28, no. 9, pp. 1198-1215, September 2009.

# Open-Loop Tip Accuracy of an MRI-Compatible Active Cannula Robot

D.B. Comber[1], E.J. Barth[1], R.J. Webster III[1], J.S. Neimat[2]

[1]*Department of Mechanical Engineering, Vanderbilt University*

[2]*Department of Neurological Surgery, Vanderbilt University Medical Center*

*eric.j.barth@vanderbilt.edu*

## INTRODUCTION

Magnetic resonance imaging (MRI) is increasingly used intraoperatively, because it provides excellent soft tissue distinction and on-the-fly adjustment to imaging slice orientation without exposing clinician or patient to radiation. For neurosurgical procedures, intraoperative MRI holds significant advantages over traditional stereotactic methods (e.g. compensation for brain shift), and has thereby led to much research toward minimally invasive treatments of brain tumors, epilepsy, and other neurological disorders. Because the tight confines of MRI scanners limit clinician access to the patient, an MRI-compatible robot is potentially useful for many procedures and additionally offers the clinician increased accuracy and degrees of freedom within the minimally invasive context.

Affecting 0.5 to 1.0% of the global population, epilepsy is a neurological disorder for which surgery has been reported superior to prolonged pharmacotherapy, yet only a small fraction of potential surgical candidates receive treatment [1]. Minimally invasive alternatives to conventional resection of seizure foci could side-step the potential morbidity and lengthy recovery associated with open brain surgery thereby making surgical treatment and cure available to a greater number of patients with less risk. Interstitial laser ablation of seizure foci has been clinically demonstrated using MRI to guide ablator placement and MR thermometry for thermal dosimetry [2]. This procedure currently requires multiple patient transfers between MRI scanner and operating room meaning that introducing an MRI-compatible robot could streamline surgical workflow. An alternative real-time MRI approach is high intensity focused ultrasound (HIFU), yet intracranial targets can be difficult to effectively treat due to high reflection and absorption of the ultrasound energy by the skull [3].

This paper reports a pneumatically-actuated active cannula robot designed for MRI-guided ablation of epileptogenic foci. An active cannula is a continuum robot consisting of concentric, superelastic nitinol tubes with pre-curved sections. Complex trajectories are realized by translation and rotation of the cannula tubes with respect to one another.

## MATERIALS AND METHODS

Since hippocampal sclerosis is present in a majority of epilepsy cases, the hippocampus was selected as the target region for thermal ablation, and an occipital trajectory was deemed optimal for maximizing coverage through a single needle insertion. Following this trajectory and performing the ablation can be accomplished with five degrees of freedom: two translations and one rotation for the active cannula, and one additional translation and rotation for the ablator. Inclusion of rotation for the ablator provides the option of using an acoustic ablator with radially sectored transducers to direct the ablative energy [4].

To manipulate the active cannula and ablator, a robotic platform was designed and built, as shown in Fig. 1. For actuators, pneumatic piston-cylinders with fail-safe rod locks were selected instead of piezoelectric motors, as standard piezoelectric motor drives degrade image quality unless powered down during imaging [5]. Furthermore, pneumatic actuators are quieter than piezoelectrics, pose fewer contamination risks than hydraulics, and can run off a hospital's instrument air facilities. A detailed mechanical design of the robot is reported in [6].

A nonlinear, model-based controller was developed for precision position tracking of the actuators [6]. The electronics dedicated to controlling one actuator are: one 5-port/4-way proportional spool valve, two pressure transducers, one optical encoder for position feedback, and one 5-port/2-way valve for rod lock control. Long pneumatic tubing (3 meters) and shielded cables connect the actuators and optical encoders on the robot to the remotely located valves, pressure transducers and system electronics. The controller was implemented in MATLAB Simulink with xPC target. A supply pressure of 687 kPa was used, providing actuator forces on the order of 40 N.

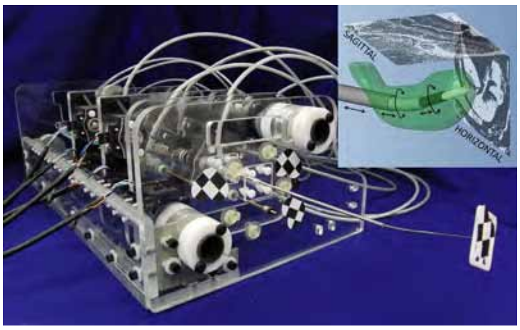



**Fig. 1** Photograph of active cannula robot. Inset shows CAD model of cannula and ablator inside hippocampus.

Three tubes were selected for the active cannula and a simulated ablator. Their dimensions are presented in Table 1. The active cannula consists of a stiff, straight outer tube and inner, pre-curved nitinol tube. The outer tube only translates and inner tube both translates and

rotates, as shown in Fig. 1 inset. The inner tube was first curved by hand, and the resulting radius of curvature was estimated using a digital image of the tube.

**Table 1** Dimensions of active cannula and simulated ablator tubes

| | |
|---|---|
| Tube 1 outer diameter | 3.18 mm |
| Tube 1 inner diameter | 2.36 mm |
| Tube 2 outer diameter | 1.65 mm |
| Tube 2 inner diameter | 1.35 mm |
| Tube 2 radius of curvature | 132.2 mm |
| Tube 2 arc length of curved portion | 52.0 mm |
| Simulated ablator outer diameter | 1.18 mm |

The simulated ablator is a superelastic nitinol tube of outer diameter 1.18 mm. This is slightly smaller than existing MRI-compatible laser ablators [2], but the rotational mechanism of the robot readily accepts larger tube diameters using an interchangeable collet design.

Prior to in-scanner experiments, an initial benchtop assessment of cannula tip accuracy was needed. Thus, tip position measurements were acquired for 28 robot poses using an optical tracking system, the Micron-Tracker 3 by Claron Technologies (XB3-BW-H3-60). Three optical markers were affixed to the robot front plate. Manufactured from acrylic using a laser cutter, the plate includes pin-sized holes to assist in placing the markers at precisely known positions. Five multi-modality fiducial markers were similarly added for registration with MRI images. An optical marker was fixed to the cannula tip for bench testing with the optical tracker; it will be removed for in-scanner experiments.

Image registration from optical tracker to robot was achieved using point-based registration of the markers on the robot's front plate. Then, for each robot pose, the expected cannula tip position was determined from the robot's forward kinematics. The resulting model-based poses of the robot are illustrated in Fig. 2. Tip error was taken as the difference between measured tip position and tip position expected from the cannula model.

## RESULTS

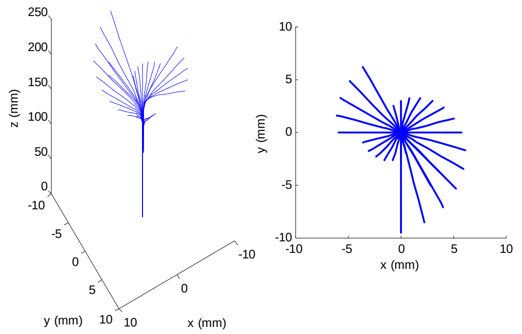



**Fig. 2** Model-based poses of the active cannula robot: 3D view (left) and view along the needle guide axis (right).

The mean and maximum tip errors for the 28 cannula poses were 1.18 mm and 2.40 mm, respectively. The fiducial registration error was 0.278 mm, and steady-state errors of the base joints were on the order of 0.050 mm (translations) and 0.5 degrees (rotations).

## DISCUSSION

Observing that the registration error and base joint tracking errors are 1 to 2 orders of magnitude below the cannula tip errors, it is reasonable to assume the majority of tip error is due to other sources. One likely cause is inaccuracy in the initial mounting of the cannula tubes; this was done by hand using a ruler and pen. Maximum tip error occurred when the precurved tube was at maximum extension. This error likely arose from the fact that the curvature preset into the curved tube may not have been perfectly circular. The shape setting could be improved by use of a high-precision jig and oven to more precisely set the circular curve.

Nonetheless, the presently observed tip errors are quite small and approach the voxel size for MRI scanners (about 1x1x1 $mm^3$), and importantly we also note that real-time imaging will be available so that an image-based control loop can be closed on tip position during cannula insertion. Thus, the overall accuracy of tip placement is not limited to the robot's free-space open loop tip accuracy, which is what is reported in this paper. Furthermore, we tested for MRI-compatibility in a Philips 3T Achieva scanner, and the robot displayed no measurable effect on the signal-to-noise ratio of an fBIRN phantom. Image distortion tests with an ADNI phantom indicate a maximum distortion of 1.3 mm.

These results demonstrate that MRI-guided pneumatic actuation is a promising solution for the minimally invasive treatment of epilepsy and of other intracranial diseases that either require or can benefit from MR imaging and thermometry. Future work includes integration of the robotic platform with the MRI scanner. Scanner experiments will focus on providing real-time feedback of tip location as well as using MR thermometry for real-time thermal dosimetry.

## REFERENCES


[1] Engel, J Jr. et al, 2003. "Practice Parameter: Temporal Lobe and Localized Neocortical Resections for Epilepsy," *Epilepsia*, 44(6):741-751.

[2] Curry, DJ et al, 2012. "MR-Guided Stereotactic Ablation of Epileptogenic Foci in Children," *Epilepsy and Behavior*, 24(4):408-414.

[3] Basak, A et al, 2012. "Implantable Ultrasonic Dual Functional Assembly for Detection and Treatment of Anomalous Growth," *IEEE Int Conf EMBS*, San Diego, 170-173.

[4] Kinsey, AM et al, 2008. "Transurethal ultrasound applicators with dynamic multi-sector control for prostate therapy: In vivo evaluation under MR guidance," *J Med Phys*, 35(5):2081-2093.

[5] Su, H et al, 2011. "High-field MRI-Compatible Needle Placement Robots for Prostate Interventions: Pneumatic and Piezoelectric Approaches," *Advances in Robotics and Virtual Reality*, T Gulrez & A Hassanien, eds, Springer-Verlag, Chap 1.

[6] Comber, DB et al, 2012. "Sliding Mode Control of an MRI-Compatible Pneumatically Actuated Robot," *Bath/ASME Symp Fluid Power & Motion Control*, DN Johnston and AR Plummer, eds, Centre for Power Transmission & Motion Control, University of Bath, UK, 283-293.

# 5-DOF Manipulation of a Magnetic Capsule in Fluid using a Single Permanent Magnet: Proof-of-Concept for Stomach Endoscopy

Arthur W. Mahoney[1], Jake J. Abbott[2]

[1]School of Computing, [2]Department of Mechanical Engineering, University of Utah
{art.mahoney, jake.abbott}@utah.edu

## INTRODUCTION

Magnetic manipulation of capsule endoscopes has the potential to make current gastrointestinal screening procedures faster, safer, and less invasive. To date, two electromagnetic systems have been developed with the ability to perform five-degree-of-freedom (5-DOF) manipulation of an untethered magnetic device such as a magnetic capsule endoscope: the OctoMag system consists of eight electromagnets arranged around a hemisphere directed toward the manipulation workspace [1]; a system has been developed by Siemens, consisting of 12 electromagnets through which a patient is positioned, for the control of a capsule endoscope in a water-filled stomach [2]. Permanent-magnet actuation systems are gaining attention for their ability to generate fields with clinically relevant strengths, inexpensively and in a compact form-factor, compared to electromagnetic systems. Previous permanent-magnet systems for capsule endoscopy have been limited to dragging and rolling capsule endoscope devices on the stomach's surface or in the large colon [3–5].

This proof-of-concept paper demonstrates magnetic 3-DOF position and 2-DOF orientation control of a mockup stomach capsule endoscope in fluid, using a single permanent magnet. 5-DOF manipulation of untethered devices has been previously demonstrated only with electromagnet systems.

## MATERIALS AND METHODS

The mockup capsule is actuated in a tank of water by an axially magnetized cylindrical NdFeB magnet with dipole moment $\mathrm{M} \in \mathbb{R}^3$ (Grade N42, $\|\mathrm{M}\| = 26.2\ \mathrm{A \cdot m^2}$), positioned by a Yaskawa Motoman MH5 6-DOF robotic manipulator. The capsule contains a cube NdFeB magnet with its dipole moment $\mathrm{m} \in \mathbb{R}^3$ (Grade N52, $\|\mathrm{m}\| = 0.126\ \mathrm{A \cdot m^2}$) arranged parallel to the capsule's principal axis; the remainder of the capsule's volume is filled with air. The capsule's weight is 0.0153 N and the buoyancy force in water is 0.0148 N. The capsule's 3-DOF position is triangulated by two Basler A602FC cameras. The actuator magnet, capsule, and experimental setup are shown in Fig. 1.

A magnetic torque $\tau_\mathrm{m} = \mu_0 \mathrm{m} \times \mathrm{H}$ and magnetic force $\mathrm{f_m} = \mu_0(\mathrm{m} \cdot \nabla)\mathrm{H}$ are applied to the center of the capsule's magnet by the magnetic field $\mathrm{H} \in \mathbb{R}^3$ generated by the actuator magnet ($\mu_0$ is the permeability of free-space). The field produced by the actuator magnet is approximated by the point-dipole model:

$$\mathrm{H} = \frac{1}{3\pi\|\mathrm{p}\|^3}(3\hat{\mathrm{p}}\hat{\mathrm{p}}^\mathrm{T} - I)\mathrm{M}, \qquad (1)$$

where $\mathrm{p} \in \mathbb{R}^3$ is the vector from the actuator magnet's center to the capsule magnet's center, $I \in \mathbb{R}^{3\times3}$ is the identity matrix, and ^ denotes scaling to unit length.

The capsule's position and heading are controlled by applying magnetic force and torque, respectively. We assume that the magnetic torque $\tau_\mathrm{m}$ instantaneously aligns the capsule dipole moment m (and the capsule's heading) with the applied magnetic field H, and the capsule's heading can be controlled by adjusting the field direction $\hat{\mathrm{H}}$ without controlling the magnetic torque $\tau_\mathrm{m}$ directly. The magnetic field (1) varies with the relative position p and the direction of the actuator dipole moment $\hat{\mathrm{M}}$. The total force f applied to the capsule consists of forces due to weight and buoyancy, which are both constant, and the magnetic force $\mathrm{f_m}$, which varies with p and $\hat{\mathrm{M}}$. In general, magnetic force also varies with m, however, we assume m to be aligned with $\hat{\mathrm{H}}$. The position p and actuator moment direction $\hat{\mathrm{M}}$ (controlled by the robot manipulator) are related to field direction $\hat{\mathrm{H}}$ and total force f by the nonlinear actuation function:

$$\begin{bmatrix}\hat{\mathrm{H}}\\ \mathrm{f}\end{bmatrix} = \mathcal{A}\left(\begin{bmatrix}\hat{\mathrm{M}}\\ \mathrm{p}\end{bmatrix}\right). \qquad (2)$$

Rather than explicitly inverting (2) to determine the necessary moment $\hat{\mathrm{M}}$ and position p of the actuator magnet, given the desired field direction $\hat{\mathrm{H}}$ and total applied force f, the Jacobian matrix $J_\mathcal{A} \in \mathbb{R}^{6\times6}$ is computed analytically, using the measured capsule position, and inverted using the Moore-Penrose pseudoinverse. The result relates small changes in the

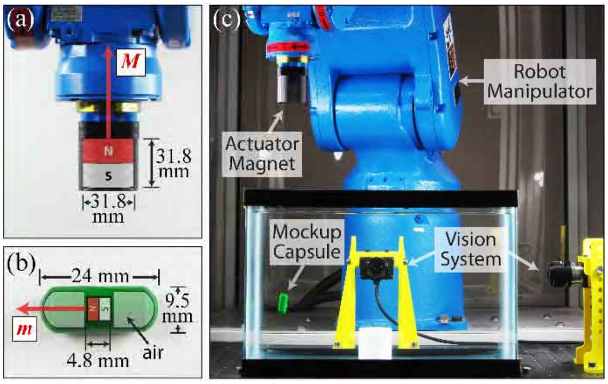



**Fig. 1** The actuator magnet (a) is used to control the mockup capsule endoscope (b) in a water-filled tank, using the robotic manipulator and vision system shown in (c).

This material is based upon work supported by the National Science Foundation under Grant No. 0952718.

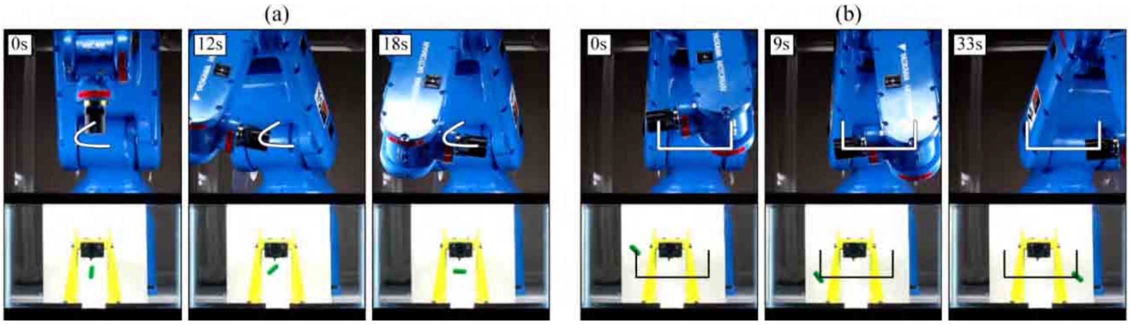



**Fig. 2** The mockup capsule can be holonomically controlled with five degrees-of-freedom. In (a), the capsule is controlled to adjust its heading while remaining stationary in space. In (b), the capsule follows a U-shaped trajectory while maintaining a constant heading. The path taken by the actuator magnet is shown in both examples. Complete video demonstrations of (a) and (b) can be found at http://www.telerobotics.utah.edu/index.php/Research/PermanentMagnet.

desired field direction and force to small changes in the actuator moment and position:

$$\begin{bmatrix} \Delta\widehat{\mathrm{M}} \\ \Delta \mathrm{p} \end{bmatrix} = J_{\mathcal{A}}{}^{\dagger} \begin{bmatrix} \Delta\widehat{\mathrm{H}} \\ \Delta \mathrm{f} \end{bmatrix}, \qquad (3)$$

which governs how the robotic manipulator moves the actuator magnet in space as the desired field heading (i.e., capsule heading) and applied force vary. The matrix $J_{\mathcal{A}}$ is always rank five, meaning that the capsule can be controlled with five degrees-of-freedom. The single uncontrollable DOF corresponds to capsule rotation about its magnetic dipole moment m.

In practice, values of $\Delta$f or $\Delta\widehat{\mathrm{H}}$ and certain system configurations can produce large changes in $\Delta$p or $\Delta\widehat{\mathrm{M}}$, which may be unachievable by the robot manipulator in the worst case. The manipulator's motion can be reduced by temporarily sacrificing control over the capsule's heading, without losing control over its position. This is performed by solving a constrained, weighted, least-squares minimization problem.

## DISCUSSION

A feedback controller, using the triangulated capsule position obtained from the vision system, is used to servo the capsule to any desired position in the workspace. At every iteration, the controller produces a desired change in force $\Delta$f, and the desired change in heading $\Delta\widehat{\mathrm{H}}$ is obtained from the user, which are converted into motion of the robotic manipulator by equation (3). An estimate of the capsule's heading is obtained from the measured position using (1), and is controlled in an open-loop fashion (i.e., the capsule's heading is not measured).

Fig. 2 shows two capsule maneuvers that prior actuation systems using a single permanent magnet are unable to perform. In Fig. 2(a), the capsule's heading is rotated from a down-pointing to a side-pointing configuration, while the feedback controller regulates position with no external contact. Nonintuitively, the actuator magnet does not remain directly above the capsule during the transition. In Fig. 2(b), the capsule's position follows a U-shaped trajectory while its heading remains constant. These examples demonstrate simple maneuvers. Since the system is capable of 5-DOF control, more complicated maneuvers are also possible.

## DISCUSSION

The control scheme presented herein relies upon the capsule's net weight (i.e., weight minus buoyancy) to apply downward forces in the direction of gravity. When the capsule is desired to move downward, the applied magnetic force is adjusted to be less than the net weight by repositioning the actuator magnet according to (3). The maximum downward force that can be applied (without placing the actuator below the capsule) is the capsule's net weight.

When the magnetic force balances the net weight, then the capsule levitates at equilibrium and is stabilized by the feedback controller. The equilibrium distance depends on the capsule's net weight and the strength of the capsule and actuator magnets, $\|\mathrm{m}\|$ and $\|\mathrm{M}\|$, respectively. If the capsule's net weight is increased, a larger actuator magnet can be used with the same results. The closer the capsule is to neutral buoyancy, the smaller the magnetic force needed for levitation. However, since the capsule's net weight is required to apply downward force, a neutrally buoyant capsule is undesired.

In a clinical setting, the vision system used for capsule localization can be replaced by more appropriate localization methods such as RF triangulation, ultrasound, magnetic tracking, and other (potentially hybrid) approaches.

## REFERENCES


[1] M. P. Kummer et al. OctoMag: An electromagnetic system for 5-DOF wireless micromanipulation. *IEEE Trans. Robot.*, 26(6):1006--1017, 2010.

[2] H. Keller et al. Method for navigation and control of a magnetically guided capsule endoscope in the human stomach. In *Proc. IEEE Int. Conf. on Biomedical Robotics and Biomechatronics*, pages 859--865, 2012.

[3] S. Yim and M. Sitti. Design and rolling locomotion of a magnetically actuated soft capsule endoscope. *IEEE Trans. Robot.*, 28(1):183--194, 2012.

[4] G. Lien et al. Magnetic control system targeted for capsule endoscopic operations in the stomach: Design, fabrication, and *in vitro* and *ex vivo* evaluations. *IEEE Trans. Biomed. Eng.*, 59(7):2068--2079, 2012.

[5] G. Ciuti et al. Robotic magnetic steering and locomotion of capsule endoscope for diagnostic and surgical endoluminal procedures. *Robotica*, 28(2):199--207, 2010.

# Endoscopic Submucosal Dissection for Gastric Lesions using a Flexible Snake Robot – Early Assessment and Feasibility Study

N.K. Patel[1], T.P. Cundy[1], J. Shang[1], C. Payne[1], C. Seneci[1], V. Vitiello[1], J.Clark[1], J. Teare[1], A. Darzi[1], G.-Z. Yang[1]

*The Hamlyn Centre for Robotic Surgery, Institute of Global Health Innovation, Imperial College London*
*nisha.patel2@imperial.ac.uk*

## INTRODUCTION

Annually, there are approximately one million cases of gastric cancer diagnosed globally. Whilst surgery has traditionally been the definitive treatment, flexible endoscopic techniques such as endoscopic submucosal dissection (ESD) are emerging as minimally invasive alternatives [1].

Thus far, the flexible endoscope has been adopted as the preferred instrument for ESD. However, this platform poses significant challenges to performing complex endoluminal surgery. Maintaining a target lesion in constant view for accurate dissection is technically and ergonomically demanding. In addition, triangulation of ESD tools is highly restricted and off-axis movements often prove problematic. Tissue traction and manipulation are also inadequate. These factors contribute to lengthy procedure times, significant operator burden and complication rates. The purpose of this study is to explore the feasibility of a flexible snake robot as a technological solution for ESD of gastric lesions.

## METHODS

The multi-articulated snake-like robot, based upon a universal-joint mechanism with embedded micromotor actuation [2], is 12.7mm in diameter and 150mm in length with a 50mm semi-rigid neck. Four distal joints permit eight degrees of freedom for kinematic configuration approaching multi-axis retroflexion capability [2]. Position-control of the motorised joints allow precise motions of the robot to be made.

A camera and light source occupy 2.8mm and 2.4mm internal channels respectively. Flexible endoscopic tools may be interchangeably deployed down a 3mm central working channel.

Two porcine upper gastrointestinal specimens were placed into a validated endoscopic surgery simulator tray (EASIE-R, ENDOSIM). The duodenum was clamped to allow gastric insufflation and simulated gastric lesions in the antrum and gastric body were created using submucosal normal saline blebs.

## RESULTS

Controlled navigation was performed within the gastric cardia, fundus and greater curve using an ergonomic interface. Ten (10-20mm) lesions in the gastric body were excised along planned dissection margins. The lesions were marked circumferentially (soft coagulation mode, 50W) and a submucosal fluid cushion under the lesion was created using a HybridKnife integrated water-jet electrocautery tool (ERBEJET® 2 console, effect 30). A mucosal incision was made peripherally around the target lesion (EndoCut-I, effect 2, cut duration 3, interval 2). A HybridKnife, T-type (ERBE) was then used for dissection (forced coagulation mode, 45W, effect 3) (Figure 1). No perforations were found on close inspection.

## CONCLUSION

This *ex vivo* feasibility study shows promising results supporting the role of the snake robot to navigate through the upper gastrointestinal tract and perform gastric ESD. Further *in vivo* studies are now required to optimise the robotic device and to establish optimal settings for ESD. This flexible snake platform offers enhanced stability, controlability, enhanced ergonomics and precision. It may overcome limitations presented by the flexible endoscope, thereby enabling the increased global uptake of ESD.

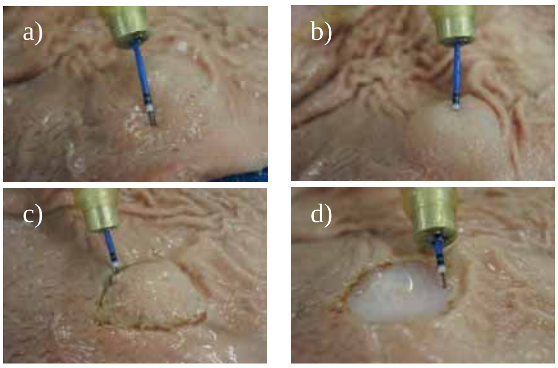



**Fig. 1** *Ex vivo* robotic ESD of gastric lesion (view taken from a flap created in the gastric body) a) marking b) submucosal cushion formation c) mucosal incision d) submucosal dissection

## REFERENCES

[1] Yamamoto H. Endoscopic submucosal dissection-current Success and future directions. Nat. Rev. Gastroenterol. Hepatol. 2012;9:519-529.

[2] Shang J., Noonan DP., Payne C., Clark J., Sodergren M., Darzi A., Yang GZ. An Articulated Universal Joint Based Flexible Access Robot for Minimally Invasive Surgery. International Conference on Robotics and Automation, Shanghai, China. 1147-1152. IEEE (2011).

# Patient Mounted CT and MRI Compatible Shoulder Arthrography Robot for Needle Guidance in Pediatric Interventional Procedures

R. Monfaredi[1,2], R. Sze[1], N. Safdar[1], K. Sharma[1], K. Cleary[1]

[1]Sheikh Zayed Institute for Pediatric Surgical Innovation, Children's National Medical Center, Washington, DC, USA

[2]Industrial Department, Azad University- South Tehran Branch, Tehran, Iran

kcleary@childrensnational.org

## INTRODUCTION

Arthrography is the evaluation of joint condition using imaging modalities such as computed tomography (CT) and magnetic resonance imaging (MRI). Among American children ages 5-14, there is on average over one sports-related injury per year, with a significant portion involving internal derangements of shoulders, hips, wrists, and other joints [1]. When there is concern for derangement of articular labral structures, as may be seen with these injuries or untreated congenital joint dysplasias, magnetic resonance (MR) arthrography is the modality of choice for evaluation of the labrum, articular cartilage, and other internal structures of the joint in children. Currently, this test requires two separate stages, an intra-articular contrast injection guided by fluoroscopy or ultrasound followed by an MRI. The inability to leverage the imaging capabilities of the MRI itself and the manual nature of needle placement lead to increased cost, anxiety, and in some cases prolonged sedation time, especially for the youngest and most anxious patients. Therefore, our ultimate goal is to develop an MRI-compatible shoulder arthrography robot. As a first step, we have developed a CT compatible prototype.

In typical manual interventions, the physician guides the needle using cross-sectional images to reach the desired position in joint space or near the bone. Traditional needle manipulation often requires multiple passes to reach the target. In MRI guided interventions, patient access can be difficult, especially for closed bored scanners. However, compared to CT imaging, MRI has advantages including: 1) no radiation exposure which is especially important for pediatrics; and 2) higher soft tissue contrast. Therefore, we are developing a novel patient-mounted robotic system to provide better targeting ability, improve the clinical workflow, and allow better access with the MRI scanner bore.

Many researchers have reported related work in the field of MRI and CT guided interventions. The high magnetic field present in the MRI environment is the major challenge to develop MRI compatible equipment. Nonmagnetic materials, MRI compatible actuators (piezo motors, pneumatic and hydraulic actuators), optical fibers, encoders, and sensors are key elements of this kind of robotic system. Walsh et al. [2] developed a patient mounted robot called Robopsy. This robot is a telerobotic system with 2 degree-of-freedom (DOF) for needle guidance and insertion system. The robot is attached to the patient via an adhesive pad and optional strap points, so the device moves passively with patient motion and is thus inherently safe. This robot can orient the needle about 2 axes and insert the needle automatically through joystick control of the physician.

Maurin et al. [3] developed a patient-mounted robot from a 5 DOF parallel structure with a semispherical workspace, particularly well suited to CT-based interventional procedures. A new robotic architecture was developed to perform interventional CT/MR procedures using both ultrasonic motors and pneumatics to position the needle and then insert it progressively. The whole robot can be sterilized and its mechanical error is less than 5mm [4].

Bricault *et al.* [5] developed a light robot with 5 DOFs to perform abdominal and thoracic punctures under CT or MRI guidance for diagnostic or therapeutic purposes. The translation accuracy is 1mm. Rotation and inclination accuracy are less than $1^{o}$. This robot is a lightweight (1 kg) and compact (15 x 23 cm). Compressed air is used as energy source.

In this paper we describe a small and lightweight patient-mounted CT and MRI robot under development for shoulder and hip arthrography for pediatric interventions. The robot has 3 DOFs and we plan to use piezo motors for actuation of the robot under MR imaging. A combination of adhesive tape and straps are planned for stable attachment of the robot to the patient body. Furthermore, to address the sterilization issues, the robot was designed to allow coverage of major portions of the robot by using sterile plastic sheet.

## MATERIALS AND METHODS

As shown in Fig. 1, the concept of a four-link parallel mechanism with a spherical joint is used to develop the robot which gives us 2 rotational DOF about the spherical joint. The whole four-link parallel mechanism slides translationally through link 4 to add the third DOF.

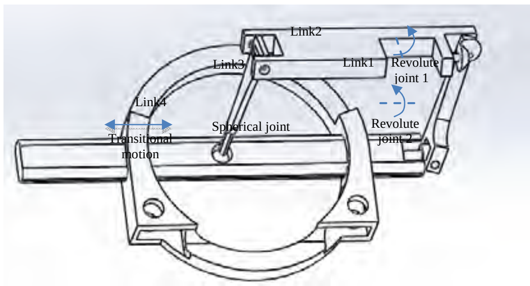
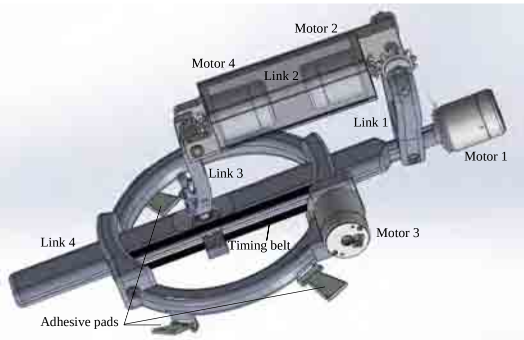



**Fig. 1** schematic of the parallel robot

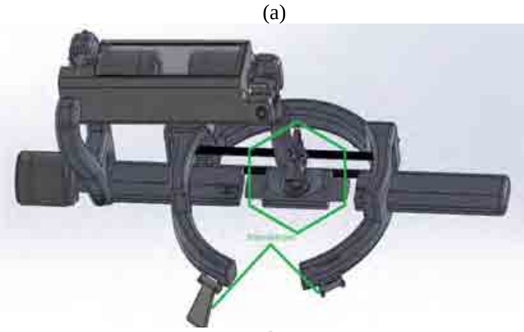
As shown in the Solidworks model in Fig. 2(a), motor 1 and motor 2 rotate the needle with respect to the spherical joint to provide the 2 rotational DOFs. Motor 3 provides translational motion along with link 4 through a timing belt and a pair of pulleys. Motor 4 is embedded in the robot to eventually drive the needle automatically by a remote command instead of manual needle insertion.

For medical robotic systems, sterilization is a critical issue that must be addressed. We considered three possibilities: 1) make the robot disposable, 2) use special material and sealing to make the robot sterilizable, 3) cover the robot with an appropriate protective sheet to avoid exposure of the robot to the environment. None of these methods alone seemed optimal for our application. Therefore, we combined these three methods and modified the first design to make the sterilization procedure easy, fast and cheap.

As shown in Fig. 2(b), by separating link 4 into three parts and link 3 into two parts it is possible to cover most parts of the robot and then assemble pieces of the links 3 and 4 together. The parts that are shown with green lines can be either disposable or sterilizable.




(a)



(b)

**Fig. 2** Solidworks 3D model of the final design (a) without considering sterilization and (b) considering sterilization.

As for control of the robot, we envision two possibilities: 1) a master-slave configuration, in which the physician can control the robot from the MRI control room with a standard joystick or with a MRI compatible joystick from the MRI procedure room; and 2) a positioning mode, in which the robot will pre-align its trajectory to some commanded path on the MRI images and an indication from the physician of the target point. In the second mode, the physician would then manually drive the needle to the target while the robot would maintain the desired trajectory.

The robotic mechanism will be interfaced to a computer through a Galil motor controller. The software will be implemented as a dialog-based MFC application in Visual C++ on the Windows operating system. The input from the user interface devices will be converted into control signals by the interfacing software to drive the robotic mechanism.

## CLINICAL WORKFLOW

Fig. 3 shows a prototype robot mechanism created from the Solidworks model using an Objet 500 rapid prototyping machine. This figure also shows how the needle is held. A protective sheet is used for separating the disposable parts from the rest of the robot.



**Fig. 3** First prototype of the robot with ABS material mounted on a body phantom. A protective cover is used to separate disposable part from the rest of the robot.

## DISCUSSION

We have completed our initial design and prototype mechanical system of a robot for shoulder arthrography. We first plan to demonstrate the workflow and targeting capability in the CT environment with the system described here. The next step will be to develop an MRI compatible version. The ultimate goal is for the robot to be capable of automatically driving a needle and injecting contrast material during a real-time MRI sequence to observe the joint function and make an accurate diagnosis.

## REFERENCES

[1] Shital Parikh, “The Trend of Pediatric Sports and Recreational Injuries in the U.S. in the Last Decade”, *American Academy of Orthopaedic Surgeons's (AAOS) Anual meeting*, 2013.

[2] Walsh, C., Hanumara, N.C., Slocum, A.H., Shepard, J.A., Gupta, R., “A Patient-Mounted, Telerobotic Tool for CT-Guided Percutaneous Interventions.” *J. of Med. Devices* 2(1), 011007.1–011007.10, 2008.

[3] Maurin, B., Bayle, B., Piccin, O., Gangloff, J., de Mathelin, M., Doignon, C., Zanne, P., Gangi, A. “A Patient-Mounted Robotic Platform for CT-Scan Guided Procedures.”, I*EEE Transactions on Biomedical Engineering* 55(10), 2417–2425, 2008.

[4] Nikolai Hungr, Céline Fouard, Adeline Robert, Ivan Bricault, Philippe Cinquin, “Interventional Radiology Robot for CT and MRI Guided Percutaneous Interventions”, *Med Image Comput Comput Assist Interv.* , 14(1):137-44, 2011.

[5] I. Bricault, E. Jouniaux, N. Zemiti, C. Fouard, E. Taillant, F. Dorandeu, and Ph. Cinquin, “ A Light Puncture Robot for CT and MRI Interventions”, *Engineering in Medicine and Biology Magazine,IEEE* May-June, 2008.

# A Novel Three-Dimensional Stereoscopic Viewer for Transanal Endoscopic Microsurgery: A Report of Two Clinical Cases

Aimee di Marco[1,2], Philip Pratt[1], Guang-Zhong Yang[1], Ara Darzi[1,2]

[1]*The Hamlyn Centre for Robotic Surgery, Imperial College London*

[2]*Department of Surgery and Cancer, Imperial College London*

## INTRODUCTION

Since its inception thirty years ago, Transanal Endoscopic Microsurgery ('TEMS') has been performed under 3D vision from the TEMS stereoscope (R. Wolf). Subsequent alternative systems, such as the TEO (Karl Storz) and TAMIS (Covidien) offer only 2D visualisation. 3D optics are said to improve the surgeon's depth perception, assisting in the accurate performance of awkward procedures such as this [1]. However, the appeal of the 3D visualisation is compromised by the fact that it is obtained by viewing directly into the stereoscope, necessitating an uncomfortable operating posture. To address this, and to permit future clinical work on intraoperative image overlay [2], a novel 3D stereoscopic viewer was developed to meet the requirements of 3D vision with improved ergonomic configuration and was employed in two clinical cases.



**Fig. 1** CAD design, stereoscopic viewer unmounted and suspended from stand.

## METHODS

Figure 1 shows the stereoscopic viewer, which was designed following the principles of the Wheatstone viewer [3]. Paired mirrors, lenses and video monitors (5.6" TVLogic VFM-056W 1280x800), receive input from the TEMS stereoscope via a pair of Storz HD cameras. The components of the viewer were mounted on a base plate, suspended from a custom-built frame (Gallops UK).

Consecutive patients listed for TEMS were recruited into this feasibility study, approved by the regional ethics review panel (reference 07/Q0703/24): an 81 year old female with a posterior T1 rectal adenocarcinoma and a 73 year old male with a posterolateral tubullovillous adenoma. The stereoscopic viewer and paired camera heads were bagged and draped for sterility and connected to the TEM stereoscope (figure 2).

Data recorded were: time taken for stereoscope setup and TEMS procedure. NASA-TLX and custom-designed usability questionnaires were completed post-operatively by the surgeon. Clinical follow-up of each case was undertaken.

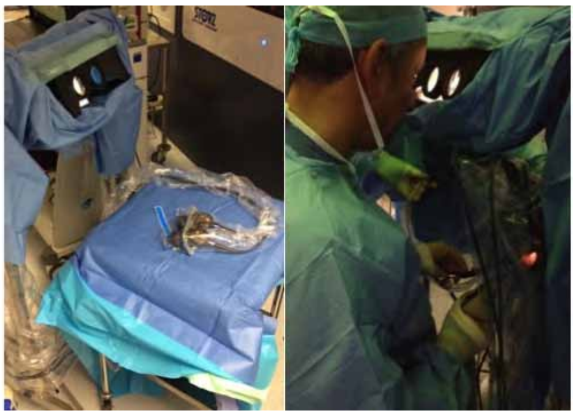


**Fig. 2** Sterile draping of stereoscopic viewer and cameras, surgeon performing TEMS using the viewer.

## RESULTS

Mean time to set up the stereoscopic viewer was 20 minutes (performed concurrently with scrub trolley preparation). Use of the stereoscopic viewer was found to be feasible in both cases (figure 2) and both tumours were successfully removed without event. Mean operative time was 63 minutes. Mean NASA-TLX score was 41.5/120 (low being good) and custom-questionnaire on usability, 80%. Specific feedback from the surgeon included 'high quality of 3D image' and 'improved comfort of head position'. Suggestions for improvement included reduced footprint of the suspension frame and relocation of video monitor cables. Both patients made uneventful recoveries with no peri-operative complications.

## CONCLUSIONS

This novel 3D stereoscopic viewer has been shown to be an effective means of visualisation in TEMS and early results from these 2 cases suggest improved ergonomics. Construction of the viewer cost under £2000 making it a simple and cost-effective solution, which is ready for more widespread clinical deployment

in TEMS and other procedures. Utilisation of such a viewer also paves the way for 3D intraoperative image augmentation in TEMS.

## REFERENCES


[1] P. Storz, G. F. Buess, W. Kunert, A. Kirschniak. 3D HD Vs 2D HD: surgical task efficiency in standardized phantom tasks. Surgical Endoscopy (2012) 26:5;1454-1460

[2] P. Pratt, A. di Marco, C. Payne, A. Darzi, G.-Z. Yang. Intraoperative Ultrasound Guidance for Transanal Endoscopic Microsurgery. MICCAI (2012) 463-470

[3] J. Kollin, A. H. Hollander. Re-engineering the stereoscope for the 21st century. Proc. SPIE (2007) 6490: pp. 64900

# The Core-Snake, the Variable Stiffness Laparoscopic Camera

Allen Jiang[1], Kaspar Althoefer[1], Prokar Dasgupta[2], Thrishantha Nanayakkara[1]

[1]*Centre for Robotics Research, King's College London,*

[2]*MRC Centre for Transplantation, NIHR Biomedical Research Centre,*
*King's College London*
*allen.jiang@kcl.ac.uk*

## INTRODUCTION

Successful and safe laparoscopic surgery is heavily dependent on its vision system, with the primary emphasis on the viewing angle and image stability [1]. Laparoscopic cameras, such as the Storz 10 mm laparoscope, are typically long, rigid tubes which have poor accessbility to target areas and require a second surgeon to operate. With a shifting enthusiam for natural orifice translumenal endoscopic surgery (NOTES), most groups prefer flexible endoscopes over the traditional rigid laparoscopes. However, these endoscopes were originally designed for intralumenal use, and tend to be application specific [1]. Thus, there is a technological and clinical need for a small, flexible camera designed for NOTES and other minimally invasive surgical procedures. It has been suggested that camera systems for NOTES also be deployable, as flexible endoscopes occupy port space, hindering the use for additional tools [1]. These tools, like the Olympus GIF TYPE 160, can be 8.6 mm in diameter, occupying over half of a 12 mm port. Deployable camera systems such as Pillcam, are unable to provide real time control due to their wireless connectivity.

The Core-Snake aims to bridge these gaps. The Core-Snake is a 10 mm diameter robot which can alter its body stiffness from being flexible to rigid via granular jamming. Most commonly seen in vacuum packed bags of rice or coffee, granular jamming is a phenomenon where a multitude of particles normally act like a fluid, but lock into a solid-like state when an external stress is applied [2],[3]. Thus, the Core-Snake is naturally compliant and can be pushed into position by the surgeon's laparoscopic tools, then it can lock its current position when a differential between the internal and external pressure is applied. In this case, the differential is induced by vacuuming the interior of the snake. This variable stiffness mechanism not only provides the surgeon with a wide viewing angle and accessibility when the snake is flexible, but also a stable vision platform when the snake is rigid [4]. Though it requires a tether for the video cables and pneumatic tubing, the cable and tube bundle is only 4 mm in diameter. The design of the robot allows the snake to be deployed into the body cavity, thus only occupying 4 mm of port space after initial insertion, a significant improvement over current endoscopes.



**Fig. 1** The Core-Snake, a low cost, granular jamming-based flexible laparaoscopic camera**.** Shown here its ability to access difficult areas, while occupying 4 mm of trocar port space.

## MATERIALS AND METHODS

The Core-Snake, seen in Fig. 1 and 2, is 10 mm in diameter, composed of three, 65 mm long segments filled with 1.5 mm diameter plastic spherical granules, and followed by a 4 mm tether. The outer membrane is made with a 0.12 mm thick PVC film. The section dividers are ABS plastic and were printed with a rapid prototyping machine. The tip camera is a 10 mm diameter CMOS sensor with a 640x480 resolution at 30 frames per second and was connected to a computer via USB. The tip also includes 4 white LEDs for light. The pneumatic line is a 2 mm outer diameter silicone rubber tube. Vacuum pressure is achieved with a Mastercool 90066-2V-220 pump, and measured by a Honeywell 0-30 PSI absolute pressure sensor.

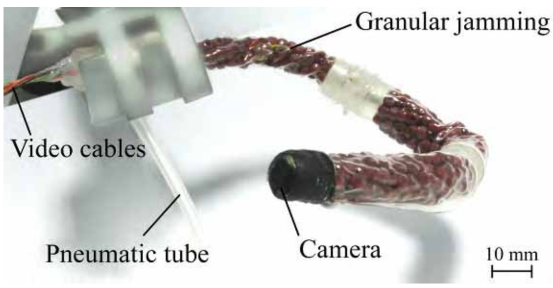



**Fig. 2** Here, jamming the Core-Snake granules locks it into its rigid state, and holding a 180 degree bend**.** The flexibility and variable stiffness of the camera system allows surgeons to navigate to a area of interest and lock the camera in the position.

To test the stiffness range of the robot, bending tests were conducted on one segment of the snake. The end of the segment was fixed, and the tip was deflected by 10 mm. The required load for this deflection was

measured by an ATI Nano17 Force/Torque sensor. The force and deflection measurements were then converted to Young's modulus E for a comparison of stiffness.

External groups utilizing granular jamming, particularly for snake-like or elephant trunk-like robots have shown that ground coffee is the ideal granule type for jamming [5]. However, in medical applications, concerns for using organic materials in a laparoscopic camera system resulted in tests to examine if there is a plastic substitute. The synthetic substitute would need to match the stiffness of ground coffee and withstand an autoclave, the most common method of disinfection.

## RESULTS

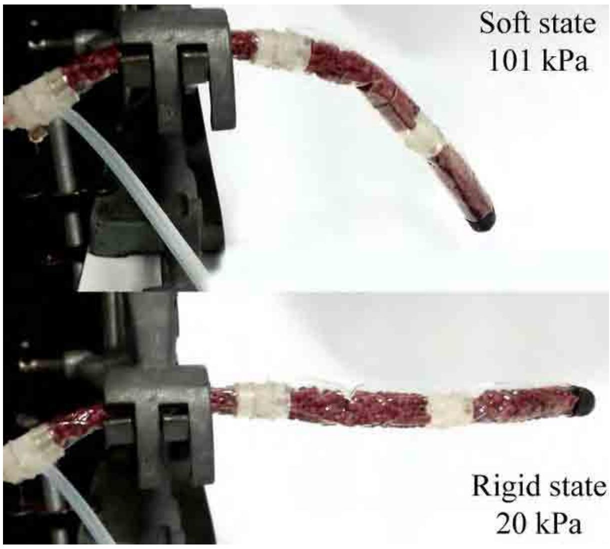



**Fig. 3** The snake bending due to weight when soft (top) vs the snake holding a horizontal position when rigid (bottom).

The bending test results show that, after deflected, one segment can exhibit 0.20 N of force at 101 kPa (soft state) and 0.42 N at 20 kPa (rigid state). The stiffness, Young's modulus E, is calculated from the bending results by $E = (4FL^3)/(3\pi dr^4)$, where F is the loading force, L is the segment length, d is the deflection distance, and r is the segment radius. Thus, E = 3.73 and 7.83 MPa for the soft and rigid states, respectively. These preliminary results show that the Core-Snake is able to increase its stiffness by 2.1 times. Fig. 3 visually shows what these stiffness values represent: the varied ability to hold the Core-Snake in a horizontal position. In other words, the rigidified snake is a stable platform.

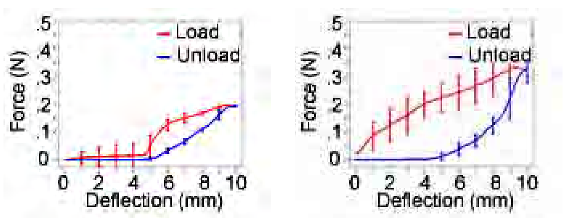



**Fig. 4** Ground coffee (left) vs plastic spheres (right) in the bending test when jammed. Plastic spheres outperformed

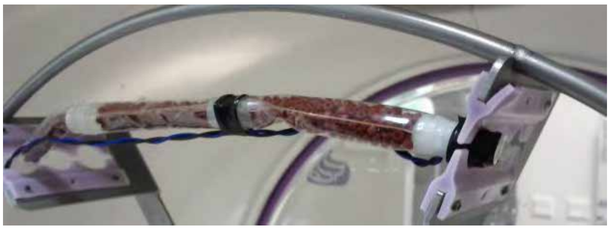


**Fig. 5** The Core-Snake inside a Labcaire Autoscope ISIS Automated Endoscope Reprocessor.

Bending tests, shown in Fig. 4, performed between ground coffee and plastic spheres for the rigid case showed that a synthetic substitute improved the stiffness. Unlike coffee particles, the plastic granules are able to withstand the sterilization process via steaming, both validating the use of granular jamming in a medical device and the use of synthetic granules.

## DISCUSSION

This paper presents a new type of NOTES-orientated laparoscopic camera system which is variable stiffness, deployable, and low cost. The total cost of the snake, excluding the vacuum pump, is approximately 20 GBP, 50 times less than traditional laparoscopes. Though some preliminary sterilization tests have been performed for the granules, they have not been done for the manipulator as a unit. However, because of the low cost nature of the system, an evaluative study should be done on the practicality of a disposable camera system. Currently, the positioning of the camera can be done by the surgeon's laparoscopic tools, reducing the need for a "cameraman." Future work involve adding a high definition camera, increasing the stiffness range of the snake, adding an integrated actuation system, and testing it in-vivo.

## ACKNOWLEDGEMENTS

This work was funded in part by the Seventh Framework Programme of the European Commission under grant agreements 287728 in the framework of EU project STIFF-FLOP and 270138 in the framework of EU project DARWIN, as well as by the National Institute for Health Research (NIHR) Biomedical Research Centre based at Guy's and St Thomas' NHS Foundation Trust and King's College London.

## REFERENCES

[1] Chang, Victoria C., et al. "A Randomized Comparison of Laparoscopic, Flexible Endoscopic… Cameras..." Surgical innovation (2012).

[2] Liu, Andrea J., and Sidney R. Nagel. "Jamming is not just cool any more." Nature 396.6706 (1998): 21-22.

[3] Aste, Tomaso, and Denis Weaire. The Pursuit of Perfect Packing. New York: Taylor & Francis, 2008. Print.

[4] Loeve, Arjo, Paul Breedveld, and Jenny Dankelman. "Scopes too flexible... and too stiff." Pulse, IEEE 1.3 (2010): 26-41.

[5] Cheng, Nadia G., et al. "Design and Analysis of a Robust, Low-cost, Highly Articulated manipulator enabled by jamming of granular media." ICRA, 2012. IEEE, 2012.

# Author Index

## S



## T



## U



## V



## W



## Y



## Z